Indian Head Division
Naval Surface Warfare Center
Indian Head, MD 20640-5035

IHCR 96-55
13 September 1996

SPHERICAL WAVES IN SATURATED SAND

Paul R. Gefken
Alexander L. Florence
Mohsen Sanai

REPORT DOCUMENTATION PAGE

Form Approved
QMB No. 0704-0188

1. AGENCY USE ONLY (*Leave Blank*)	2. REPORT DATE	3. REPORT TYPE AND DATES COVERED
	13 September 1996	Final—Sept. 1994 to Sept. 1995

4. TITLE AND SUBTITLE

SPHERICAL WAVES IN STATURATED SAND

5. FUNDING NUMBERS

N60921-94-C-0061

6. AUTHOR(S)

Paul R. Gefken
Mohsen Sanai
Alexander L. Florence

7. PERFORMING ORGANIZATIONS NAME(S) AND ADDRESS(ES)

SRI International
Menlo Park, CA 94025-3493

8. PERFORMING ORGANIZATION REPORT NUMBER

SRI PYU-6214

9. SPONSORING/MONITORING AGENCY NAME(S) AND ADDRESS(ES)

Indian Head Division
Naval Surface Warfare Center
Indian Head, MD 20640-5035

10. SPONSORING/MONITORING AGENCY REPORT NUMBER

IHCR 96-55

11. SUPPLEMENTARY NOTES

12a. DISTRIBUTION/AVAILABILITY STATEMENT

Approved for public release; distribution is unlimited.

12b. DISTRIBUTION CODE

13. ABSTRACT (*Maximum 200 words*)

The Naval Surface Warfare Center needs to develop the capability to determine numerically the characteristics of a propagating stress wave in saturated sand. To provide needed experimental data, SRI International performed precision experiments with the objective of measuring saturated sand material response resulting from the detonation of a spherical explosive charge. The instrumentation consisted of particle velocity gages as the primary measurement tool and stress gages as a secondary measurement tool.

Four experiments were performed using Eglin Beach sand at nominal saturation levels of 100%, 95%, and 78%, and 77%. The particle velocity time histories of the 100% and 78% saturated sand models showed 20% higher peak particle velocities in the 78% saturated sand model at ranges up to 2.04 cm from the charge and 30% lower peak particle velocities in the 78% saturated sand model at ranges beyond 3.05 cm from the charge. The higher peak particle velocity in the 78% saturated sand model near the charge is due to the lower inertial resistance because of less water in the pore space. The lower peak particle velocity in the 78% saturated sand model farther away from the charge is the result of larger attenuation of the particle velocity.

14. SUBJECT TERMS

Saturation value	Spherical wave	Stress measurements
Sand grain density	Pore volume	Sand grain size
In-situ dry density	Dry sand model density	Particle velocity

15. NUMBER OF PAGES

182

16. PRICE CODE

17. SECURITY CLASSIFICATION OF REPORT	18. SECURITY CLASSIFICATION OF THIS PAGE	19. SECURITY CLASSIFICATION OF ABSTRACT	20. LIMITATION OF ABSTRACT
UNCLASSIFIED	UNCLASSIFIED	UNCLASSIFIED	SAR

FOREWORD

The work described herein was performed by SRI International for the Naval Surface Warfare Center (NSWC) under Contract No. N60921-94-C-0061. The NSWC technical monitor was Mr. Tom Young and the technical supervisor was Dr. Howard Chen.

This work was performed under the general supervision of Dr. James Colton, Poulter Laboratory Director. Dr. Mohsen Sanai, Associate Director, was the SRI Project Supervisor and Mr. Paul Gefken, Research Engineer III, was the SRI Project Leader. Dr. Alexander Florence, Senior Staff Scientist, provided general consulting. Dr. James K. Gran, Department Director, provided technical support on the design and interpretation of stress gage records. Special thanks is given to Messrs. Mario Oyola, Michael Merritt, and Robert Boyle for performing the experiments and to Mrs. Bonita Lew and Mr. James Kempf for performing the data reduction.

Approved by:

R.M. McKeown
Director, Warheads Dynamics Division

Released by:

William M. Hinckley
Head, Underwater Warheads Technology and
Development Department

CONTENTS

ILLUSTRATIONS

ILLUSTRATIONS (Continued)

ILLUSTRATIONS (Continued)

ILLUSTRATIONS (Continued)

ILLUSTRATIONS (Continued)

ILLUSTRATIONS (Continued)

ILLUSTRATIONS (Continued)

ILLUSTRATIONS (Continued)

ILLUSTRATIONS (Continued)

ILLUSTRATIONS (Continued)

ILLUSTRATIONS (Continued)

ILLUSTRATIONS (Concluded)

TABLES

SECTION 1

INTRODUCTION

The Naval Surface Warfare Center (NSWC) needs to develop the capability to numerically determine the characteristics of a propagating stress wave in saturated sand. Satisfying this need requires a robust material model that covers the sand behavior for a wide range of sand saturation levels. To provide the data needed to develop and validate this material model, SRI International performed precision experiments to characterize the saturated sand response resulting from detonation of a spherical explosive charge.

The objectives of SRI's tests were to: (1) fabricate sand models with saturation levels between 100% and 80% of pore volume, (2) characterize the saturation uniformity of the models, and (3) measure the saturated sand material response resulting from the detonation of a spherical explosive charge. The instrumentation consisted of particle velocity gages as the primary measurement tool and stress gages as the secondary measurement tool. We made material response measurements for stress levels between 1 and 10 kbar (14.5 and 145 ksi).

Particle velocity measurements have been used at SRI in over 600 experiments[1-17] to characterize the geologic material response to shock wave propagation from an explosive source. The particle velocity gage, experimental apparatus, magnetic field source, and electronic data acquisition systems have been developed and calibrated at SRI to provide a measurement accuracy of ±2%. The experimental procedure consists of placing wire loops within the geologic material model which are concentric about a spherical explosive charge. The model is placed within the pressure vessel facility shown in Figure 1-1, which can be pressurized up to 69 bar (1 ksi) of overburden pressure. To measure particle velocity, a solenoid is placed around the geologic model to generate a magnetic field and induce an electromagnetic force in the wire loops, which is proportional to the wire loop radial pacticle velocity.

We have made numerous stress measurements using the SRI fabricated, miniflatpack, stress gage.[13,15,17,18-25] These experiments have focused on measuring the radial stress component from a spherical explosive source in homogeneous materials (such as rock and rock matching grouts).

In Section 2, we describe our technique for fabricating the saturated sand models, characterizing the saturation uniformity, measuring particle velocity and stress, and performing saturated sand model experiments with a spherical explosive charge. In Section 3, we present a

summary of results from four experiments. Experiments were performed at nominal saturation levels of 100%, 95%, 78%, and 77%. In Sections 4 through 7, we present the complete results from each experiment. In Section 8, we discuss our interpretation of the experimental results. In Section 9, we present our conclusion and recommendations for future work. Records from the stress gages are shown in Appendix A. Governing equations used to process the spherical wave particle velocity are given in Appendix B. Error analysis for the experimental measurements is given in Appendix C.

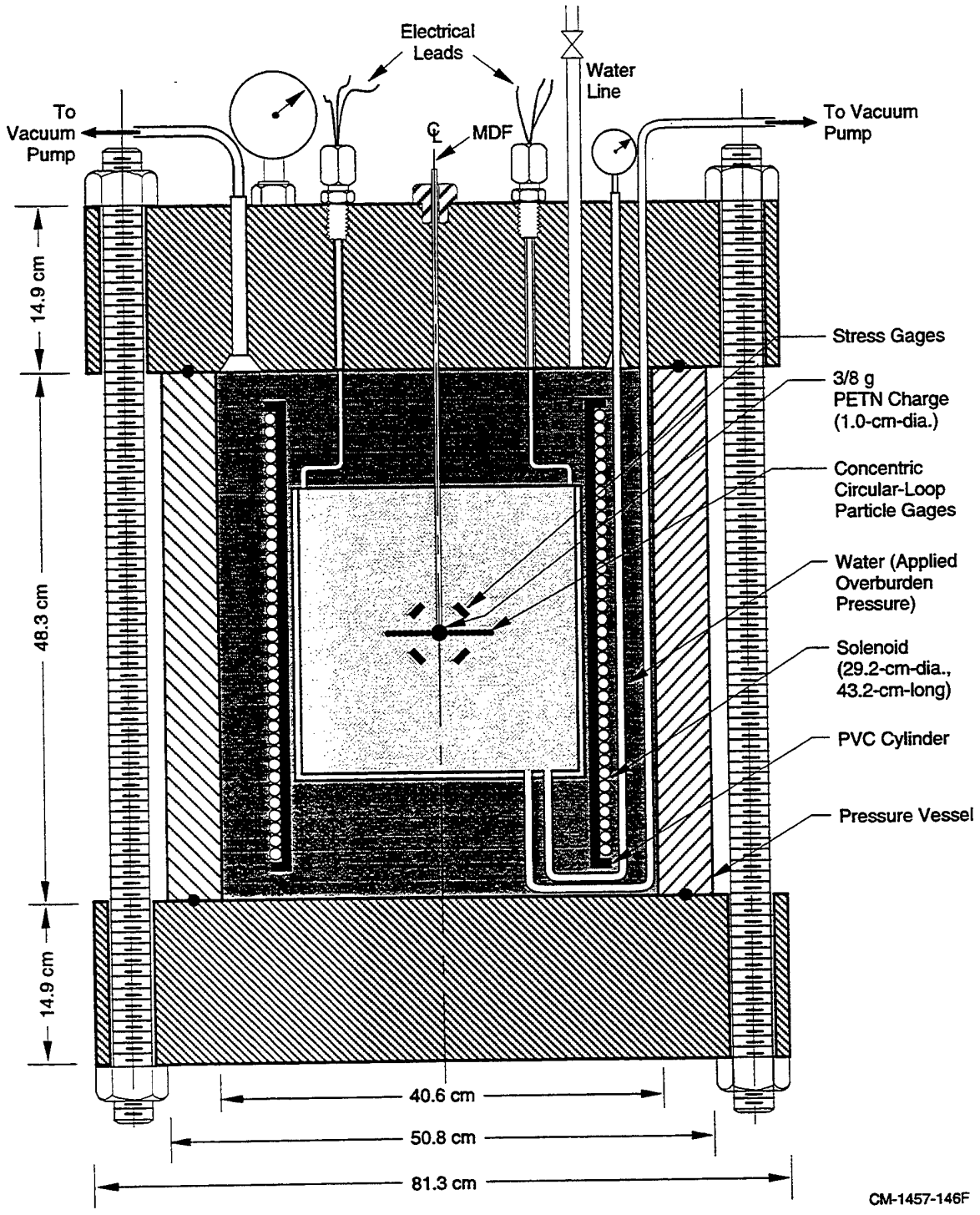

FIGURE 1-1. PRESSURE VESSEL CONFIGURATION FOR SAND MODEL SATURATION AND FOR PERFORMING SPHERICAL WAVE EXPERIMENT.

SECTION 2

EXPERIMENTAL TECHNIQUE

SAND MODEL PREPARATION AND CHARACTERIZATION

We obtained sand for our experiments from Eglin Air Force Base in Florida. Extensive material property characterization on Eglin Beach sand has been performed by Chitty et al., 1994.[26] The general material characteristics are:

Grain Density	2.653 g/cm^3
Minimum Dry Density	1.428 g/cm^3
Maximum Dry Density	1.676 g/cm^3
Grain Size	0.2 to 0.8 mm
In-Situ Dry Density	1.615 g/cm^3

Three sand model preparation techniques were developed to facilitate obtaining nominal 100%, 95%, and 78% saturation levels with respect to pore volume. These saturation values correspond, respectively, to 0%, 2%, and 10% air filled voids with respect to the total volume. The error estimations given below are based on accounting for the error associated with the weight scales used and for other possible error sources such as measurement of sand volume. A complete discussion of the error analysis is given in Appendix C.

We made the 100% saturation model by raining dry sand through a No. 20 sieve from a height of 61 cm (2 ft) into a cylindrical aluminum container. The 6061-T6 aluminum container had an inside diameter of 25.720 $\pm$ 0.003 cm (10.126 $\pm$ 0.001 in.), a length of 30.480 $\pm$ 0.051 cm (12.00 $\pm$ 0.02 in.), and a thickness of 1.27 $\pm$ 0.03 cm (0.50 $\pm$ 0.01 in.). The container bottom was a 1.3 $\pm$ 0.1-cm-thick 6061-T6 aluminum plate (0.50 $\pm$ 0.04 in.) Sand was rained into the container to form four 7.6 cm (3 in.) layers. After each layer, the container was vibrated for 15 minutes. After the fourth layer was formed, a 52 kg (115 lb) mass was placed on top of the sand and the sand was vibrated for an additional 30 minutes. This fabrication procedure was devised based on our investigation of several other techniques and was found to produce the most repeatable and uniform sand dry density characteristics.

Using the above technique, five sand models were fabricated with measured bulk dry densities of 1.628, 1.648, 1.663, 1.661, and 1.675 g/cm^3. These values give an average dry

density of 1.655 g/cm^3 with a standard deviation of 0.018 g/cm^3. The estimated maximum error associated with the bulk dry density measurement is $\pm$0.008 g/cm^3 ($\pm$0.5%). The average calculated porosity was 37.62 $\pm$ 0.30% [Porosity % = (1 - Dry Density/Grain Density) x 100].

To determine the sand dry density uniformity, we placed sample cups (2.540 $\pm$ 0.002 cm diameter by 2.540 $\pm$ 0.001 cm long) at different heights and azimuthal angles in the sand model during the sand raining procedure. Figure 2-1 shows the location and designation of the 12 sample cups. Table 2-1 gives the 12 sand dry density measurements for three models. For each model, the maximum variation with respect to the mean dry density was less than $\pm$0.031 g/cm ^{3} ($\pm$2%). The estimated maximum error associated with the dry density measurement from the sample cups is $\pm$0.045 g/cm^3 ($\pm$2.8%). In addition, there are no obvious trends between the sand dry density near the bottom as compared with the sand dry density near the top. Thus, the sand dry density values were random throughout the sand model.

TABLE 2-1. CHARACTERIZATION OF DRY DENSITY UNIFORMITY

Sample Cup	Model No. 1	Model No. 2	Model No. 3
1	1.639	1.608	NA
2	1.655	1.639	1.663
3	1.647	1.632	1.647
4	1.655	1.632	1.663
5	1.647	1.624	1.670
6	1.655	1.624	1.655
7	1.647	1.616	1.670
8	1.647	1.624	1.663
9	1.639	1.639	1.686
10	1.639	1.632	1.678
11	1.647	1.625	1.632
12	1.655	1.639	NA
Mean	1.648	1.628	1.663
Standard Deviation	0.006	0.010	0.015

To achieve 100% saturation, we placed the sand model in the pressure vessel shown in Figure 2-2. The air within the sand pore volume was removed by evacuating air directly from the sand model bottom as well as from the volume surrounding the model. Once the sand model was evacuated, deionized, and degassed, we placed water in the sand model at an overburden pressure of 1.2 bar (18 psi) until 100% saturation was achieved. Based on bulk weight measurements of

sand and water, this procedure produced total saturation levels for three different models of 100%, 101%, and 100%. The average saturation level from these three models was 100% and the standard deviation was 0.6%. The estimated maximum error associated with the bulk saturation measurement was ±1%.

As described above for the dry sand model, we characterized the saturation uniformity using sample cups placed in the model during the sand raining procedure, as shown in Figure 2-1. However, the sample cups used for the saturation measurements had a No. 100 mesh screen placed over the bottom end to confine the sand and allow the water to freely pass through the cup. After saturation, the sample cups were carefully removed, weighed to obtain the saturated density, and then dried and weighed to obtain the dry density. Figure 2-3 shows a profile of saturation versus height obtained from the sample cups. Except for a single sample cup that indicated 96% saturation, all sample cups indicated saturation levels in excess of 100%. Because it is not possible to achieve saturation levels in excess of 100%, the measured saturated levels in excess of 100% are attributed to the relatively large error associated with determining differences between small quantities of material. The estimated maximum error associated with the sample cup saturation measurement is ±7%.

To obtain the 95% saturated model, we first made a 100% saturated model as described above and then allowed the model to drain through a 1.3 ± 0.1-cm-thick (0.5 ± 0.04 in.) 6061-T6 aluminum plate that was perforated with 1.3-cm-diameter (0.5 in.) holes spaced at a center to center distance of 1.9 cm. To prevent the sand from passing through these holes, a No. 100 mesh was placed over the perforated plate. Bulk weight measurements indicated a saturation level of 95% ±1% after water drainage for a period of 91 hours. During the water drainage period, the top of the sand model was sealed to prevent evaporation. To determine the saturation uniformity, we used a coring technique in place of the sample cup technique described above. The coring technique was employed because we believed the No. 100 mesh screen on the sample cup bottom would restrict water drainage. The coring tool was fabricated from individual 2.230 ± 0.025-cm-diameter (0.878 in.) by 2.540 ± 0.006 cm long (1.000 in.) tubes. The individual tubes are taped together to form a 30.5-cm-long (12.0 in.) continuous tube that could be easily separated into individual sections by simply cutting the tape. The estimated maximum error associated with the core technique is ±10%, which is larger than the estimated error associated with the sample cup technique because the separation of the core into individual sections exposes two free ends rather than a single end associated with the sample cups. Free ends can induce error because the sand grains may be slightly above or below the free edge, and therefore cause error in the estimated sand volume. The cores were inserted into the sand by tapping the end with a rubber mallet. Because

the sand state is near its maximum density and saturation level, the insertion of the cores caused noticable expansion of the sand top surface and percolation of water.

Figure 2-4 shows the measured variation of saturation level with height obtained from one core at the center (No. 1) and four cores placed at a radius of 7.6 cm (3.0 in.) and at azimuthal angles of 0, 90, 180, and 270 degrees (Nos. 2, 3, 4, and 5). Several trial sand models were fabricated and cored in order to perfect the technique and obtain the results shown in Figure 2-4. The cores show the trend of saturation levels between 93% and 99% near the bottom and saturation levels between 78% and 88% at the midplane (15 cm). Above a height of 20 cm, no results are shown due to disruption of the sand within the core sections. The average measured saturation from 35 core sections was 88%, which is lower than the average saturation level from the bulk weight measurement by 7%. Because of this difference, we are skeptical of the results from the core measurements.

Because the technique of fabricating a 100% saturated model and then allowing the model to drain to achieve a reduced saturation level did not produce an adequate saturation uniformity, we used a different technique to generate partially saturated sand models with saturation levels between 77% and 78%.

We made the partially saturated, 77% and 78% models by mixing measured quantities of sand and water together to produce a specific saturation level. With this procedure, the maximum attainable dry density was nominally 1.45 g/cm^3 and the minimum porosity was nominally 45%. These values differ by approximately 10% from the dry density and porosity values obtained for the 100% and 95% saturated models. In the three sand models fabricated, the average saturation levels were 80%, 73%, and 76% based on bulk weight measurements of sand and water. Using the coring technique already described, we measured the saturation uniformity for the three sand models at the same locations described earlier for the 95% saturated model. Because these models are not at their maximum consolidation and saturation levels, the insertion of the cores was much easier than for the 95% saturated model. In addition, there was little or no noticable sand movement or water percolation. From 50 core samples for each sand model, the average measured saturation was 81%, 75%, and 75%, respectively. The standard deviation was typically 3%. The similarity of the average core saturation value and the bulk measurement saturation value helps validate our novel saturation characterization technique.

Figure 2-5 shows the saturation uniformity for the sand model with the bulk weight saturation level of 76%. The maximum saturation variation from the average value of 75% between a height of 7.2 cm (3 in.) and 22.8 cm (9 in.) is within $\pm$4%.

INSTRUMENTATION

The primary measurement objective of the experiments was to characterize the saturated sand material response with respect to particle velocity. A secondary measurement objective was to characterize the material response with respect to radial and circumferential stress components.

To measure particle velocity, we placed wire loops within the saturated sand medium and concentric with a spherical explosive charge. Figure 2-6 shows the experimental arrangement for the particle velocity gages, which were located at radii of 0.54, 1.01, 1.55, 2.04, 2.54, 3.05, 3.55, and 4.05 cm. The estimated measured error associated with the wire loop location is $\pm$0.05 cm. The wire loops have a diameter of 0.30 mm (0.012 in.) and a density of 6.21 g/cm^3. The wire loop diameter is approximately the same as the average sand grain size. Although the wire density is larger than the grain sand density (2.653 g/cm^3), extensive experience has shown that the wire loops travel with the sand particle motion. Surrounding the sand model is a solenoid, as shown in Figure 2-2, which generates a vertically oriented magnetic field (B = 0.181 Tesla) through the midplane containing the particle velocity gage loops. The motion of these loops through the magnetic field flux lines generates a measurable electromagnetic force (ε) in volts. Using Faraday's law, the particle velocity $u = \varepsilon/Bl$, where l is the length ($2\pi r$) of the particle velocity gage. Because the gage particle velocity results in an increase in the gage length at each data point (approximately every 100 ns), a new gage length is determined through temporal integration of the particle velocity record ($l = 2\pi (r + \Delta r)$. The new gage length is then used to determine the particle velocity for the next data point.

Stress measurements that we have made using the SRI fabricated, miniflatpack, stress gage have focused primarily on measuring the radial stress component from a spherical explosive source in homogeneous materials (such as rock and rock matching grouts).[13,15,17,18-25] Typically, results in these material types have indicated a precision level within $\pm$20%. Using the miniflatpack stress gage in saturated sand may have an associated larger level of uncertainty because the saturated sand is most likely inhomogeneous. Furthermore, the saturated sand inhomogeneity may be greatest near the miniflatpack stress gage due to the inclusion effect of the gage. We expected the fabrication procedure for the 100% saturated sand model to produce a more homogeneous saturated sand material, particularly near the stress gage, than did the fabrication technique for the 95%,78%, and 77% saturated sand models.

Figure 2-7 shows the miniflatpack stress gage that we used. The gage package consisted of a Dynasen (Model No. YB4-50-EK), 3.2-mm-square (0.125 in.), ytterbium, sensing element sandwiched between two, 0.15-mm-thick (0.006 in.), stainless steel plates. The ytterbium was

electrically isolated from the stainless steel plates using a 0.025-mm-thick (0.001 in.) layer of Kapton tape. The stainless steel plates were connected to ground for gage shielding.

To measure the radial stress component, we oriented the stress gage so that the gage face was perpendicular to the incident stress wave plane. To measure the circumferential stress component, we oriented the stress gage so that the gage face was parallel to the incident stress wave plane. In Experiments 1 and 2 (100% and 95% saturated sand models), two radial and two circumferential stress gages were both placed at nominal ranges of 2 cm (0.79 in.) and 3 cm (1.18 in.). Figure 2-8 shows the radial and circumferential stress gage layout for Experiments 1 and 2. In Experiments 3 and 4 (78% and 77% saturated sand models), four radial stress gages were placed at a nominal range of 2 cm (0.79 in.) and a nominal range of 3 cm (1.18 in.).

Because ytterbium is sensitive to in-plane strain, we made miniflatpack strain gages in the same manner as described above for the ytterbium stress gages and placed them at the same orientations and ranges as the stress gages. The strain-time histories from these gages were used in the data reduction for the stress gages to reduce the ambiguity of the stress measurement due to possible in-plane strain.

Figure 2-9 shows sequential photographs taken during the placement of particle velocity and stress gages within the aluminum container. Figures 2-9(a) and (b) show close-ups of particle velocity gage loops and radial and circumferential stress gages. The particle velocity gage loops were held in place using a web made from thin thread. The stress gagse were held in place using a brass tube rigidly connected to the aluminum container wall. Figure 2-9(c) shows the complete particle velocity and stress gage configuration along with the spherical explosive charge at the center.

EXPLOSIVE CHARGE

Figure 2-10 shows the spherical explosive charge used to generate a spherically divergent wave in the saturated sand. The charge consisted of 3/8 g of PETN explosive powder packed to a density of 1.0 g/cm^3. The PETN was contained within a spherical shell of Lexane with an outside diameter of 1.00 ± 0.01 cm (0.39 in.) and a wall thickness of 0.050 ± 0.005 cm (0.020 in.). The PETN was detonated at its center using a 2 g/ft (0.42 g/m) mild detonating fuse (MDF), which was contained within a stainless steel tube to minimize the wave generated from the MDF detonation. The MDF consisted of PETN encased within a lead sheath. The mass per unit length of the PETN is 0.42 g/m and of the lead is 6.5 g/m. The MDF detonation velocity is 6902 m/s. A thin coat (0.08 mm thick) of urethane rubber is placed around the Lexan sphere to prevent seepage of water into the PETN from the saturated sand.

The PETN charge used here has been employed in numerous experiments and has a reliable Jones-Wilkins-Lee (JWL) equation of state for inclusion in numerical simulations. For example, Reference 15 shows a comparison of calculated with experimental particle velocities in limestone. To obtain the calculated particle velocities here, we used the standard JWL equation-of-state parameters for PETN.

The JWL equation of state defines the pressure as

$$p = A\left(1 - \frac{\omega}{R_1 V}\right)e^{-R_1 V} + B\left(1 - \frac{\omega}{R_2 V}\right)e^{-R_2 V} + \frac{\omega E}{V} \qquad (2.1)$$

where p is the pressure, E is the energy, and V is the ratio of volume of the detonation products to the volume of the undetonated explosive. For PETN with a density of 1.0 g/cm^3, the JWL parameters are

$A = 7300$ kbar
$B = 100$ kbar
$R_1 = 7.0$
$R_2 = 2.0$
$\omega = 0.28$

with an initial energy E_o of 57 kbar, a detonation velocity of 5600 m/s, and a Chapman-Jouguet (CJ) pressure of 75 kbar.

OTHER SAND CHARACTERIZATION EXPERIMENTS

Table 2-2 summarizes the sonic wave speed measurements made in sand with different saturation levels at 1 atm pressure and at a temperature of 20°C. The sonic wave speed measurements were made using two parametric transducers with a fixed frequency of 0.5 MHz. These transducers were placed within a Lucite tube to allow for separating the transducers between a known weight and volume of sand and water mixture. For reference, with air only between the transducers, the measured sound speed was 338 m/s (published value = 331.3 m/s). For deionized (but not degassed) water only between the transducers, the measured sound speed was 1438 m/s (published value = 1450 m/s). For dry sand with a density of 1.60 g/cm^3, the measured sound speed was 760 m/s.

To saturate the sand, we mixed a measured weight of water with the sand and then vibrated and repacked the combined sand/water mixture in the Lucite tube housing. In this way, we could achieve some degree of uniformity. However, this process tends to produce relatively higher porosity levels than consolidating dry sand, as is shown in Table 2-2. This is the reason for the

initial drop in sonic velocity from 760 to 643 m/s associated with dry and 30% saturated values, respectively. The data indicate a decrease in sound speed from the maximum value of 1687 m/s at 100% to 953 m/s at 81.5% saturation.

TABLE 2-2. CHARACTERIZATION OF SONIC WAVE SPEED FOR DIFFERENT SAND SATURATION LEVELS

Dry Density (g/cm^3)	Total Porosity (%)	Saturated Density (g/cm^3)	Wave Speed (m/s)	Saturation Level (%)
1.60	40.0	—	760	Dry
1.46	44.8	1.59	643	30.0
1.51	43.1	1.75	799	56.7
1.56	41.2	1.86	800	72.7
1.54	42.1	1.88	953	81.5
1.57	41.0	1.94	1617	91.8
1.58	40.6	1.97	1687	96.1

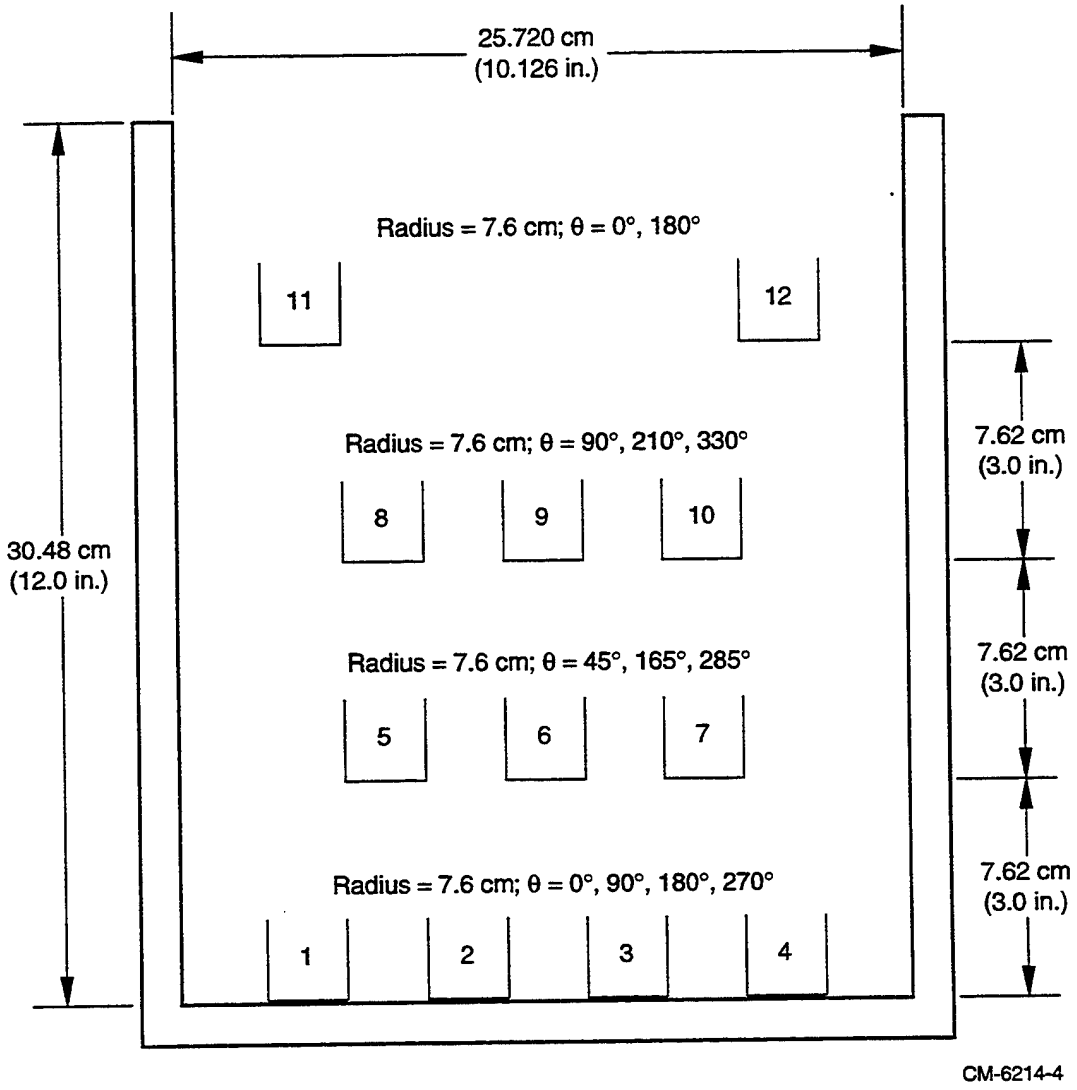

FIGURE 2-1. LOCATION OF SAMPLE CUPS FOR SAND DRY DENSITY AND SATURATION UNIFORMITY CHARACTERIZATION

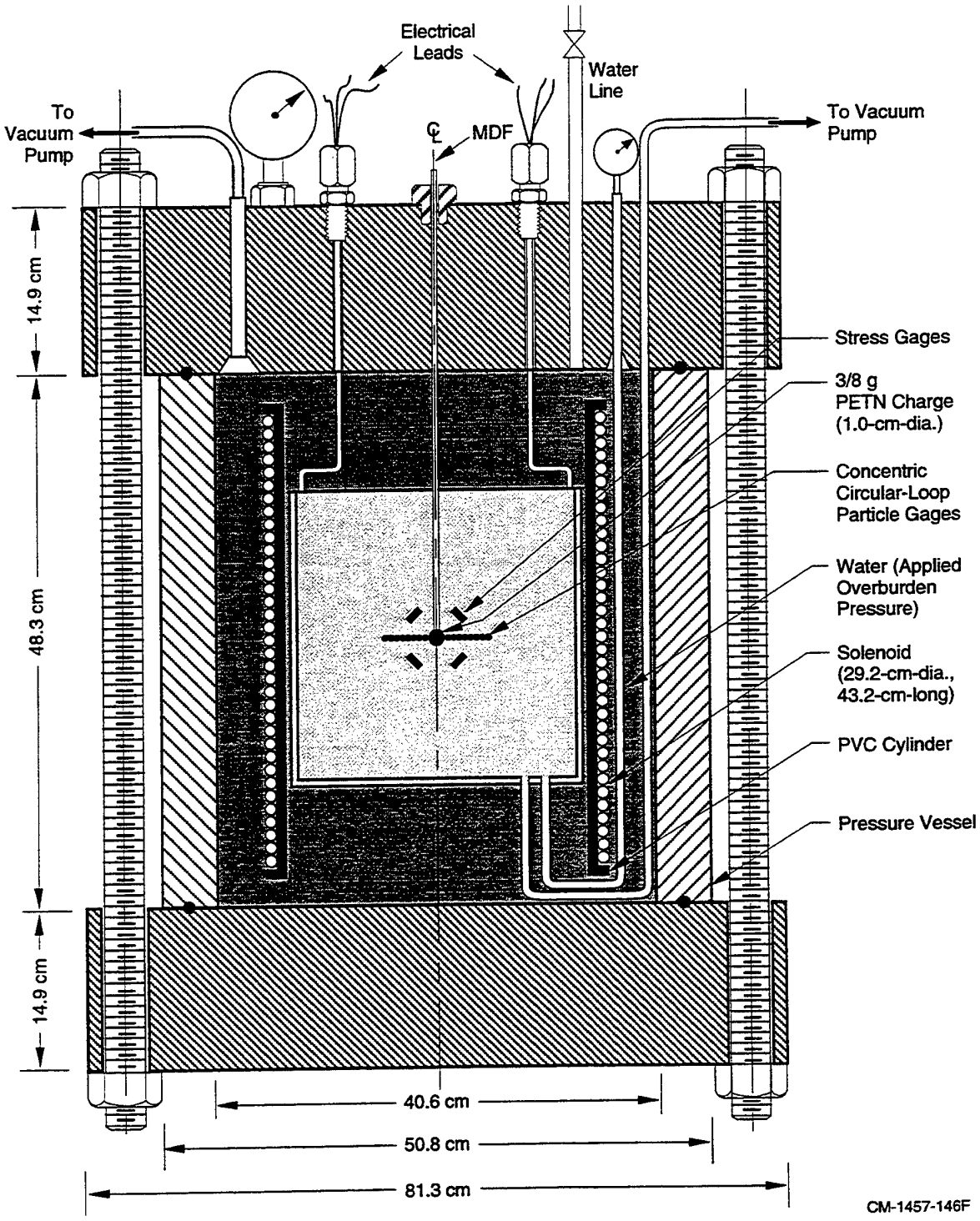

FIGURE 2-2. PRESSURE VESSEL CONFIGURATION FOR SAND MODEL SATURATION AND FOR PERFORMING SPHERICAL WAVE EXPERIMENT.

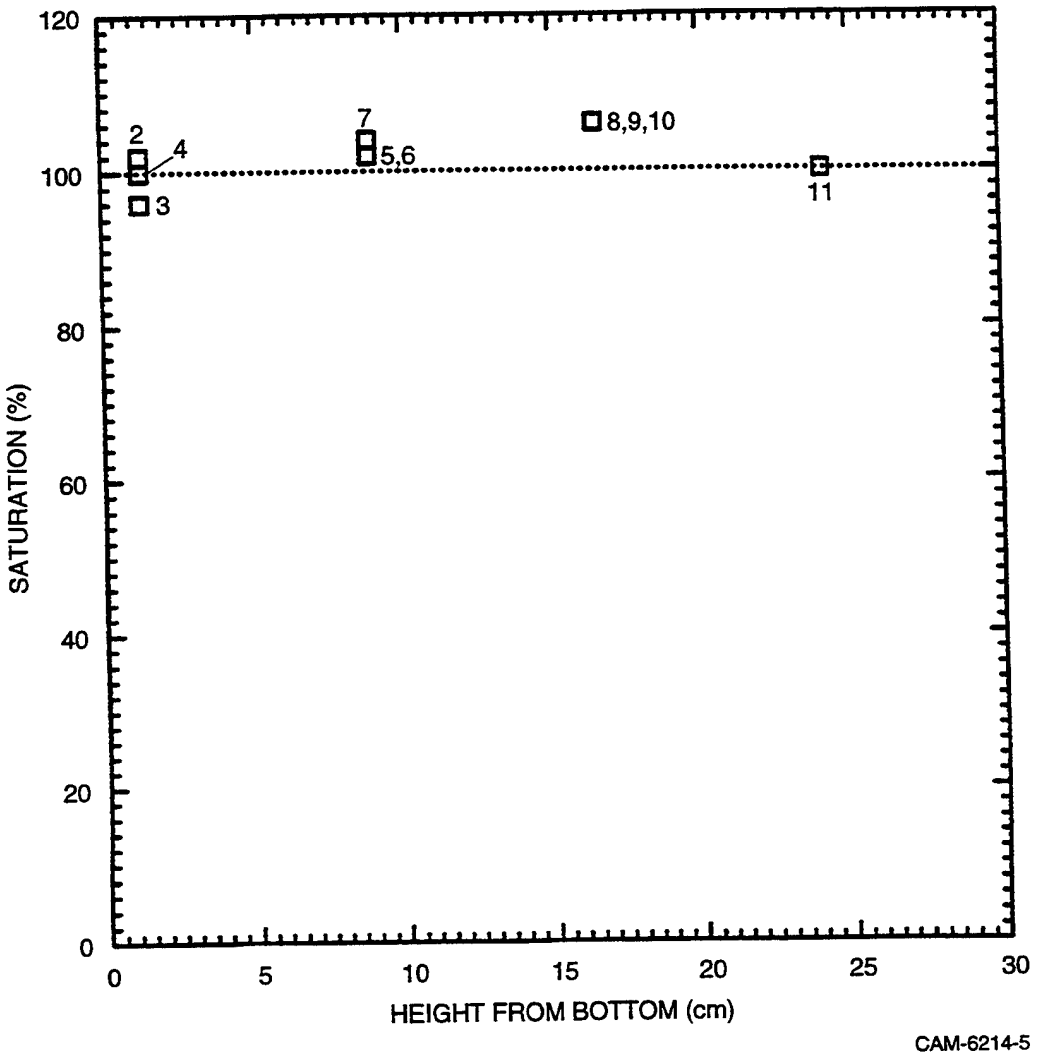

FIGURE 2-3. SATURATION UNIFORMITY FOR 100% SATURATED SAND MODEL

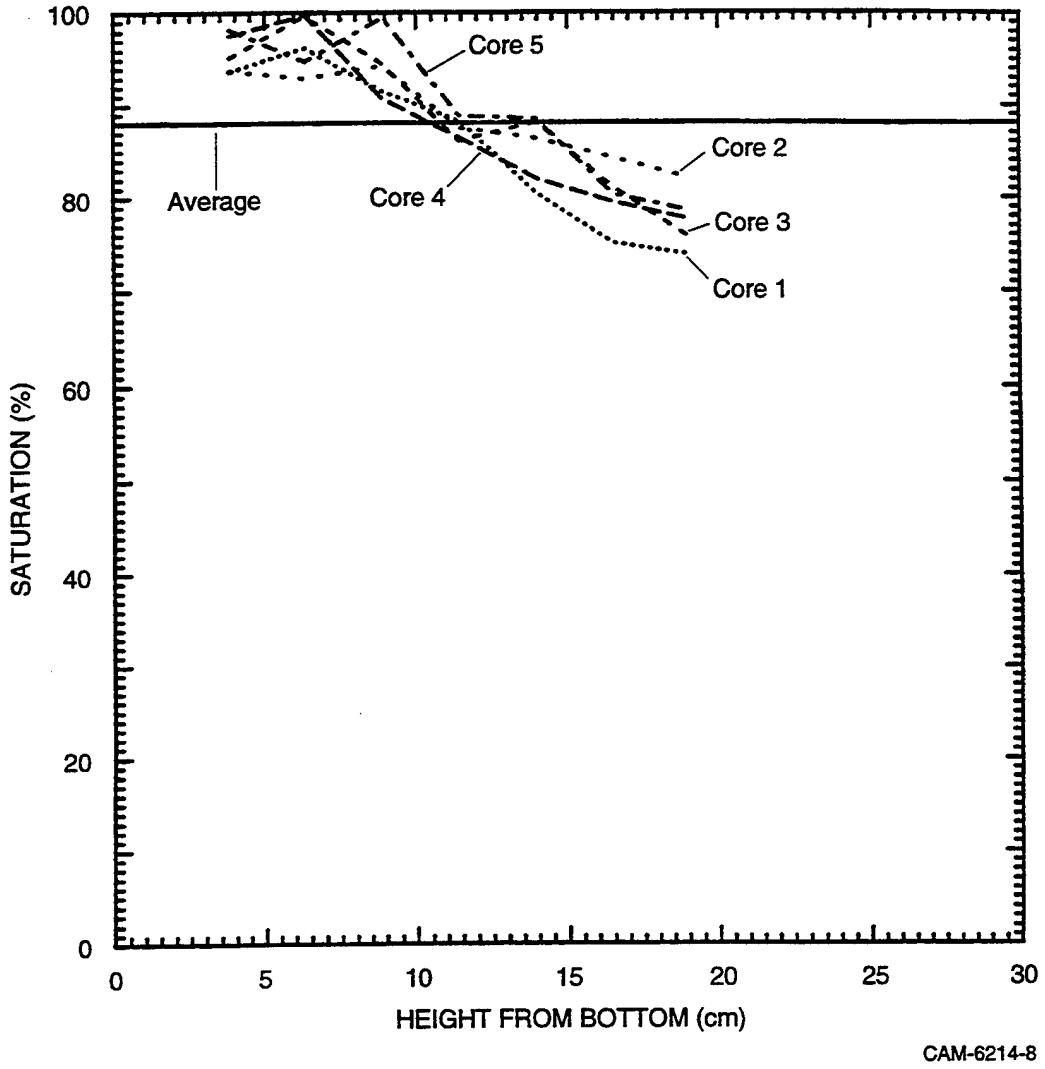

FIGURE 2-4. SATURATION UNIFORMITY FOR 95% SATURATED SAND MODEL

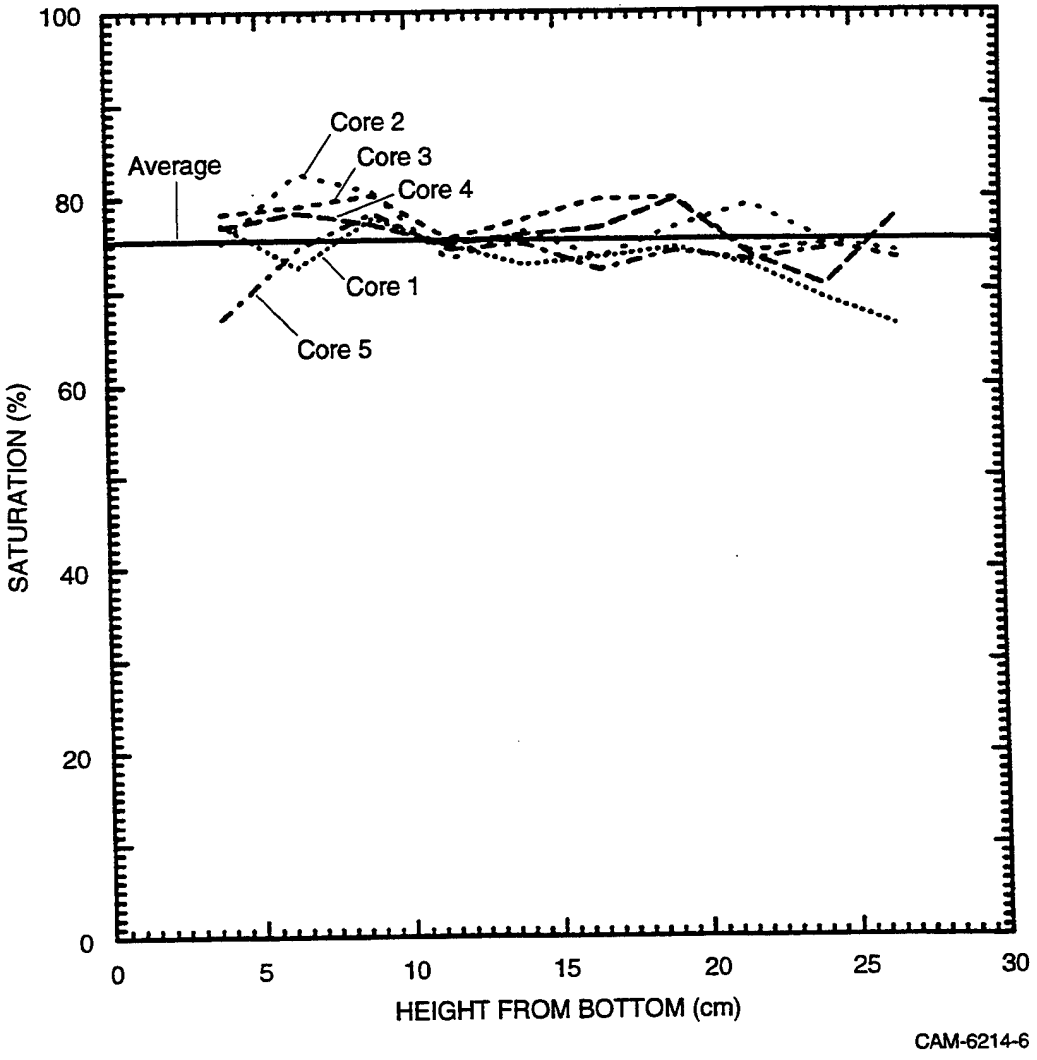

FIGURE 2-5. SATURATION UNIFORMITY FOR 75% SATURATED SAND MODEL

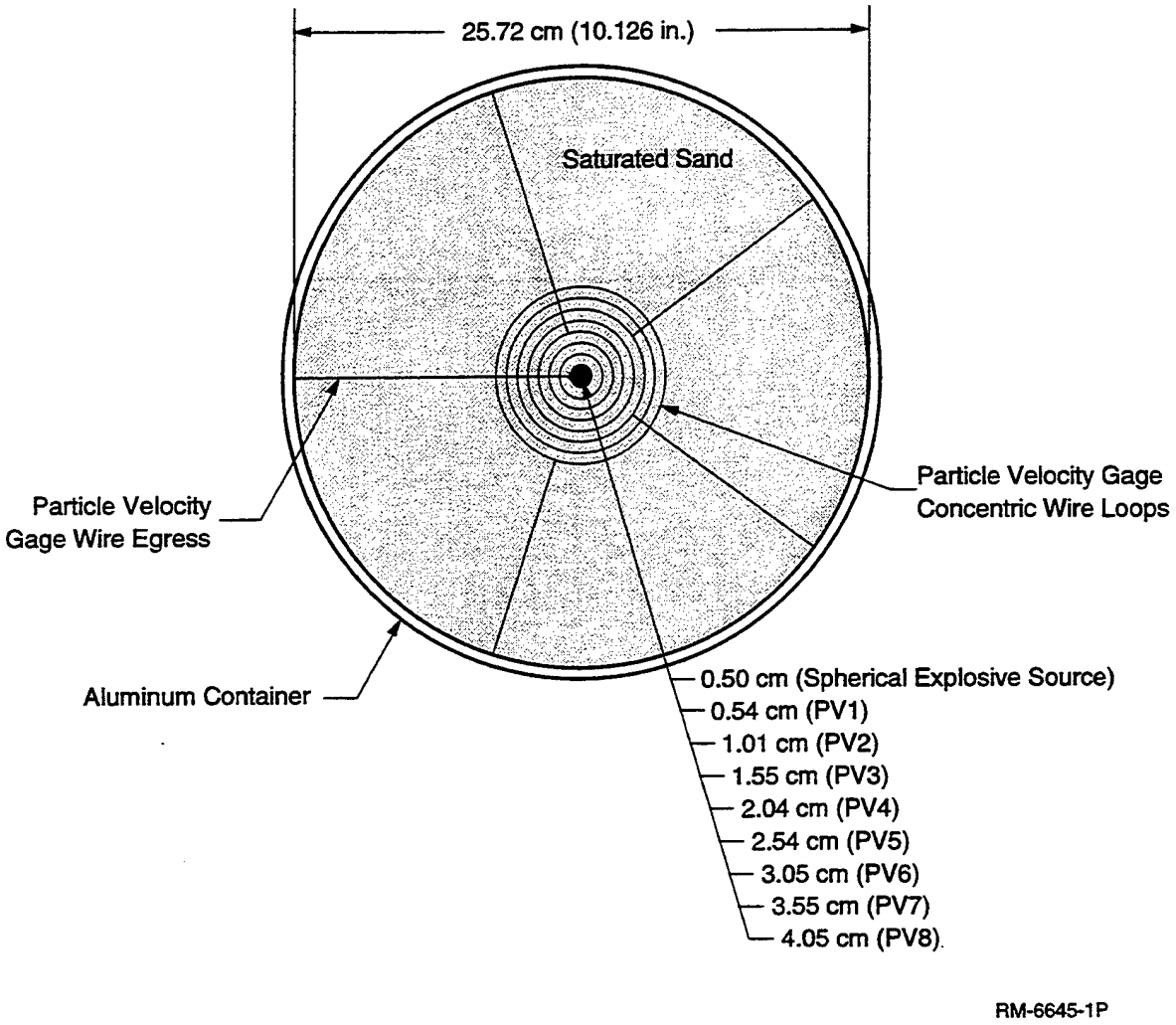

FIGURE 2-6. MIDHEIGHT CROSS SECTION OF SAND MODEL SHOWING PARTICLE VELOCITY GAGE LOCATIONS AND LEAD EGRESS

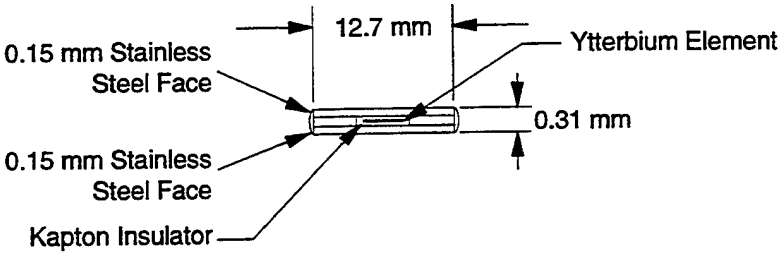

(a) Front View

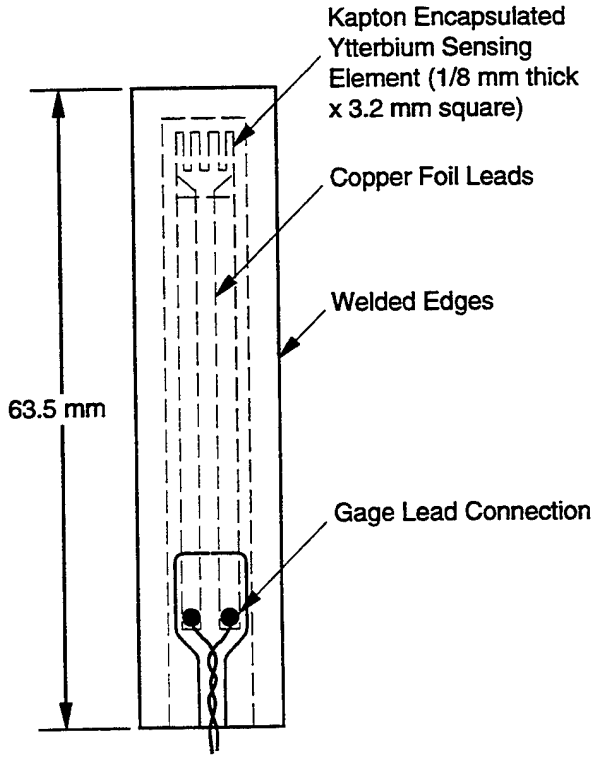

(b) Top View

JM-8321-46E

FIGURE 2-7. SRI MINIFLATPACK STRESS GAGE

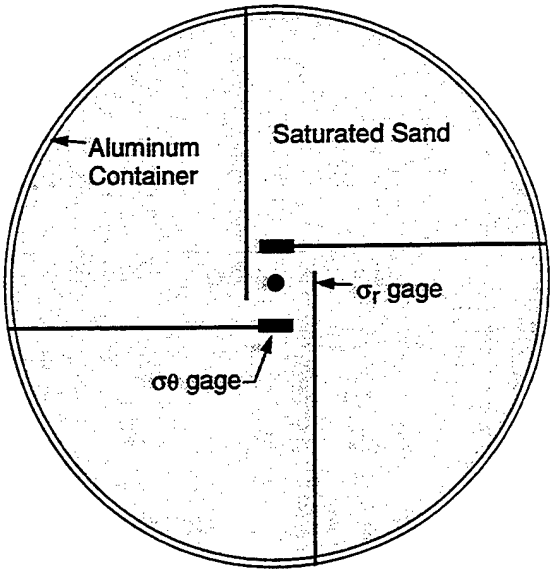

(a) Stress Gage Arrangement at 2 cm Range

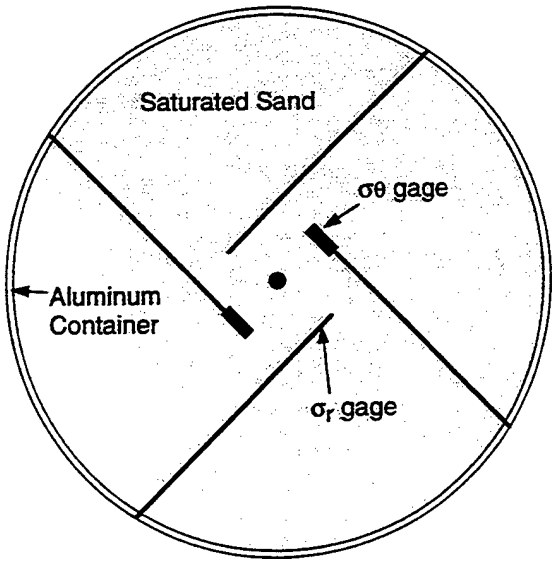

(b) Stress Gage Arrangement at 3 cm Range

σ_r = radial stress
σ_θ = circumferential stress CM-317581-101B

FIGURE 2-8. STRESS GAGE CONFIGURATIONS FOR EXPERIMENTS 1 AND 2

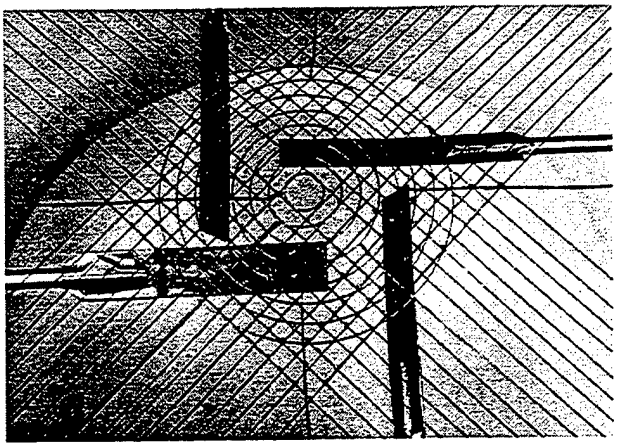

(a) Particle Velocity Gage Loops

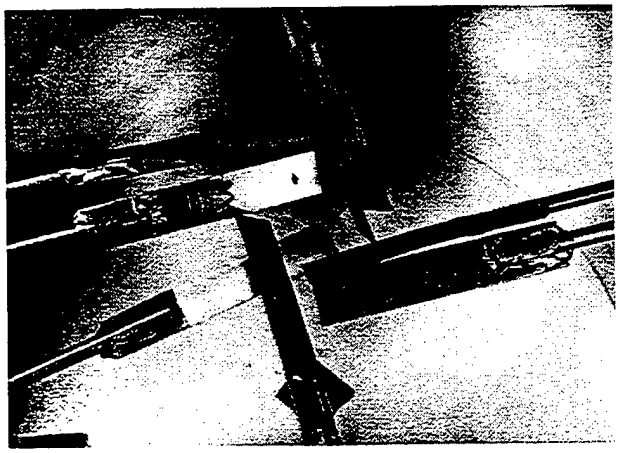

(b) Radial and Circumferential Stress Gages

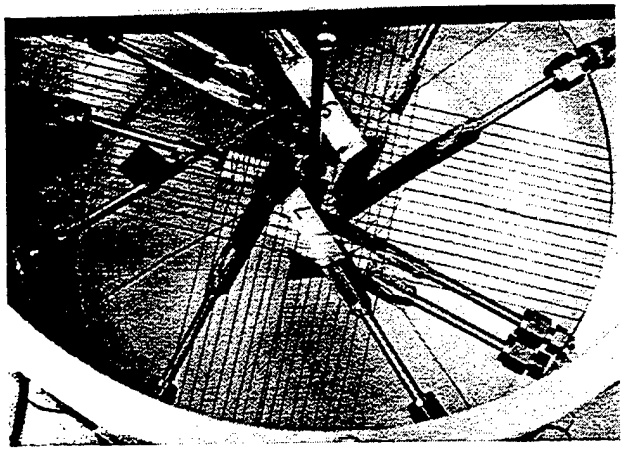

(c) Complete Particle Velocity and Stress Gage Configuration

C-6214-7

FIGURE 2-9. PLACEMENT OF PARTICLE VELOCITY AND STRESS GAGES IN SAND MODEL ALUMINUM CONTAINER

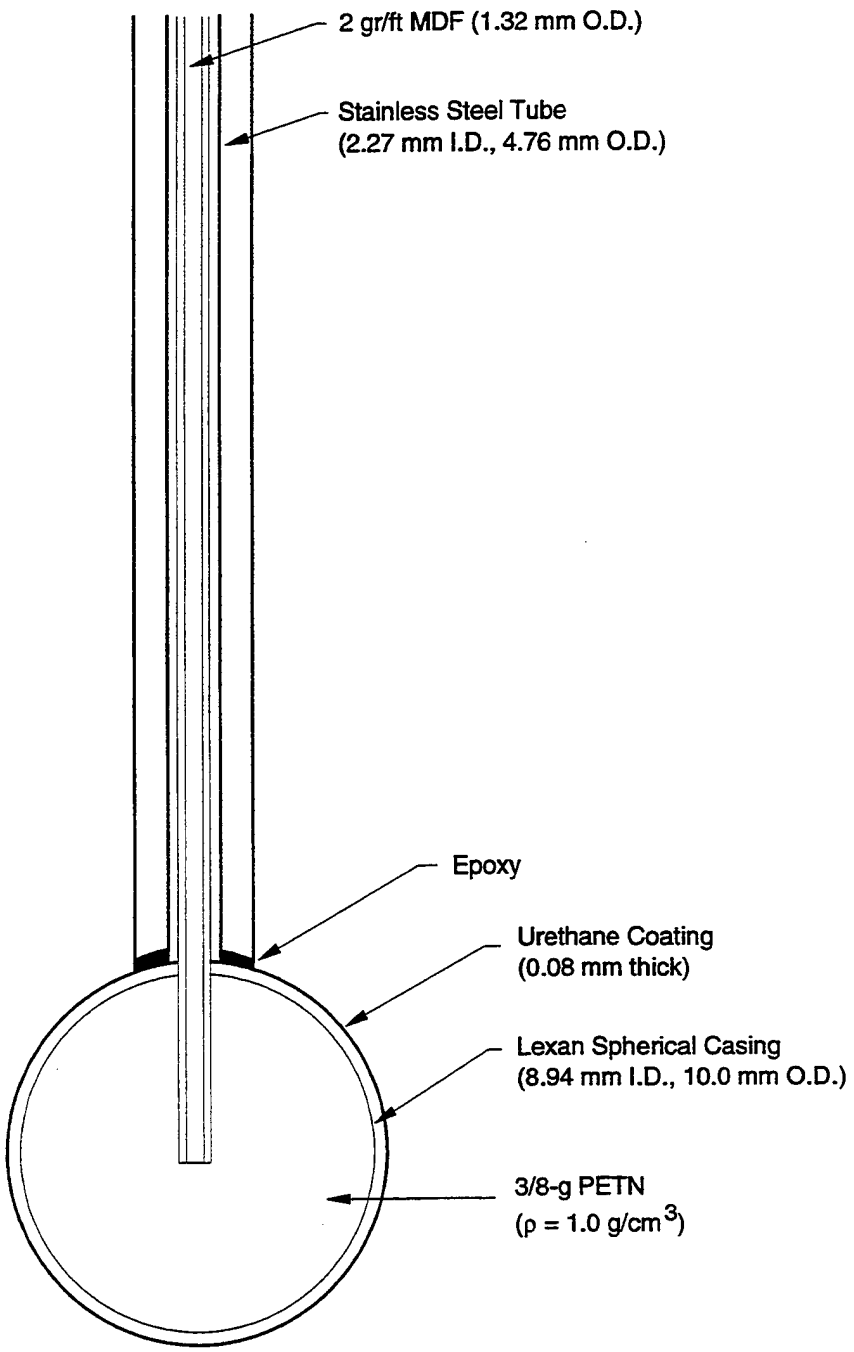

FIGURE 2-10. 3/8-g PETN CHARGE CONFIGURATION.

SECTION 3

SUMMARY OF EXPERIMENTAL RESULTS

We performed four experiments using the experimental techniques described in Section 2. Table 3-1 summarizes the sand model conditions based on bulk weight measurements taken before each experiment. The saturation levels given in Table 3-1 are percentage of pore volume. The 100%, 95%, 78%, and 77% saturation levels correspond to 0%, 2%, 10%, and 10% air voids of the total volume.

TABLE 3-1. SAND MODEL EXPERIMENTAL PROPERTIES

Experiment No.	Dry Density ($g/cm^3 \pm 0.008$)	Porosity (% ± 0.3)	Saturated Density ($g/cm^3 \pm 0.011$)	Total Saturation (% ± 1)
1	1.678	36.8	2.051	100
2	1.659	37.5	2.012	95
3	1.465	44.8	1.815	78
4	1.452	45.3	1.802	77

In this section, we present a summary of experimental results. Detailed discussions of experimental results are presented in Section 4 for Experiment 1, Section 5 for Experiment 2, Section 6 for Experiment 3, and Section 7 for Experiment 4. In Section 8, we compare Experiment 1, Experiment 2, and Experiment 3 (100%, 95%, and 78% saturated sand models).

PARTICLE VELOCITY MEASUREMENTS

As described in Section 1, the technique for particle velocity measurements has been perfected to provide an estimated error of ±2% and has been used in over 600 experiments in geologic materials at SRI.[1-17]

The 100% saturated model produced the particle velocity-time histories shown in Figure 3-1. The abrupt drop in particle velocity seen at approximately 20, 60, and 130 μs for gages at ranges of 1.01, 1.55, and 2.04 cm, respectively, signifies the gage failure due to excessive hoop strain. The peak particle velocity varied from approximately 192 m/s at a range of

1.01 cm to 26 m/s at a range of 4.05 cm. Based on the time of arrival (TOA) of the particle velocity the wave front speed varied between 2750 m/s at a range of 1.01 cm to 1750 m/s at a range of 4.05 cm. The arrival of the reflected wave from the aluminum cylindrical container occurs approximately after 130 μs for particle velocity gages located between the charge and a range of 4.05 cm. After this time, the wave is no longer spherical.

To obtain an estimate of the peak radial stress, we use the equation

$$\sigma_r = \rho c u \tag{3.1}$$

where ρ is the saturated density given in Table 3-1, c is the wave front speed, and u is the peak particle velocity. The estimated radial peak stress varied between 10.5 kbar (152 ksi) at a range of 1.01 cm and 0.9 kbar (13.1 ksi) at a range of 4.05 cm. Because Equation (3.1) is derived based on the assumption of an instantaneous rise to peak particle velocity (i.e., single planar shock jump condition), using Equation (3.1) for cases where there is a finite rise time to the peak will generate some degree of uncertainty.

The 95% saturated model produced the particle velocity-time histories shown in Figure 3-2. Gage failure occurred at approximately 15, 45, and 95 μs in particle velocity gages located at ranges of 1.01, 1.55, and 2.04 cm, respectively. The peak particle velocity varied from approximately 185 m/s at a range of 1.01 cm to 25 m/s at a range of 4.05 cm. The wave speed varied from approximately 2701 m/s at a range of 1.01 cm to 1587 m/s at a range of 4.05 cm. The arrival of the reflected wave from the aluminum cylinder container occurs approximately after 130 μs for particle velocity gages located between the charge and a range of 4.05 cm. After this time, the wave is no longer spherical. Using Equation (3.1) the estimated peak radial stress varied from 10.1 kbar (146 ksi) at a range of 1.01 cm to 0.8 kbar (11.6 ksi) at a range of 4.05 cm.

The 78% saturated model produced the particle velocity-time histories shown in Figure 3-3. Gage failure occurred at approximately 15, 30, 98, 165, 260, 340, and 390 μs for gages located at ranges between 1.01 and 4.05 cm, respectively. The peak particle velocity varied from approximately 194 m/s at a range of 1.01 cm to 18 m/s at a range of 4.05 cm. The wave front speed varied from approximately 1711 m/s at a range of 1.01 cm to 361 m/s at a range of 4.05 cm. The arrival of the reflected wave from the aluminum cylinder container occurs approximately after 500 μs for particle velocity gages located between the charge and a range of 4.05 cm. After this time the wave is no longer spherical. Using Equation (3.1), the estimated peak radial stress varied from 6.0 kbar (87.0 ksi) at a range of 1.01 cm to 0.1 kbar (1.5 ksi) at a range of 4.05 cm.

The 77% saturated model produced the particle velocity-time histories shown in Figure 3-4. Gage failure occurred at approximately 15, 40, 92, and 225 μs for gages located at ranges between

1.01 and 3.05 cm , respectively. The peak particle velocity varied from 192 m/s at a range of 1.01 cm to 17 m/s at a range of 4.05 cm. The wave front speed varied from 1908 m/s at a range of 1.01 cm to 455 m/s at a range of 4.05 cm. The arrival of the reflected wave from the aluminum container occurs approximately after 500 μs for particle velocity gages located between the charge and a range of 4.05 cm. After this time, the wave is no longer spherical. Using Equation (3.1), the estimated peak radial stress varied from 6.6 kbar (95.7 ksi) at a range of 1.01 cm to 0.1 kbar (1.5 ksi) at a range of 4.05 cm.

The 78% and 77% saturated models are essentially identical, so the particle velocity results can be compared to assess the reproducibility of the experimental technique. Figures 3-5 through 3-7 illustrate the reproducibility of particle velocity waveform shape for gages located at ranges of 1.01, 2.04, and 4.05 cm, respectively. In general, the particle velocity waveform shapes compare reasonably well. The average difference between peak particle velocities from each experiment was 2.6%. The average difference between wave front TOA from each experiment was 14.2%. The largest difference between the two experiments occurred at a range of 4.05 cm: the wave front arrival times differed by 16.7% and the peak particle velocities differed by 6.7%. These differences are attributed mostly to the variation in saturation uniformity, which is estimated to be ±3.3%.

STRESS MEASUREMENTS

We attempted to make radial and circumferential stress measurements; however, stress measurements in low-density granular materials are inherently difficult due to difficulties in material placement that can produce localized nonuniform conditions around the gage, to in-plane strain within the stress gage ytterbium sensing element that can result in a spurious gage signal interpreted as stress, and to large particle displacements that can produce nonidentical stress and flow conditions for gages located at the same initial range. As discussed in Section 2, we developed sand model fabrication techniques to optimize the saturation uniformity and fielded flatpack strain gages to reduce the stress interpretation uncertainty due to in-plane strain.

Figure 3-8 shows typical, measured, radial stress-time histories for two flatpack stress gages located at the same range. Both gages measured peak stresses of 1.5 kbar (21.8 ksi), which is within 15% of the estimated peak stress from the particle gages using Equation (3.1). However, the postpeak residual stress levels show a marked difference. Gage 3 indicates a value of 0.1 kbar (1.5 ksi), while Gage 4 indicates a value of -0.15 kbar (-2.2 ksi), which is not physically possible. Typically, the radial stress measurements in each experiment showed reproducible peak stresses, with the peak stresses in good agreement with estimated peak stresses from the particle velocity records. Significant differences were typically observed for the postpeak residual stress levels

between gages at the same range. These differences may be attributable to the large particle displacements that produced different stress flow conditions around the gage or different in-plane strain conditions within each gage. Furthermore, the Dynasen ytterbium sensing elements used are well characterized for only uniaxial loading. Thus, there is inherently greater uncertainty in the unloading portion of the stress measurements due to the lack of Dynasen ytterbium behavior data. In our data reduction of the stress measurements, we estimate a Dynasen ytterbium unloading curve by assuming mechanical ytterbium properties obtained from experiments performed at SRI on other ytterbium element types.

Circumferential stress measurements made in Experiments 1 and 2 for 100% and 95% saturated models, respectively, showed as much as 30% variation in peak stress and postpeak residual stress for gages at the same range. Furthermore, the trends in the circumferential stress waveforms were not qualitatively consistent with radial stress waveforms at some range locations. For example, some circumferential peak stress measurements exceeded the peak radial stress measurements.

We suggest that only the peak radial stress information from the measurements be quantitatively used. The postpeak, residual, radial stress and the complete, circumferential stress waveforms should not be used due to the lack of reproducibility. The complete stress measurements from each experiment are illustrated in Appendix A.

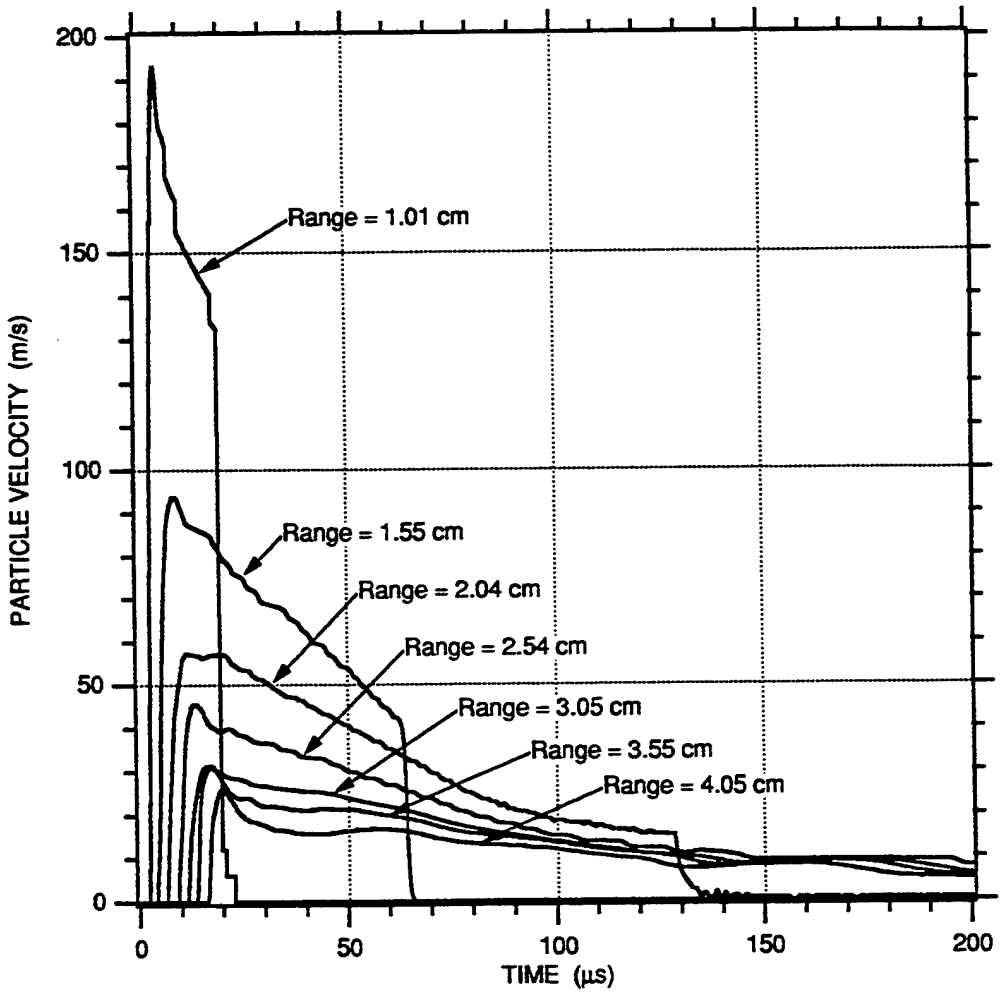

FIGURE 3-1. PARTICLE VELOCITY-TIME HISTORIES MEASURED IN 100% SATURATED EGLIN BEACH SAND FOR A 3/8 g PETN EXPLOSIVE CHARGE

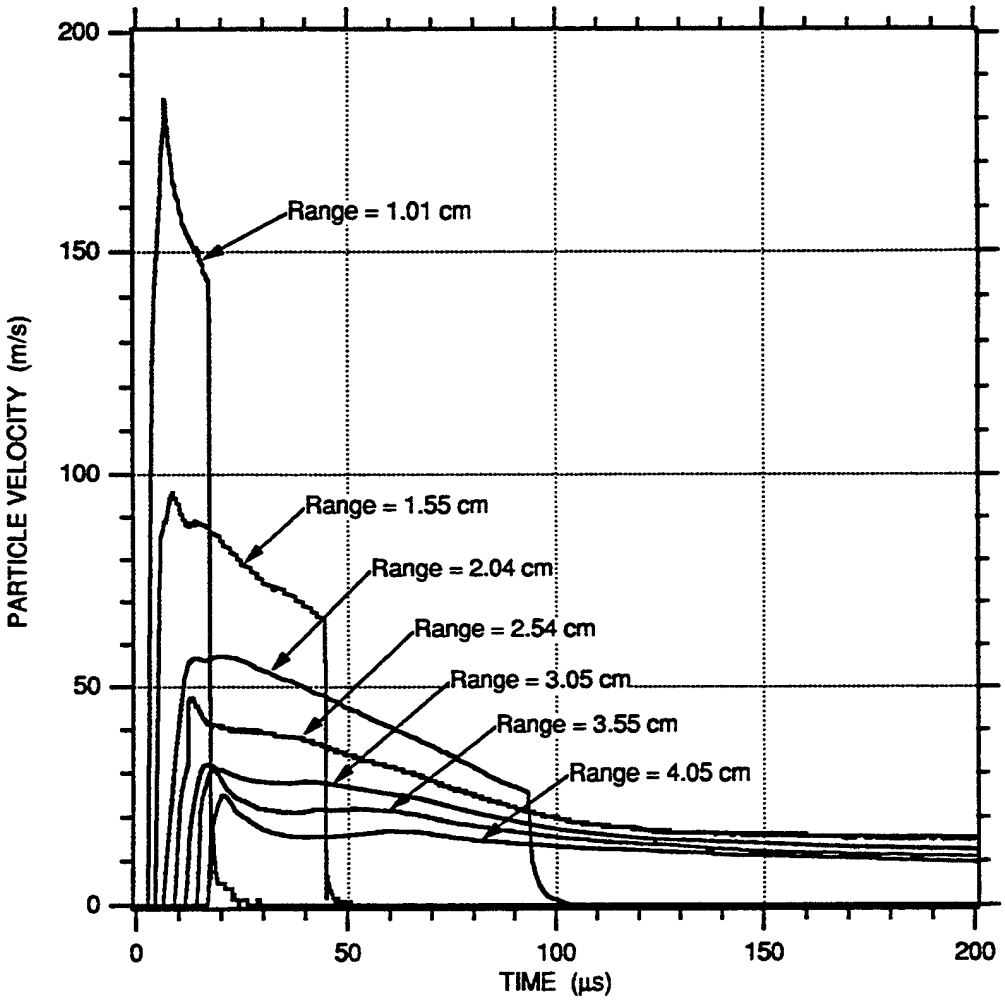

FIGURE 3-2. PARTICLE VELOCITY-TIME HISTORIES MEASURED IN 95% SATURATED EGLIN BEACH SAND FOR A 3/8 g PETN EXPLOSIVE CHARGE

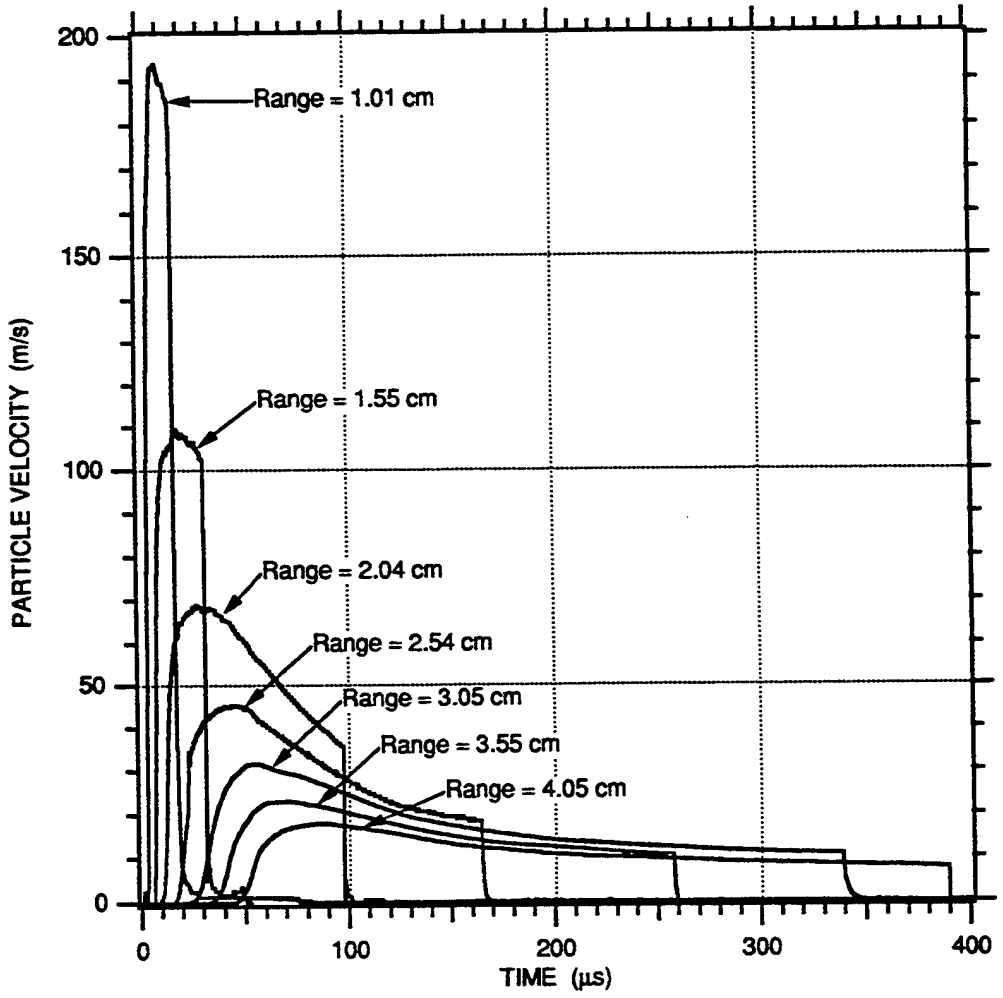

FIGURE 3-3. PARTICLE VELOCITY-TIME HISTORIES MEASURED IN 78% SATURATED EGLIN BEACH SAND FOR A 3/8 g PETN EXPLOSIVE CHARGE

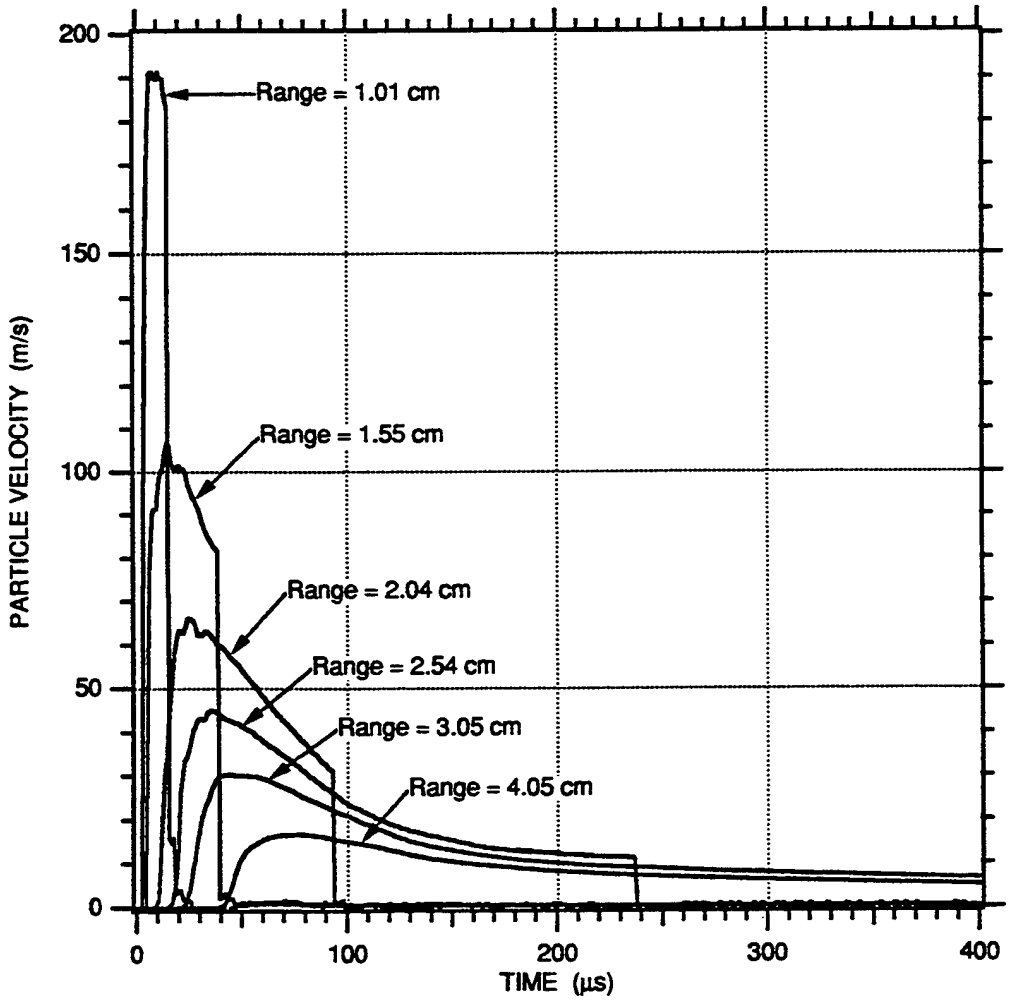

FIGURE 3-4. PARTICLE VELOCITY-TIME HISTORIES MEASURED IN 77% SATURATED EGLIN BEACH SAND FOR A 3/8 g PETN EXPLOSIVE CHARGE

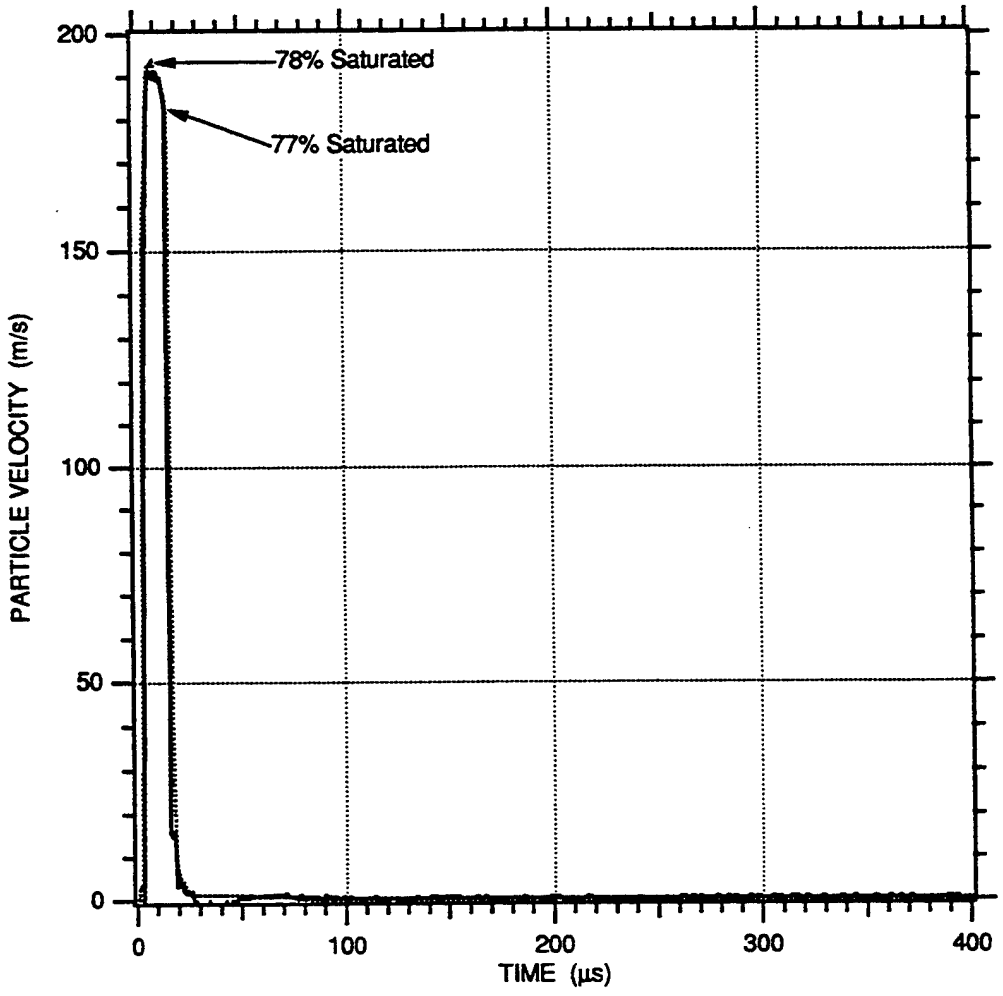

FIGURE 3-5. COMPARISON OF PARTICLE VELOCITY-TIME HISTORIES MEASURED IN 78% AND 77% SATURATED EGLIN BEACH SAND FOR A 3/8 g PETN EXPLOSIVE CHARGE AT A RANGE OF 1.01 cm

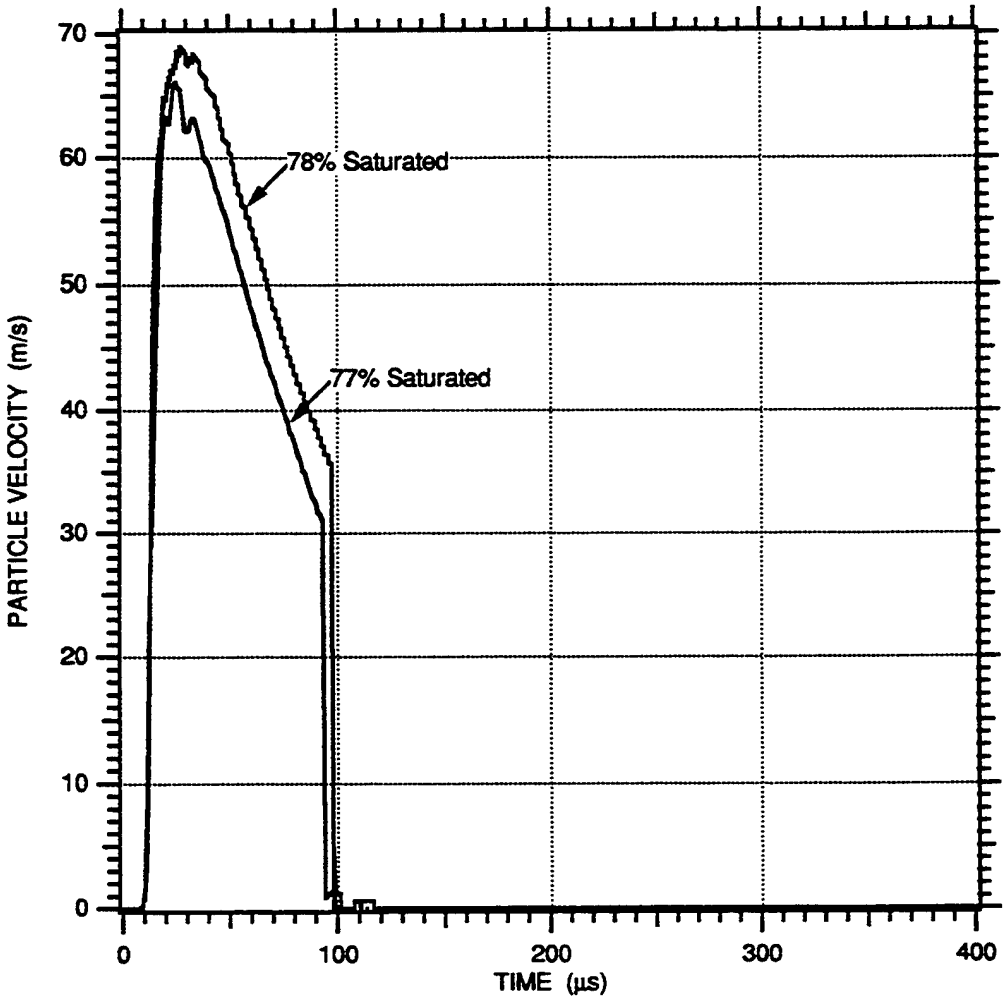

FIGURE 3-6. COMPARISON OF PARTICLE VELOCITY-TIME HISTORIES MEASURED IN 78% AND 77% SATURATED EGLIN BEACH SAND FOR A 3/8 g PETN EXPLOSIVE CHARGE AT A RANGE OF 2.04 cm

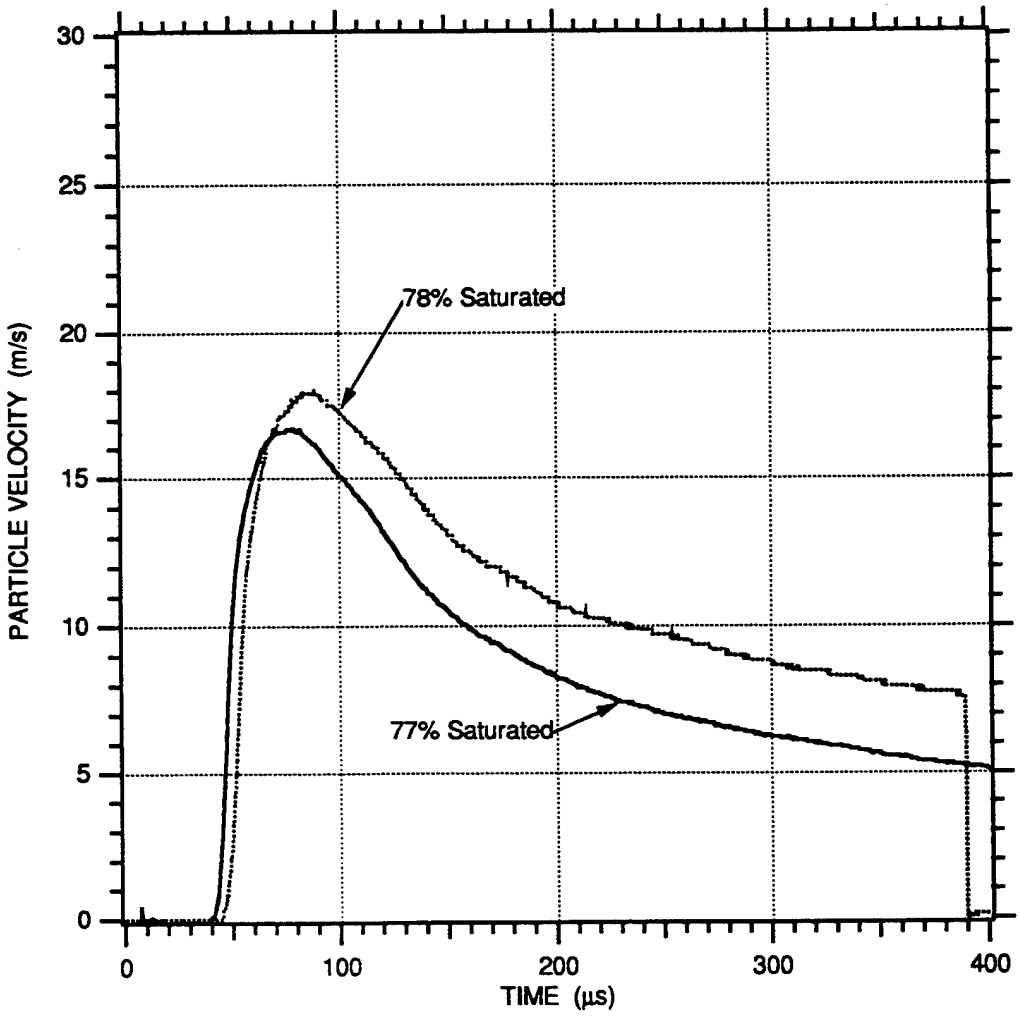

FIGURE 3-7. COMPARISON OF PARTICLE VELOCITY-TIME HISTORIES MEASURED IN 78% AND 77% SATURATED EGLIN BEACH SAND FOR A 3/8 g PETN EXPLOSIVE CHARGE AT A RANGE OF 4.05 cm

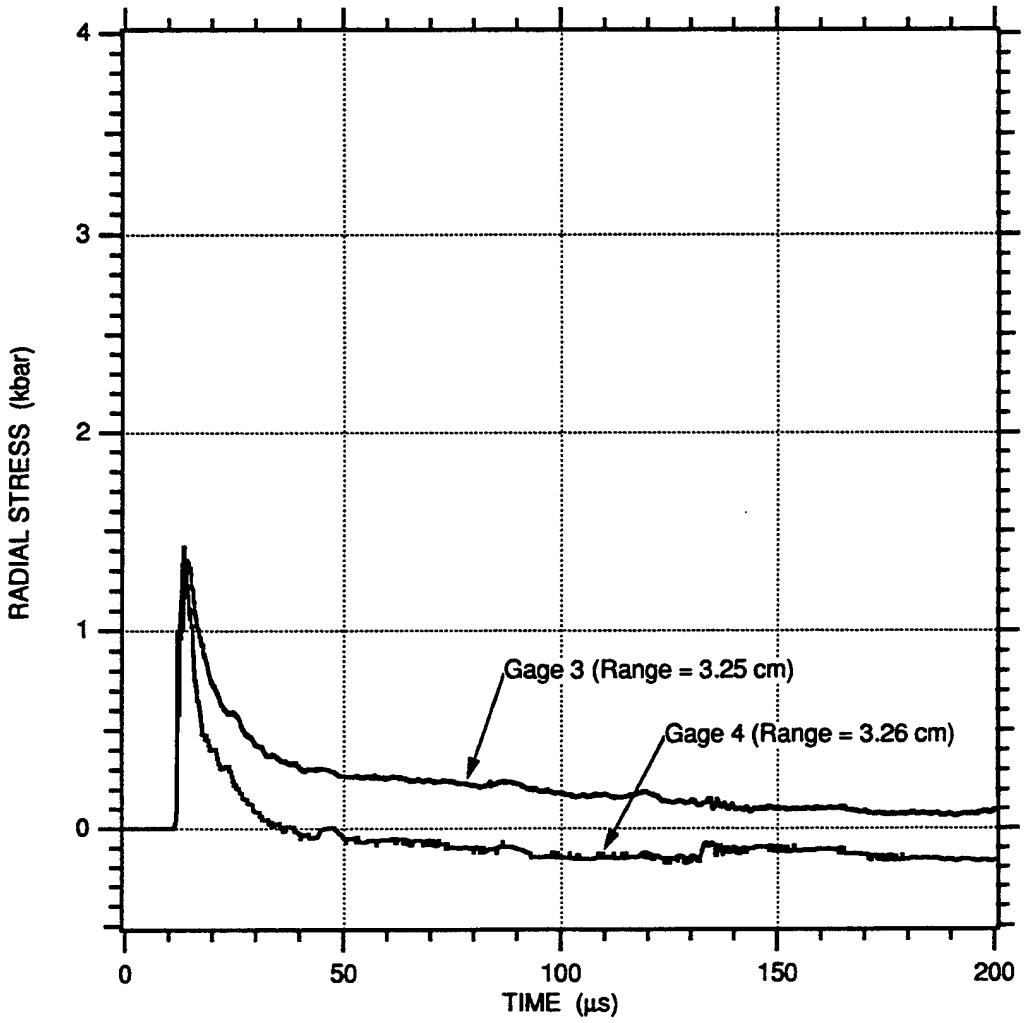

FIGURE 3-8. RADIAL STRESS-TIME HISTORIES MEASURED IN 100% SATURATED EGLIN BEACH SAND FOR A 3/8 g PETN EXPLOSIVE CHARGE

SECTION 4

DETAILED RESULTS FOR 100% SATURATED SAND MODEL

The 100% saturated sand model had a measured dry density of 1.678 ± 0.008 g/cm^3, a calculated porosity of $36.8 \pm 0.3\%$ [Porosity % = (1 - Dry Density/Grain Density) x 100], and a calculated saturated density of 2.046 ± 0.011 g/cm^3. The measured saturated density was 2.051 ± 0.011 g/cm^3. The estimated error associated with the total saturated level of 100% is -1% based on making bulk weight measurements. Figure 2-3 shows a reference saturation uniformity characteristic for the 100% saturated sand model.

PARTICLE VELOCITY MEASUREMENTS

Figures 4-1 through 4-7 show the particle velocity records measured at ranges from 1.01 to 4.05 cm. The gage failure indicated in the figures is attributed to breakage of the wire loop resulting from radial displacement, which generates a hoop strain in excess of the wire failure strain of approximately 20% to 25%. The particle velocity gage at a range of 0.54 cm (Gage No. PV1), which is adjacent to the spherical charge, is not shown due to breakage before the peak particle velocity. The particle velocity records show approximately a linear rise to the peak particle velocity followed by a decay to a lower particle velocity. The reflection from the aluminum container boundary is seen as an increase in the particle velocity and occurs between 130 and 150 μs at ranges between 4.05 and 3.05 cm, respectively. Beyond a time of 130 μs, the wave front is no longer spherically divergent.

Figure 4-8 shows a profile of range versus TOA. The data points have been fitted with a least squares second order polynomial having the form of

$$\text{Range} = 0.378 + 0.281\ \text{TOA} - 0.00339\ \text{TOA}^2 \qquad (4.1)$$

where range is in centimeters and TOA is in microseconds. The wave front speed at any given range can be determined by differentiating Equation (4.1) to produce

$$c = 0.281 - 0.00678\ \text{TOA} \qquad (4.2)$$

were c is the wave front speed in centimeters per microsecond. Converting c to units of meters per second, the wave front speed varies from 2750 m/s at a range of 0.54 cm to 1710 m/s at a range of 4.05 cm.

Figure 4-9 shows the attenuation of peak particle velocity with increased range. Using Equation (3.1), the peak particle velocity (m/s) can be multiplied by the saturated density (kg/m^3) and wave front speed (m/s) to produce an estimate for the peak radial stress (Pa). Table 4-1 summarizes the TOA, wave front speed, peak particle velocity, and estimated radial stress for the 100% saturated sand model.

TABLE 4-1. SUMMARY OF EXPERIMENTAL RESULTS FROM PARTICLE VELOCITY MEASUREMENTS FOR THE 100% SATURATED SAND MODEL

Range (cm ± 0.05 cm)	TOA (μs ± 0.2 μs)	Wave Front Speed (m/s ± 10%)	Peak Particle Velocity (m/s ± 2%)	Estimated Peak Stress (kbar)
0.54	0.9	2750	NA	NA
1.01	2.1	2670	193.2	10.6
1.55	4.1	2530	93.4	5.1
2.04	6.4	2380	57.3	2.8
2.54	8.6	2230	45.1	2.1
3.05	11.3	2050	31.3	1.3
3.55	13.4	1900	31.5	1.2
4.05	16.2	1710	25.9	0.9

PARTICLE DISPLACEMENTS AND STRAINS

The particle velocity-time histories shown in Figures 4-1 through 4-7 can be temporally integrated to obtain displacement-time histories. Figure 4-10 shows the particle displacement-time histories.

Figures 4-11 to 4-16 shows fractional radial (ε_r), circumferential (ε_θ), and volumetric (ε_v) engineering strains. The governing equations used to calculate these strains are given in Appendix B. The strains are based on the relative displacements between adjacent particle velocity gages. Positive strains indicate compression. Negative strains indicate elongation for the circumferential strains and dilation for the volumetric strains. The volumetric strain-time histories show that each fractional shell volume dilates after an initial compression.

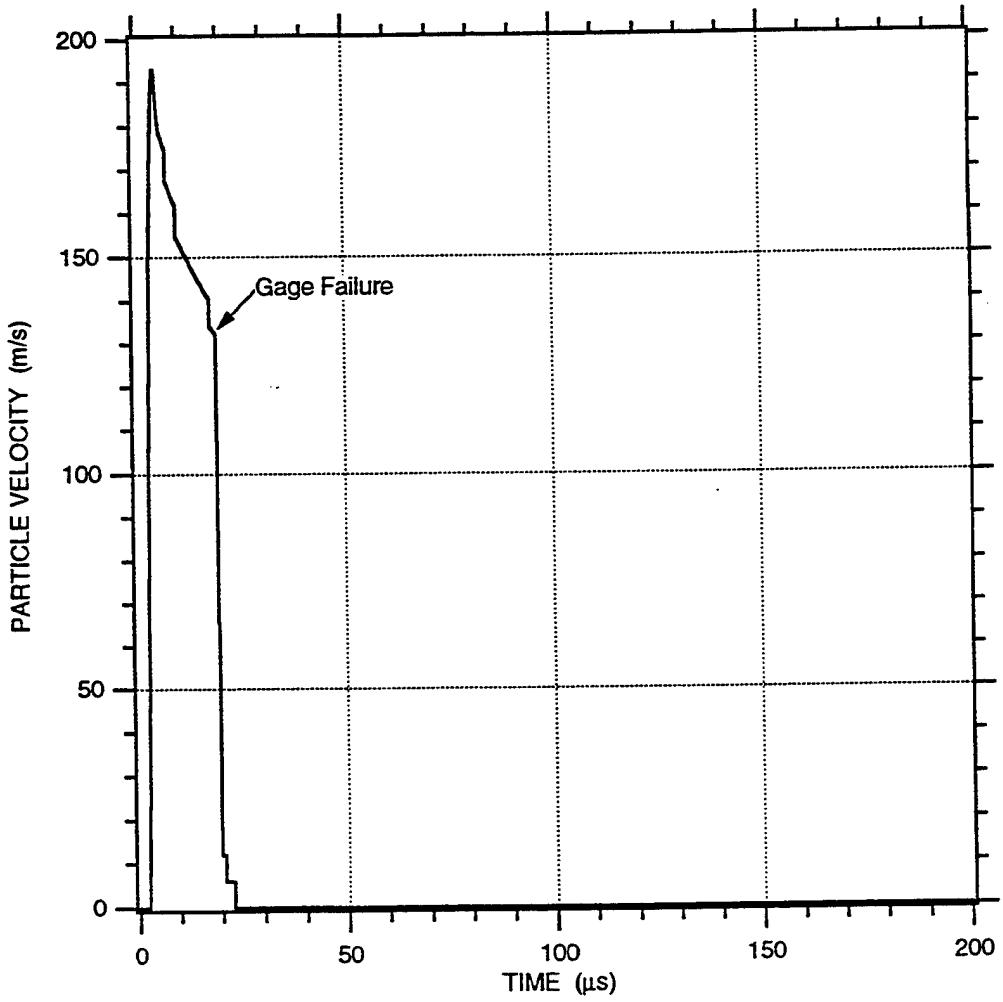

FIGURE 4-1. PARTICLE VELOCITY-TIME HISTORY MEASURED IN 100% SATURATED EGLIN BEACH SAND FOR A 3/8 g PETN EXPLOSIVE CHARGE AT A RANGE OF 1.01 cm

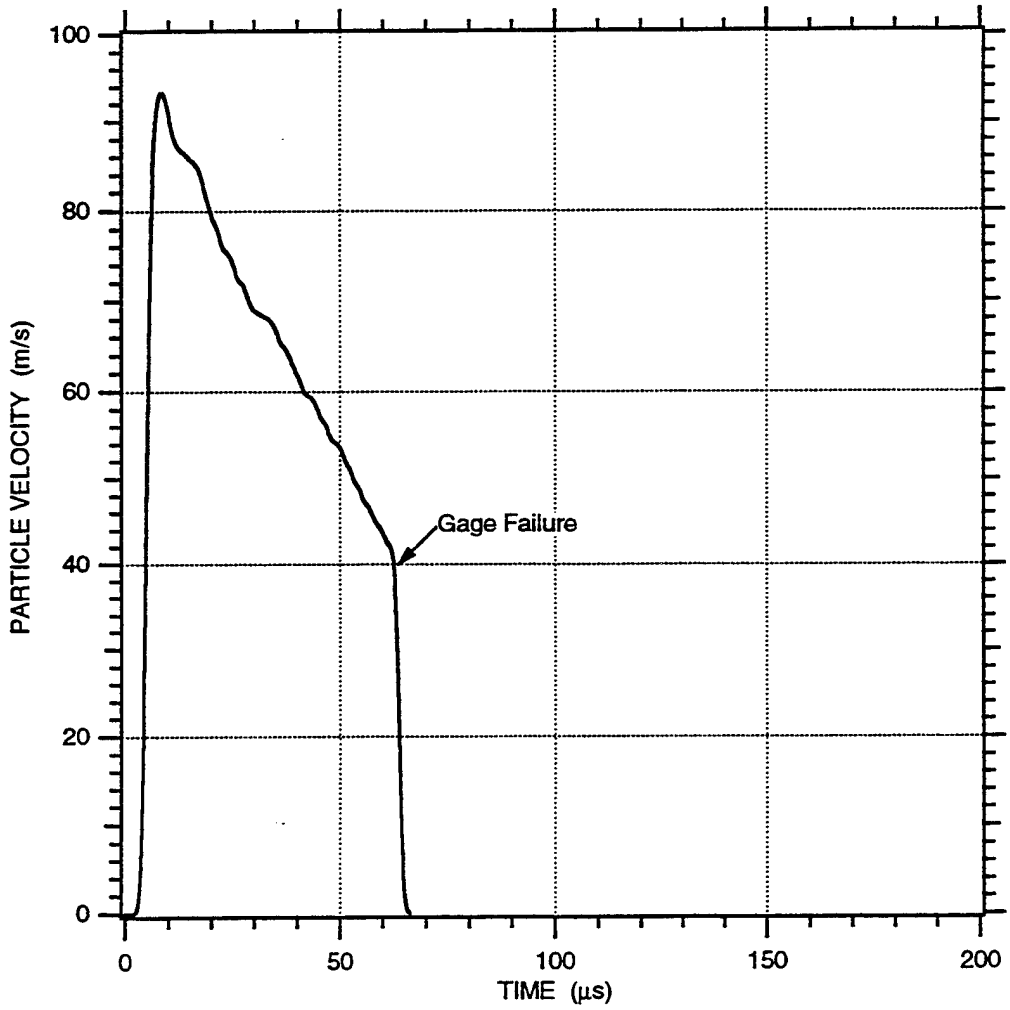

FIGURE 4-2. PARTICLE VELOCITY-TIME HISTORY MEASURED IN 100% SATURATED EGLIN BEACH SAND FOR A 3/8 g PETN EXPLOSIVE CHARGE AT A RANGE OF 1.55 cm

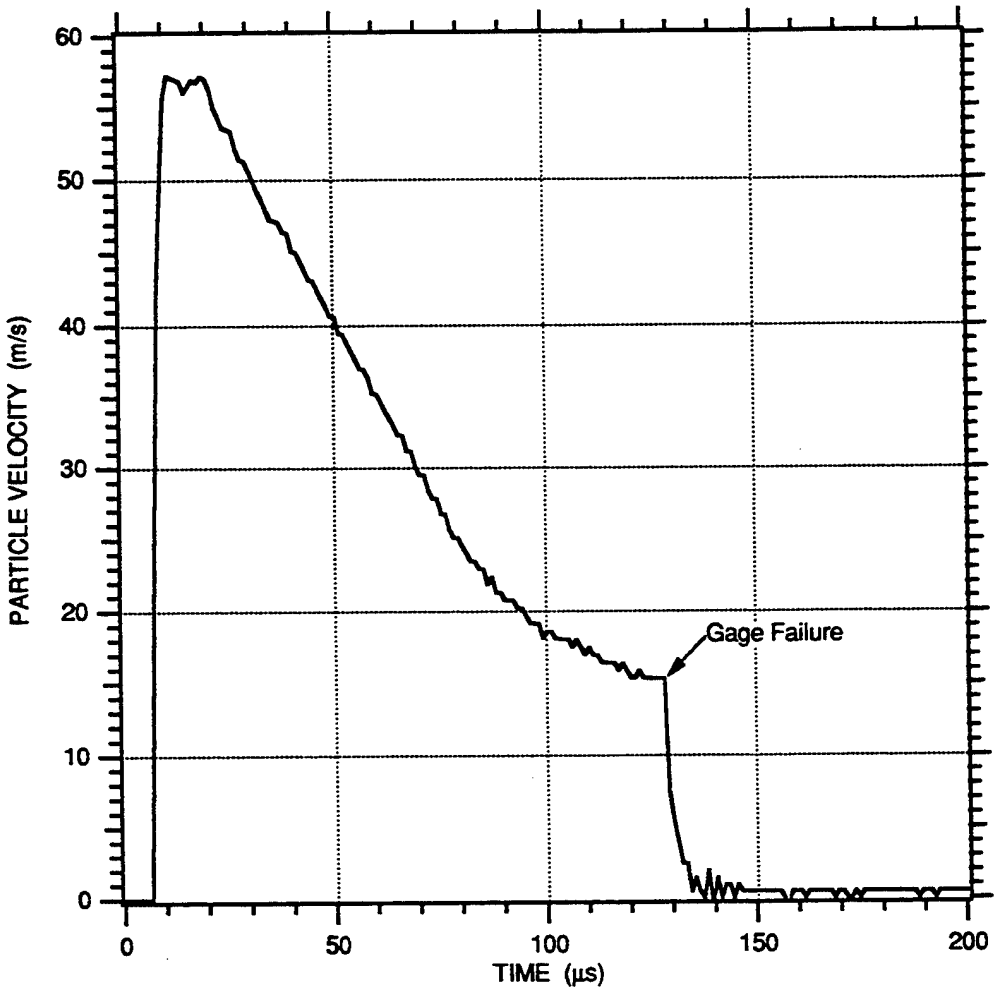

FIGURE 4-3. PARTICLE VELOCITY-TIME HISTORY MEASURED IN 100% SATURATED EGLIN BEACH SAND FOR A 3/8 g PETN EXPLOSIVE CHARGE AT A RANGE OF 2.04 cm

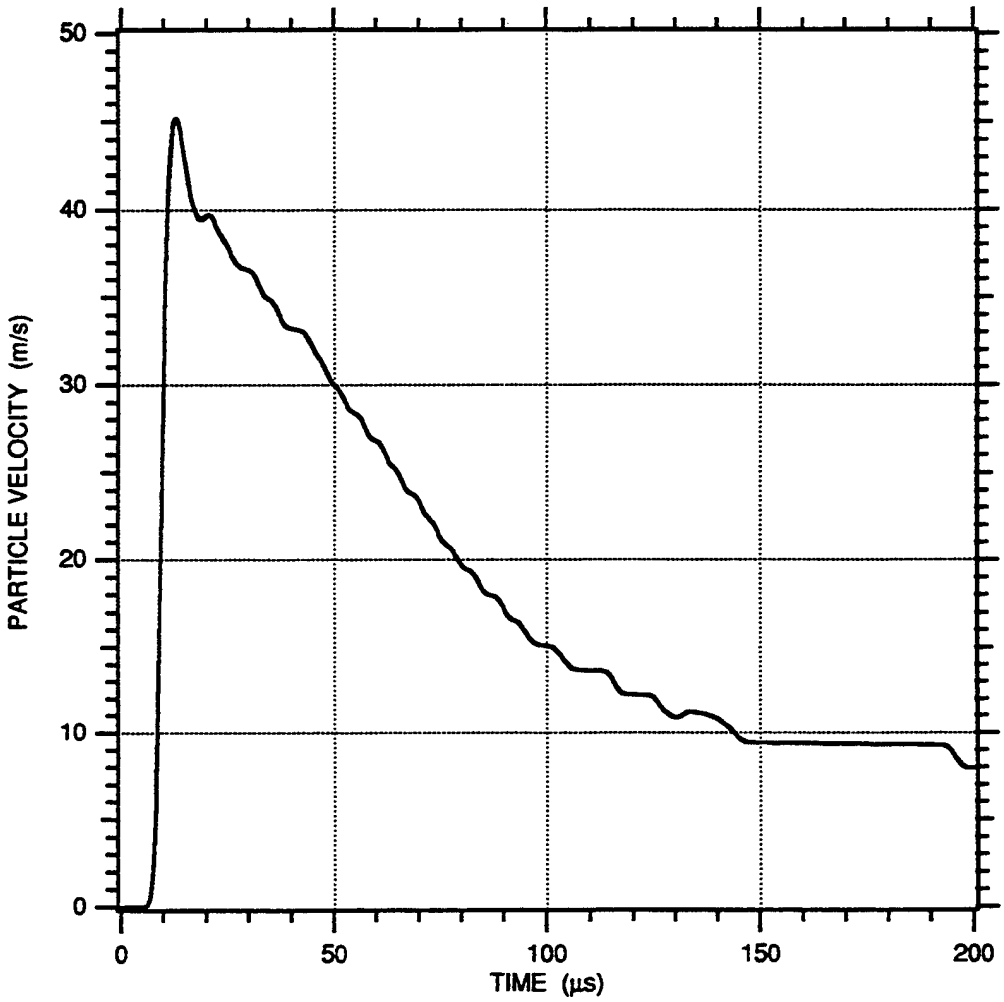

FIGURE 4-4. PARTICLE VELOCITY-TIME HISTORY MEASURED IN 100% SATURATED EGLIN BEACH SAND FOR A 3/8 g PETN EXPLOSIVE CHARGE AT A RANGE OF 2.54 cm

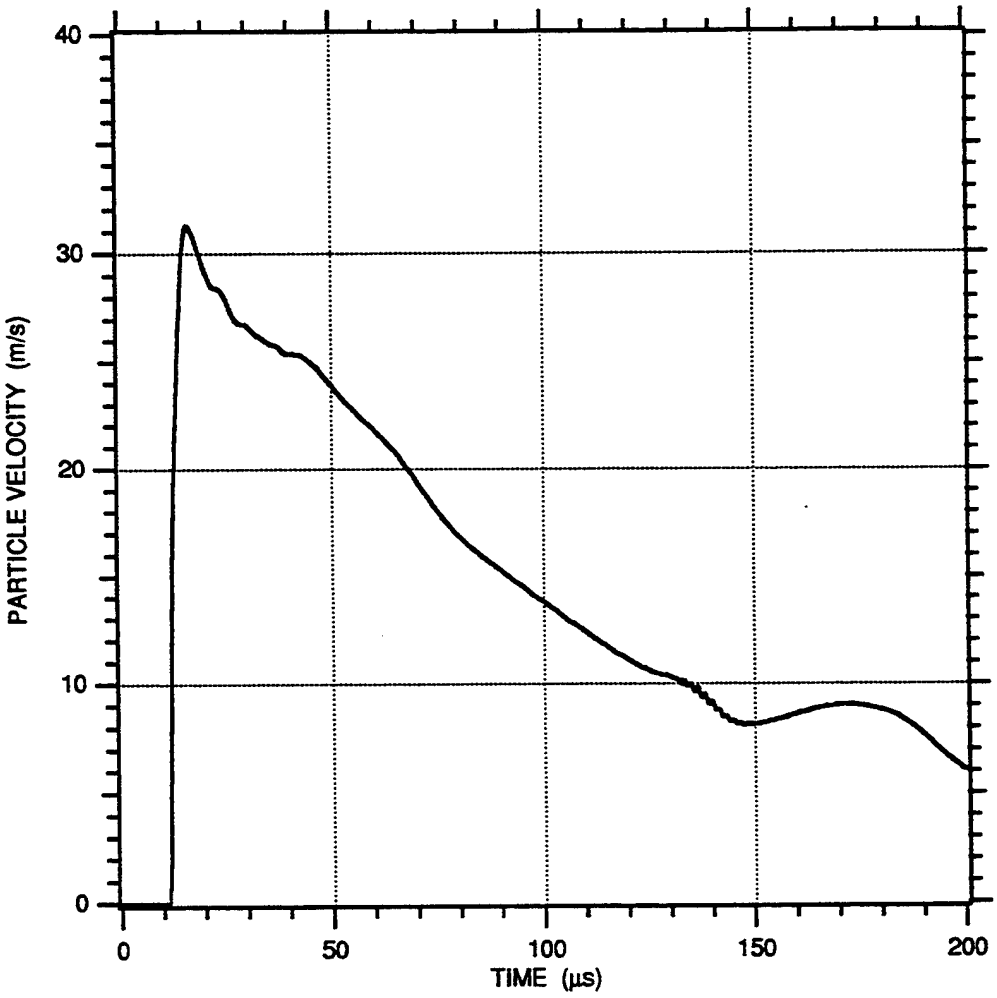

FIGURE 4-5. PARTICLE VELOCITY-TIME HISTORY MEASURED IN 100% SATURATED EGLIN BEACH SAND FOR A 3/8 g PETN EXPLOSIVE CHARGE AT A RANGE OF 3.05 cm

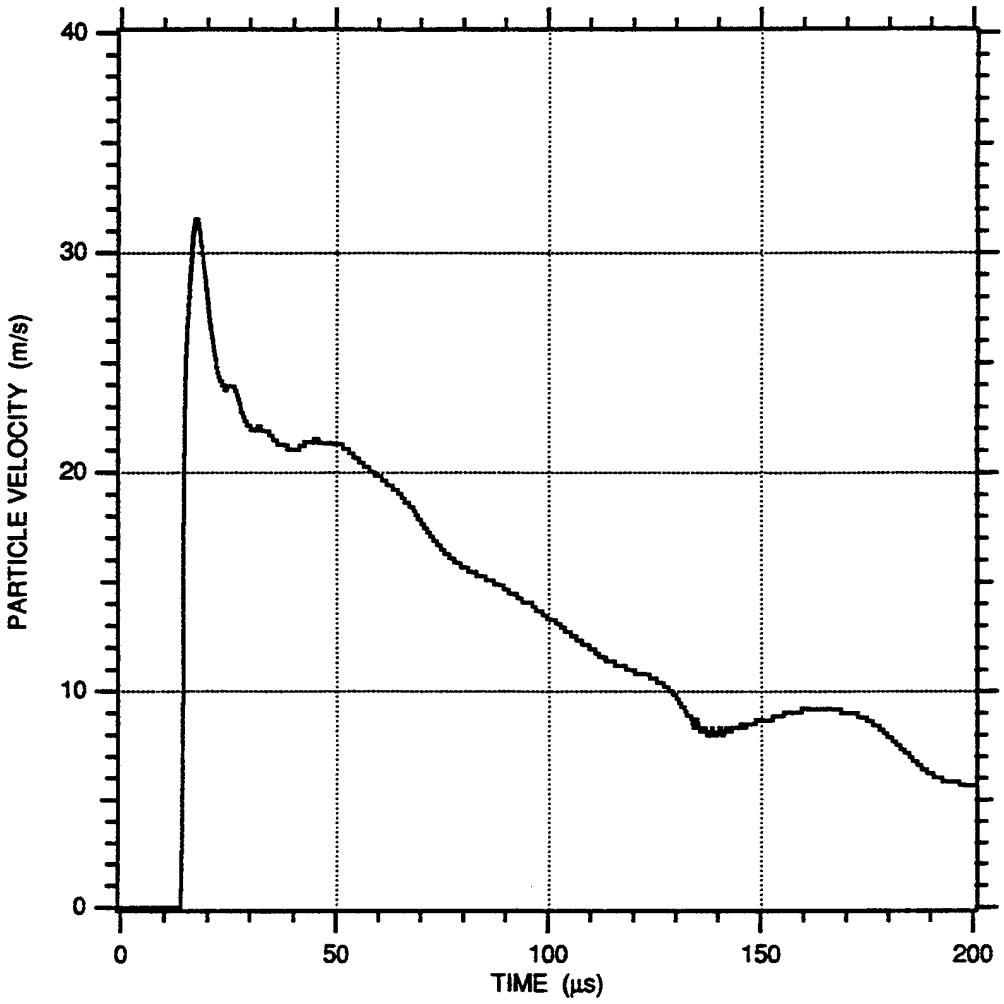

FIGURE 4-6. PARTICLE VELOCITY-TIME HISTORY MEASURED IN 100% SATURATED EGLIN BEACH SAND FOR A 3/8 g PETN EXPLOSIVE CHARGE AT A RANGE OF 3.55 cm

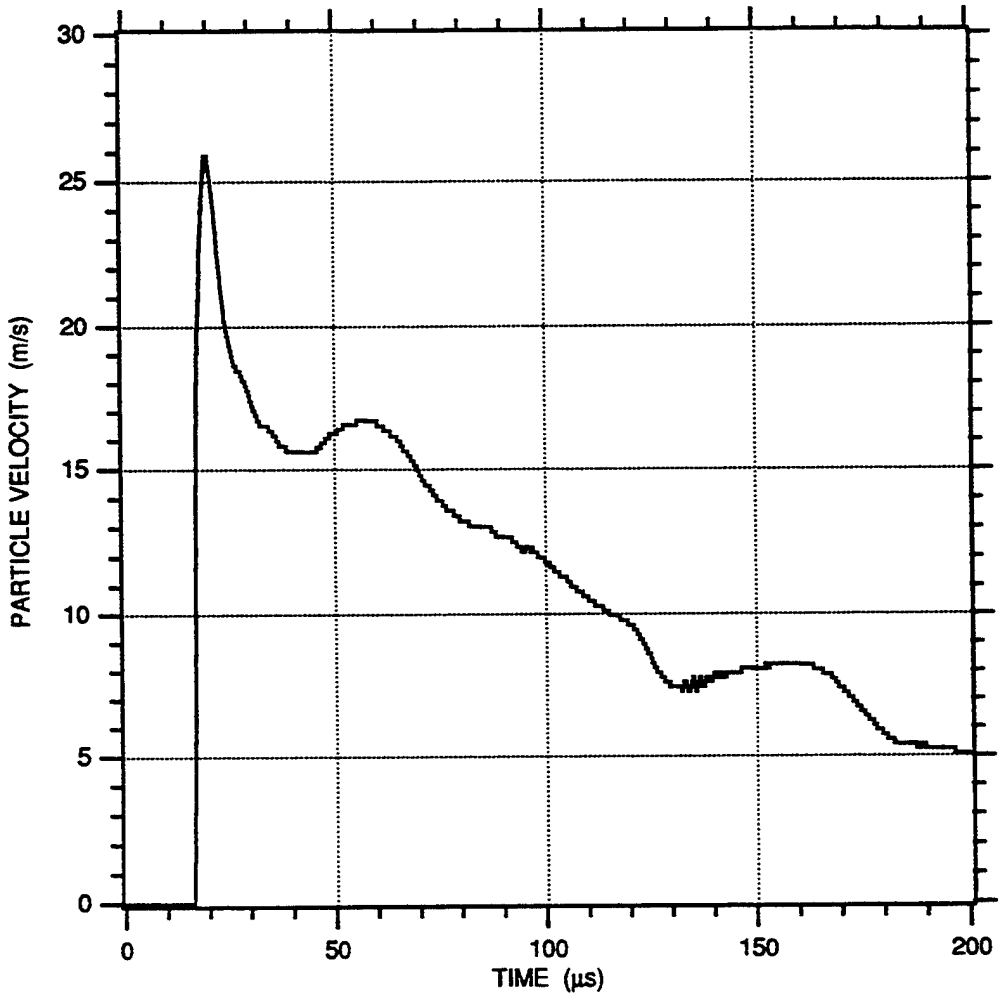

FIGURE 4-7. PARTICLE VELOCITY-TIME HISTORY MEASURED IN 100% SATURATED EGLIN BEACH SAND FOR A 3/8 g PETN EXPLOSIVE CHARGE AT A RANGE OF 4.05 cm

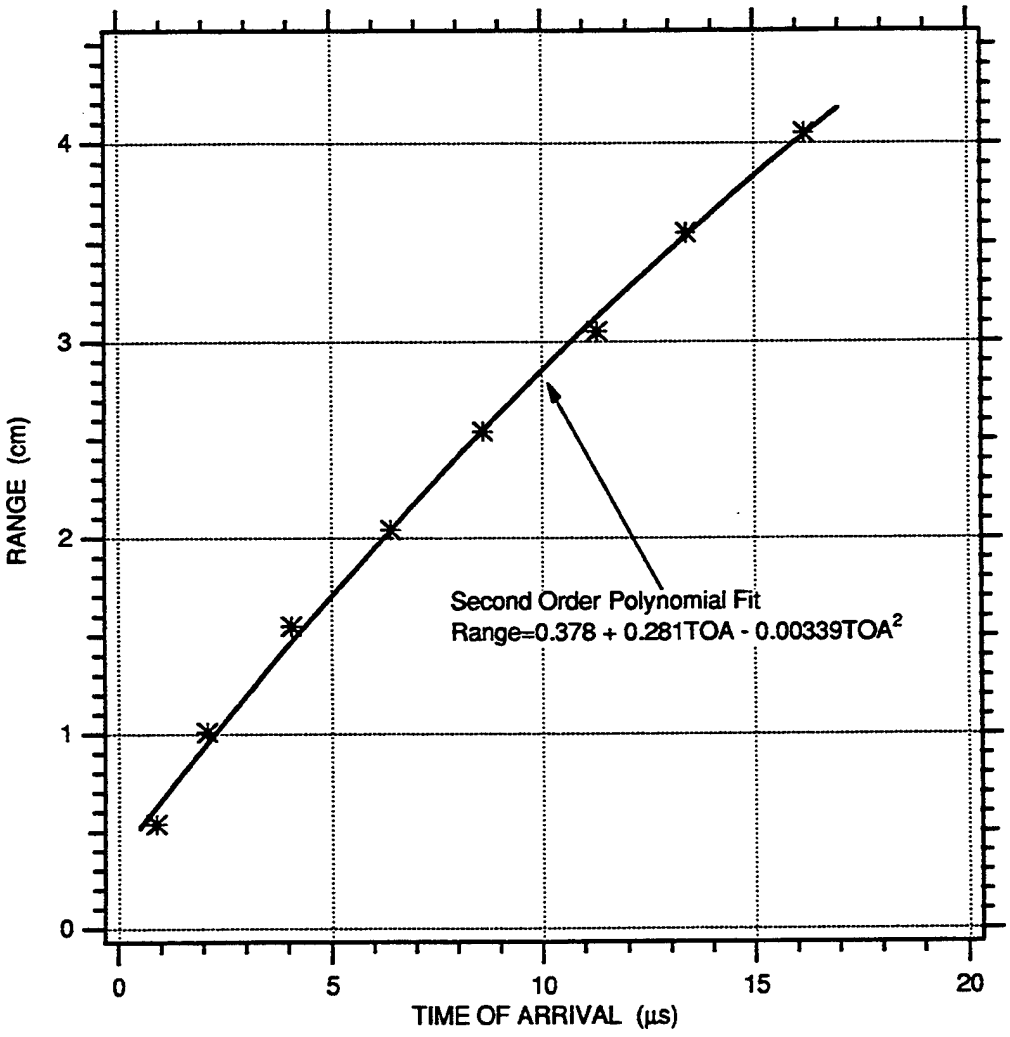

FIGURE 4-8. RANGE VERSUS TIME OF ARRIVAL MEASURED IN 100% SATURATED EGLIN BEACH SAND FOR A 3/8 g PETN EXPLOSIVE CHARGE

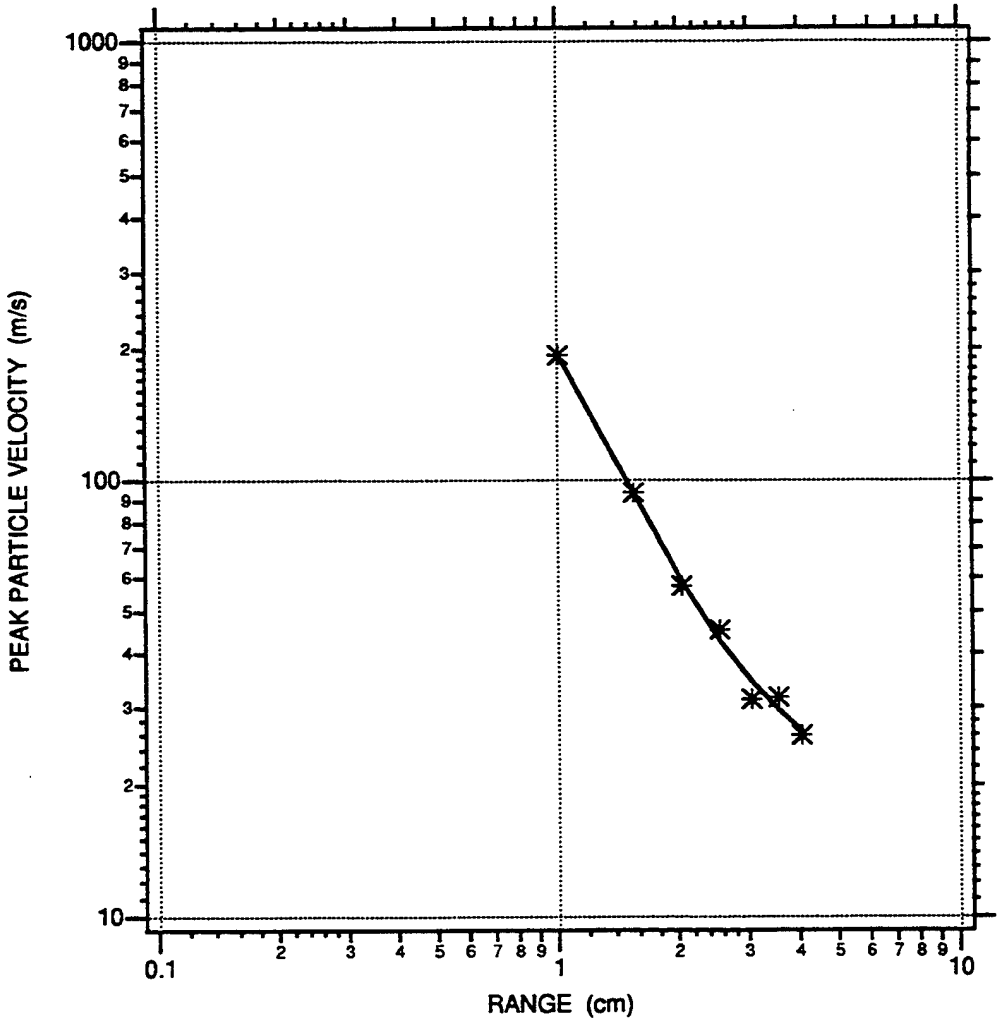

FIGURE 4-9. ATTENUATION OF PEAK PARTICLE VELOCITY MEASURED IN 100% SATURATED EGLIN BEACH SAND FOR A 3/8 g PETN EXPLOSIVE CHARGE

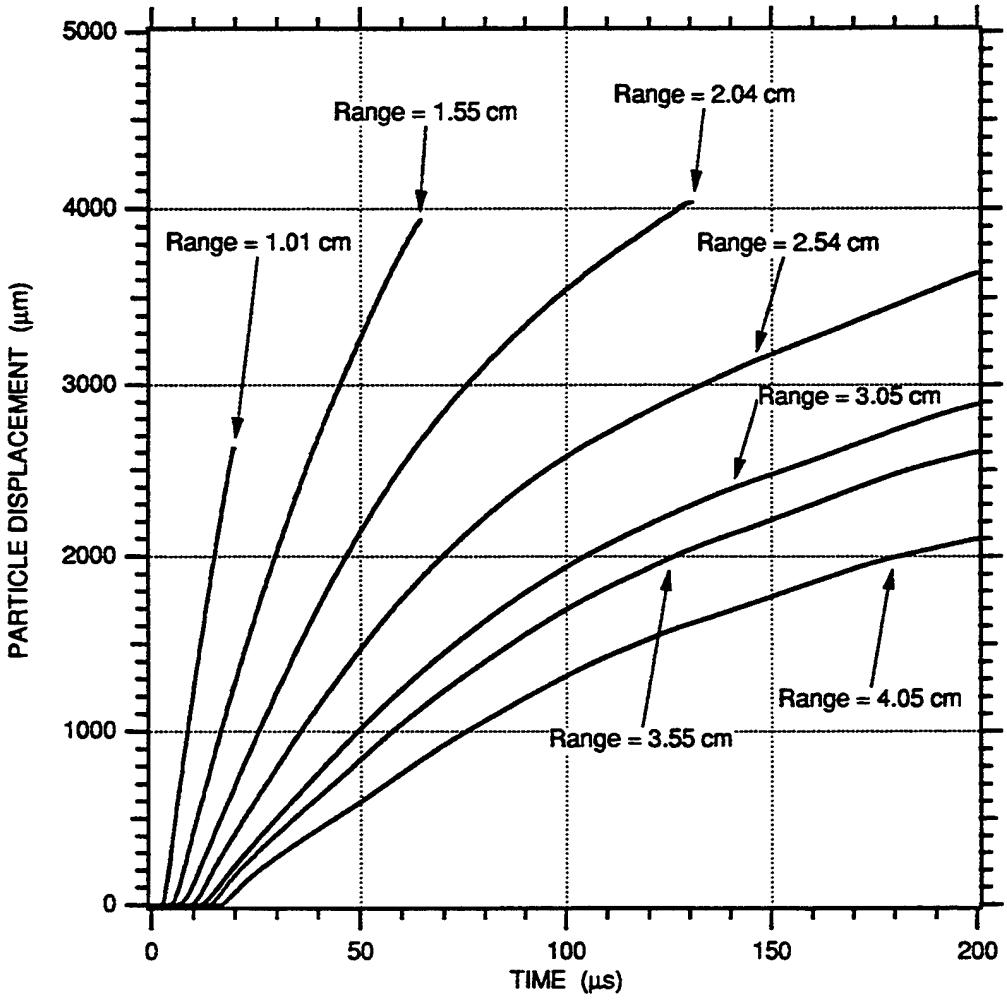

FIGURE 4-10. PARTICLE DISPLACEMENT-TIME HISTORIES MEASURED IN 100% SATURATED EGLIN BEACH SAND FOR A 3/8 g PETN EXPLOSIVE CHARGE

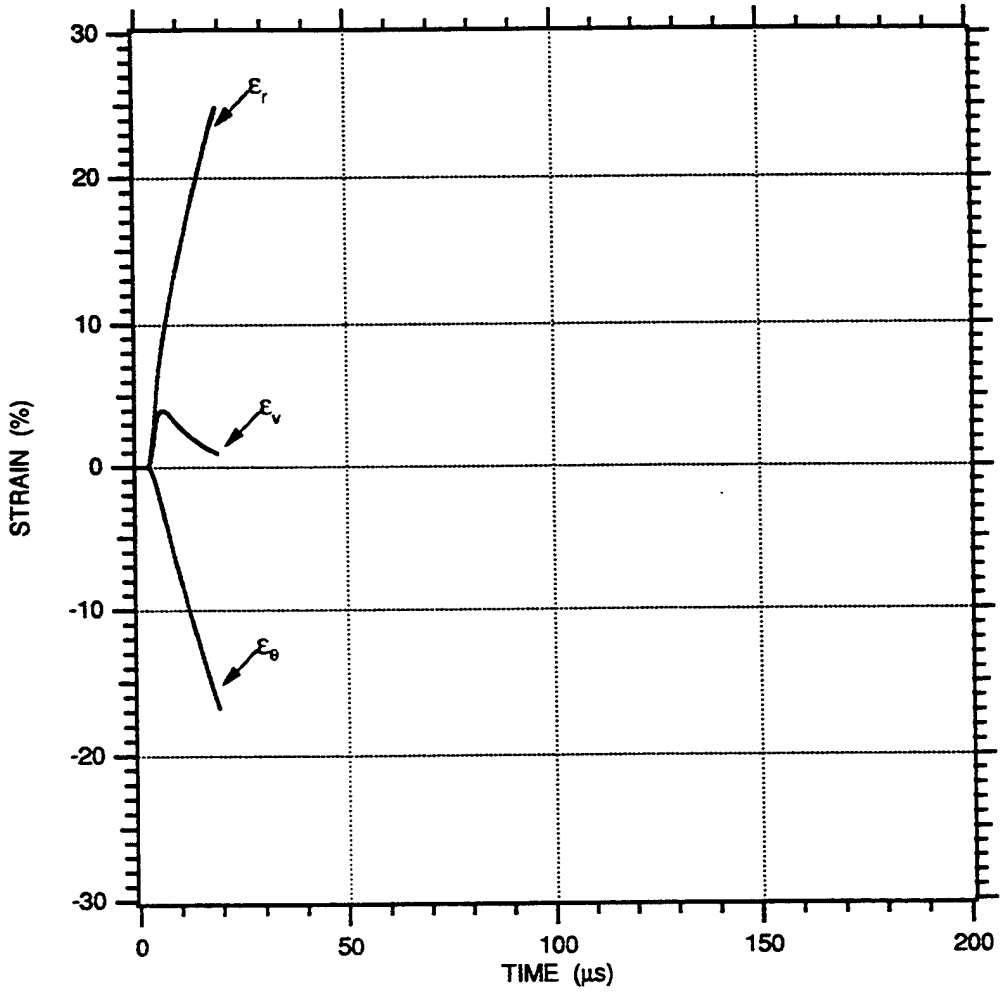

FIGURE 4-11. STRAIN-TIME HISTORIES MEASURED IN 100% SATURATED EGLIN BEACH SAND FOR A 3/8 g PETN EXPLOSIVE CHARGE AT A RANGE BETWEEN 1.01 AND 1.55 cm

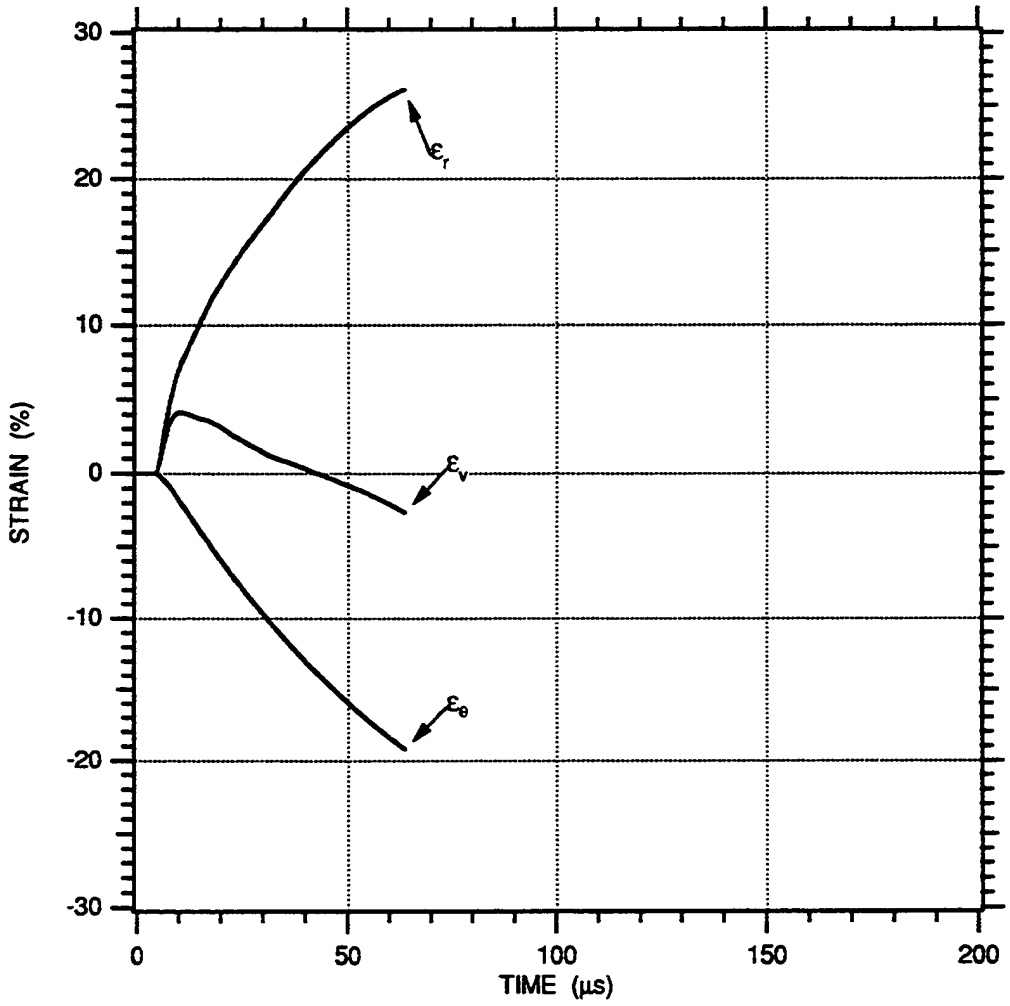

FIGURE 4-12. STRAIN-TIME HISTORIES MEASURED IN 100% SATURATED EGLIN BEACH SAND FOR A 3/8 g PETN EXPLOSIVE CHARGE AT A RANGE BETWEEN 1.55 AND 2.04 cm

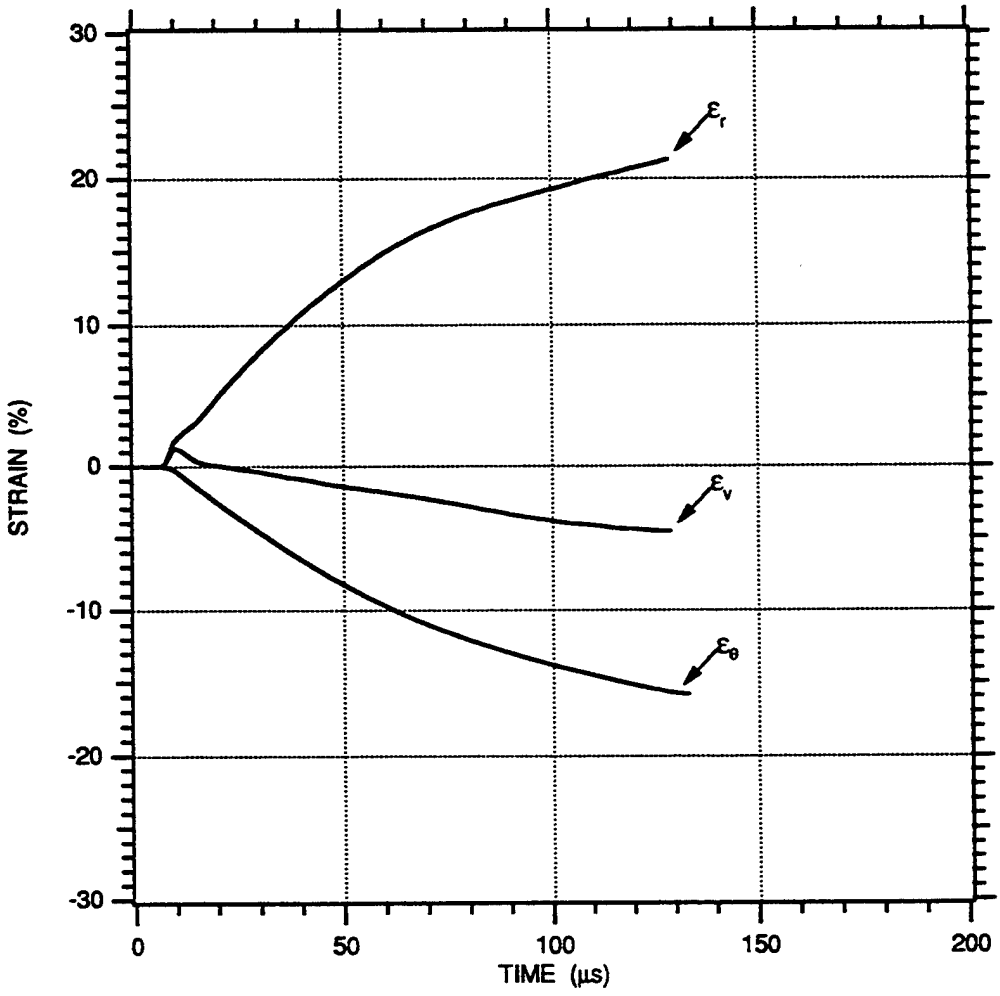

FIGURE 4-13. STRAIN-TIME HISTORIES MEASURED IN 100% SATURATED EGLIN BEACH SAND FOR A 3/8 g PETN EXPLOSIVE CHARGE AT A RANGE BETWEEN 2.04 AND 2.54 cm

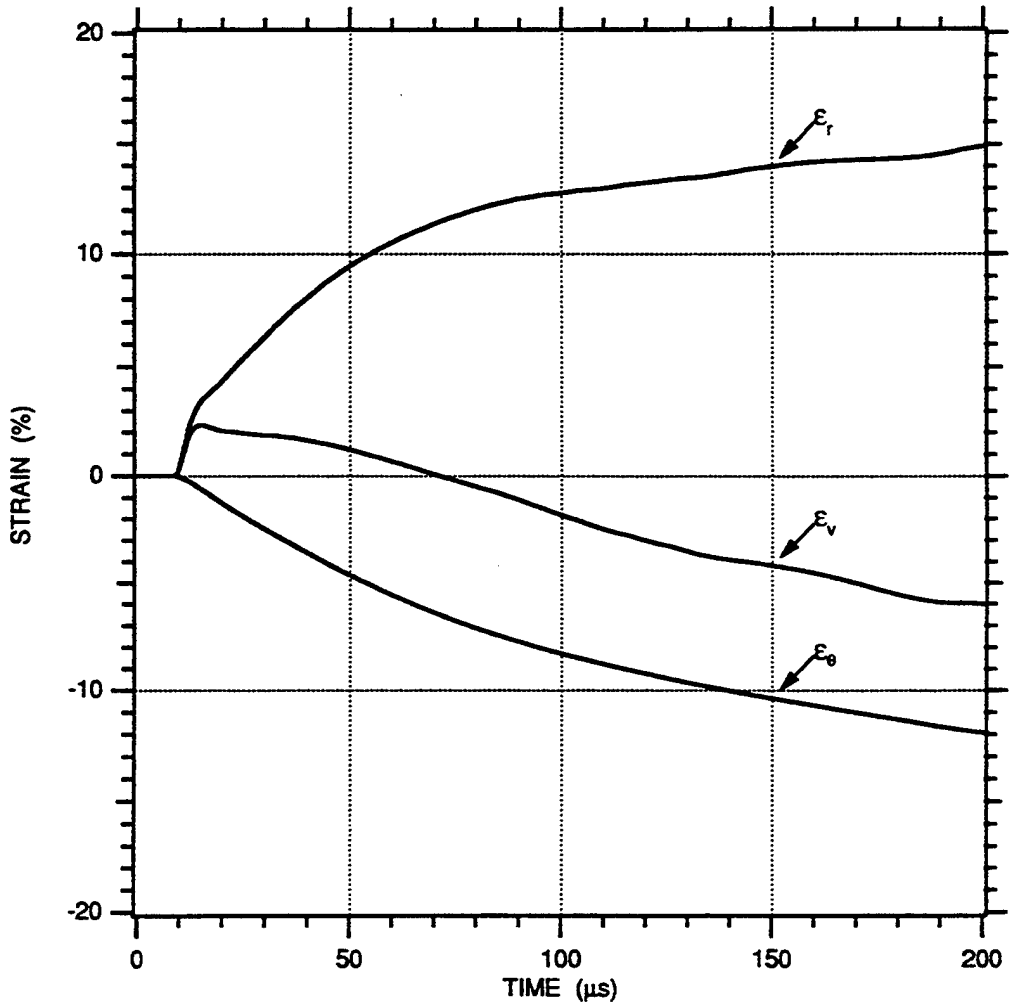

FIGURE 4-14. STRAIN-TIME HISTORIES MEASURED IN 100% SATURATED EGLIN BEACH SAND FOR A 3/8 g PETN EXPLOSIVE CHARGE AT A RANGE BETWEEN 2.54 AND 3.05 cm

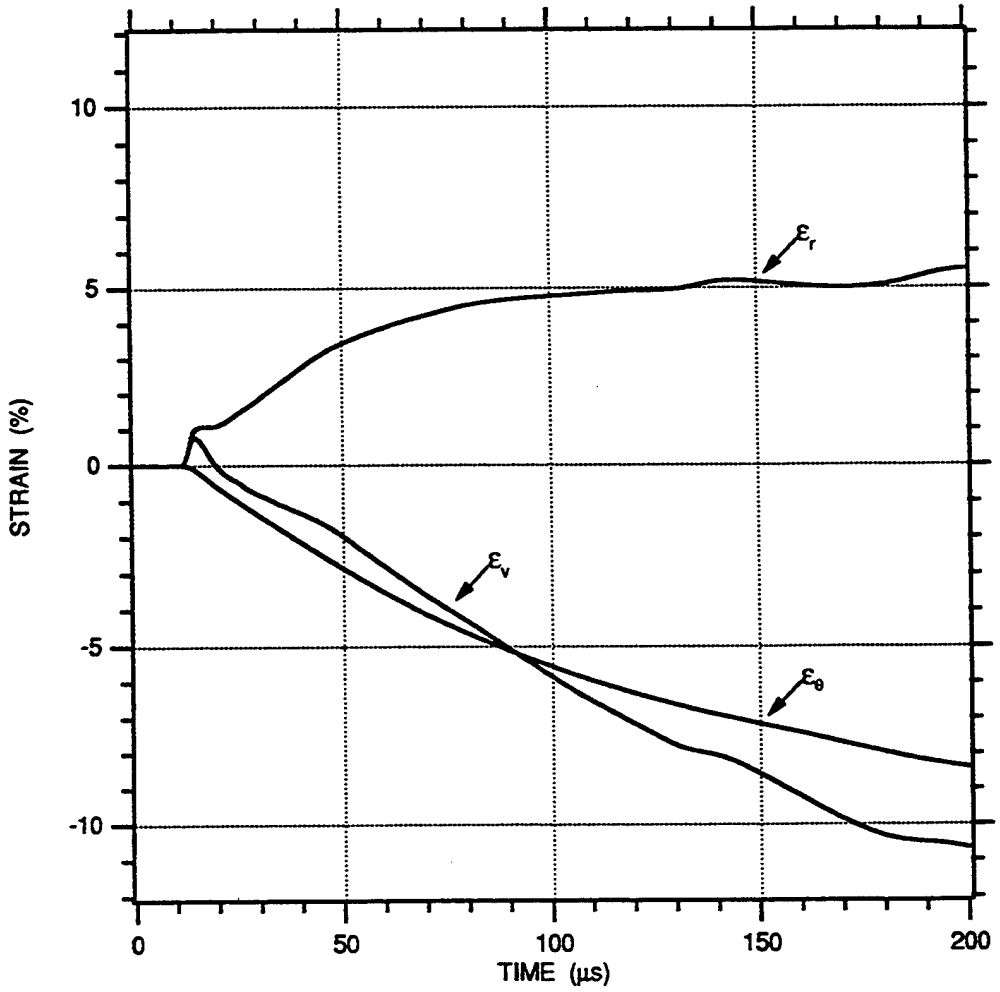

FIGURE 4-15. STRAIN-TIME HISTORIES MEASURED IN 100% SATURATED EGLIN BEACH SAND FOR A 3/8 g PETN EXPLOSIVE CHARGE AT A RANGE BETWEEN 3.05 AND 3.55 cm

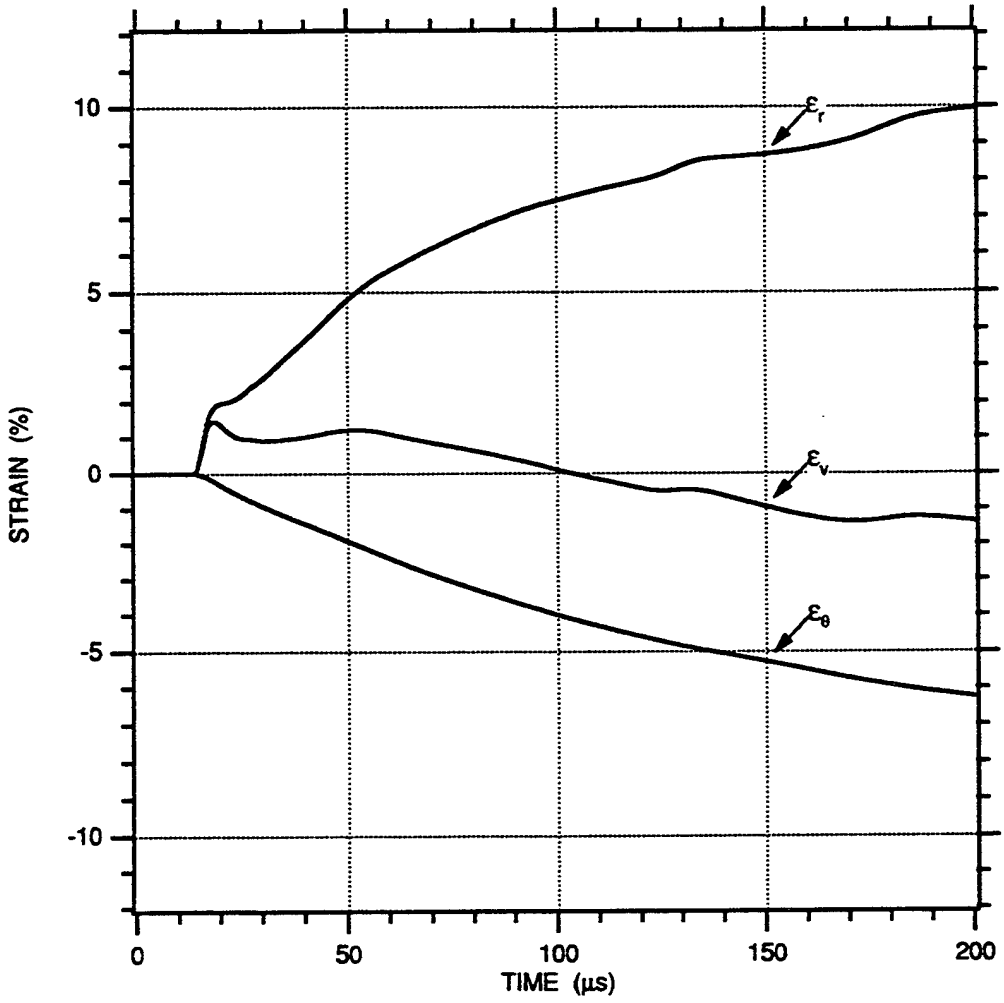

FIGURE 4-16. STRAIN-TIME HISTORIES MEASURED IN 100% SATURATED EGLIN BEACH SAND FOR A 3/8 g PETN EXPLOSIVE CHARGE AT A RANGE BETWEEN 3.55 AND 4.05 cm

SECTION 5

DETAILED RESULTS FOR 95% SATURATED SAND MODEL

The 95% saturated sand model had a measured dry density of 1.659 ± 0.008 g/cm^3, a calculated porosity of $37.5 \pm 0.3\%$ [Porosity % = (1 - Dry Density/Grain Density) x 100], and a calculated saturated density of 2.015 ± 0.0119/cm^3. The measured saturated density was 2.012 ± 0.011 g/cm^3. The estimated error associated with the total saturated level of 95% is $\pm 1\%$ based on bulk weight measurements. Figure 2-4 shows a reference saturation uniformity characteristic for a 95% saturated sand model.

PARTICLE VELOCITY MEASUREMENTS

Figures 5-1 through 5-7 show the particle velocity records measured at ranges from 1.01 to 4.05 cm. The gage failure indicated in the figures is attributed to breakage of the wire loop resulting from radial displacement, which generates a hoop strain in excess of the wire failure strain of approximately 20% to 25%. The particle velocity gage at a range of 0.54 cm (Gage No. PV1), and which is adjacent to the spherical charge, is not shown due to breakage before the peak particle velocity. The particle velocity records show approximately a linear rise to the peak particle velocity followed by a decay to a lower particle velocity. The reflection from the aluminum container boundary occurs between 130 and 150 μs at ranges between 4.05 and 3.05 cm, respectively. Beyond a time of 130 μs, the wave front is no longer spherically propagating.

Figure 5-8 shows a profile of range versus TOA. The data points have been fitted with a least squares second order polynomial having the form of

$$\text{Range} = 0.304 + 0.291\ \text{TOA} - 0.00403\ \text{TOA}^2 \qquad (5.1)$$

where range is in centimeters and TOA is in microseconds. The wave front speed at any given range can be determined by differentiating Equation (5.1) to produce

$$c = 0.291 - 0.00806\ \text{TOA} \qquad (5.2)$$

where c is the wave front speed in centimeters per microsecond. Converting c to units of meters per second, the wave front speed varies from 2840 m/s at a range of 0.54 cm to 1590 m/s at a range of 4.05 cm.

Figure 5-9 shows the attenuation of peak particle velocity with increased range. Using Equation (3.1), the peak particle velocity (m/s) can be multiplied by the saturated density (kg/m^3) and wave front speed (m/s) to produce an estimate for the peak radial stress (Pa). Table 5-1 summarizes the TOA, wave front speed, peak particle velocity, and estimated radial stress for the 95% saturated sand model.

TABLE 5-1. SUMMARY OF EXPERIMENTAL RESULTS FROM PARTICLE VELOCITY MEASUREMENTS FOR THE 95% SATURATED SAND MODEL

Range (cm ± 0.05 cm)	TOA (μs ± 0.2 μs)	Wave Front Speed (m/s ± 10%)	Peak Particle Velocity (m/s ± 2%)	Estimated Peak Stress (kbar)
0.54	0.9	2840	NA	NA
1.01	2.6	2700	184.5	10.0
1.55	4.4	2560	95.8	4.9
2.04	6.2	2410	57.2	2.8
2.54	8.9	2200	47.6	2.1
3.05	11.3	2000	32.1	1.3
3.55	13.9	1790	30.7	1.1
4.05	16.5	1590	25.0	0.8

PARTICLE DISPLACEMENTS AND STRAINS

The particle velocity-time histories shown in Figures 5-1 through 5-7 can be temporally integrated to obtain displacement-time histories. Figure 5-10 shows the particle displacement-time-histories.

Figures 4-11 to 4-16 shows fractional radial (ε_r), circumferential (ε_θ), and volumetric (ε_v) engineering strains. The governing equations used to calculate these strains are given in Appendix B. The strains are based on the relative displacements between adjacent particle velocity gages. Positive strains indicate compression. Negative strains indicate elongation for the circumferential strains and dilation for the volumetric strains. The volumetric strain-time histories show that each fractional shell volume dilates after an initial compression.

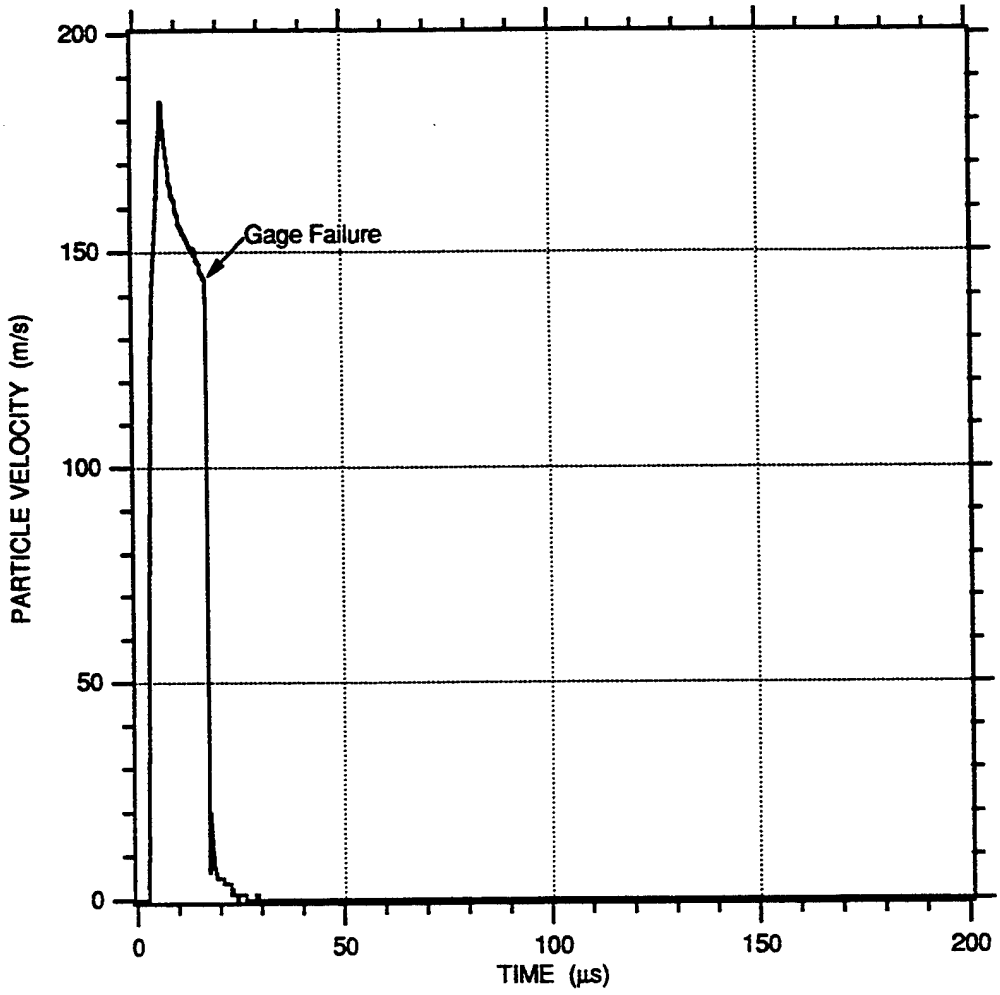

FIGURE 5-1. PARTICLE VELOCITY-TIME HISTORY MEASURED IN 95% SATURATED EGLIN BEACH SAND FOR A 3/8 g PETN EXPLOSIVE CHARGE AT A RANGE OF 1.01 cm

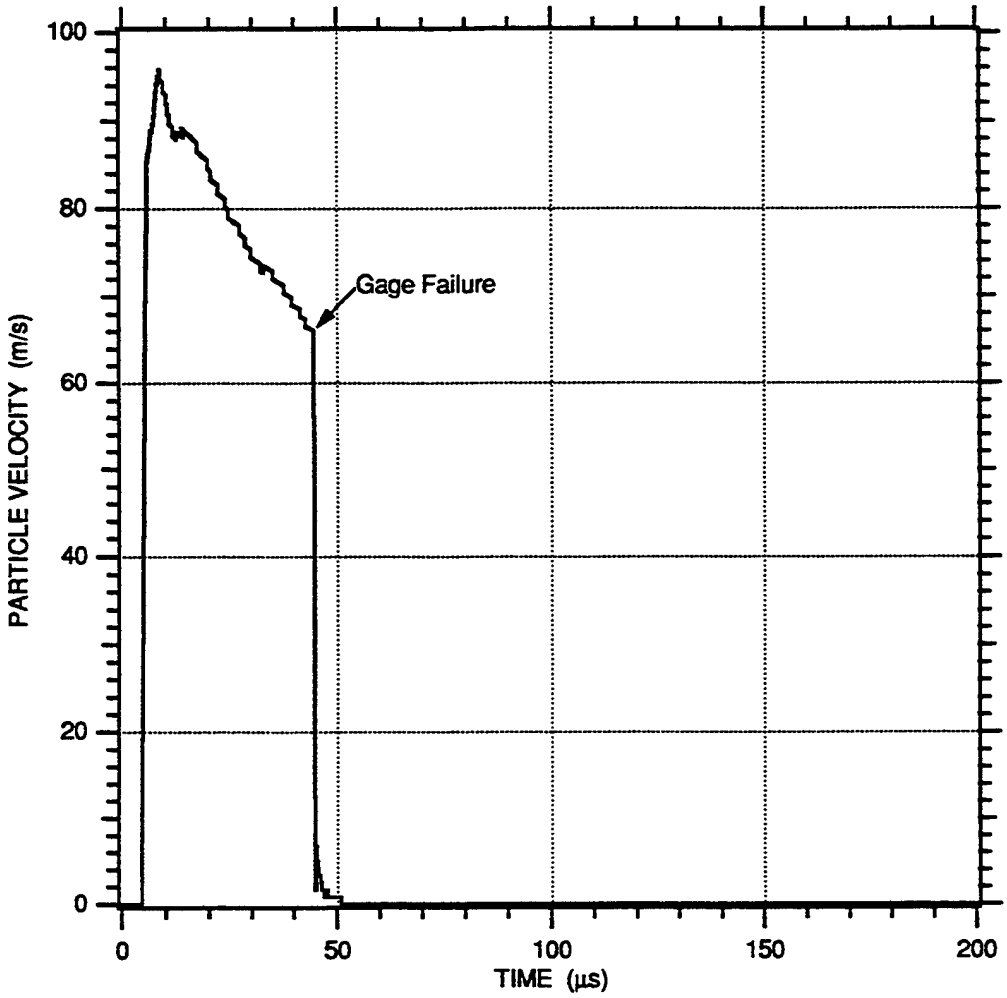

FIGURE 5-2. PARTICLE VELOCITY-TIME HISTORY MEASURED IN 95% SATURATED EGLIN BEACH SAND FOR A 3/8 g PETN EXPLOSIVE CHARGE AT A RANGE OF 1.55 cm

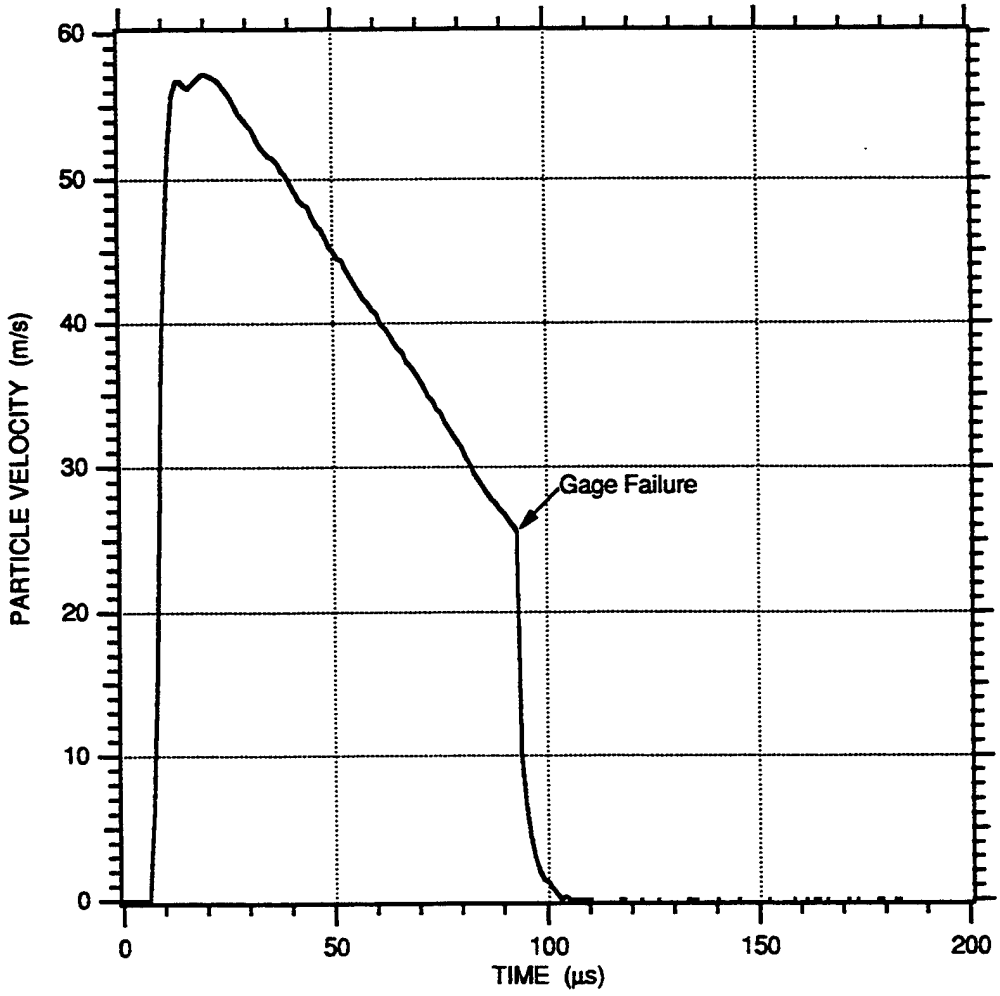

FIGURE 5-3. PARTICLE VELOCITY-TIME HISTORY MEASURED IN 95% SATURATED EGLIN BEACH SAND FOR A 3/8 g PETN EXPLOSIVE CHARGE AT A RANGE OF 2.04 cm

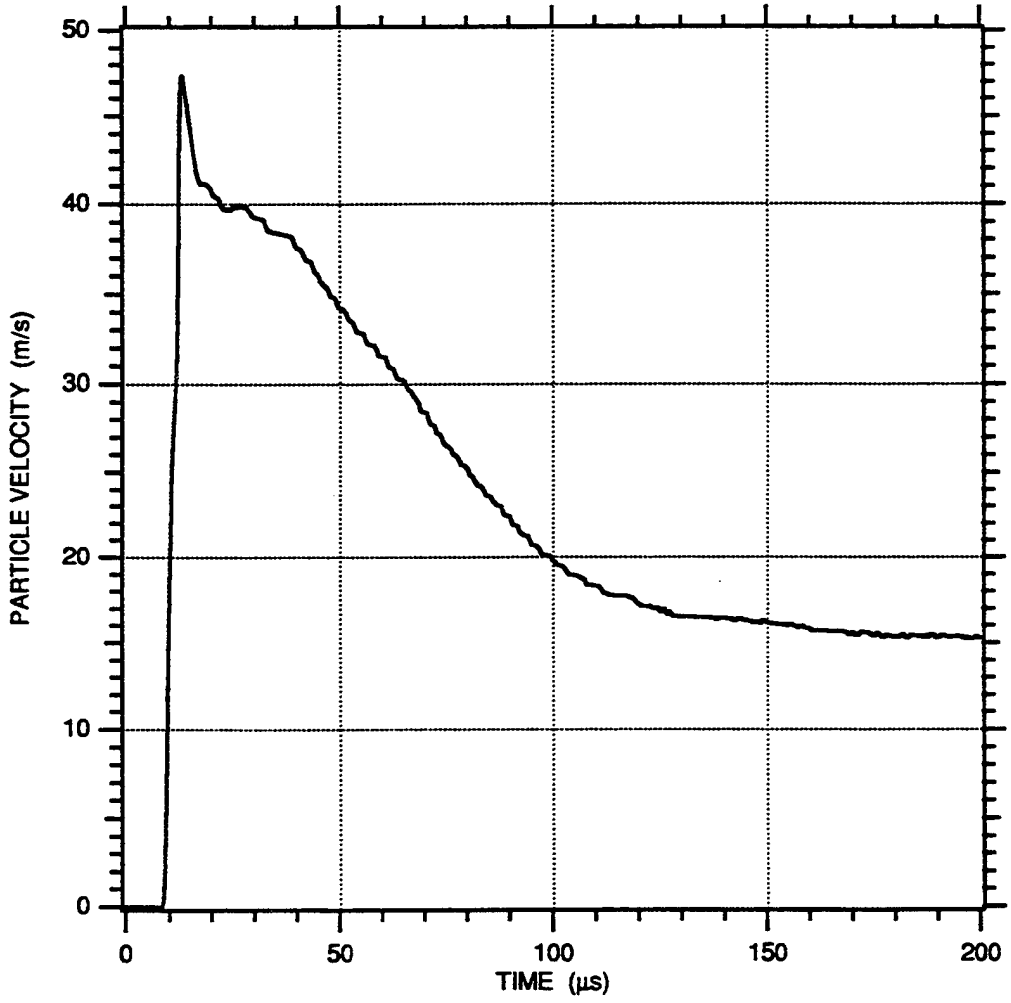

FIGURE 5-4. PARTICLE VELOCITY-TIME HISTORY MEASURED IN 95% SATURATED EGLIN BEACH SAND FOR A 3/8 g PETN EXPLOSIVE CHARGE AT A RANGE OF 2.54 cm

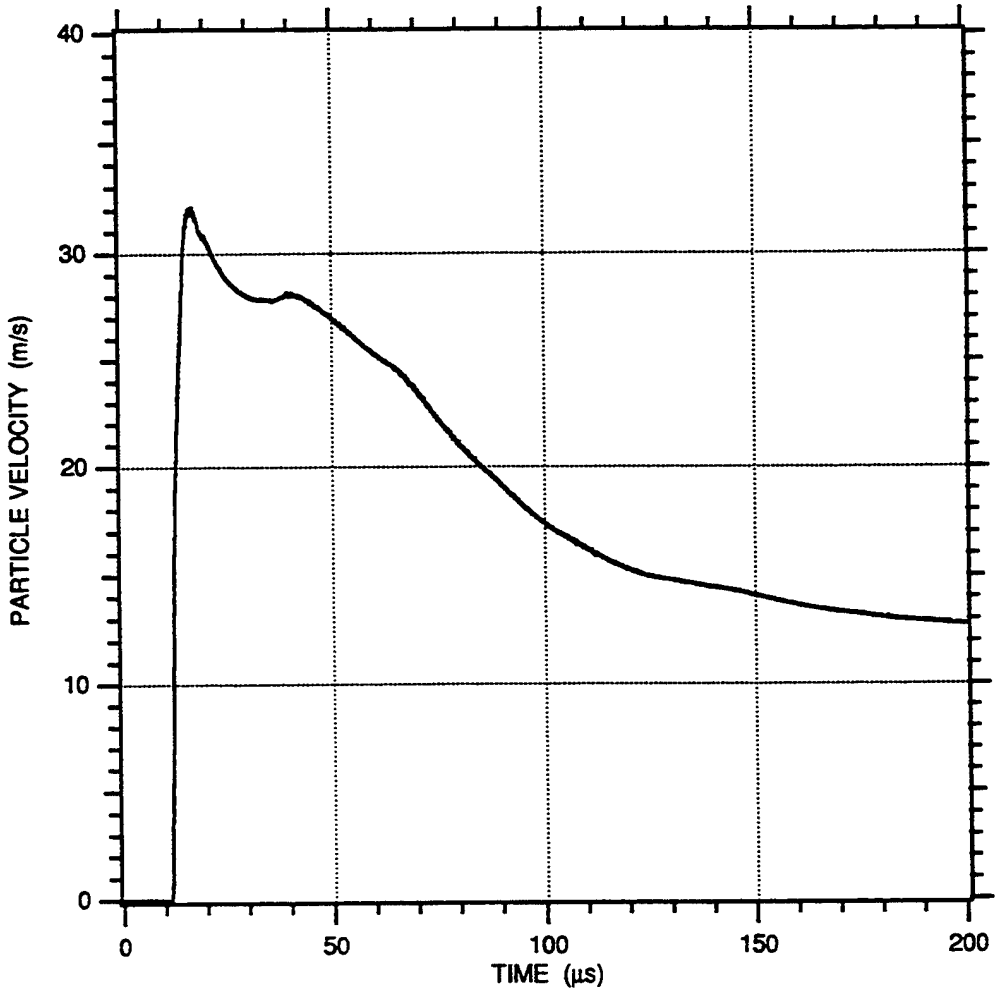

FIGURE 5-5. PARTICLE VELOCITY-TIME HISTORY MEASURED IN 95% SATURATED EGLIN BEACH SAND FOR A 3/8 g PETN EXPLOSIVE CHARGE AT A RANGE OF 3.05 cm

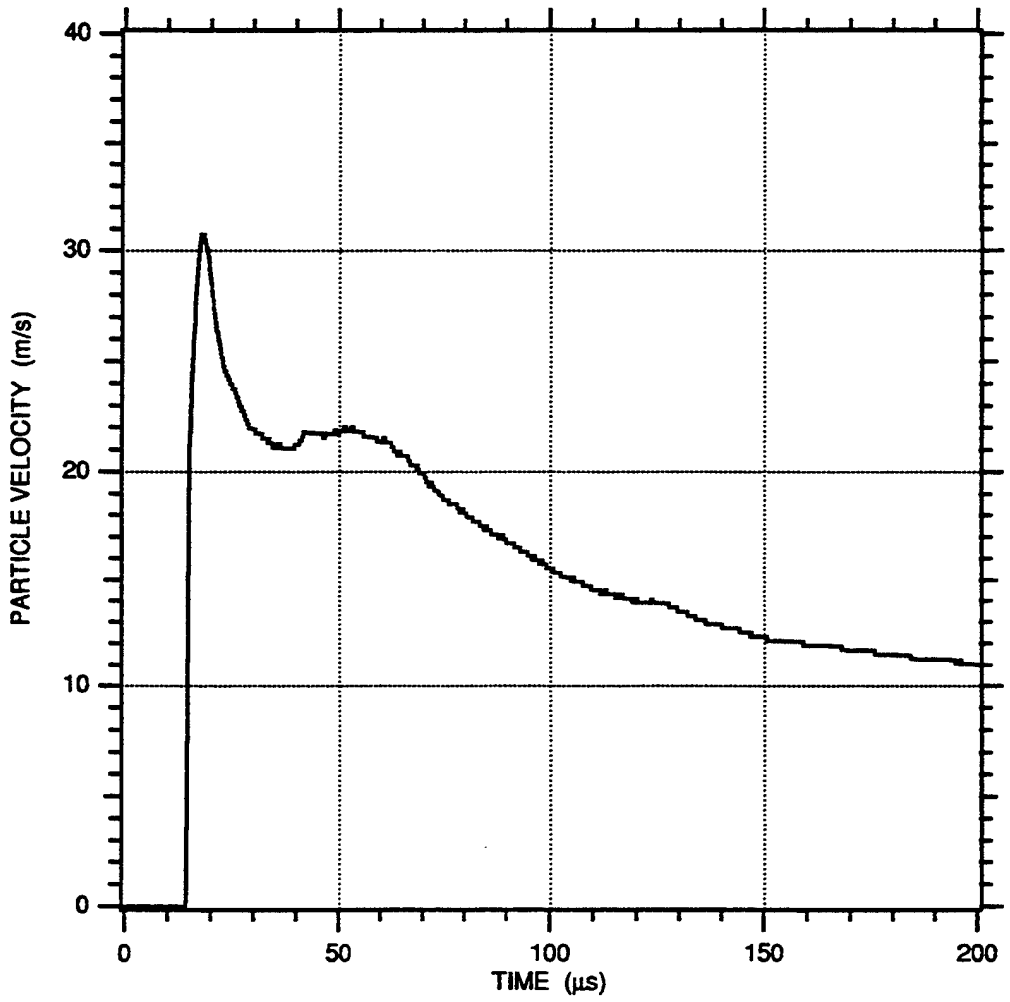

FIGURE 5-6. PARTICLE VELOCITY-TIME HISTORY MEASURED IN 95% SATURATED EGLIN BEACH SAND FOR A 3/8 g PETN EXPLOSIVE CHARGE AT A RANGE OF 3.55 cm

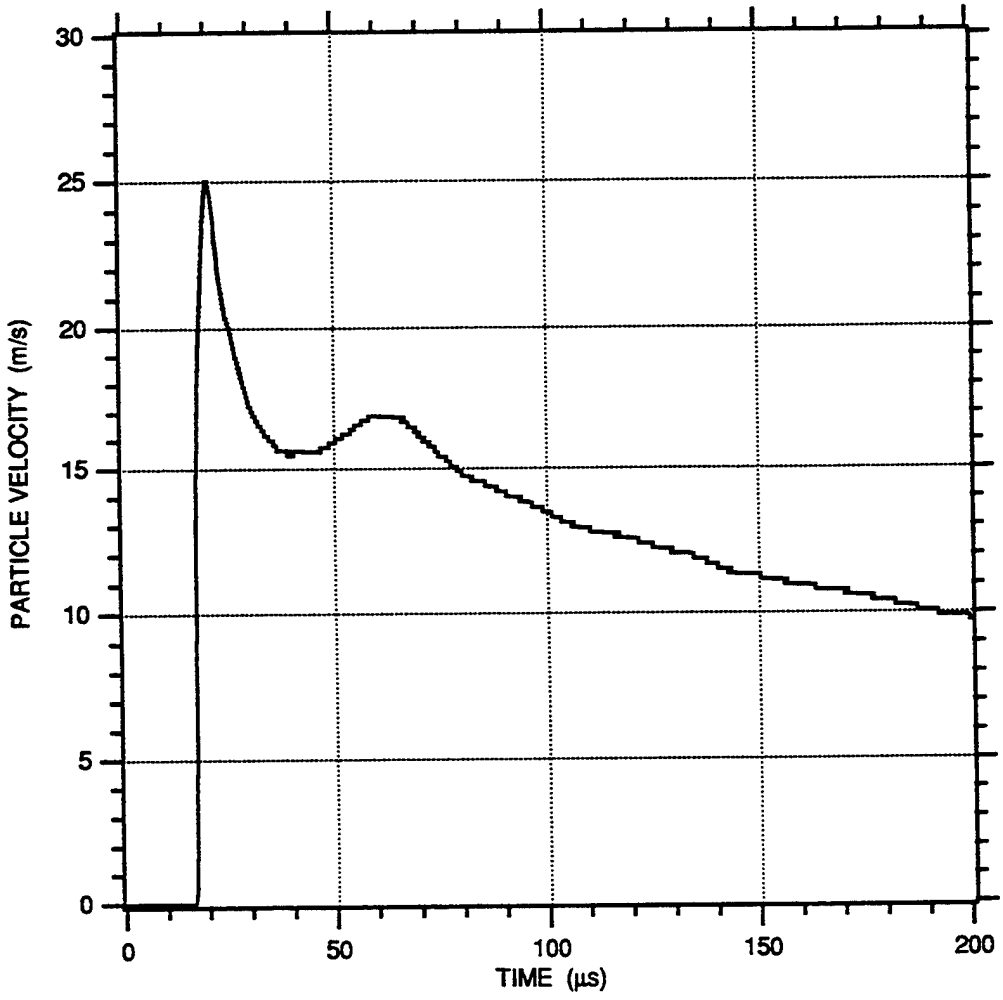

FIGURE 5-7. PARTICLE VELOCITY-TIME HISTORY MEASURED IN 95% SATURATED EGLIN BEACH SAND FOR A 3/8 g PETN EXPLOSIVE CHARGE AT A RANGE OF 4.05 cm

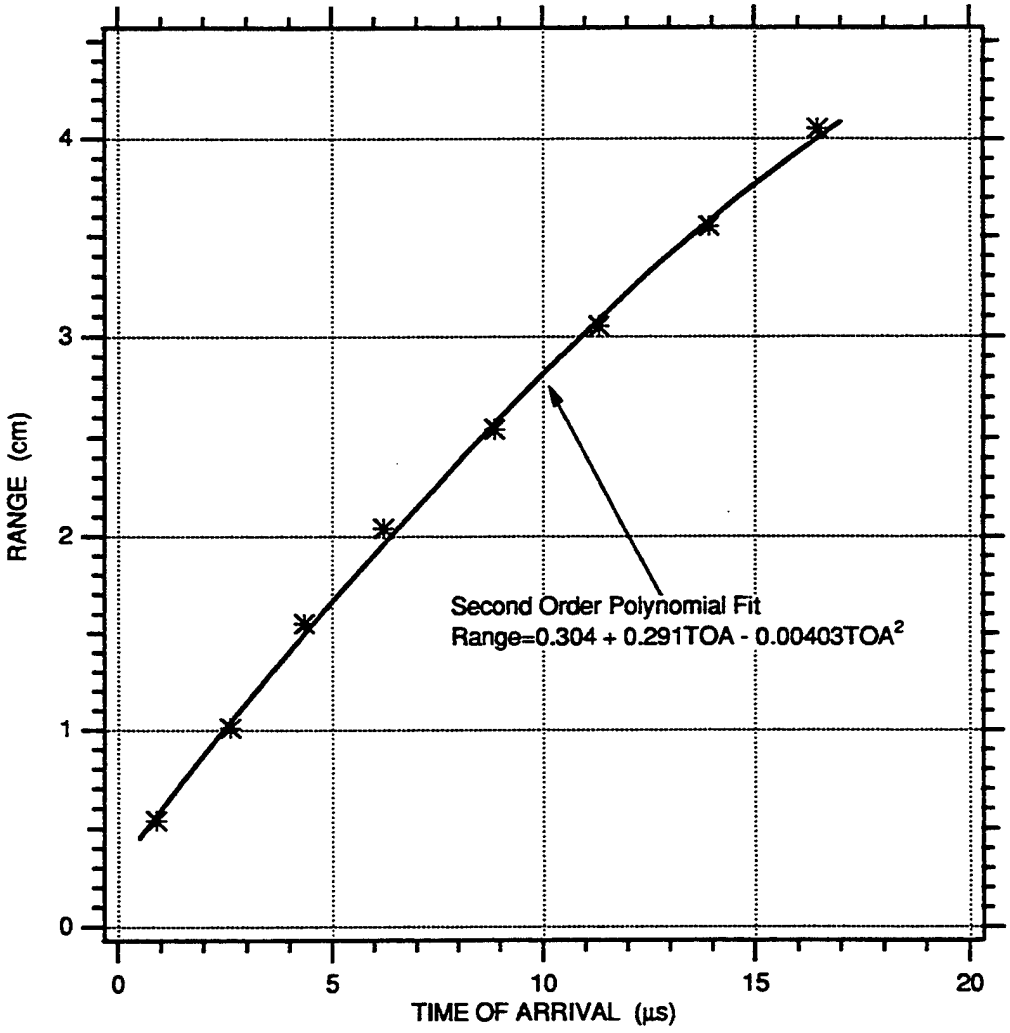

FIGURE 5-8. RANGE VERSUS TIME OF ARRIVAL MEASURED IN 95% SATURATED EGLIN BEACH SAND FOR A 3/8 g PETN EXPLOSIVE CHARGE

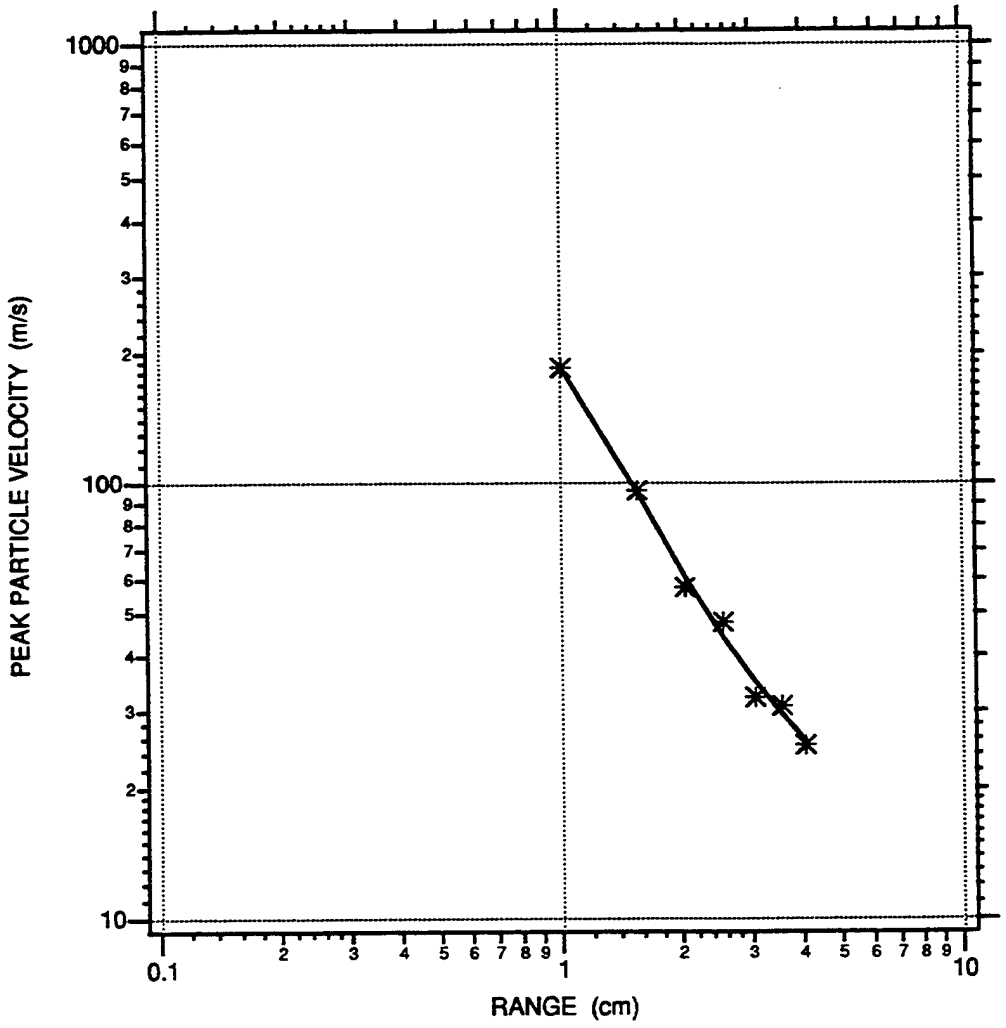

FIGURE 5-9. ATTENUATION OF PEAK PARTICLE VELOCITY MEASURED IN 95% SATURATED EGLIN BEACH SAND FOR A 3/8 g PETN EXPLOSIVE CHARGE

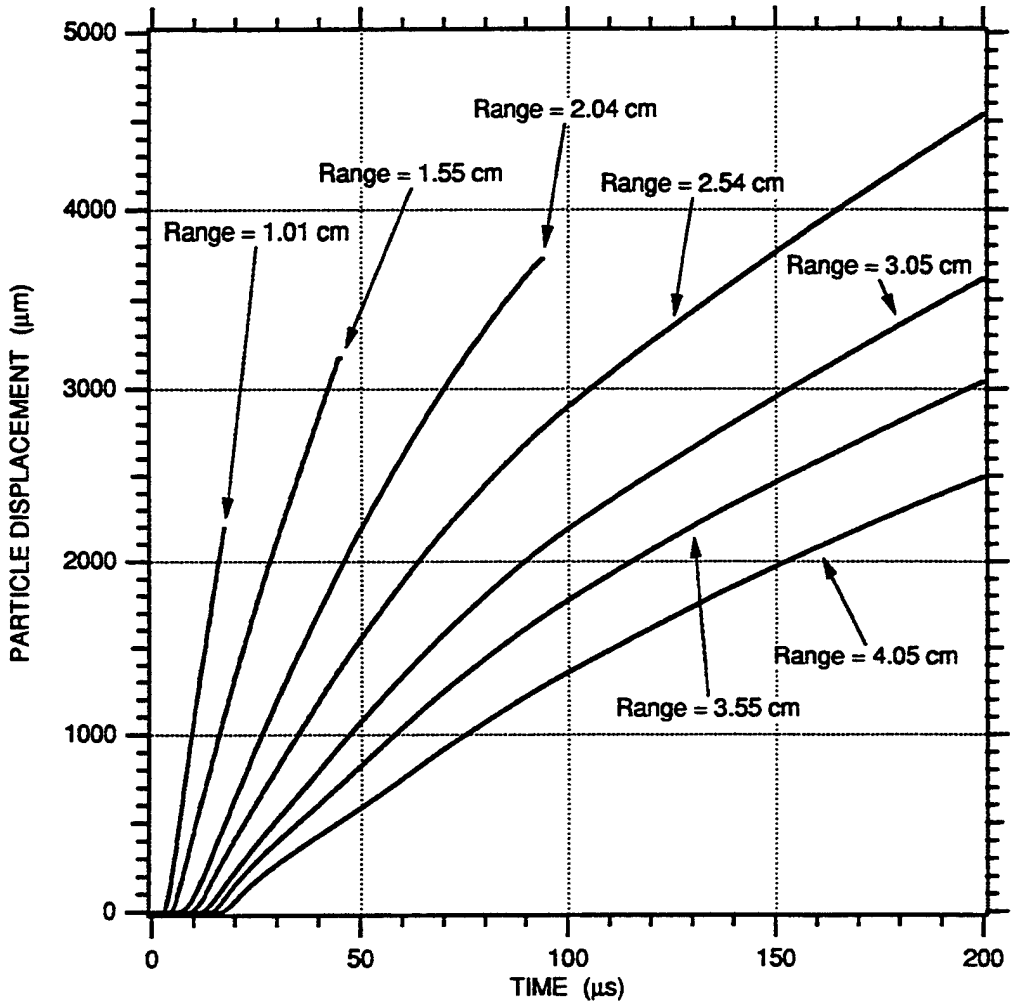

FIGURE 5-10. PARTICLE DISPLACEMENT-TIME HISTORIES MEASURED IN 95% SATURATED EGLIN BEACH SAND FOR A 3/8 g PETN EXPLOSIVE CHARGE

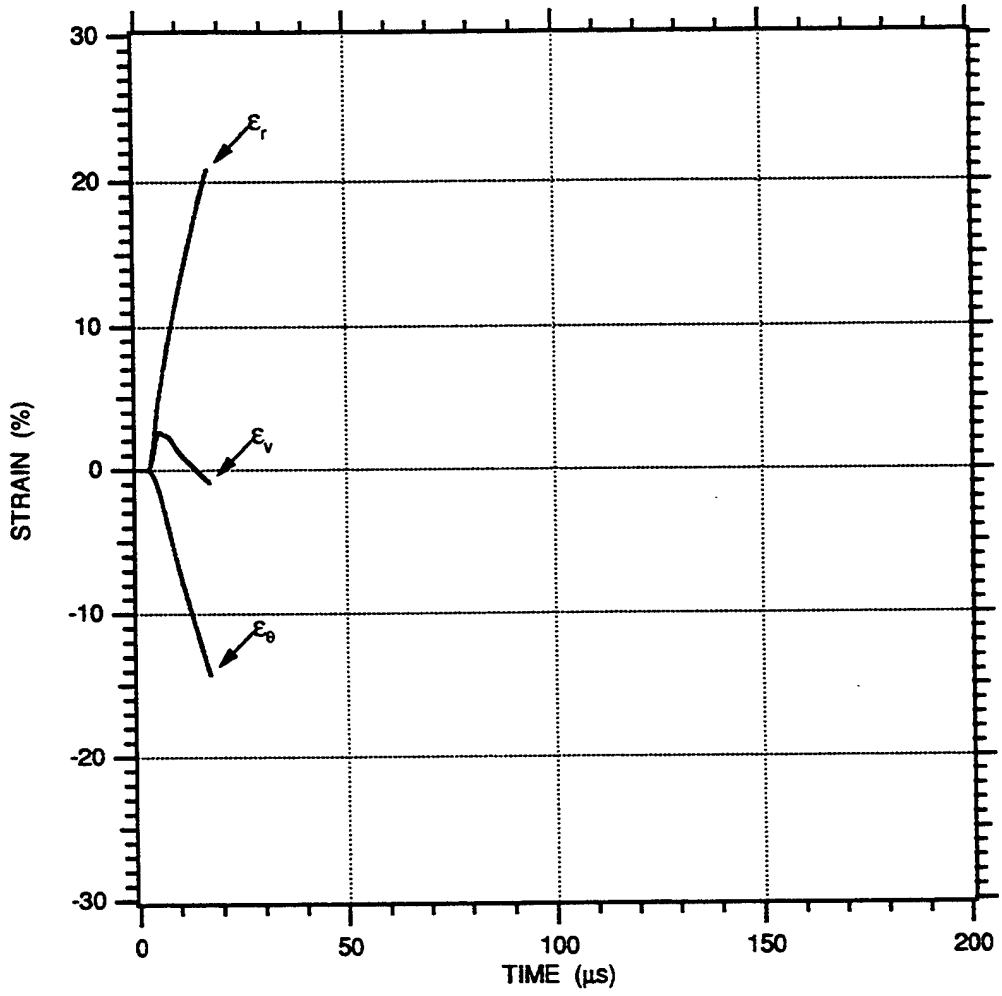

FIGURE 5-11. STRAIN-TIME HISTORIES MEASURED IN 95% SATURATED EGLIN BEACH SAND FOR A 3/8 g PETN EXPLOSIVE CHARGE AT A RANGE BETWEEN 1.01 AND 1.55 cm

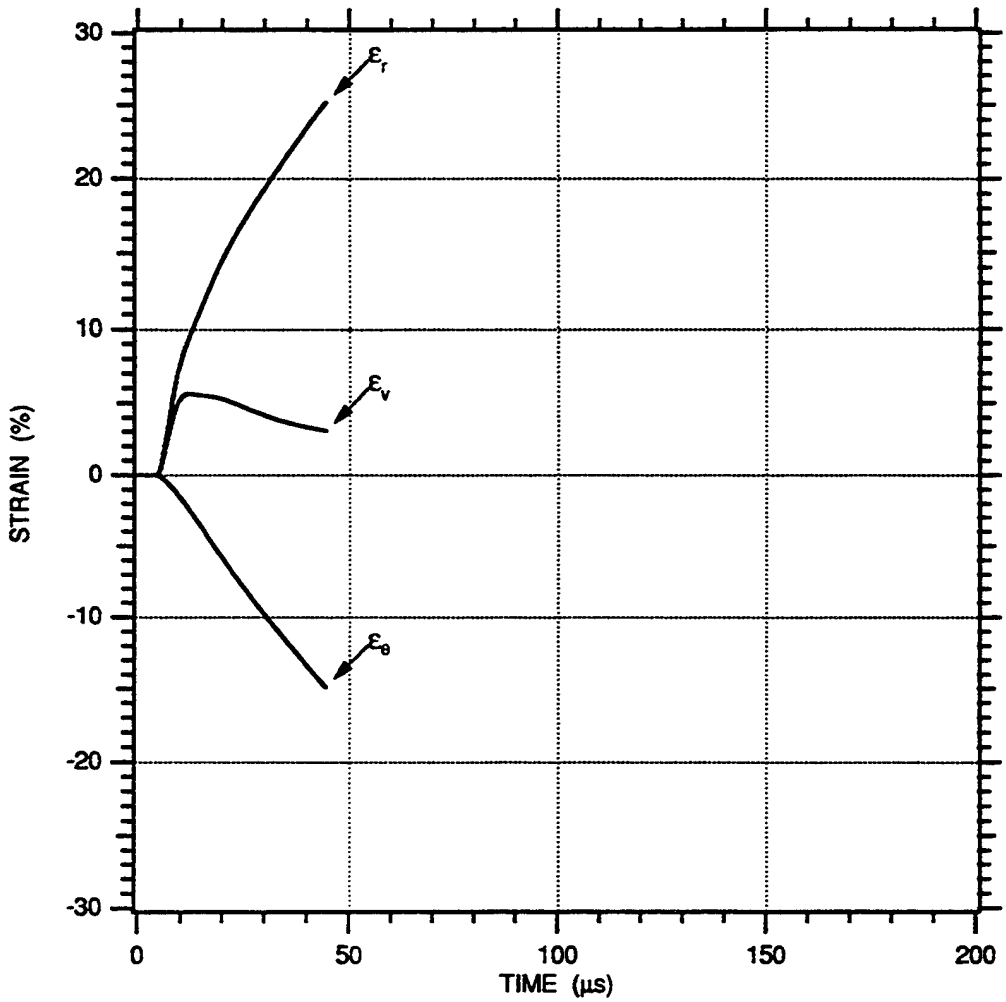

FIGURE 5-12. STRAIN-TIME HISTORIES MEASURED IN 95% SATURATED EGLIN BEACH SAND FOR A 3/8 g PETN EXPLOSIVE CHARGE AT A RANGE BETWEEN 1.55 AND 2.04 cm

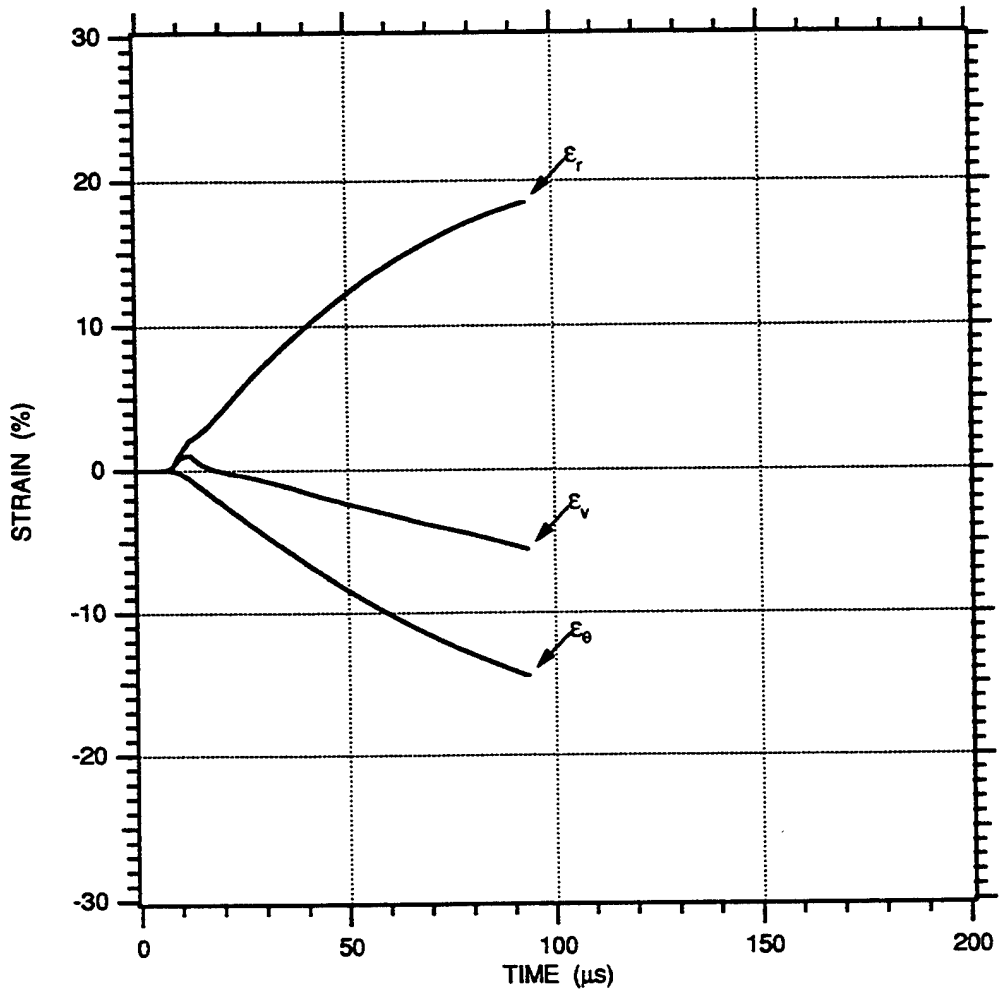

FIGURE 5-13. STRAIN-TIME HISTORIES MEASURED IN 95% SATURATED EGLIN BEACH SAND FOR A 3/8 g PETN EXPLOSIVE CHARGE AT A RANGE BETWEEN 2.04 AND 2.54 cm

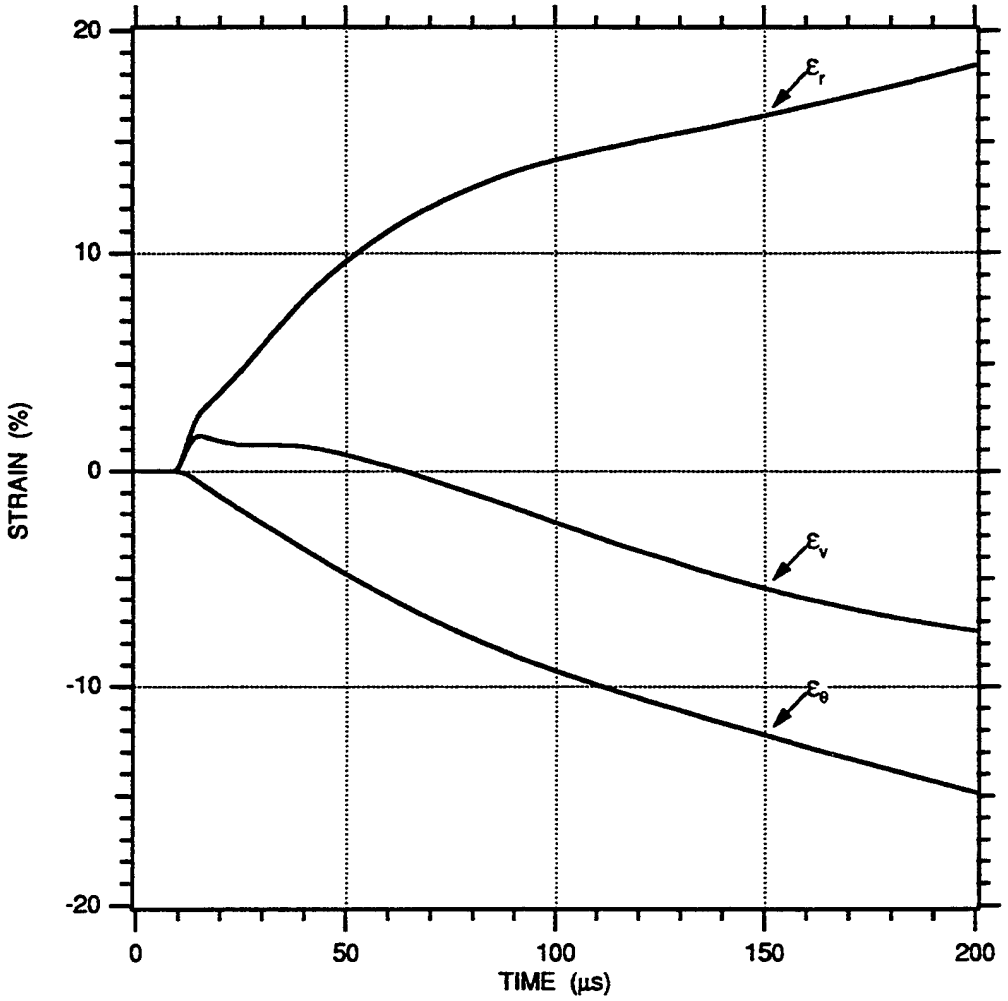

FIGURE 5-14. STRAIN-TIME HISTORIES MEASURED IN 95% SATURATED EGLIN BEACH SAND FOR A 3/8 g PETN EXPLOSIVE CHARGE AT A RANGE BETWEEN 2.54 AND 3.05 cm

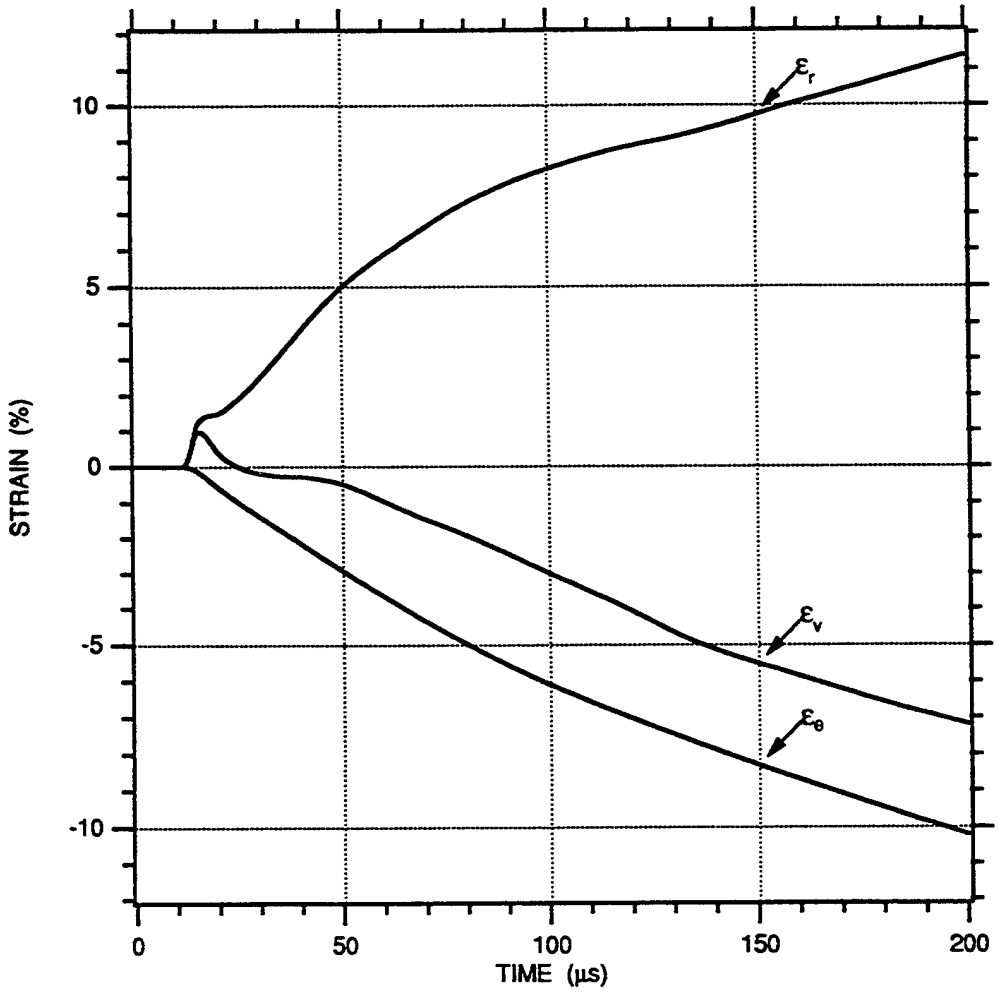

FIGURE 5-15. STRAIN-TIME HISTORIES MEASURED IN 95% SATURATED EGLIN BEACH SAND FOR A 3/8 g PETN EXPLOSIVE CHARGE AT A RANGE BETWEEN 3.05 AND 3.55 cm

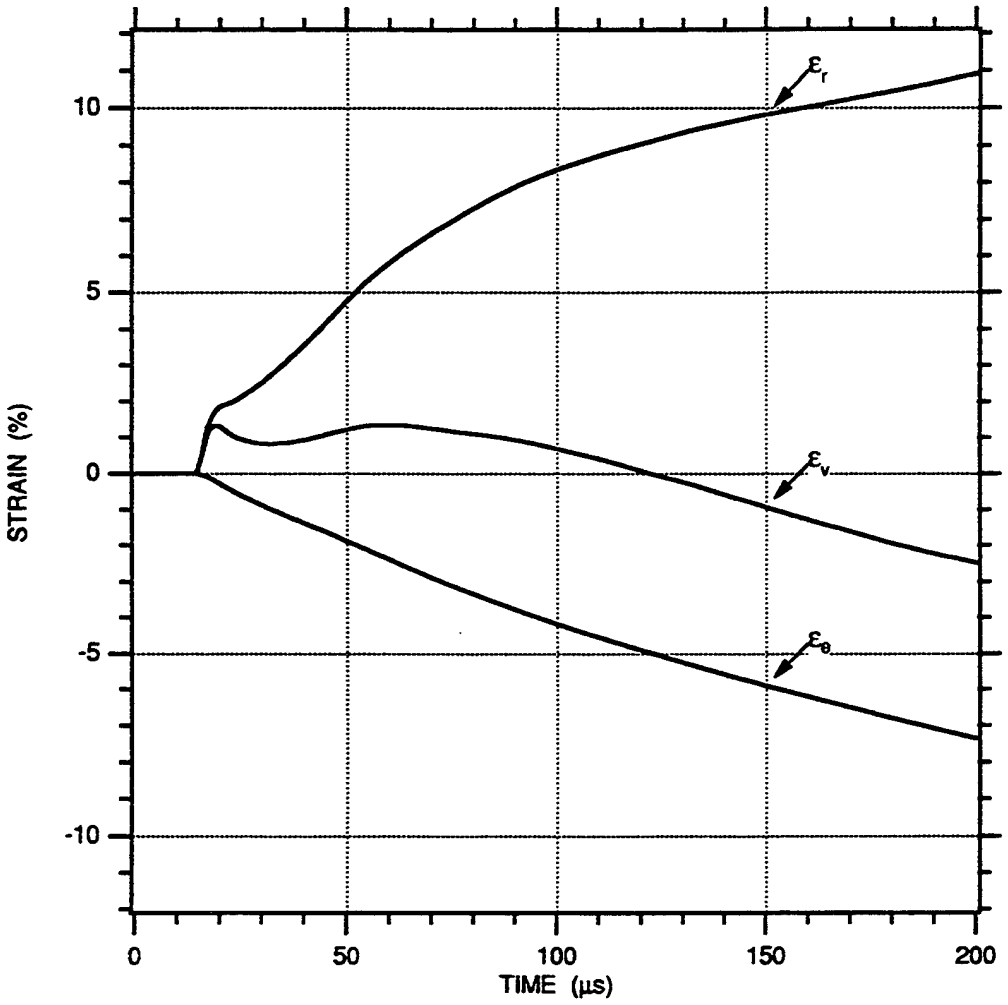

FIGURE 5-16. STRAIN-TIME HISTORIES MEASURED IN 95% SATURATED EGLIN BEACH SAND FOR A 3/8 g PETN EXPLOSIVE CHARGE AT A RANGE BETWEEN 3.55 AND 4.05 cm

SECTION 6

DETAILED RESULTS FOR 78% SATURATED SAND MODEL

The 78% saturated sand model had a measured dry density of 1.465 ± 0.008 g/cm^3, a calculated porosity of 44.8 ± 0.3 % [Porosity % = (1 - Dry Density/Grain Density) x 100], and a calculated saturated density of 1.814 ± 0.011 g/cm^3. The measured saturated density was 1.815 ± 0.011 g/cm^3. The estimated error associated with the total saturated level of 78% is ± 1% based on bulk weight measurements. The 78% saturation level with respect to the pore volume corresponds to 10% air voids with respect to the total volume. Figure 2-5 shows a reference saturation uniformity characteristic for a 78% saturated sand model.

PARTICLE VELOCITY MEASUREMENTS

Figures 6-1 through 6-7 show the particle velocity records measured at ranges from 1.01 to 4.05 cm. The gage failure indicated in the figures is attributed to breakage of the wire loop resulting from radial displacement, which generates a hoop strain in excess of the wire failure strain of approximately 20% to 25%. The particle velocity gage at a range of 0.54 cm (Gage No. PV1), which is adjacent to the spherical charge, is not shown due to breakage before the peak particle velocity. The particle velocity records show approximately a linear rise to the peak particle velocity followed by a decay to almost a constant lower particle velocity. The reflection from the aluminum container boundary occurs after 500 μs for particle velocity gages between the charge and a range of 4.05 cm. Thus, for the record durations shown in Figures 6-1 through 6-7, the wave remains spherical.

Figure 6-8 shows a profile of range versus TOA. The data points have been fitted with a least squares third order polynomial having the form of

$$\text{Range} = 0.272 + 0.194\ \text{TOA} - 3.45\text{E-}03\ \text{TOA}^2 + 2.50\text{E-}05\ \text{TOA}^3 \qquad (6.1)$$

where range is in centimeters and TOA is in microseconds. Equation (6.1) is valid up to a TOA of 46 μs. The wave front speed at any given range can be determined by differentiating Equation (6.1) to produce

$$c = 0.194 - 6.90\text{E-}03\ \text{TOA} + 7.50\text{E-}05\ \text{TOA}^2 \qquad (6.2)$$

where c is the wave front speed in centimeters per microsecond. Converting c to units of meters per second, the wave front speed varies from 1879 m/s at a range of 0.54 cm to 353 m/s at a range of 4.05 cm.

Figure 6-9 shows the attenuation of peak particle velocity with increased range. Using Equation (3.1), the peak particle velocity (m/s) can be multiplied by the saturated density (kg/m^3) and wave front speed (m/s) to produce an estimate for the peak radial stress (Pa). Table 6-1 summarizes the TOA, wave front speed, peak particle velocity, and estimated radial stress for the 78% saturated sand model.

TABLE 6-1. SUMMARY OF EXPERIMENTAL RESULTS FROM PARTICLE VELOCITY MEASUREMENTS FOR THE 78% SATURATED SAND MODEL

Range (cm ± 0.05 cm)	TOA (μs ± 0.2 μs)	Wave Front Speed (m/s ± 10%)	Peak Particle Velocity (m/s ± 2%)	Estimated Peak Stress (kbar)
0.54	0.9	1879	NA	NA
1.01	2.9	1746	193.8	6.1
1.55	6.0	1553	109.6	3.1
2.04	9.9	1330	69.0	1.7
2.54	16.3	1014	45.3	0.8
3.05	23.0	750	31.6	0.4
3.55	31.5	510	23.0	0.2
4.05	45.3	353	17.9	0.1

PARTICLE DISPLACEMENTS AND STRAINS

The particle velocity-time histories shown in Figures 6-1 through 6-7 can be temporally integrated to obtain displacement-time histories. Figure 6-10 shows the particle displacement-time histories.

Figures 6-11 to 6-16 shows fractional radial (ε_r), circumferential (ε_θ), and volumetric (ε_v) engineering strains. The governing equations used to calculate these strains are given in Appendix B. The strains are based on the relative displacements between adjacent particle velocity gage locations. Positive strains indicate compression. Negative strains indicate elongation for the circumferential strains and dilation for the volumetric strains. The volumetric strain-time histories show that each fractional shell volume experiences only compression and no dilation.

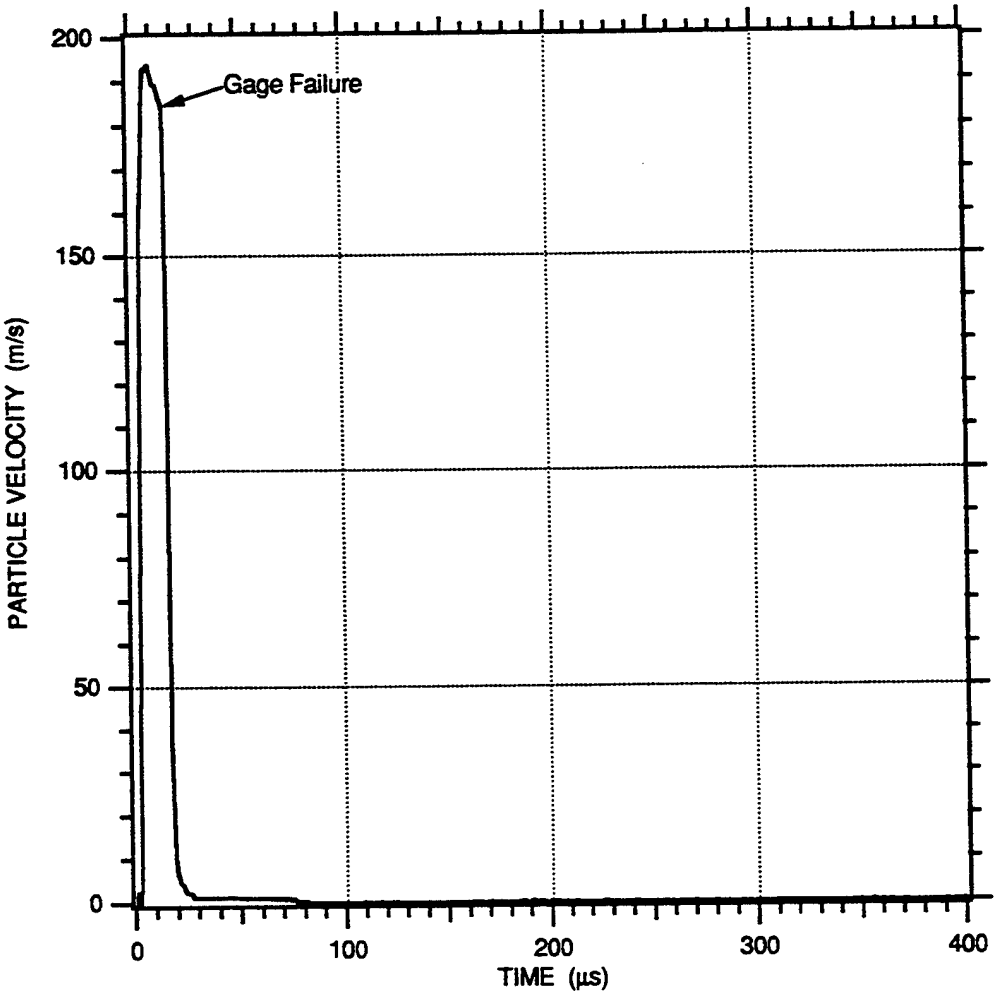

FIGURE 6-1. PARTICLE VELOCITY-TIME HISTORY MEASURED IN 78% SATURATED EGLIN BEACH SAND FOR A 3/8 g PETN EXPLOSIVE CHARGE AT A RANGE OF 1.01 cm

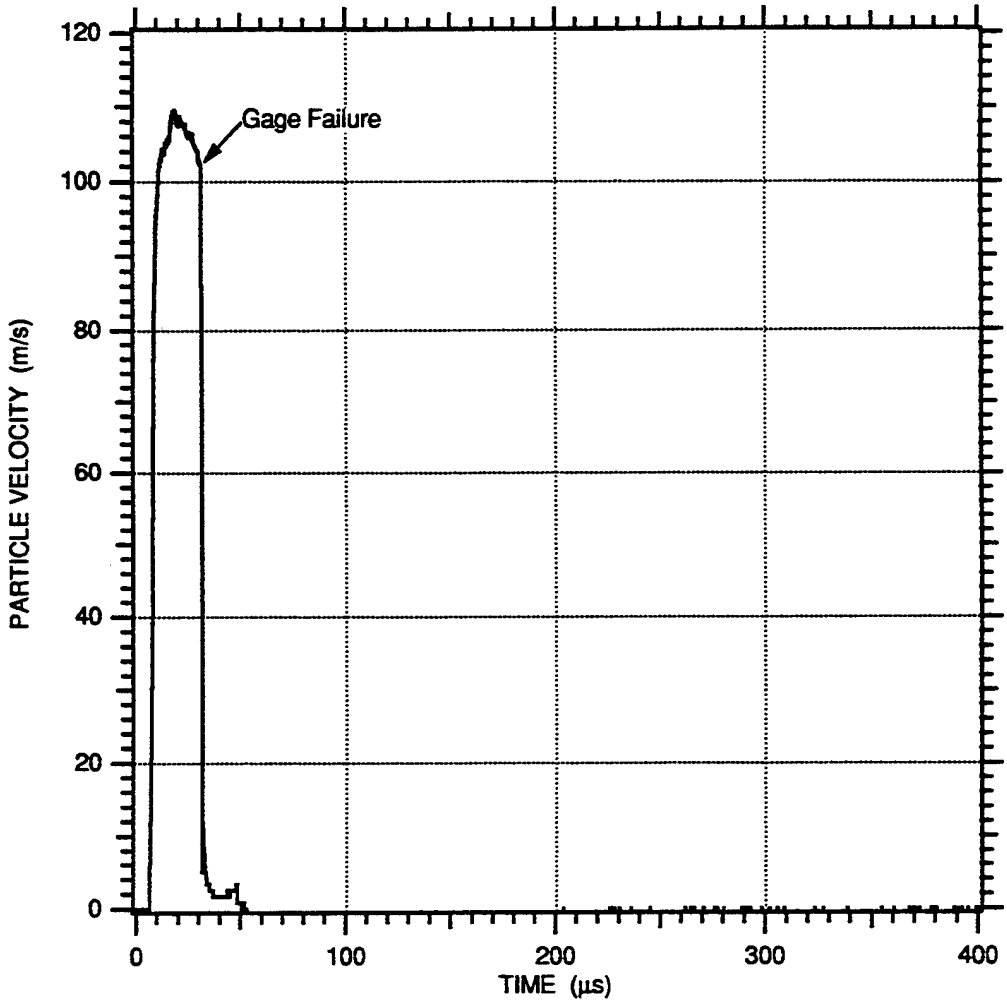

FIGURE 6-2. PARTICLE VELOCITY-TIME HISTORY MEASURED IN 78% SATURATED EGLIN BEACH SAND FOR A 3/8 g PETN EXPLOSIVE CHARGE AT A RANGE OF 1.55 cm

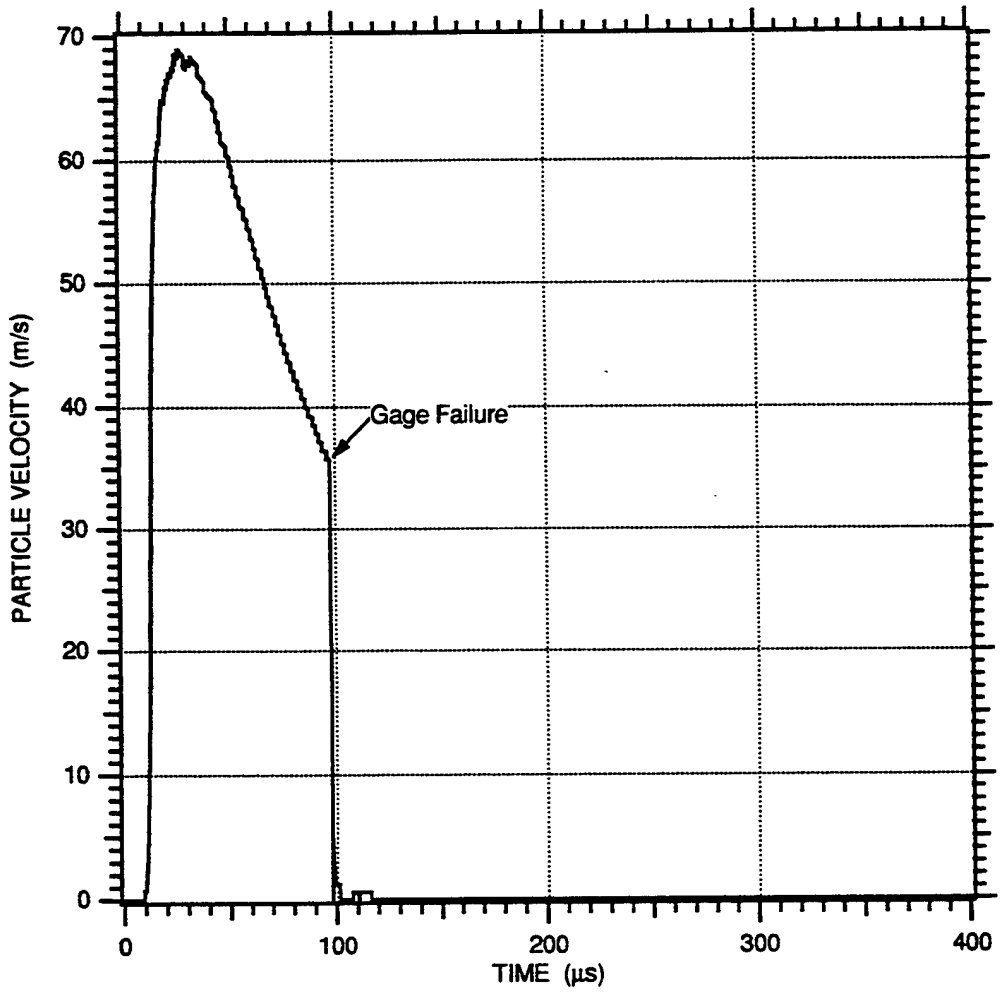

FIGURE 6-3. PARTICLE VELOCITY-TIME HISTORY MEASURED IN 78% SATURATED EGLIN BEACH SAND FOR A 3/8 g PETN EXPLOSIVE CHARGE AT A RANGE OF 2.04 cm

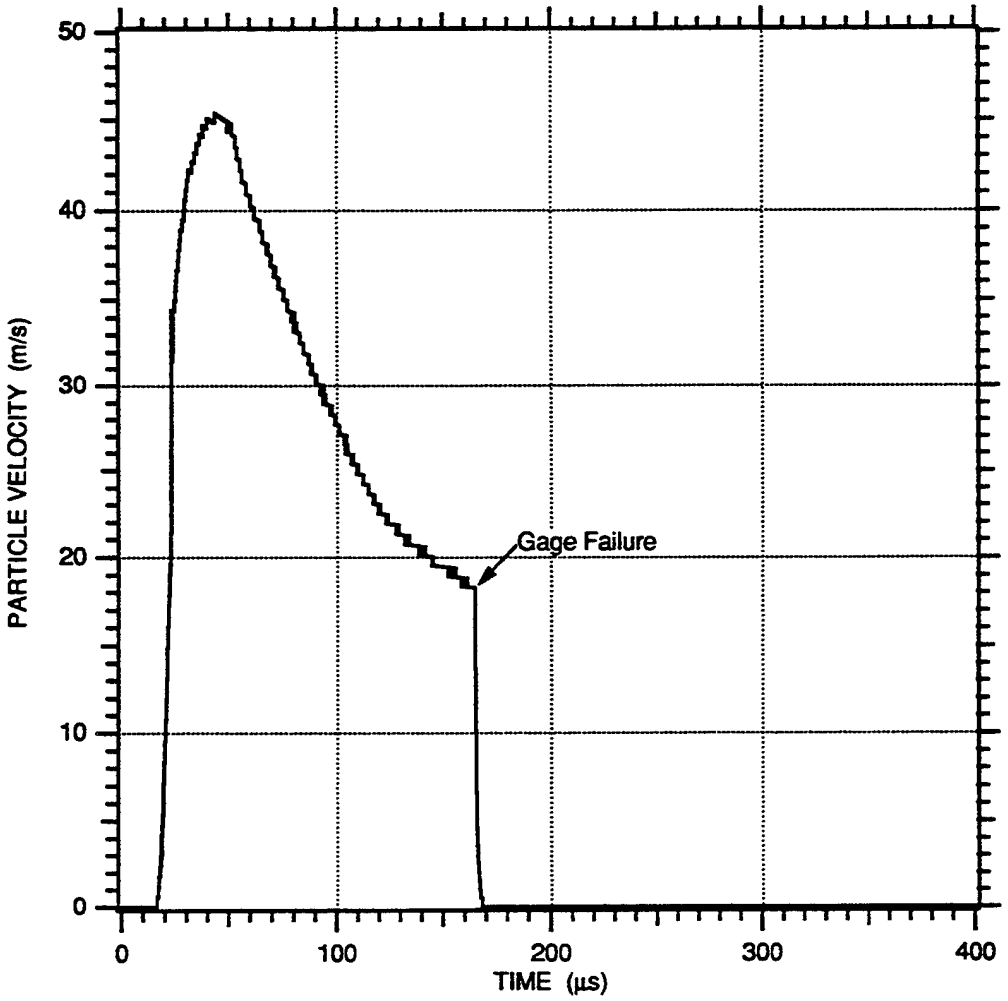

FIGURE 6-4. PARTICLE VELOCITY-TIME HISTORY MEASURED IN 78% SATURATED EGLIN BEACH SAND FOR A 3/8 g PETN EXPLOSIVE CHARGE AT A RANGE OF 2.54 cm

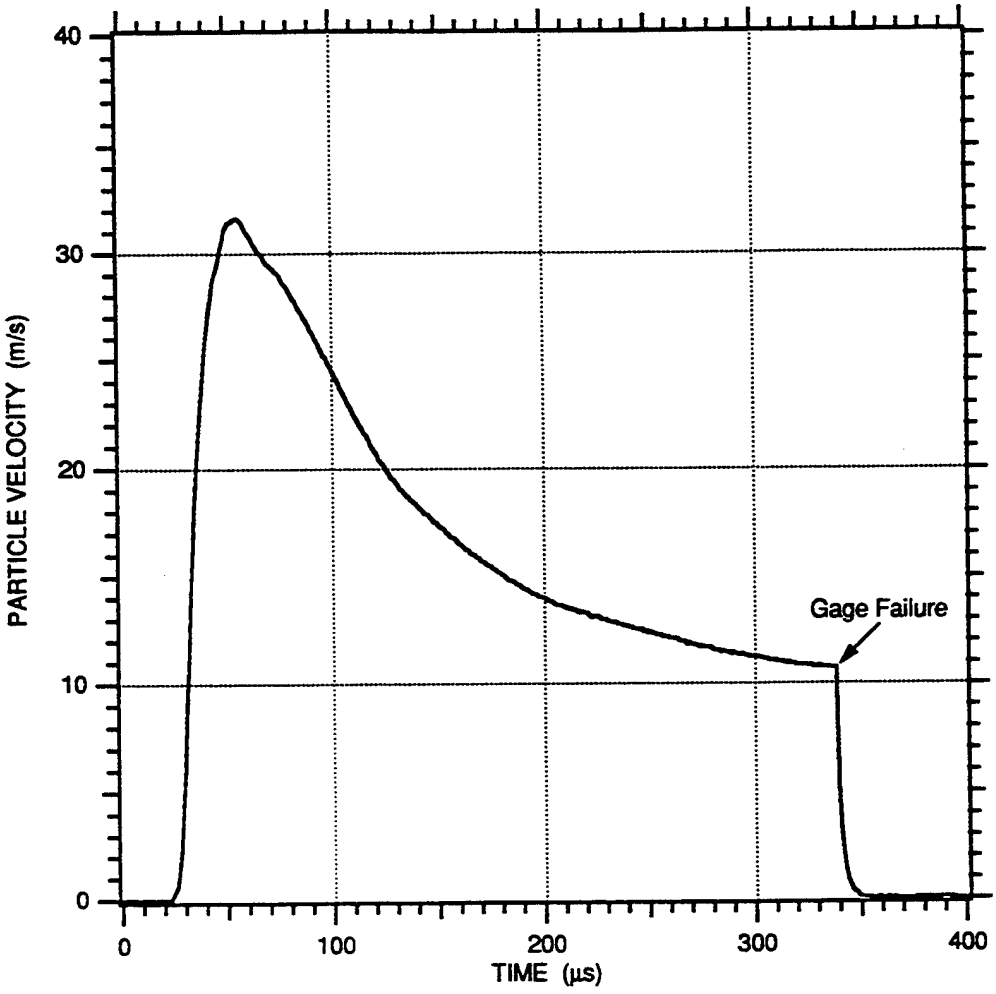

FIGURE 6-5. PARTICLE VELOCITY-TIME HISTORY MEASURED IN 78% SATURATED EGLIN BEACH SAND FOR A 3/8 g PETN EXPLOSIVE CHARGE AT A RANGE OF 3.05 cm

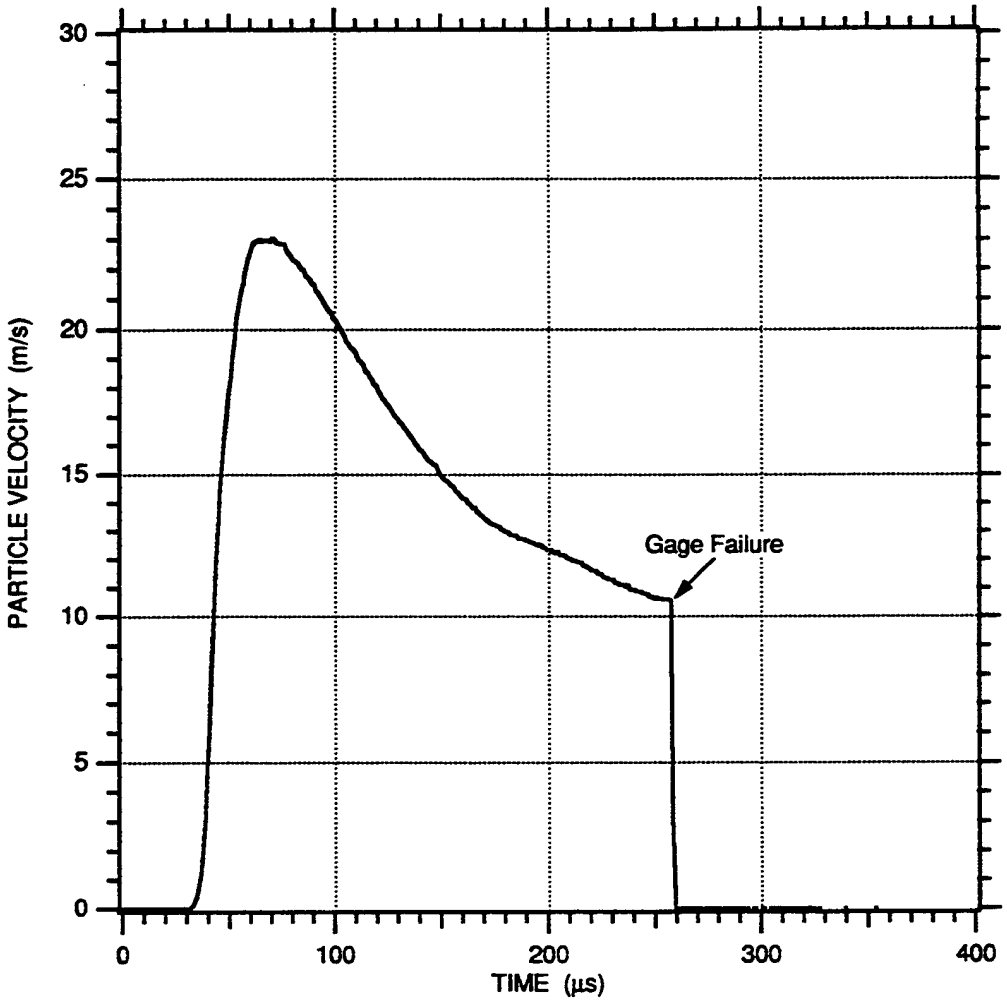

FIGURE 6-6. PARTICLE VELOCITY-TIME HISTORY MEASURED IN 78% SATURATED EGLIN BEACH SAND FOR A 3/8 g PETN EXPLOSIVE CHARGE AT A RANGE OF 3.55 cm

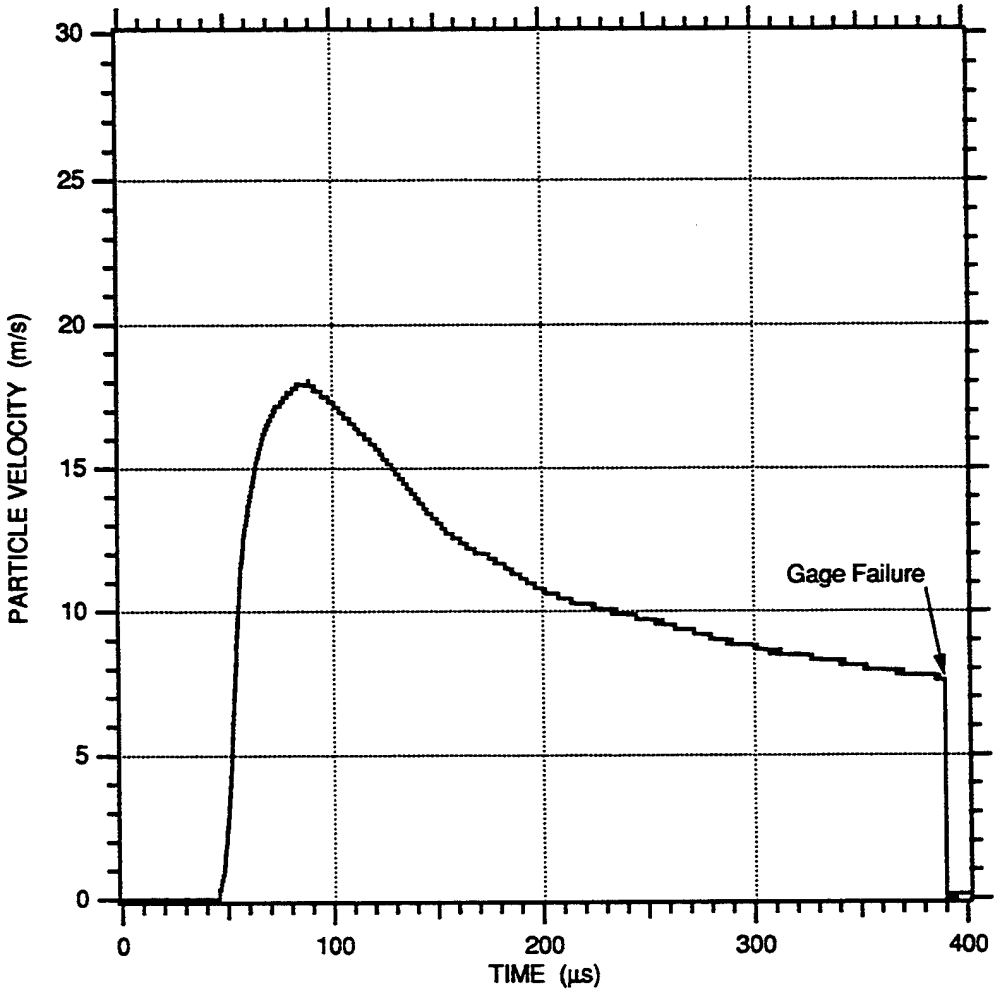

FIGURE 6-7. PARTICLE VELOCITY-TIME HISTORY MEASURED IN 78% SATURATED EGLIN BEACH SAND FOR A 3/8 g PETN EXPLOSIVE CHARGE AT A RANGE OF 4.05 cm

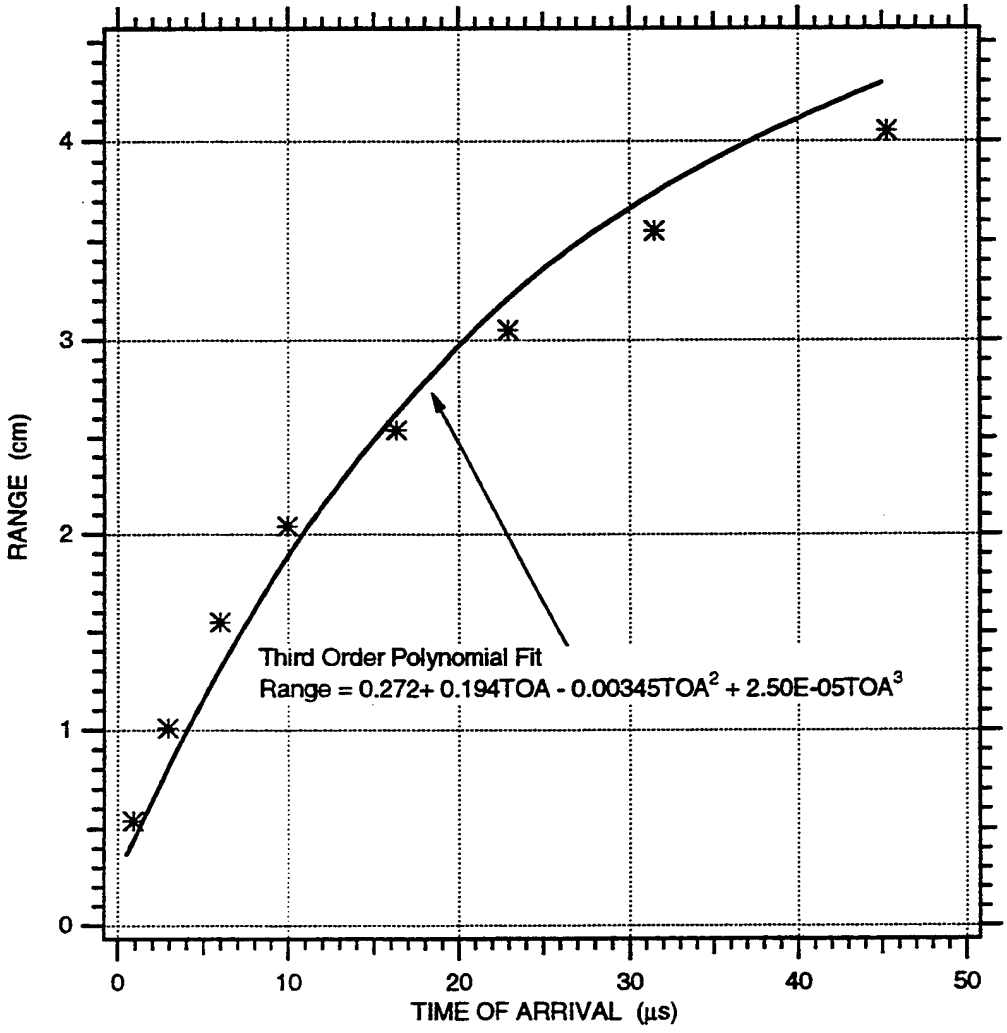

FIGURE 6-8. RANGE VERSUS TIME OF ARRIVAL MEASURED IN 78% SATURATED EGLIN BEACH SAND FOR A 3/8 g PETN EXPLOSIVE CHARGE

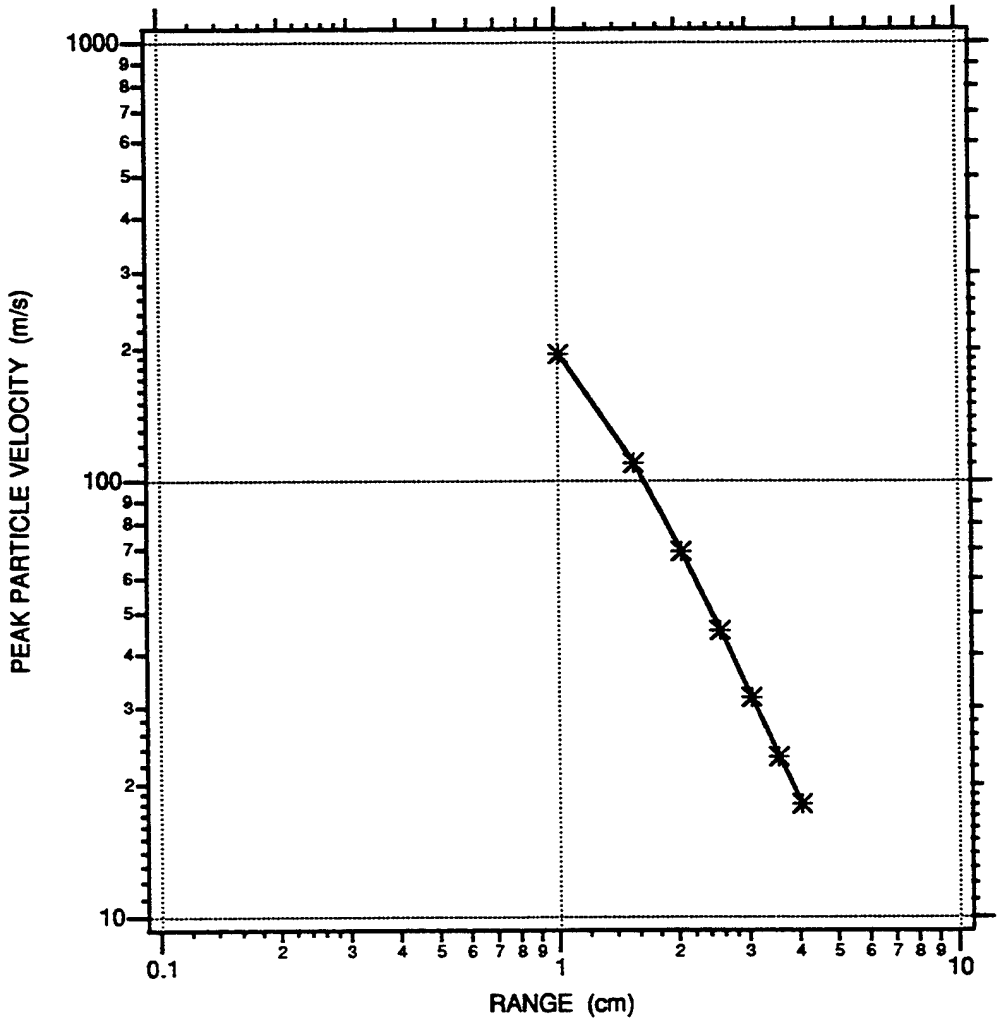

FIGURE 6-9. ATTENUATION OF PEAK PARTICLE VELOCITY MEASURED IN 78% SATURATED EGLIN BEACH SAND FOR A 3/8 g PETN EXPLOSIVE CHARGE

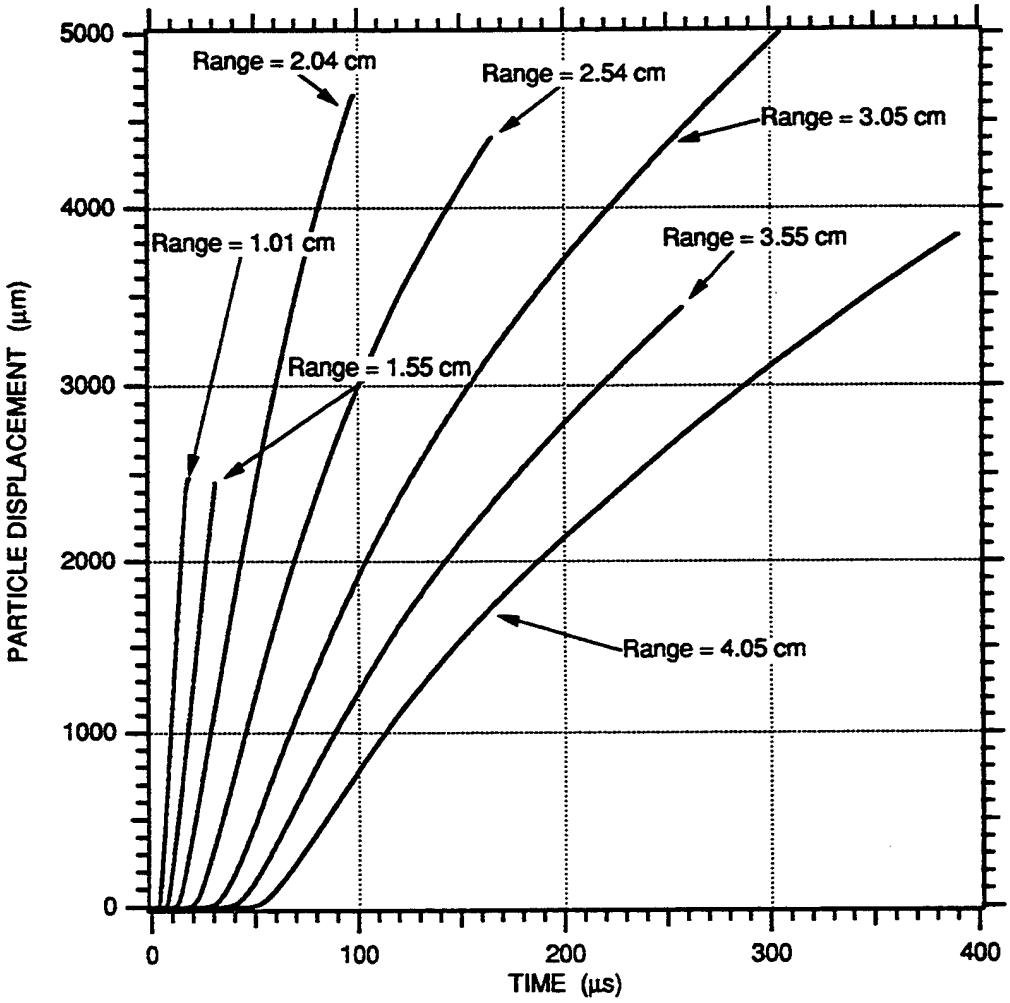

FIGURE 6-10. PARTICLE DISPLACEMENT-TIME HISTORIES MEASURED IN 78% SATURATED EGLIN BEACH SAND FOR A 3/8 g PETN EXPLOSIVE CHARGE

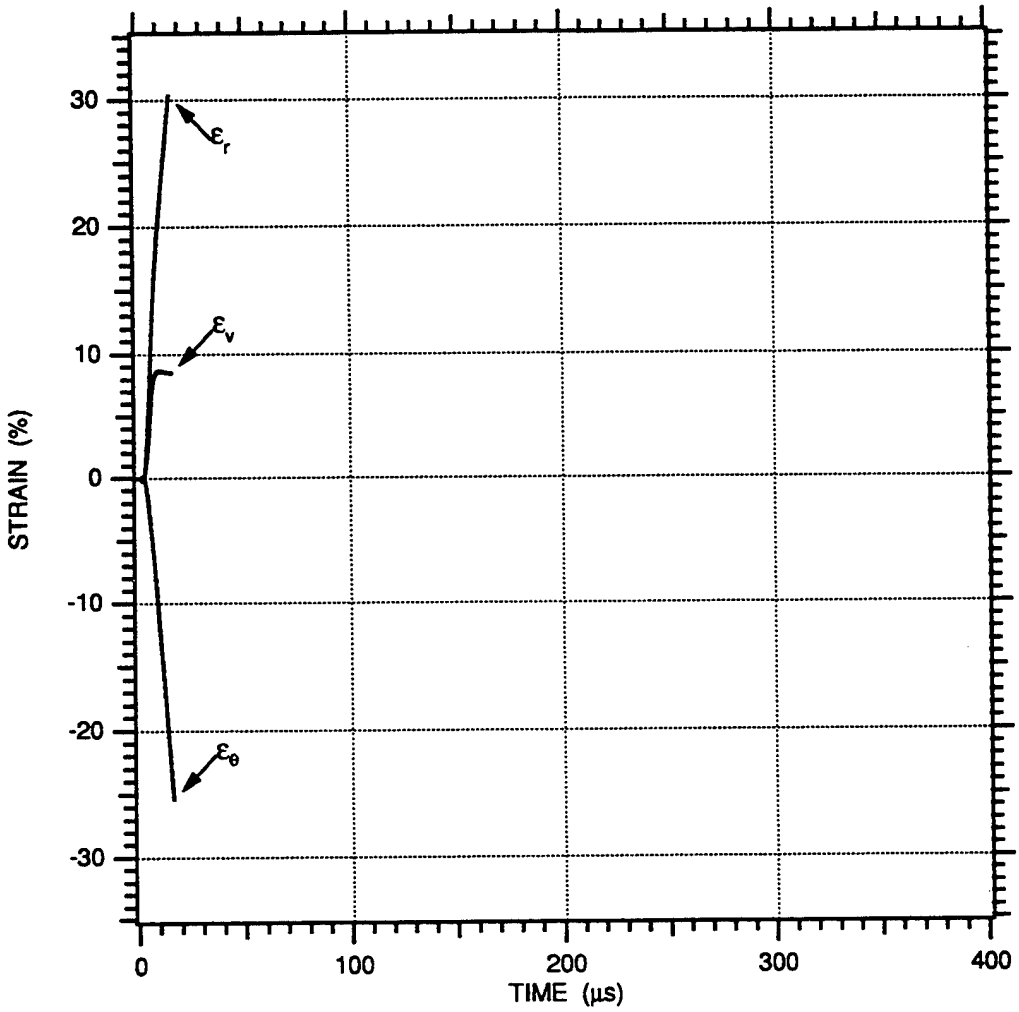

FIGURE 6-11. STRAIN-TIME HISTORIES MEASURED IN 78% SATURATED EGLIN BEACH SAND FOR A 3/8 g PETN EXPLOSIVE CHARGE AT A RANGE BETWEEN 1.01 AND 1.55 cm

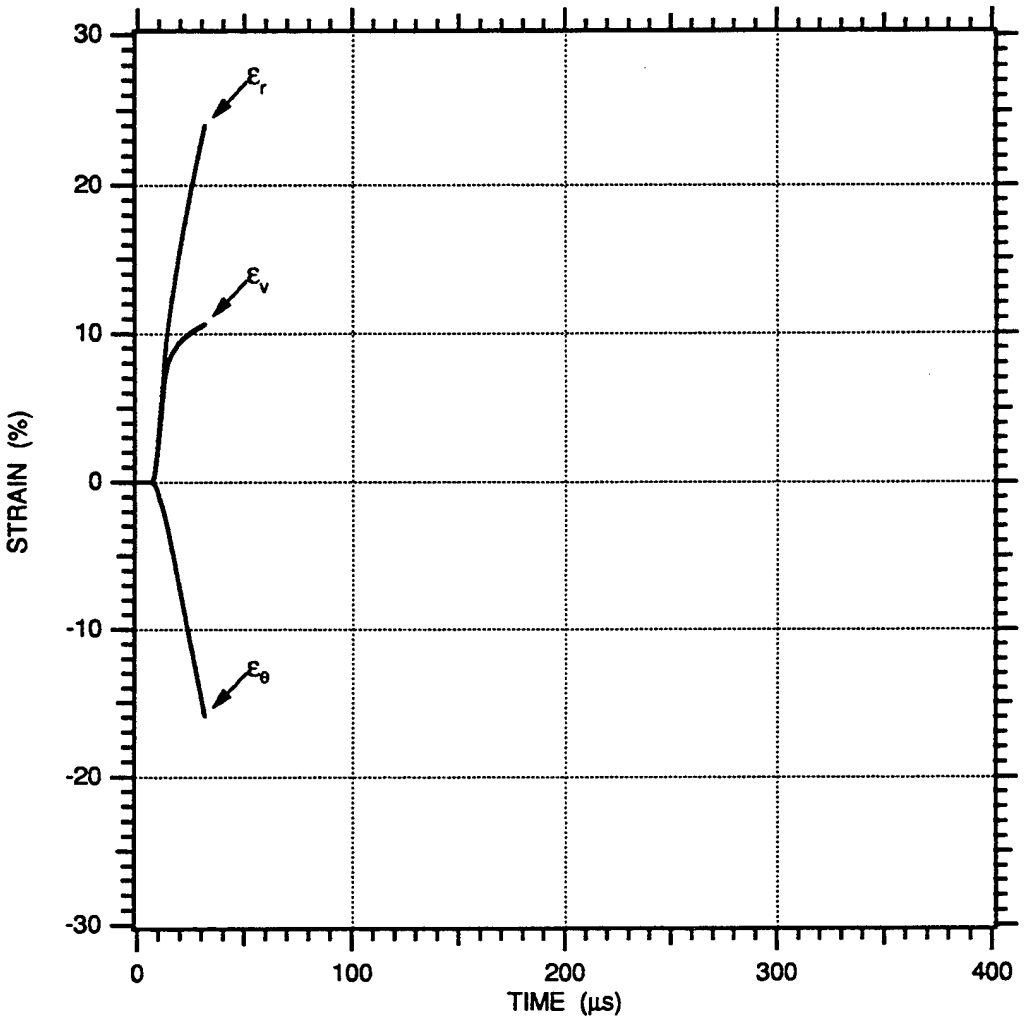

FIGURE 6-12. STRAIN-TIME HISTORIES MEASURED IN 78% SATURATED EGLIN BEACH SAND FOR A 3/8 g PETN EXPLOSIVE CHARGE AT A RANGE BETWEEN 1.55 AND 2.04 cm

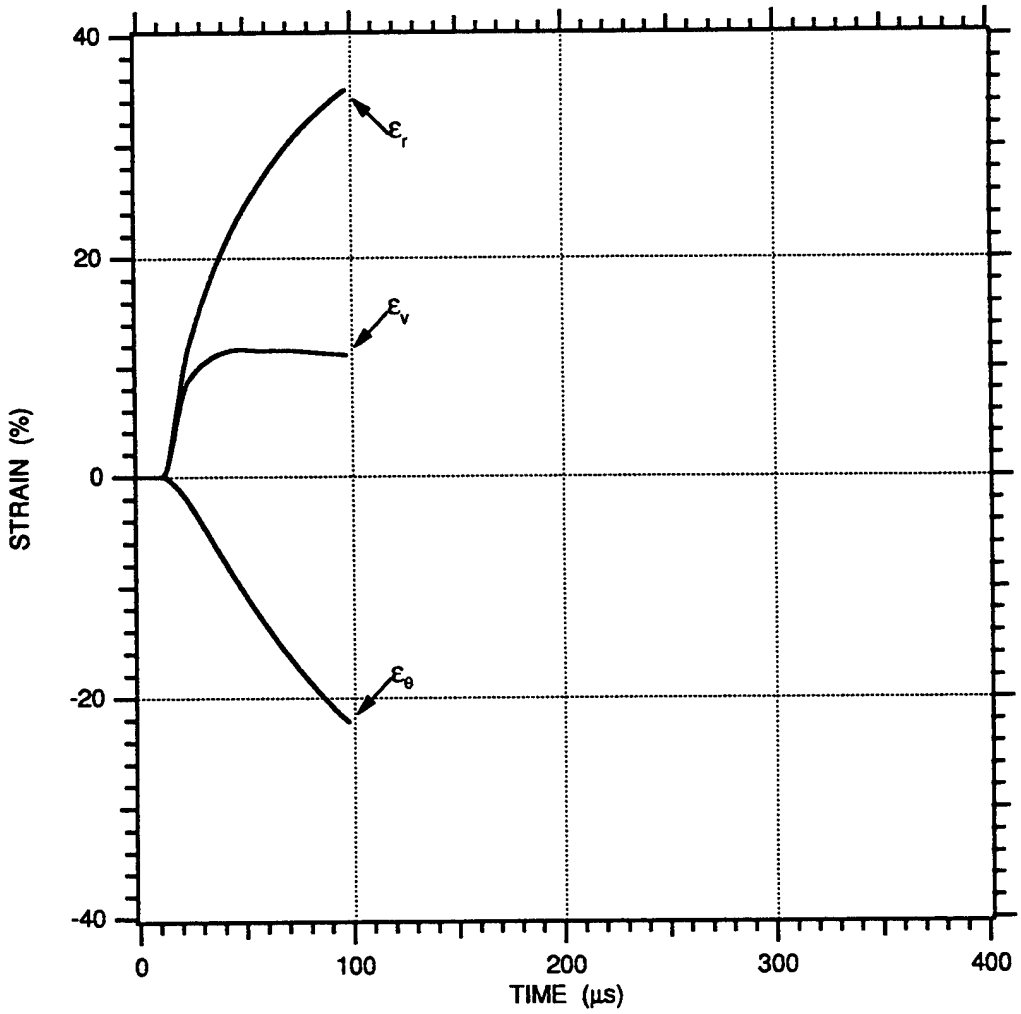

FIGURE 6-13. STRAIN-TIME HISTORIES MEASURED IN 78% SATURATED EGLIN BEACH SAND FOR A 3/8 g PETN EXPLOSIVE CHARGE AT A RANGE BETWEEN 2.04 AND 2.54 cm

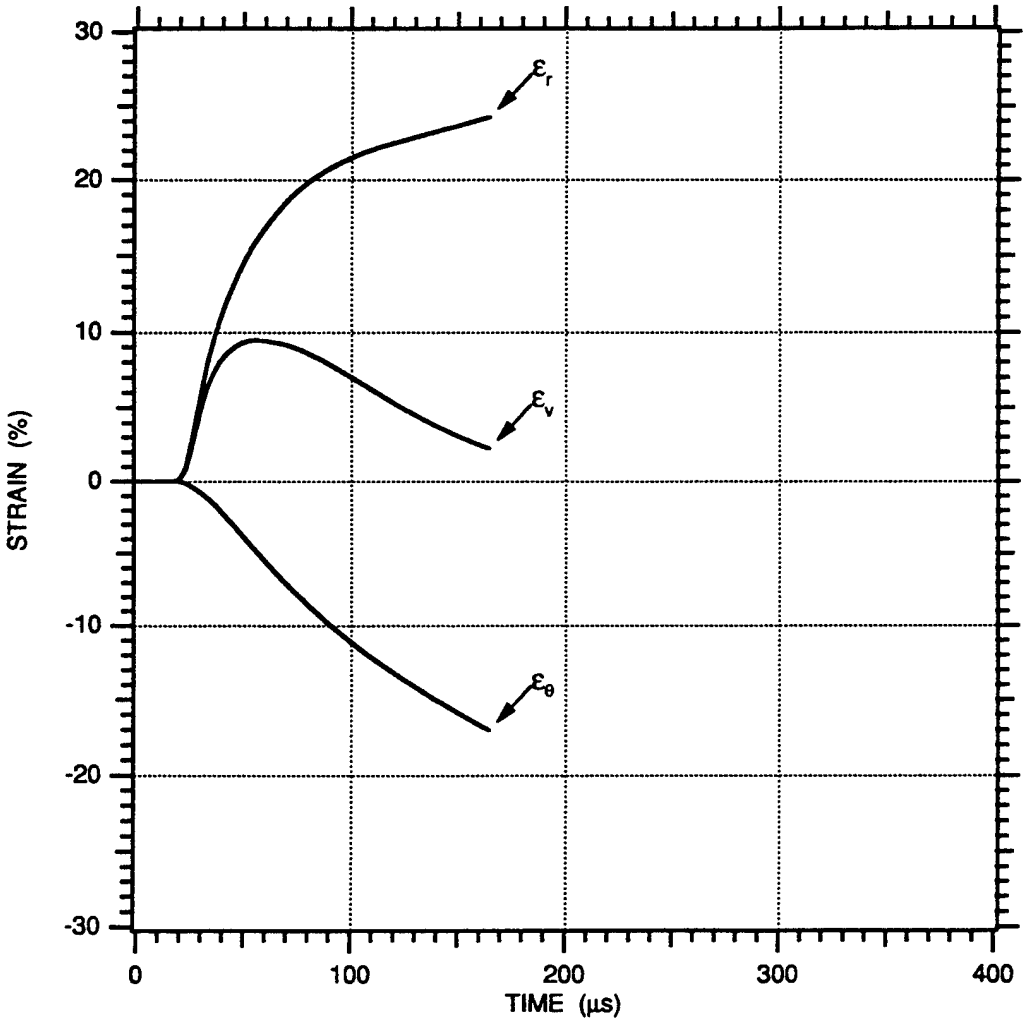

FIGURE 6-14. STRAIN-TIME HISTORIES MEASURED IN 78% SATURATED EGLIN BEACH SAND FOR A 3/8 g PETN EXPLOSIVE CHARGE AT A RANGE BETWEEN 2.54 AND 3.05 cm

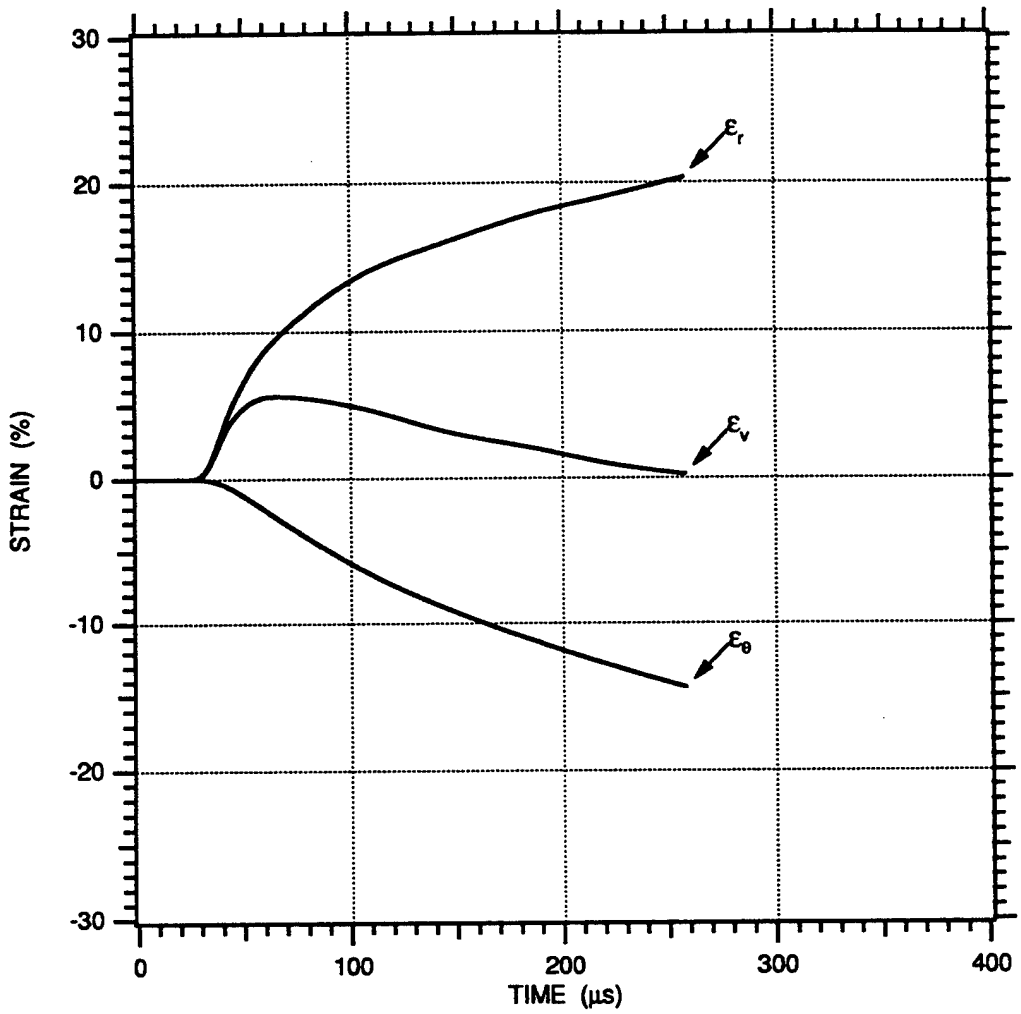

FIGURE 6-15. STRAIN-TIME HISTORIES MEASURED IN 78% SATURATED EGLIN BEACH SAND FOR A 3/8 g PETN EXPLOSIVE CHARGE AT A RANGE BETWEEN 3.05 AND 3.55 cm

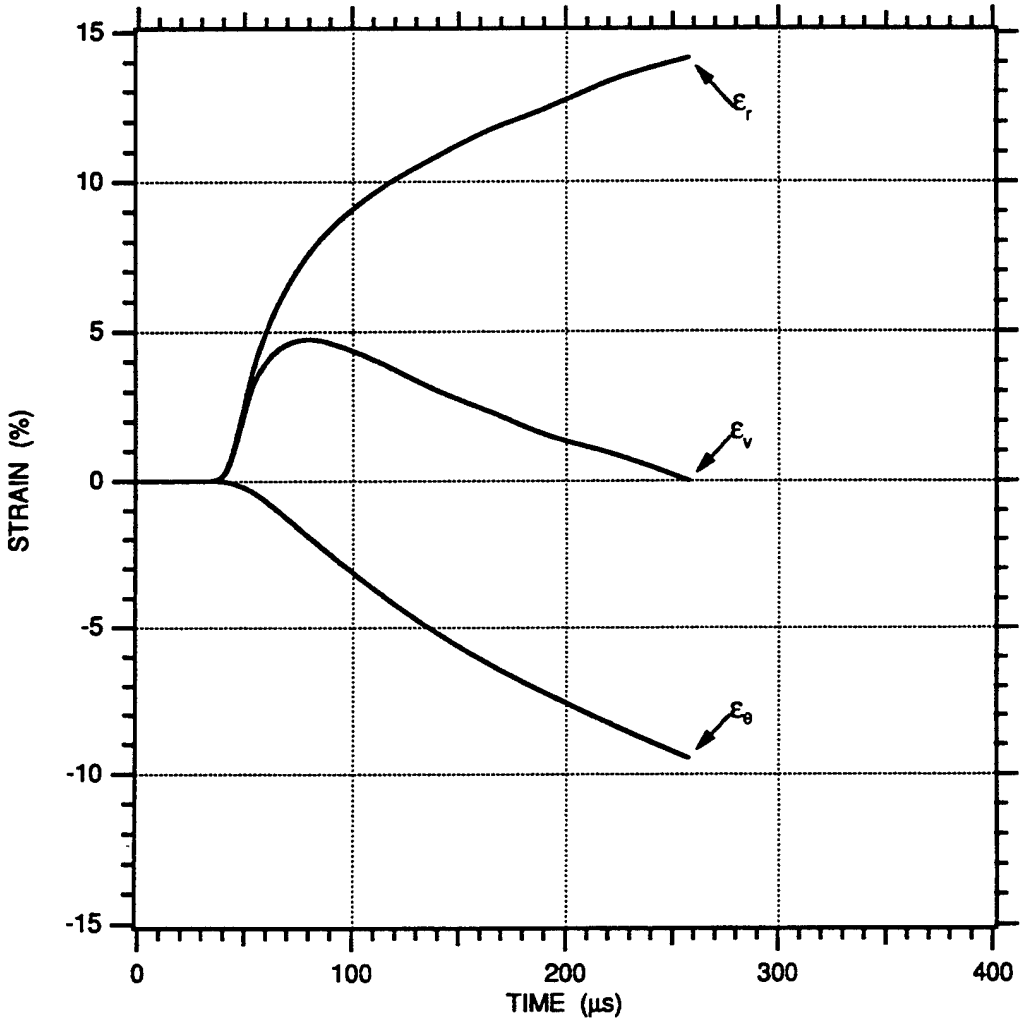

FIGURE 6-16. STRAIN-TIME HISTORIES MEASURED IN 78% SATURATED EGLIN BEACH SAND FOR A 3/8 g PETN EXPLOSIVE CHARGE AT A RANGE BETWEEN 3.55 AND 4.05 cm

SECTION 7

DETAILED RESULTS FOR 77% SATURATED SAND MODEL

The 77% saturated sand model had a measured dry density of 1.452 ± 0.008 g/cm^3, a calculated porosity of 45.3 ± 0.3 % [Porosity % = (1 - Dry Density/Grain Density) x 100], and a calculated saturated density of 1.801 ± 0.011 g/cm^3. The measured saturated density was 1.802 ± 0.011 g/cm^3. The estimated error associated with the total saturated level of 77% is ± 1% based of bulk weight measurements. The 77% saturation level with respect to the pore volume corresponds to 10% air voids with respect to the total volume. Figure 2-5 shows a reference saturation uniformity characteristics for a 77% saturated sand model.

PARTICLE VELOCITY MEASUREMENTS

Figures 7-1 through 7-6 show the particle velocity records measured at ranges from 1.01 to 4.05 cm. The gage failure indicated in the figures is attributed to breakage of the wire loop resulting from radial displacement, which generates a hoop strain in excess of the wire failure strain of approximately 20% to 25%. The particle velocity gage at a range of 0.54 cm (Gage No. PV1), which is adjacent to the spherical charge, is not shown due to breakage before the peak particle velocity. No record was obtained from the particle velocity gage (Gage No. PV7) at a range of 3.55 cm. The particle velocity records show approximately a linear rise to the peak particle velocity followed by a decay to almost a constant lower particle velocity. Particle velocity gages at ranges of 3.05 and 4.05 cm are shown out to a time of 600 μs due to gage survival. The reflection from the aluminum container boundary occurs after 500 μs for particle velocity gages located between the charge and a range of 4.05 cm. Thus, for the record durations shown in Figures 7-1 through 7-6, the wave remains spherical.

Figure 7-7 shows a profile of range versus TOA. The data points have been fitted with a least squares third order polynomial having the form of

$$\text{Range} = 0.401 + 0.214\ \text{TOA} - 4.41\text{E-}03\ \text{TOA}^2 + 3.87\text{E-}05\ \text{TOA}^3 \qquad (7.1)$$

where range is in centimeters and TOA is in microseconds. Equation (7.1) is valid up to a TOA of 38 μs. The wave front speed at any given range can be determined by differentiating Equation (7.1) to produce

$$c = 0.214 - 8.82\text{E-}03\ \text{TOA} + 1.16\text{E-}04\ \text{TOA}^2 \qquad (7.2)$$

where c is the wave front speed in centimeters per microsecond. Converting c to units of meters per second, the wave front speed varies from 2060 m/s at a range of 0.54 cm to 460 m/s at a range of 4.05 cm.

Figure 7-8 shows the attenuation of peak particle velocity with increased range. Using Equation (3.1), the peak particle velocity (m/s) can be multiplied by the saturated density (kg/m^3) and wave front speed (m/s) to produce an estimate for the peak radial stress (Pa). Table 7-1 summarizes the TOA, wave front speed, peak particle velocity, and estimated radial stress for the 77% saturated sand model.

TABLE 7-1. SUMMARY OF EXPERIMENTAL RESULTS FROM PARTICLE VELOCITY MEASUREMENTS FOR THE 77% SATURATED SAND MODEL

Range (cm ± 0.05 cm)	TOA (μs ± 0.2 μs)	Wave Speed (m/s ± 10%)	Peak Particle Velocity (m/s ± 2%)	Estimated Peak Stress (kbar)
0.54	0.9	2060	NA	NA
1.01	2.5	1926	191.5	6.6
1.55	4.4	1774	106.6	3.4
2.04	8.2	1494	66.1	1.8
2.54	14.3	1115	45.0	0.9
3.05	20.3	827	30.4	0.5
3.55	NA	NA	NA	NA
4.05	37.8	463	16.7	0.1

PARTICLE DISPLACEMENTS AND STRAINS

The particle velocity-time histories shown in Figure 7-1 through 7-6 can be temporally integrated to obtain displacement-time histories. Figure 7-9 shows the particle displacement-time histories.

Figures 7-11 to 7-14 show fractional radial (ε_r), circumferential (ε_θ), and volumetric (ε_v) engineering strains. The governing equations used to calculate the strains are given in Appendix B. The strains are based on the relative displacements between adjacent particle velocity gages. Positive strains indicate compression. Negative strains indicate elongation for the circumferential strains and dilation for the volumetric strains. The volumetric strain-time histories show that each fractional shell volume experiences only compression and no dilation.

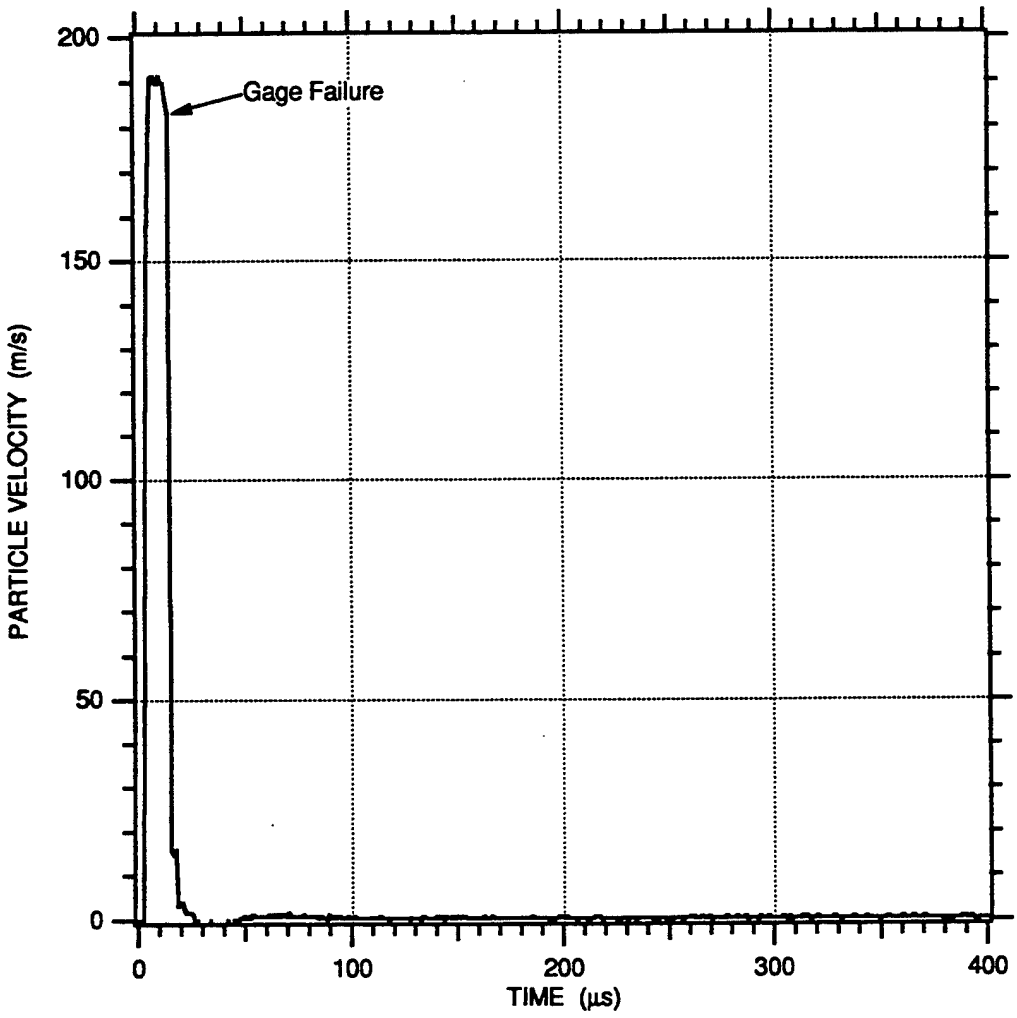

FIGURE 7-1. PARTICLE VELOCITY-TIME HISTORY MEASURED IN 77% SATURATED EGLIN BEACH SAND FOR A 3/8 g PETN EXPLOSIVE CHARGE AT A RANGE OF 1.01 cm

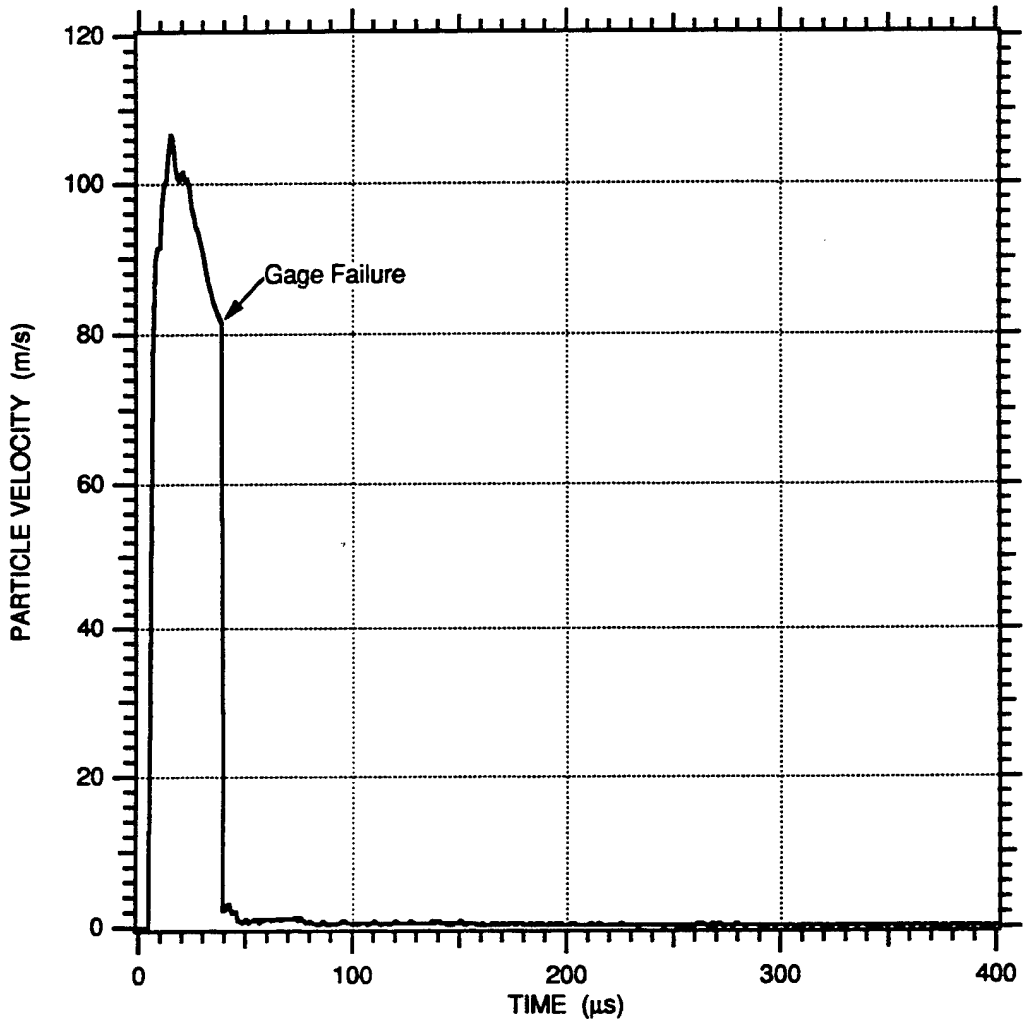

FIGURE 7-2. PARTICLE VELOCITY-TIME HISTORY MEASURED IN 77% SATURATED EGLIN BEACH SAND FOR A 3/8 g PETN EXPLOSIVE CHARGE AT A RANGE OF 1.55 cm

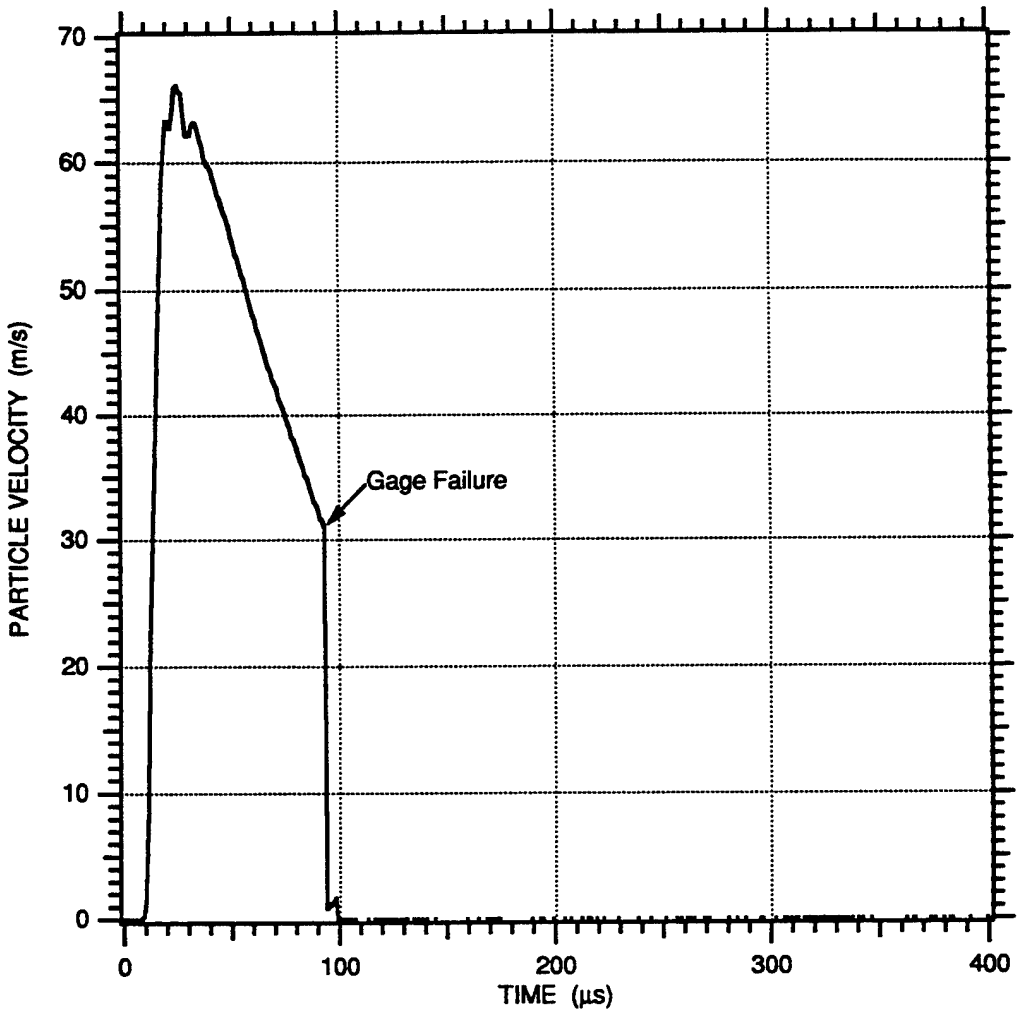

FIGURE 7-3. PARTICLE VELOCITY-TIME HISTORY MEASURED IN 77% SATURATED EGLIN BEACH SAND FOR A 3/8 g PETN EXPLOSIVE CHARGE AT A RANGE OF 2.04 cm

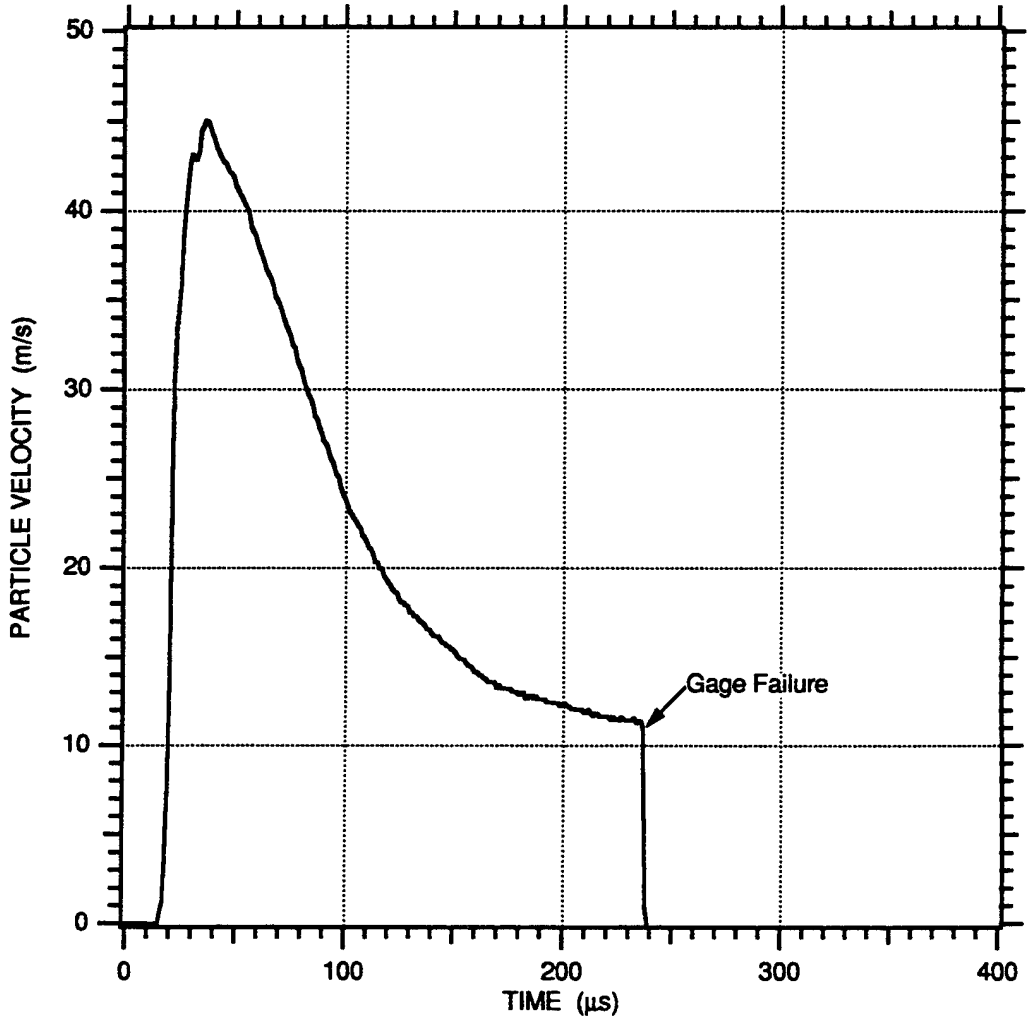

FIGURE 7-4. PARTICLE VELOCITY-TIME HISTORY MEASURED IN 77% SATURATED EGLIN BEACH SAND FOR A 3/8 g PETN EXPLOSIVE CHARGE AT A RANGE OF 2.54 cm

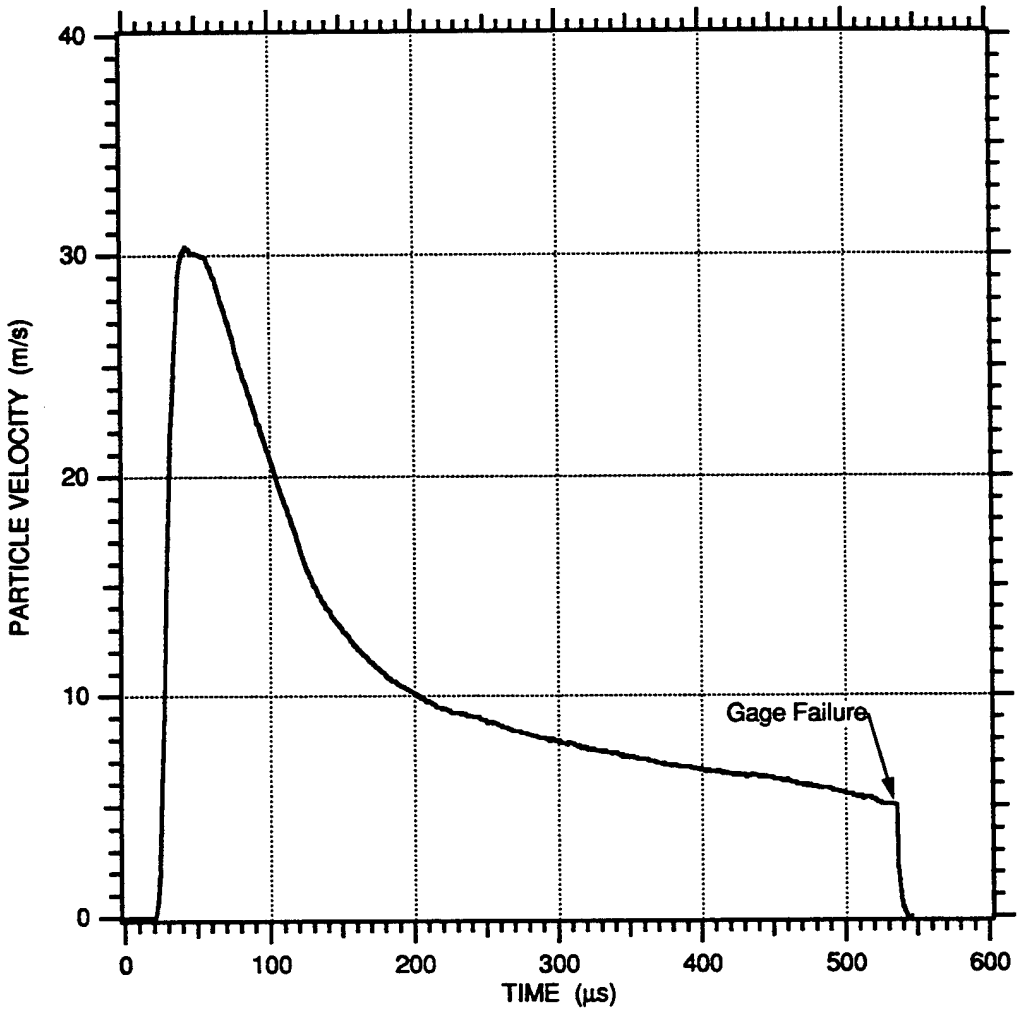

FIGURE 7-5. PARTICLE VELOCITY-TIME HISTORY MEASURED IN 77% SATURATED EGLIN BEACH SAND FOR A 3/8 g PETN EXPLOSIVE CHARGE AT A RANGE OF 3.05 cm

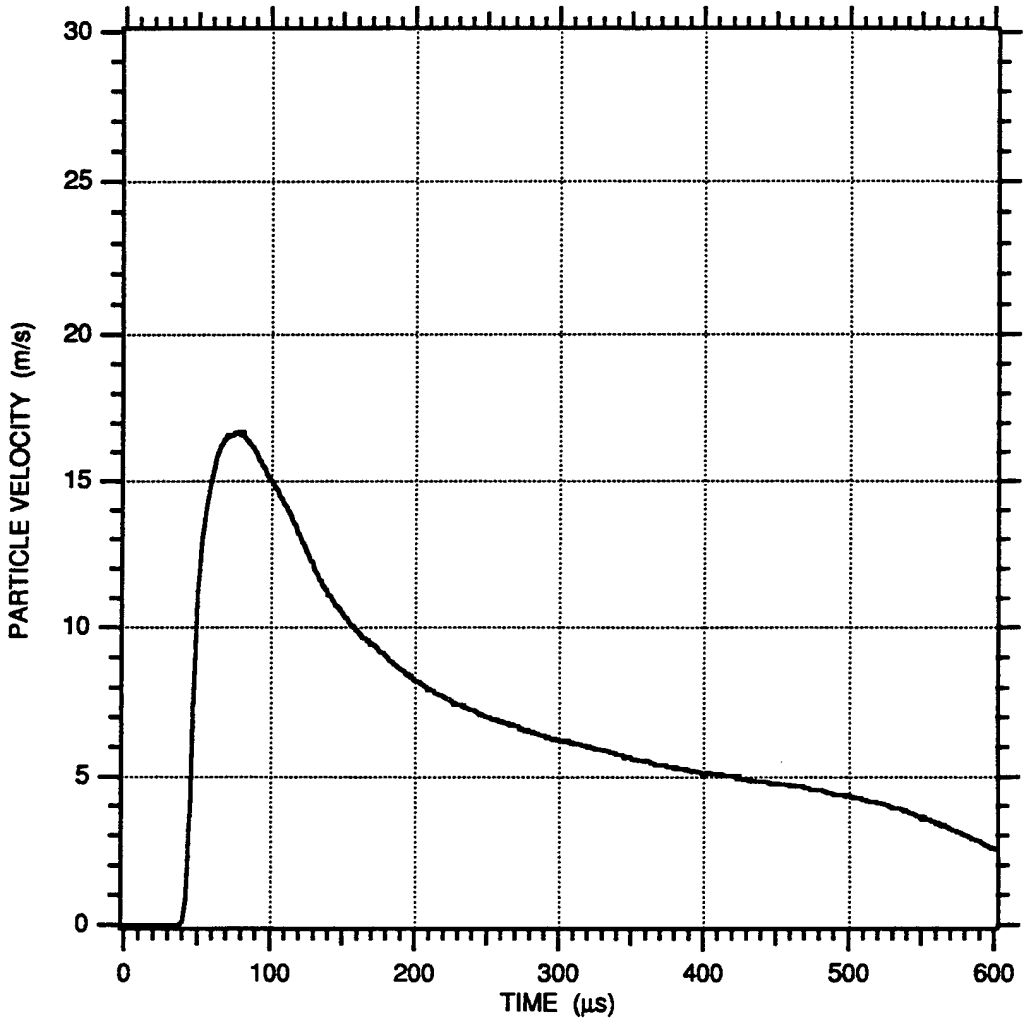

FIGURE 7-6. PARTICLE VELOCITY-TIME HISTORY MEASURED IN 77% SATURATED EGLIN BEACH SAND FOR A 3/8 g PETN EXPLOSIVE CHARGE AT A RANGE OF 4.05 cm

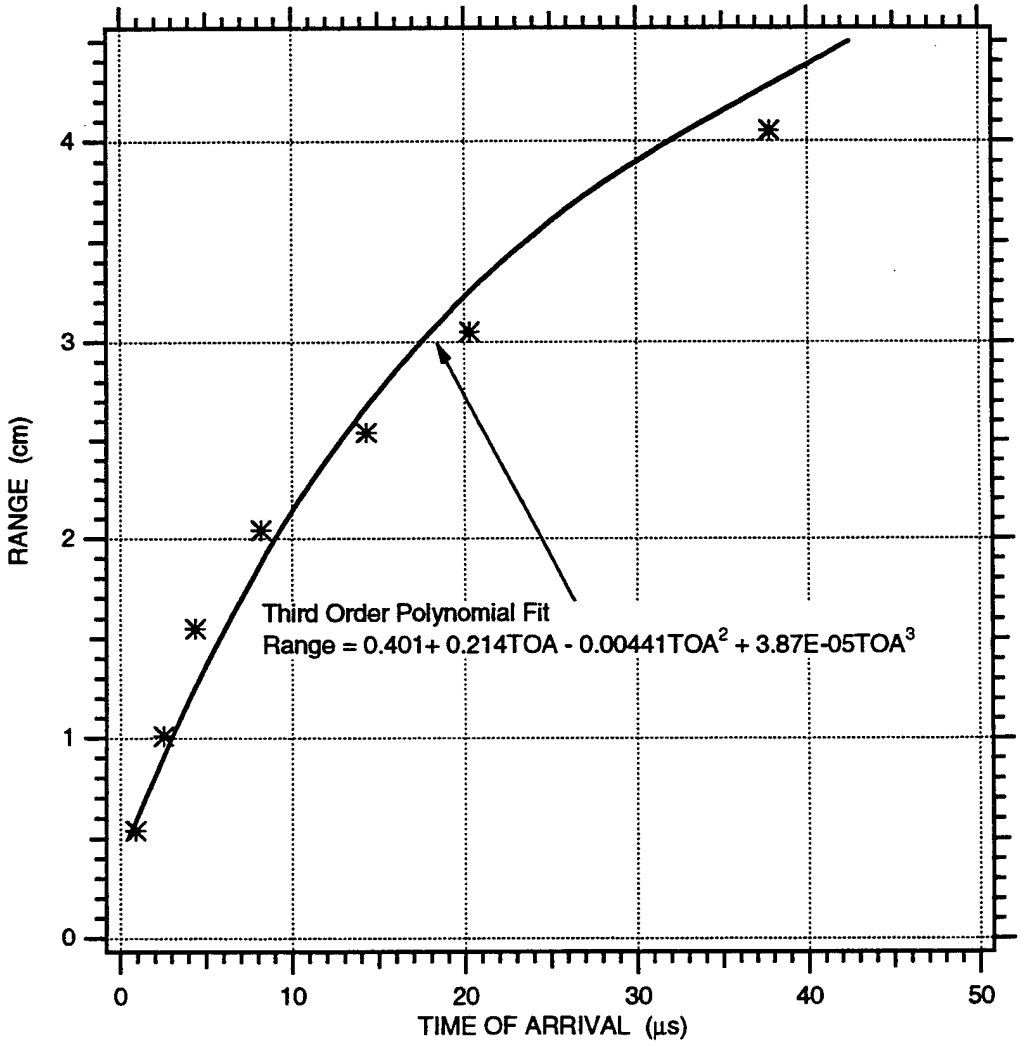

FIGURE 7-7. RANGE VERSUS TIME OF ARRIVAL MEASURED IN 77% SATURATED EGLIN BEACH SAND FOR A 3/8 g PETN EXPLOSIVE CHARGE

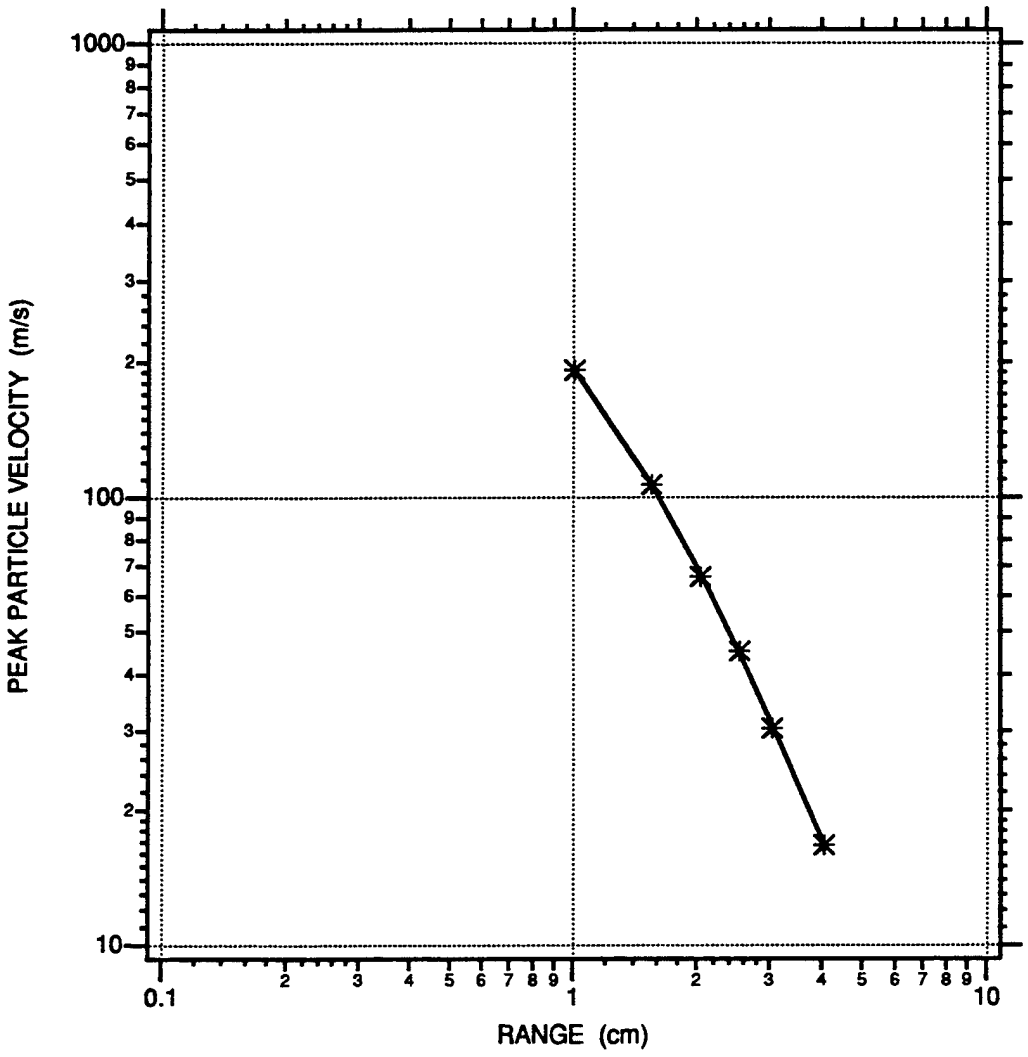

FIGURE 7-8. ATTENUATION OF PEAK PARTICLE VELOCITY MEASURED IN 77% SATURATED EGLIN BEACH SAND FOR A 3/8 g PETN EXPLOSIVE CHARGE

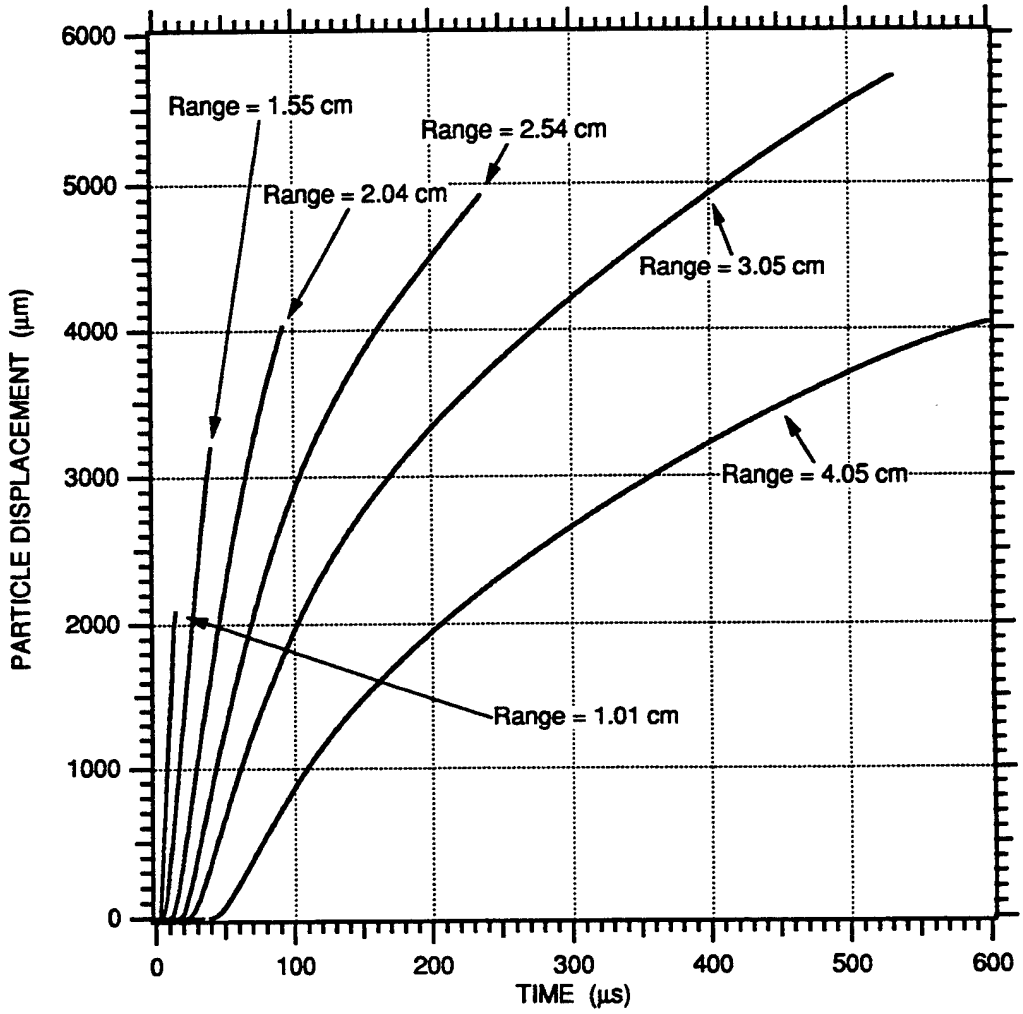

FIGURE 7-9. PARTICLE DISPLACEMENT-TIME HISTORIES MEASURED IN 77% SATURATED EGLIN BEACH SAND FOR A 3/8 g PETN EXPLOSIVE CHARGE

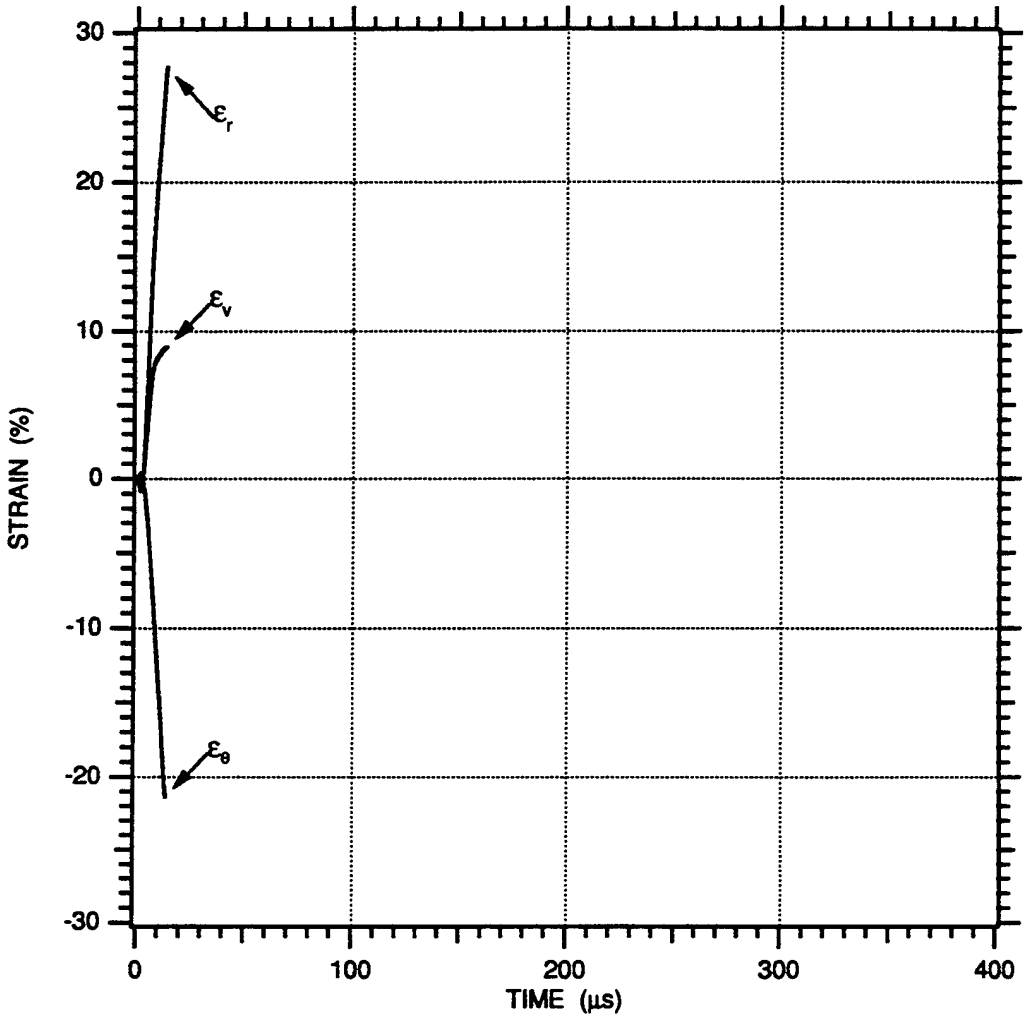

FIGURE 7-10. STRAIN-TIME HISTORIES MEASURED IN 77% SATURATED EGLIN BEACH SAND FOR A 3/8 g PETN EXPLOSIVE CHARGE AT A RANGE BETWEEN 1.01 AND 1.55 cm

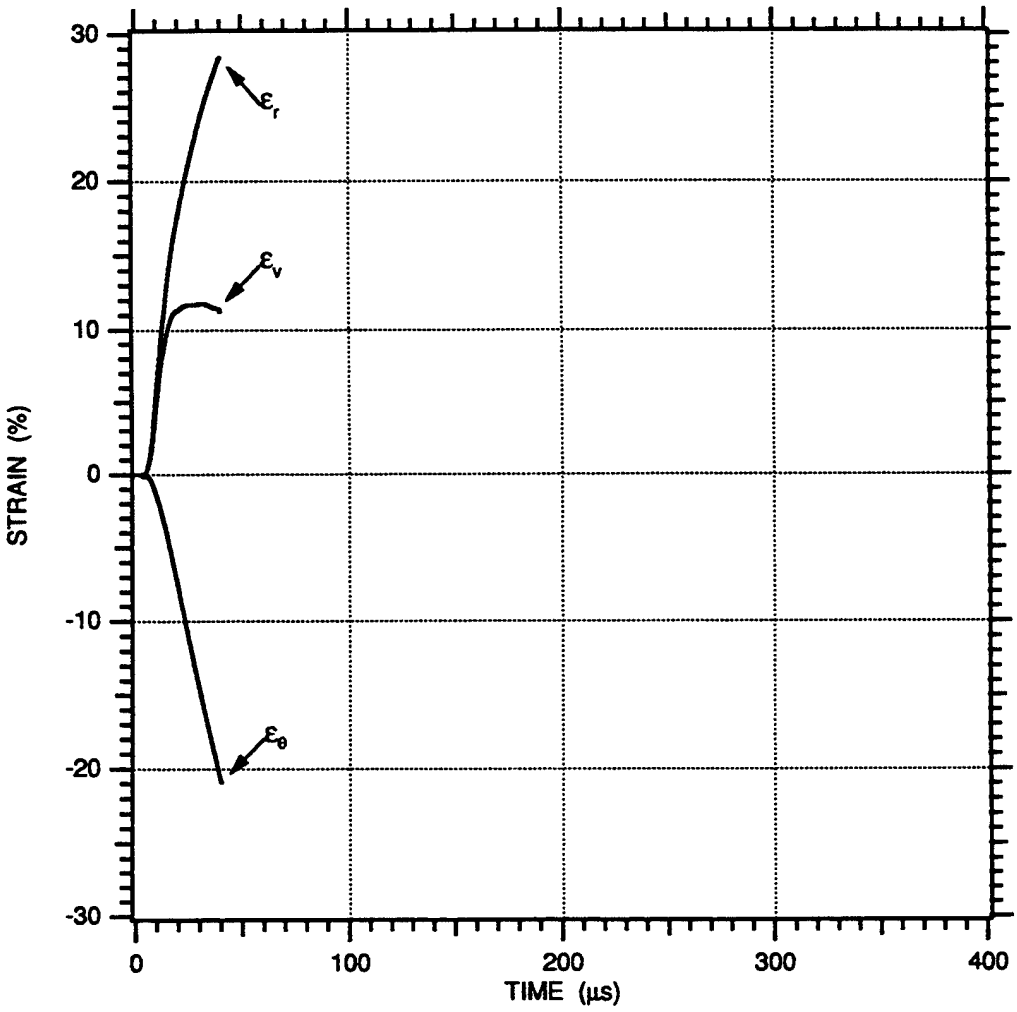

FIGURE 7-11. STRAIN-TIME HISTORIES MEASURED IN 77% SATURATED EGLIN BEACH SAND FOR A 3/8 g PETN EXPLOSIVE CHARGE AT A RANGE BETWEEN 1.55 AND 2.04 cm

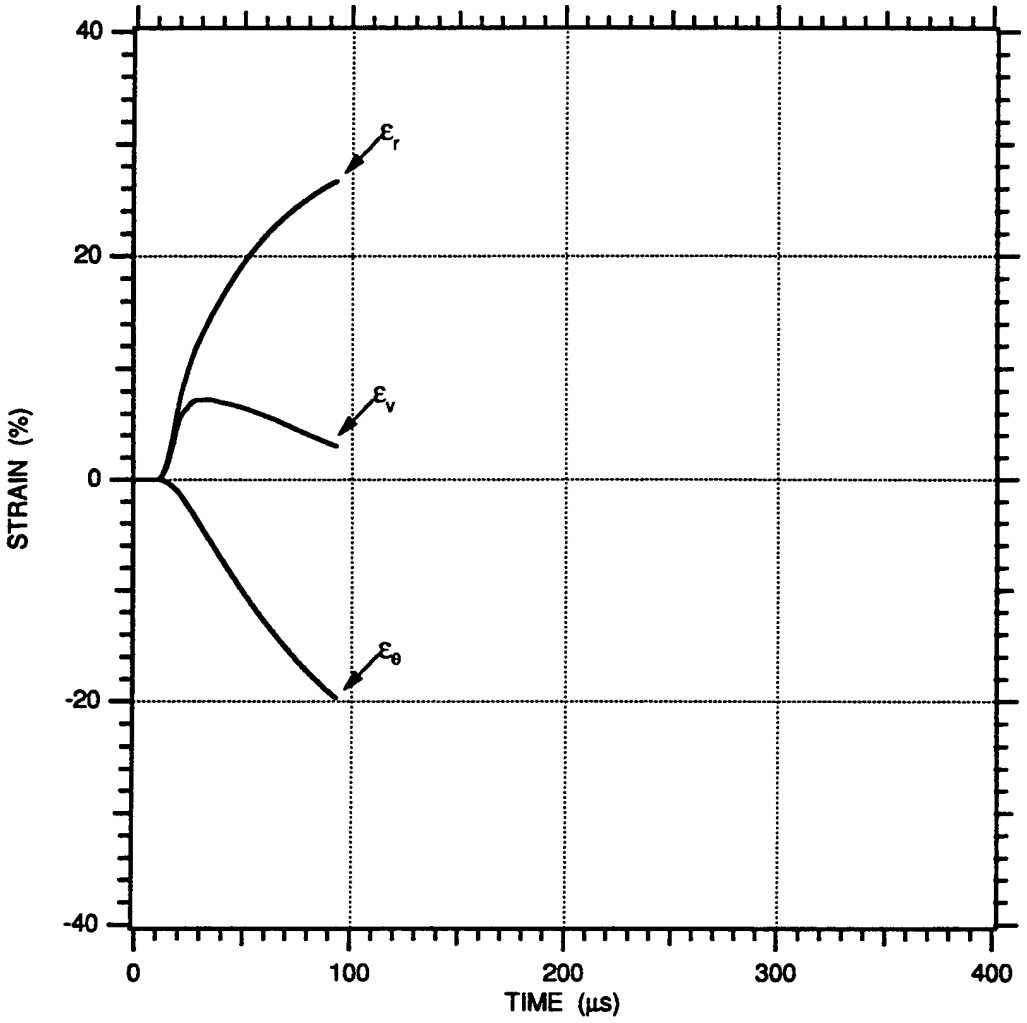

FIGURE 7-12. STRAIN-TIME HISTORIES MEASURED IN 77% SATURATED EGLIN BEACH SAND FOR A 3/8 g PETN EXPLOSIVE CHARGE AT A RANGE BETWEEN 2.04 AND 2.54 cm

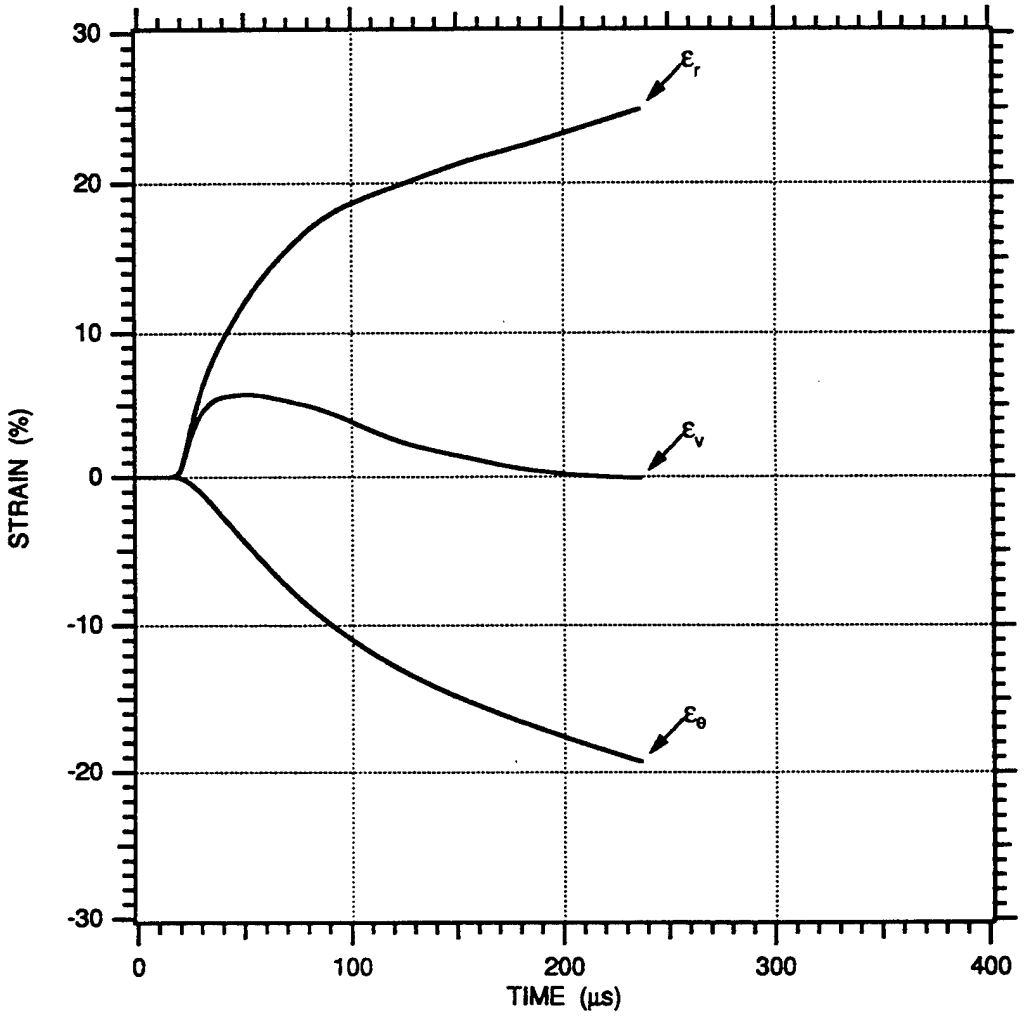

FIGURE 7-13. STRAIN-TIME HISTORIES MEASURED IN 77% SATURATED EGLIN BEACH SAND FOR A 3/8 g PETN EXPLOSIVE CHARGE AT A RANGE BETWEEN 2.54 AND 3.05 cm

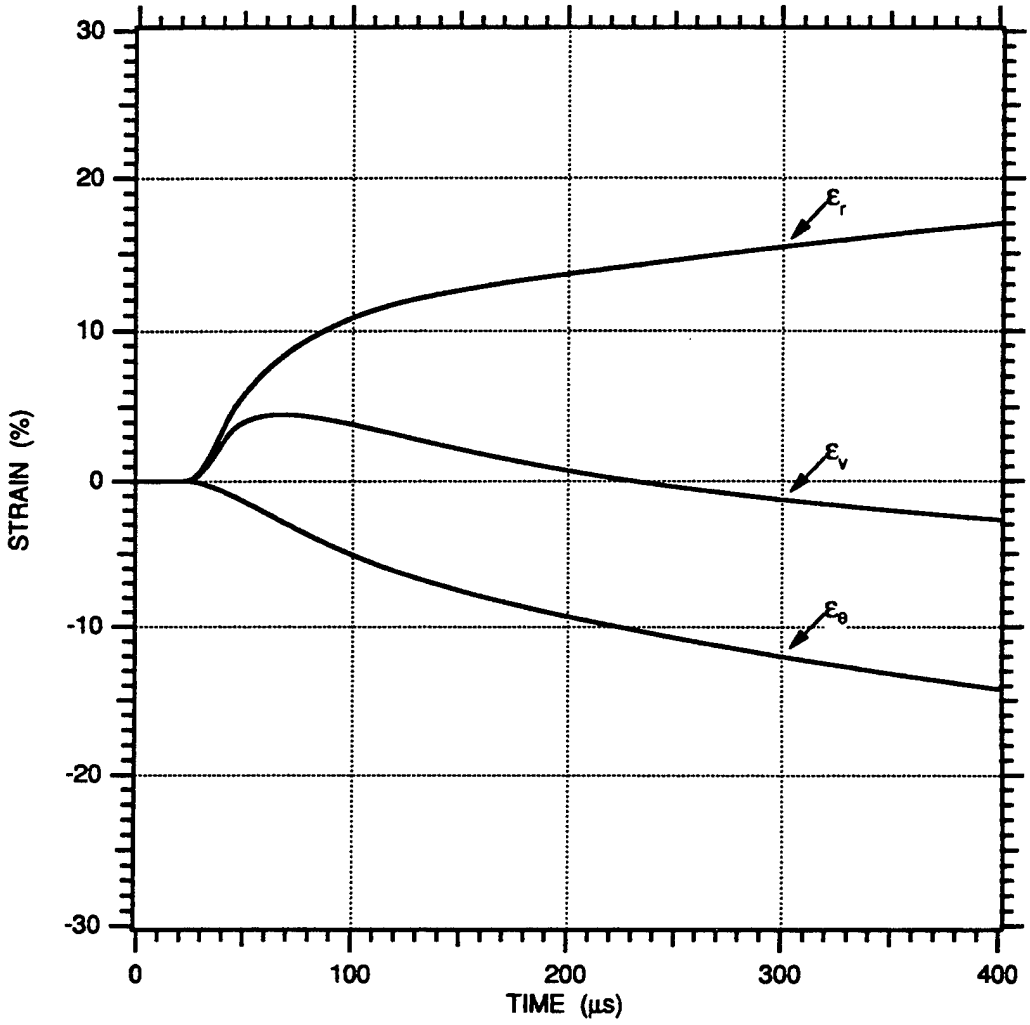

FIGURE 7-14. STRAIN-TIME HISTORIES MEASURED IN 77% SATURATED EGLIN BEACH SAND FOR A 3/8 g PETN EXPLOSIVE CHARGE AT A RANGE BETWEEN 3.05 AND 4.05 cm

SECTION 8

COMPARISON OF EXPERIMENTAL RESULTS

Our discussion in this chapter focuses on comparing the experimental results among sand models with saturation levels of 100%, 95%, and 78% with respect to the pore volume. These saturation levels correspond to 0%, 2%, and 10% air voids with respect to the total volume. Comparisons will be shown here for particle velocity, TOA, peak particle velocity attenuation, particle displacement, and fractional volumetric strains. Because the 77% saturated sand model produced results similar to those for the 78% saturated sand model, the 77% model is not included in the comparison.

PARTICLE VELOCITIES

Figures 8-1 through 8-7 show comparisons of particle velocity-time histories for 100%, 95%, and 78% saturated sand models. The particle velocity waveforms are very similar between the 100% and 95% saturation levels. The only noticeable differences are slightly higher particle velocities for the 95% saturated sand model during the unloading portion of the waveform. This higher particle velocity translates into a slightly higher particle displacement, which could be associated with an increase in pore space collapse due to the 2% of air void within the sand model volume.

Figure 8-8 shows a profile of range versus TOA for the 100%, 95%, and 78% saturated sand models. The 100% and 95% profiles are the same. The 78% profile shows a significantly larger attenuation of the wave front speed compared with the 100% and 95% saturated sand models.

Figure 8-9 shows the peak particle velocity attenuation for the 100%, 95%, and 78% saturated sand models. The peak particle velocities are the same for the 100% and 95% saturated sand models. Comparison of the 100% and 78% saturated sand models shows 20% higher peak particle velocities in the 78% saturated sand model at ranges of 1.55 and 2.04 cm, similar peak particle velocities at ranges of 2.54 and 3.05 cm, and 30% lower peak particle velocities in the 78% saturated sand model at ranges of 3.55 and 4.05 cm. The higher peak particle velocities near the charge is due to the lower inertial resistance opposing particle motion because of less water in the pore space. The lower peak particle velocity farther away from the charge is the result of larger attenuation of the particle velocity.

PARTICLE DISPLACEMENTS AND STRAINS

Figures 8-10 through 8-16 show comparisons of particle displacement-time histories for the 100%, 95%, and 78% saturated sand models. These records show the trends of the smallest displacements occurring in the 100% saturated sand model and the largest displacements occurring in the 78% saturated sand model. The displacements for the 95% saturated sand model typically were between the 100% and 78% saturated sand model values.

Fractional volumetric (ε_v) strains are shown in Figures 8-17 to 8-22. The strains are based on the relative displacements between adjacent particle velocity gages. Positive strains indicate compression and negative strains indicate dilation. For the 100% and 95% saturated sand models each fractional shell element experiences compression followed by dilation. For the 78% saturated sand model, each fractional shell volume experiences only compression. Typically, there was 200% more compression in the 78% saturated sand model as compared with the 100% and 95% saturated sand models.

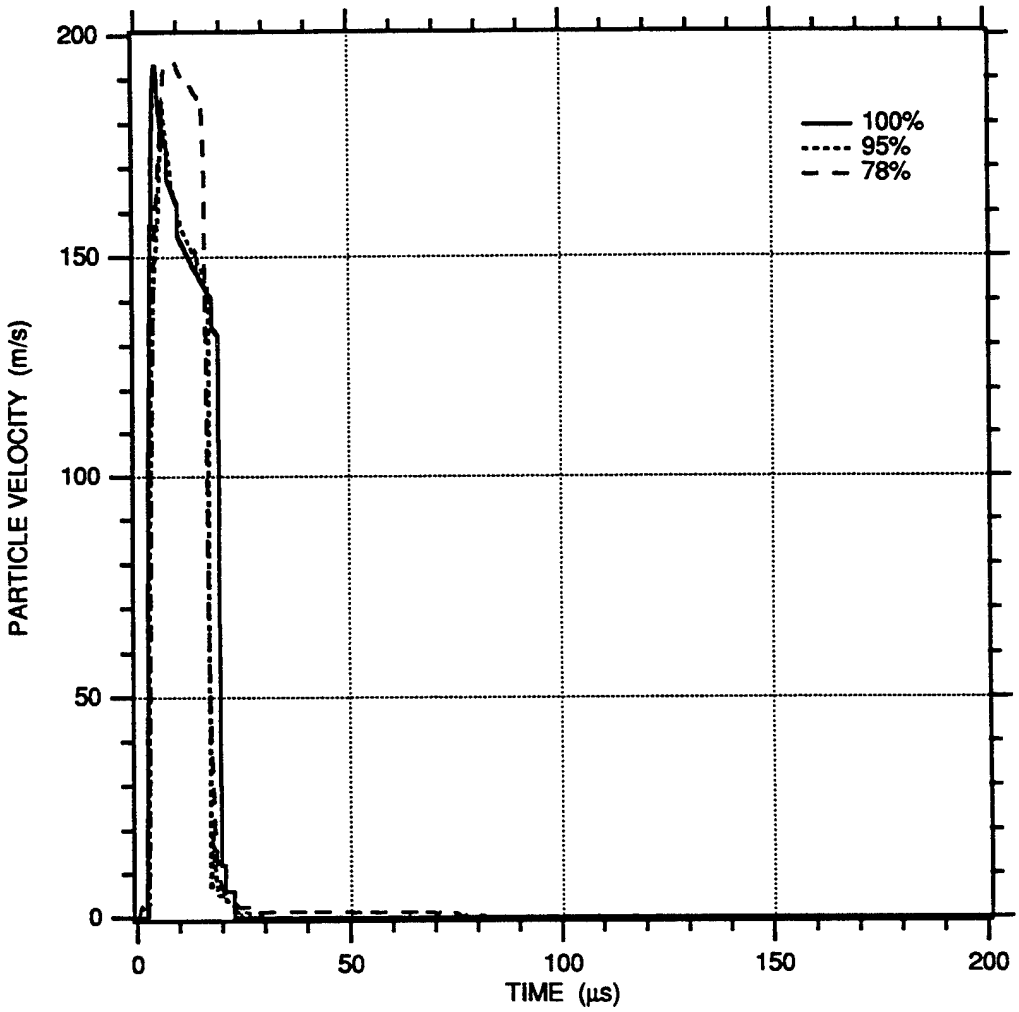

FIGURE 8-1. COMPARISON OF PARTICLE VELOCITY-TIME HISTORIES MEASURED IN 100%, 95%, AND 78% SATURATED EGLIN BEACH SAND FOR A 3/8 g PETN EXPLOSIVE CHARGE AT A RANGE OF 1.01 cm

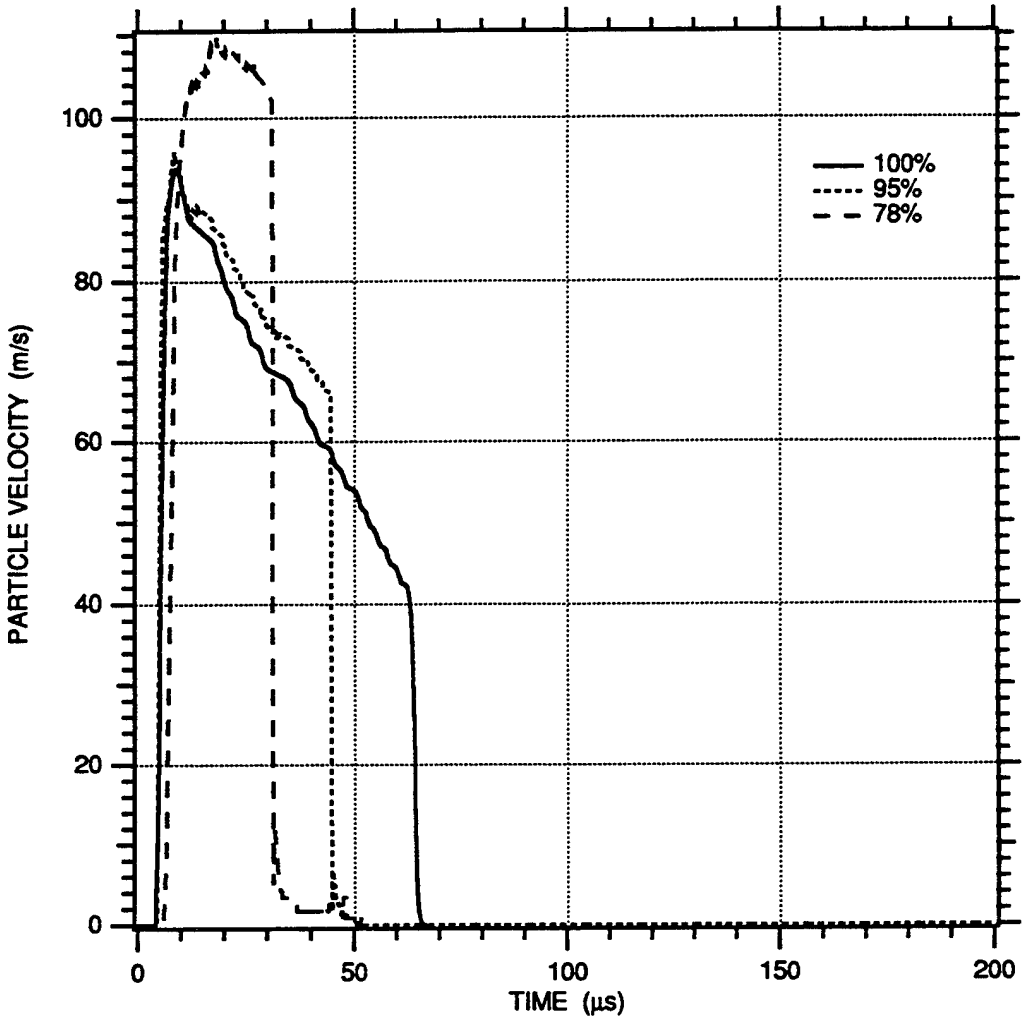

FIGURE 8-2. COMPARISON OF PARTICLE VELOCITY-TIME HISTORIES MEASURED IN 100%, 95%, AND 78% SATURATED EGLIN BEACH SAND FOR A 3/8 g PETN EXPLOSIVE CHARGE AT A RANGE OF 1.55 cm

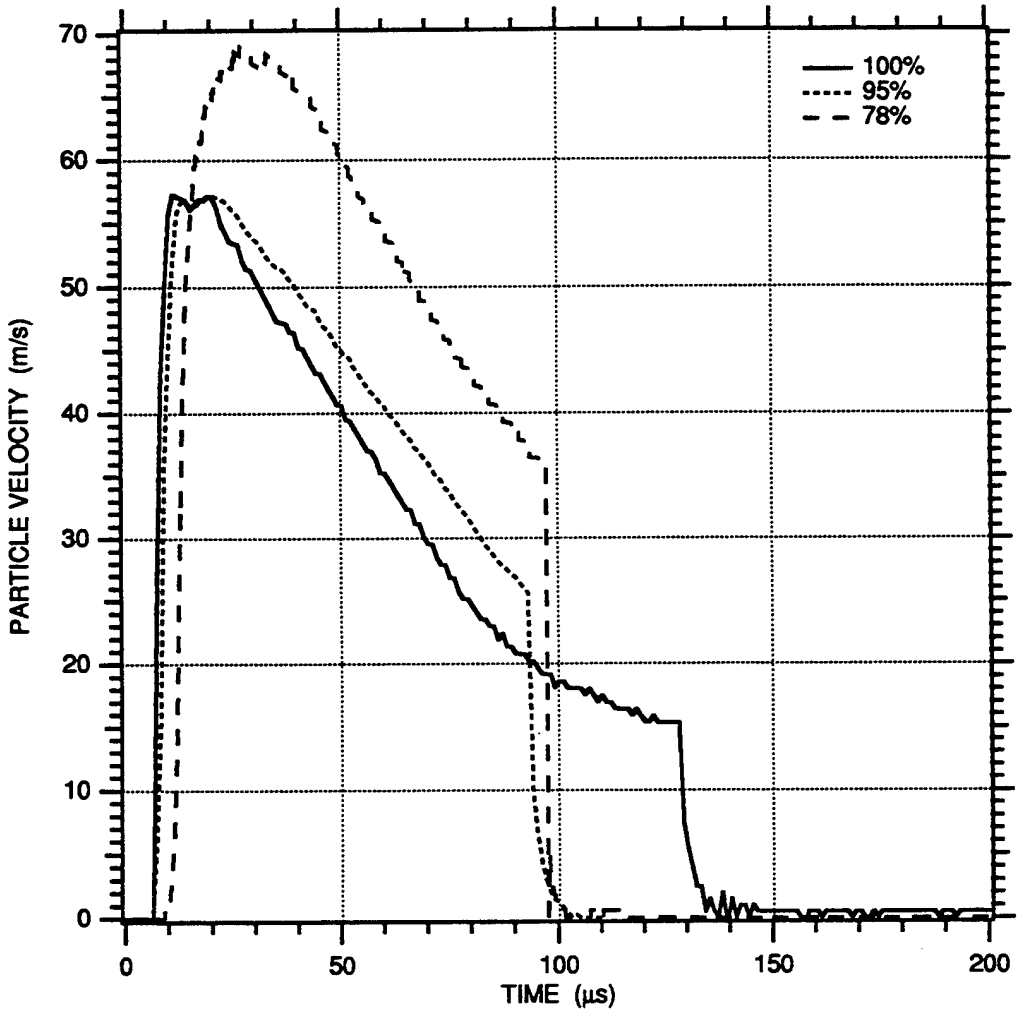

FIGURE 8-3. COMPARISON OF PARTICLE VELOCITY-TIME HISTORIES MEASURED IN 100%, 95%, AND 78% SATURATED EGLIN BEACH SAND FOR A 3/8 g PETN EXPLOSIVE CHARGE AT A RANGE OF 2.04 cm

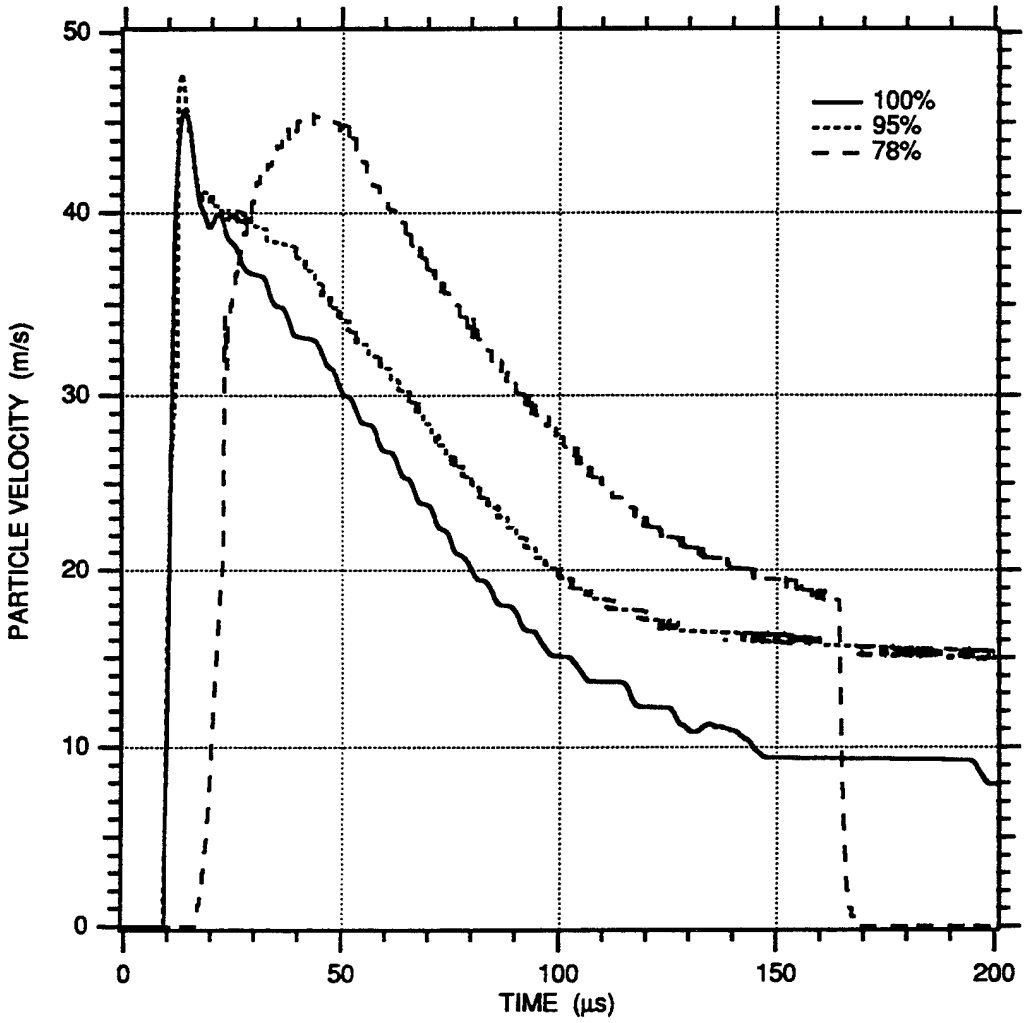

FIGURE 8-4. COMPARISON OF PARTICLE VELOCITY-TIME HISTORIES MEASURED IN 100%, 95%, AND 78% SATURATED EGLIN BEACH SAND FOR A 3/8 g PETN EXPLOSIVE CHARGE AT A RANGE OF 2.54 cm

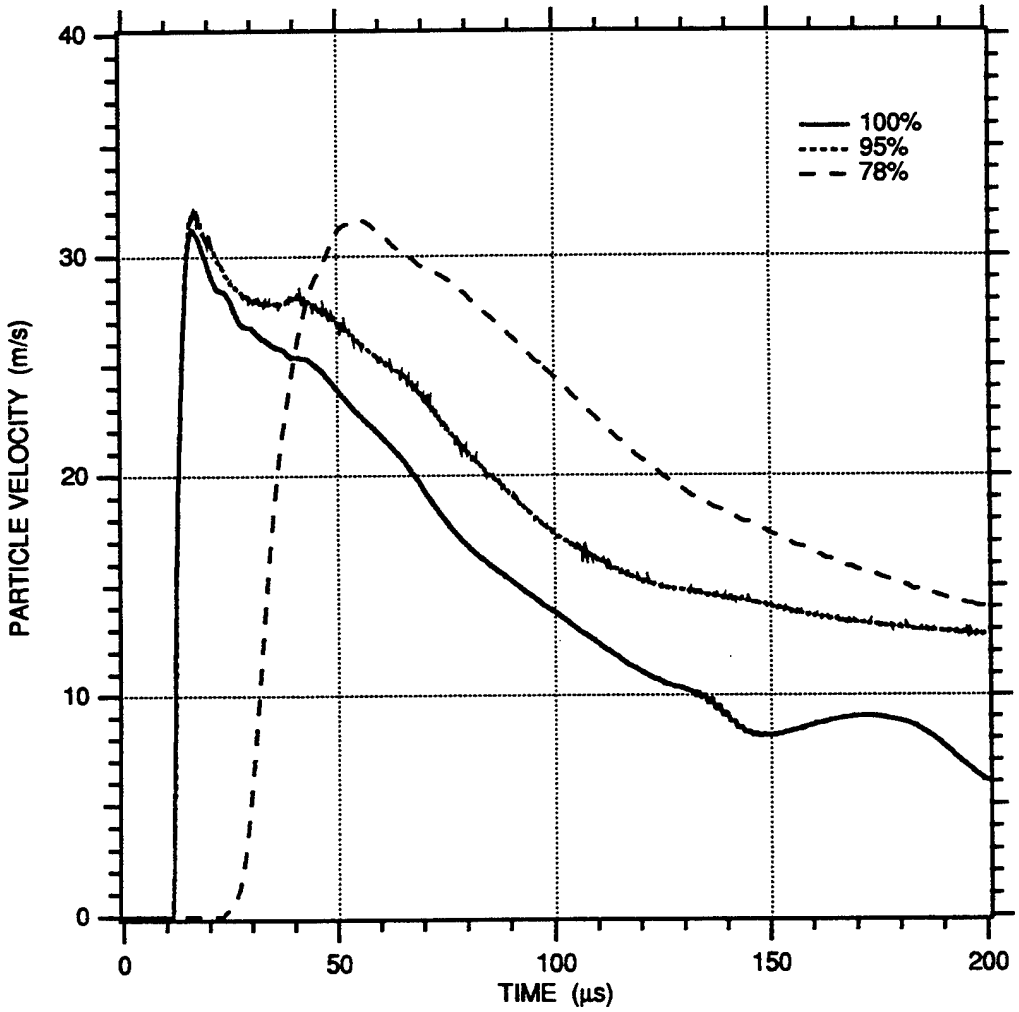

FIGURE 8-5. COMPARISON OF PARTICLE VELOCITY-TIME HISTORIES MEASURED IN 100%, 95%, AND 78% SATURATED EGLIN BEACH SAND FOR A 3/8 g PETN EXPLOSIVE CHARGE AT A RANGE OF 3.05 cm

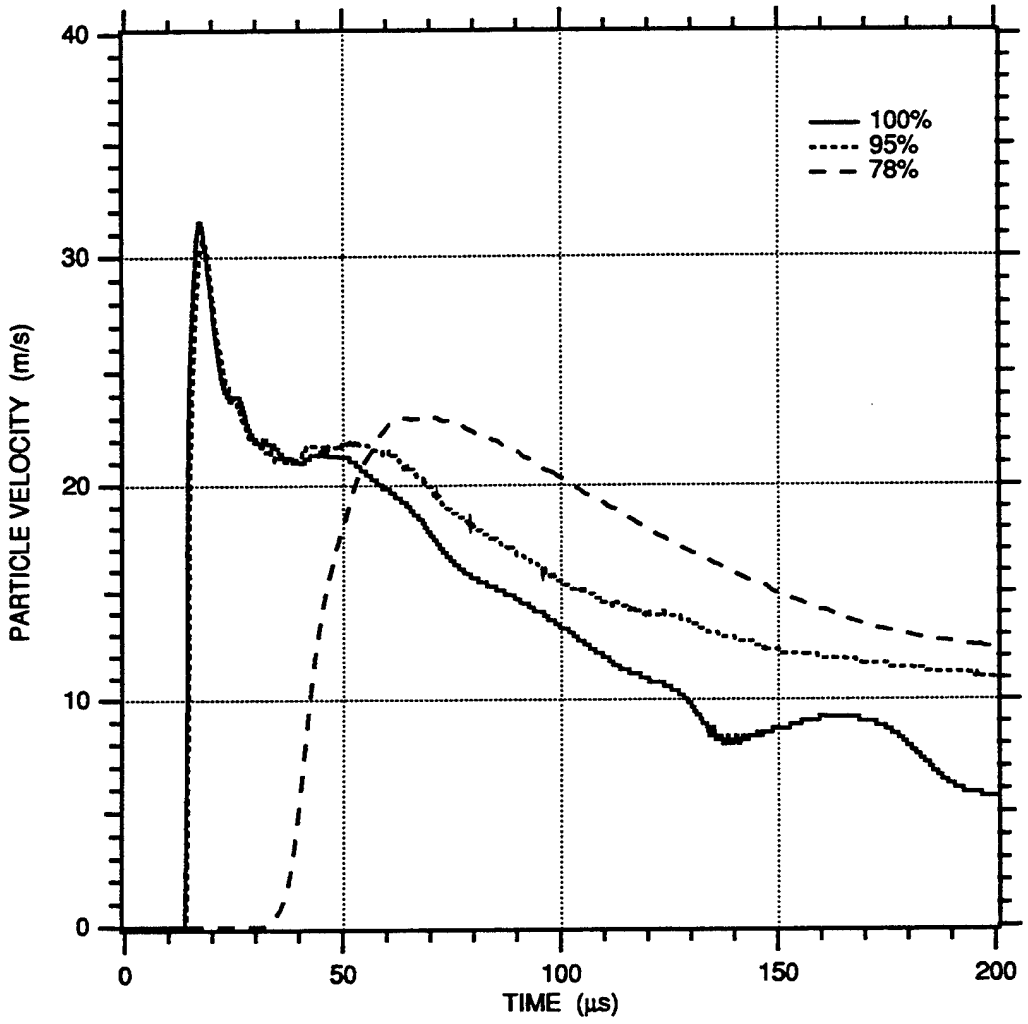

FIGURE 8-6. COMPARISON OF PARTICLE VELOCITY-TIME HISTORIES MEASURED IN 100%, 95%, AND 78% SATURATED EGLIN BEACH SAND FOR A 3/8 g PETN EXPLOSIVE CHARGE AT A RANGE OF 3.55 cm

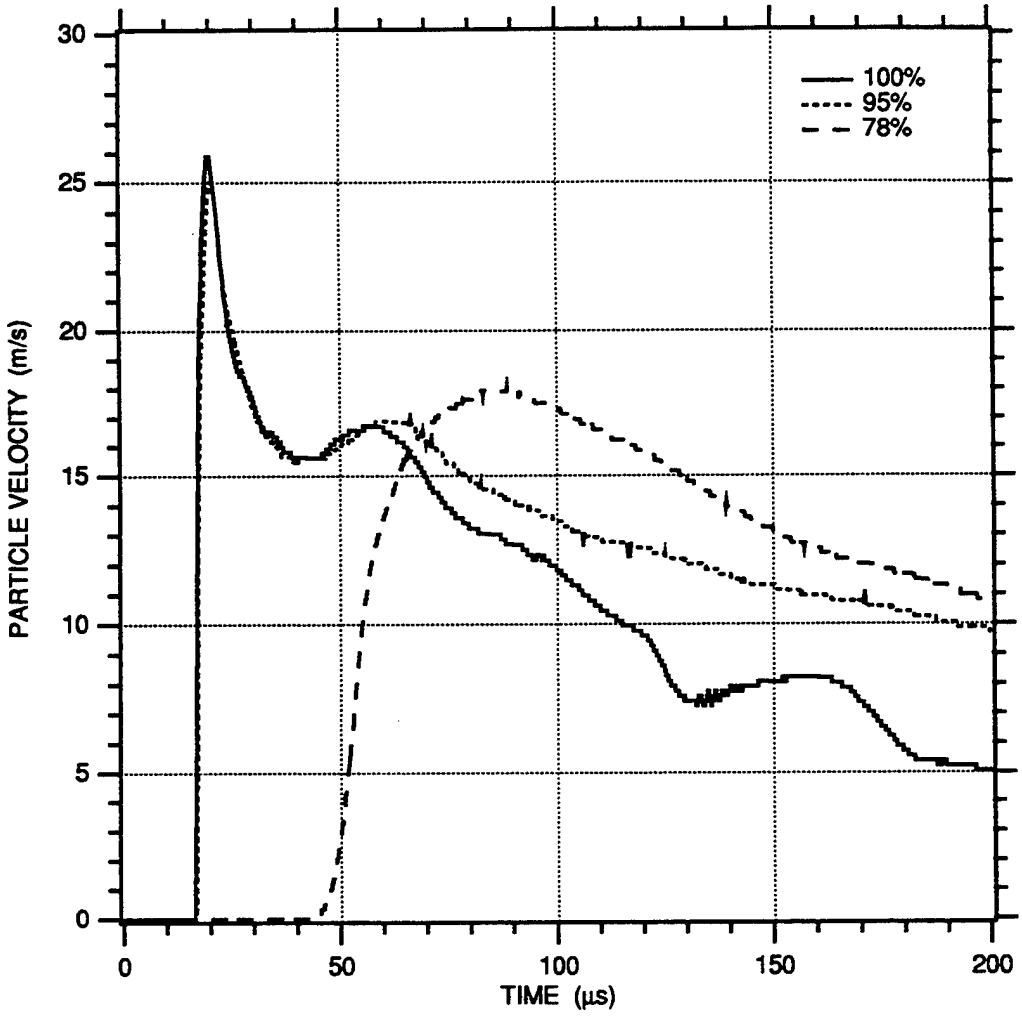

FIGURE 8-7. COMPARISON OF PARTICLE VELOCITY-TIME HISTORIES MEASURED IN 100%, 95%, AND 78% SATURATED EGLIN BEACH SAND FOR A 3/8 g PETN EXPLOSIVE CHARGE AT A RANGE OF 4.05 cm

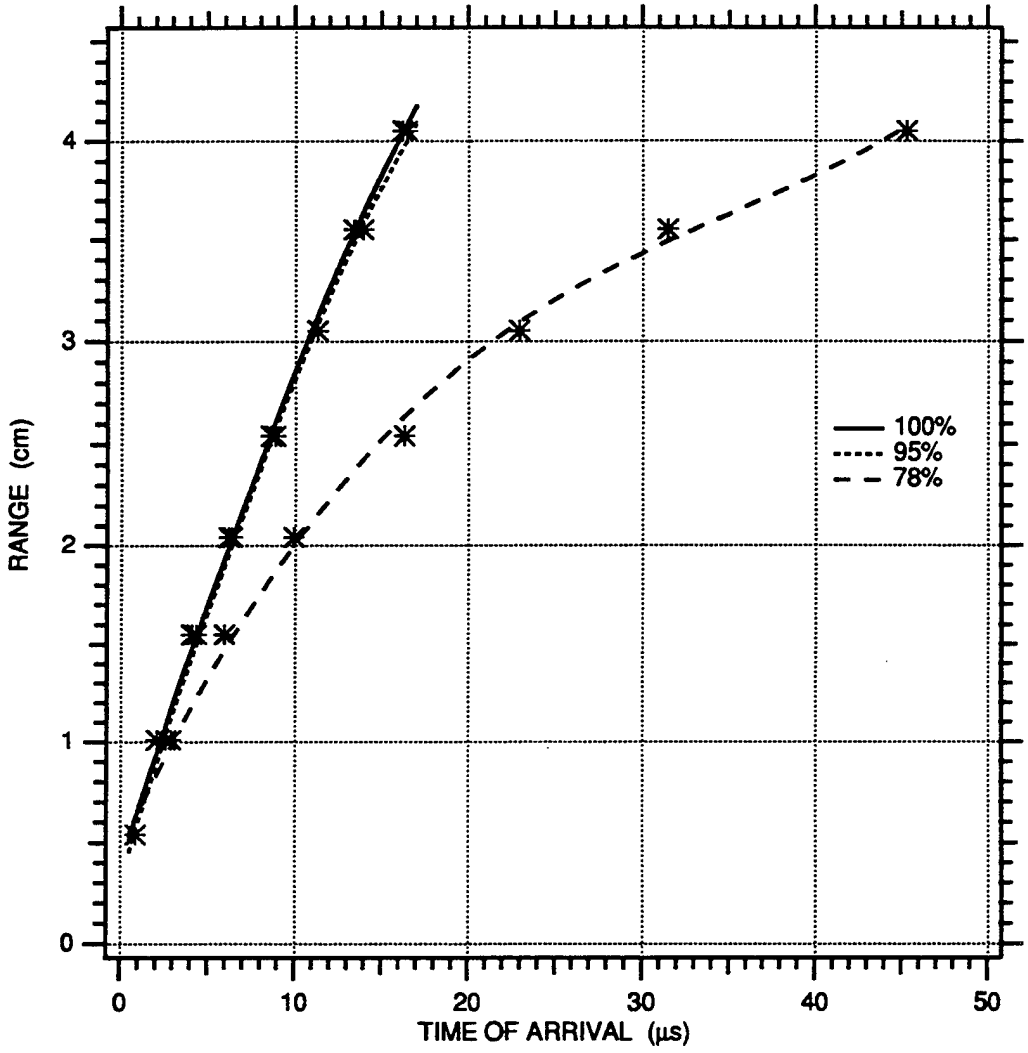

FIGURE 8-8. COMPARISON OF RANGE VERSUS TIME OF ARRIVAL MEASURED IN 100%, 95%, AND 78% SATURATED EGLIN BEACH SAND FOR A 3/8 g PETN EXPLOSIVE CHARGE

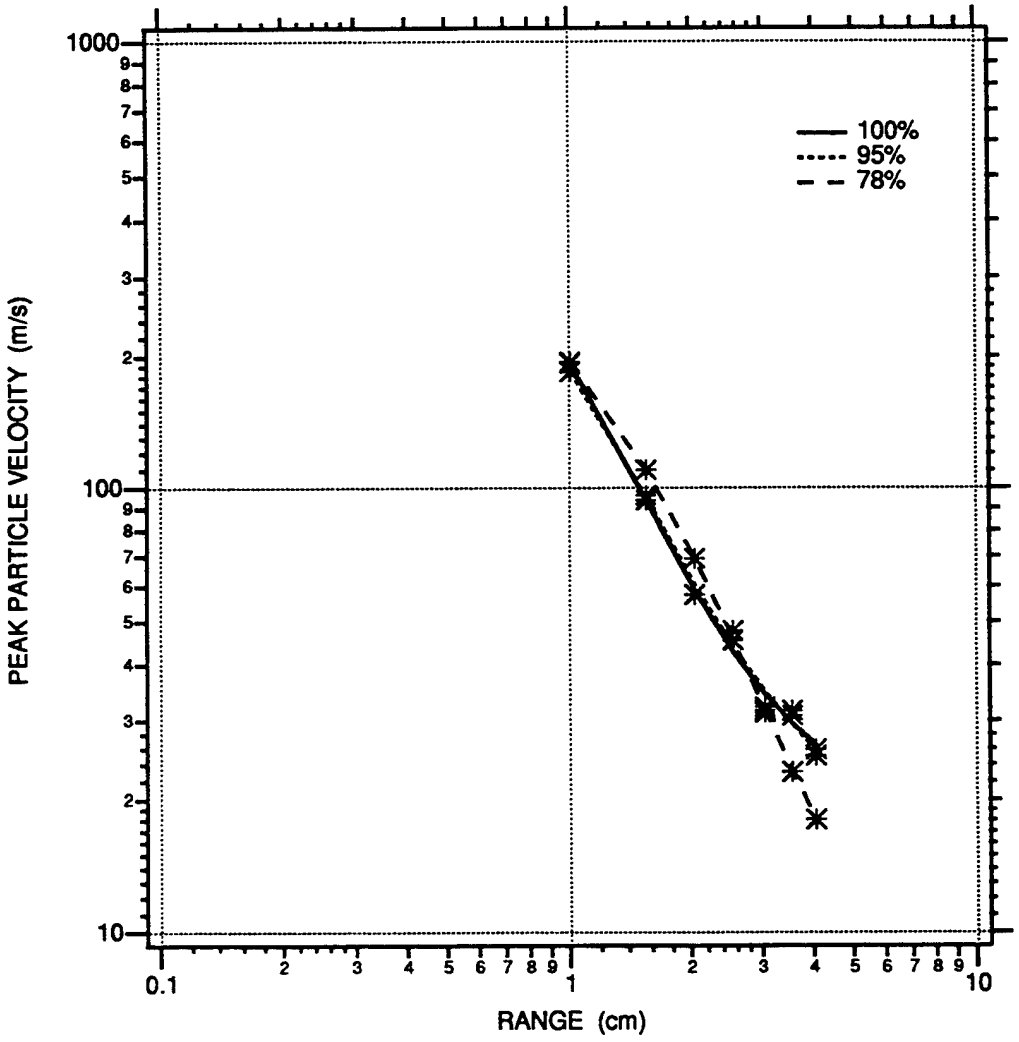

FIGURE 8-9. COMPARISON OF PEAK PARTICLE VELOCITY VERSUS RANGE MEASURED IN 100%, 95%, AND 78% SATURATED EGLIN BEACH SAND FOR A 3/8 g PETN EXPLOSIVE CHARGE

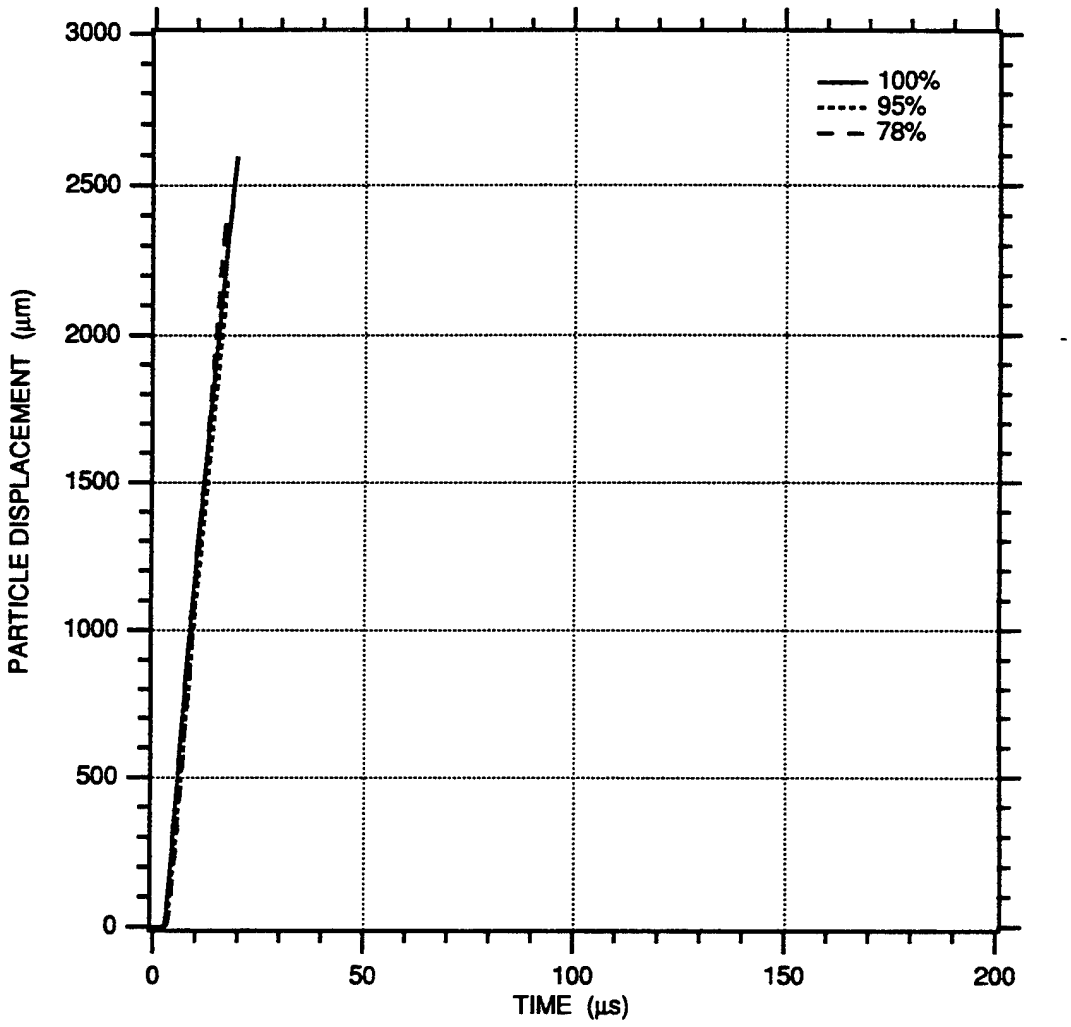

FIGURE 8-10. COMPARISON OF PARTICLE DISPLACEMENT-TIME HISTORIES MEASURED IN 100%, 95%, AND 78% SATURATED EGLIN BEACH SAND FOR A 3/8 g PETN EXPLOSIVE CHARGE AT A RANGE OF 1.01 cm

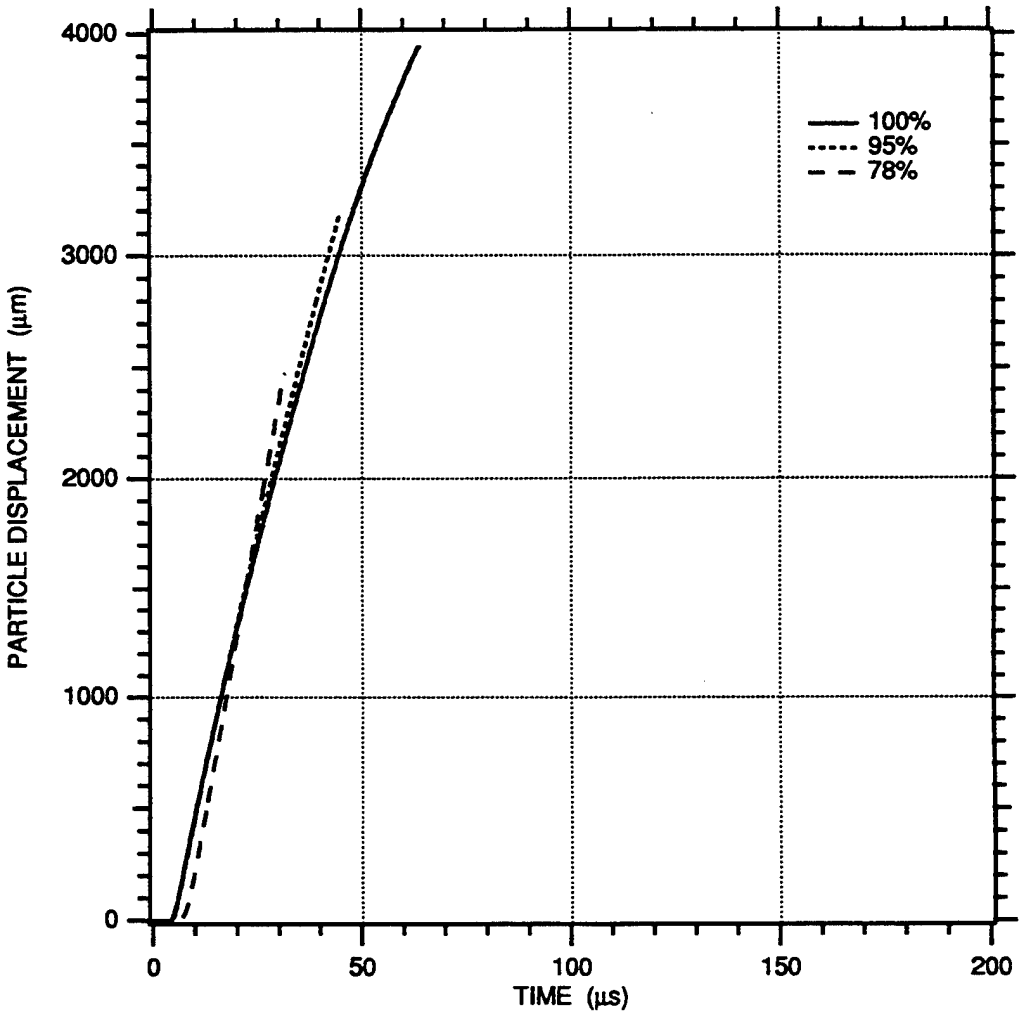

FIGURE 8-11. COMPARISON OF PARTICLE DISPLACEMENT-TIME HISTORIES MEASURED IN 100%, 95%, AND 78% SATURATED EGLIN BEACH SAND FOR A 3/8 g PETN EXPLOSIVE CHARGE AT A RANGE OF 1.54 cm

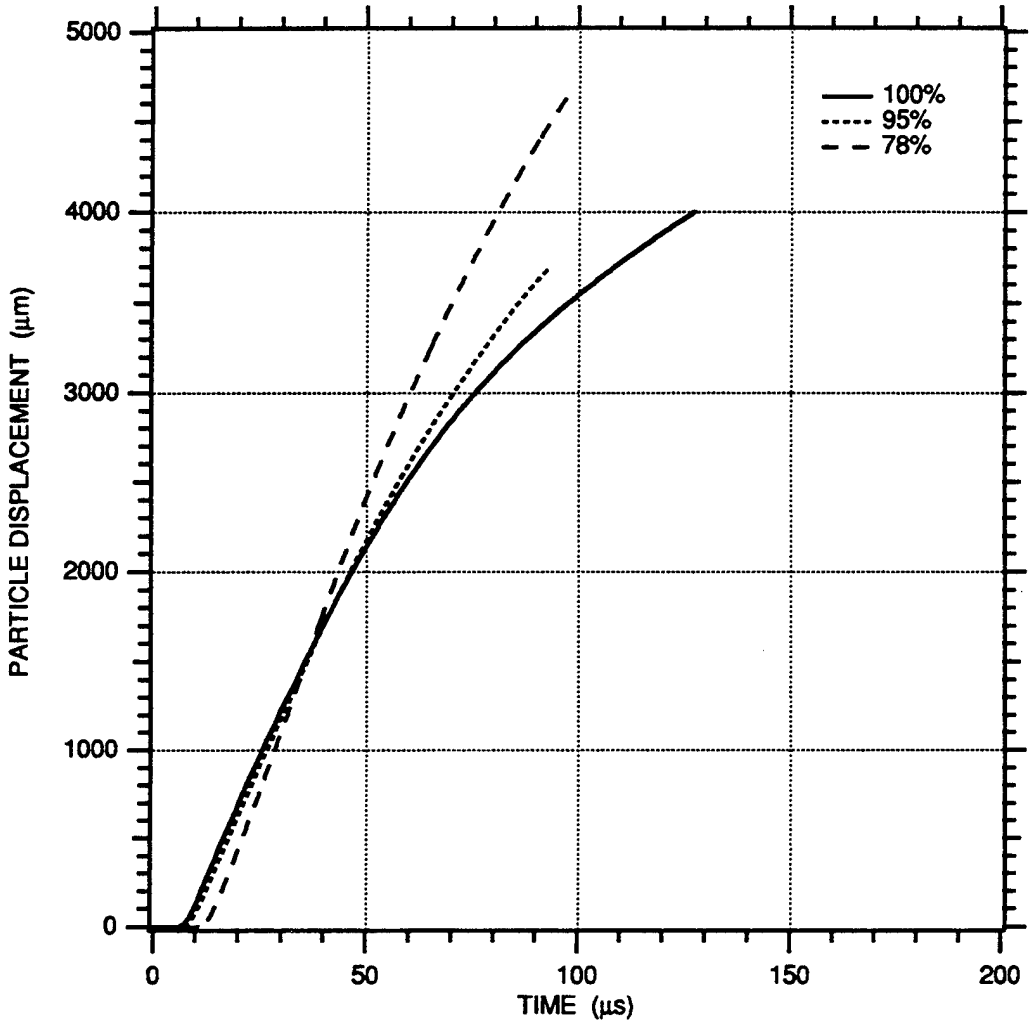

FIGURE 8-12. COMPARISON OF PARTICLE DISPLACEMENT-TIME HISTORIES MEASURED IN 100%, 95%, AND 78% SATURATED EGLIN BEACH SAND FOR A 3/8 g PETN EXPLOSIVE CHARGE AT A RANGE OF 2.04 cm

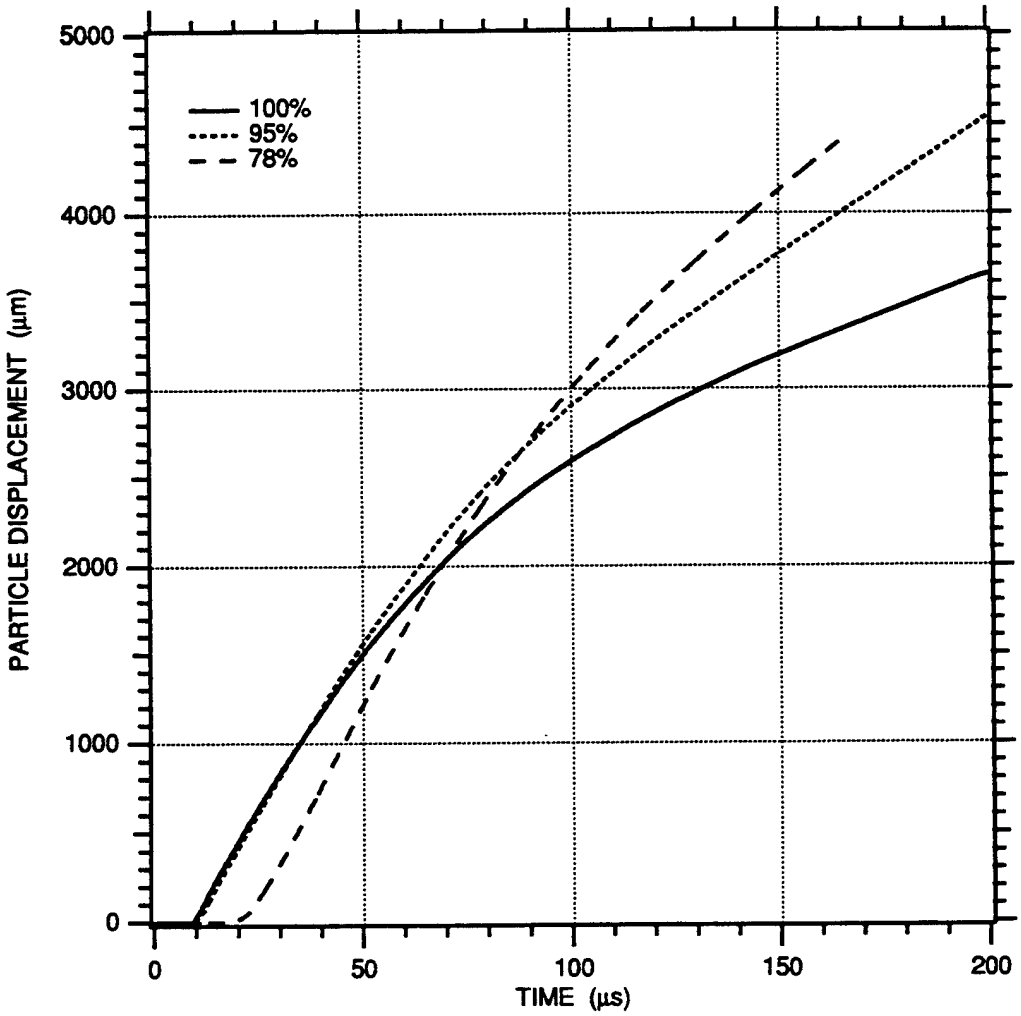

FIGURE 8-13. COMPARISON OF PARTICLE DISPLACEMENT-TIME HISTORIES MEASURED IN 100%, 95%, AND 78% SATURATED EGLIN BEACH SAND FOR A 3/8 g PETN EXPLOSIVE CHARGE AT A RANGE OF 2.54 cm

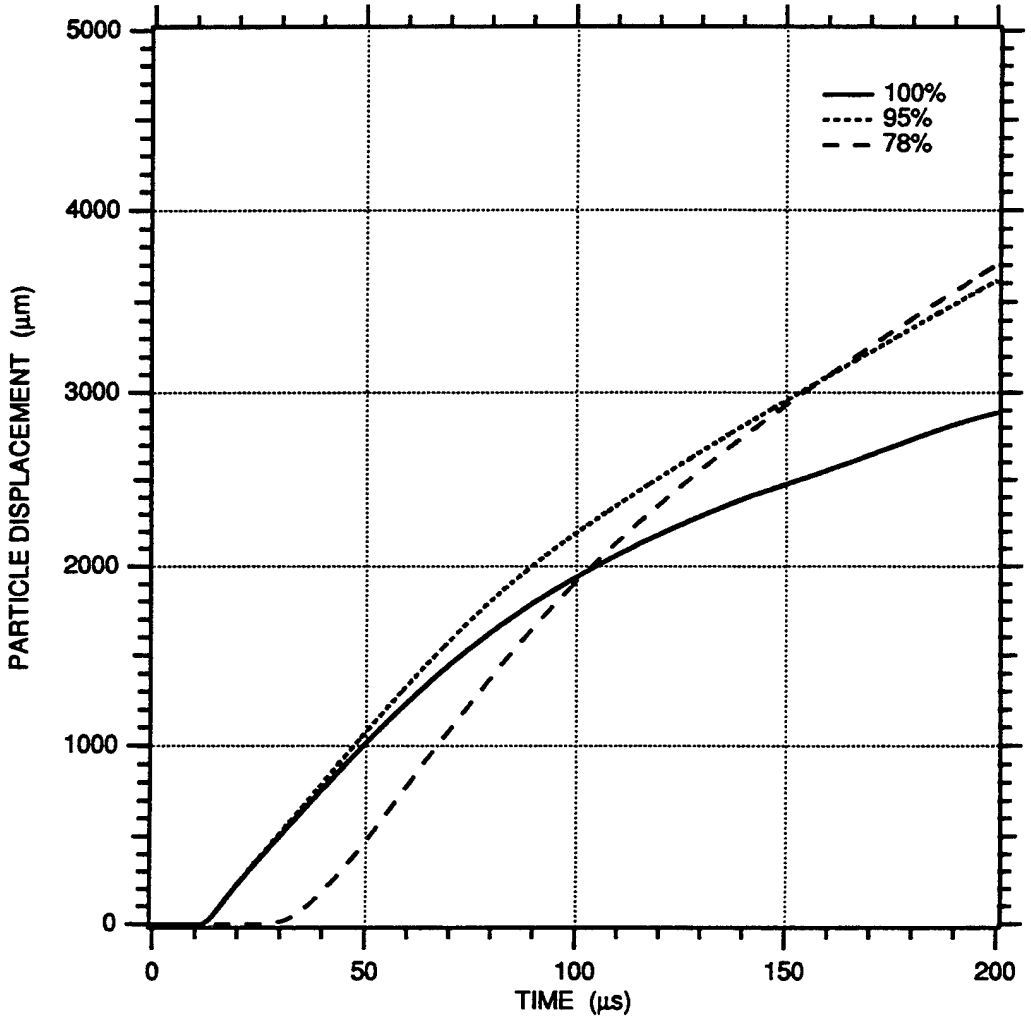

FIGURE 8-14. COMPARISON OF PARTICLE DISPLACEMENT-TIME HISTORIES MEASURED IN 100%, 95%, AND 78% SATURATED EGLIN BEACH SAND FOR A 3/8 g PETN EXPLOSIVE CHARGE AT A RANGE OF 3.05 cm

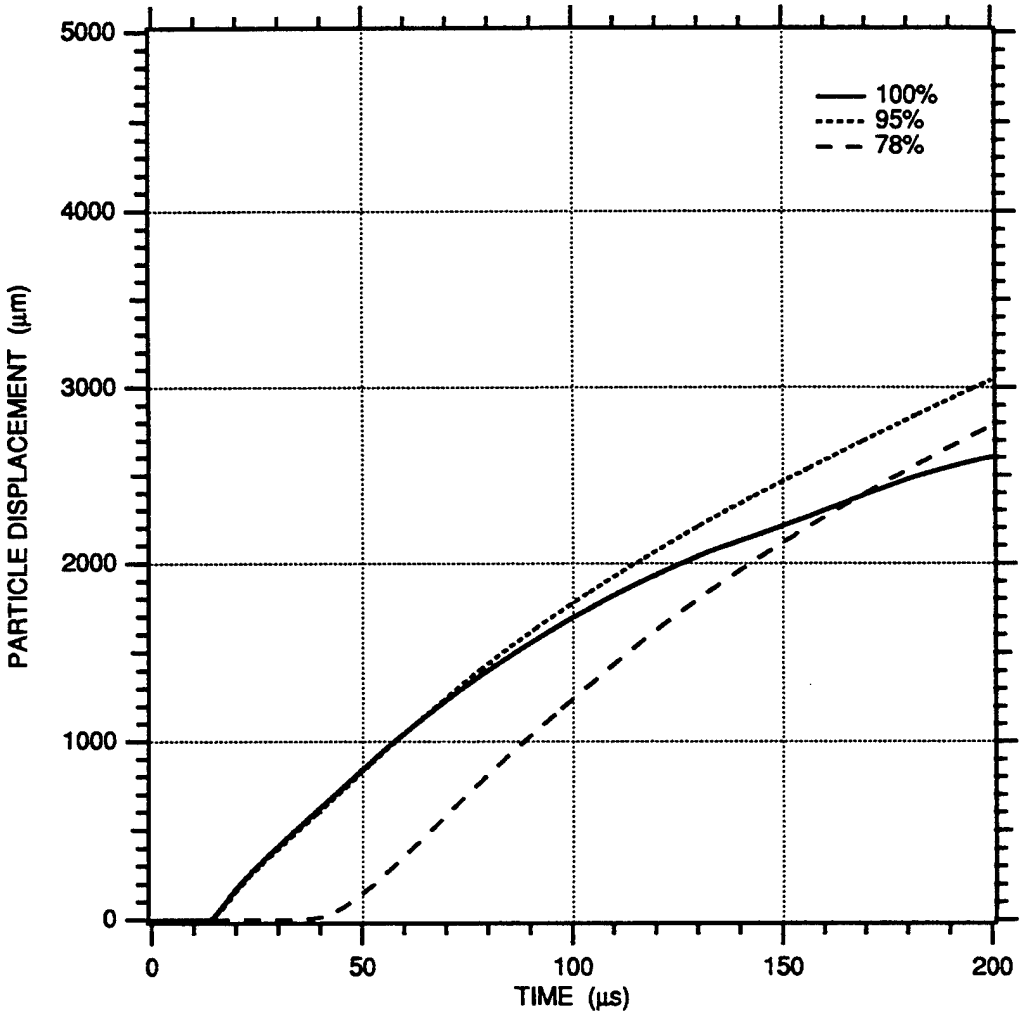

FIGURE 8-15. COMPARISON OF PARTICLE DISPLACEMENT-TIME HISTORIES MEASURED IN 100%, 95%, AND 78% SATURATED EGLIN BEACH SAND FOR A 3/8 g PETN EXPLOSIVE CHARGE AT A RANGE OF 3.55 cm

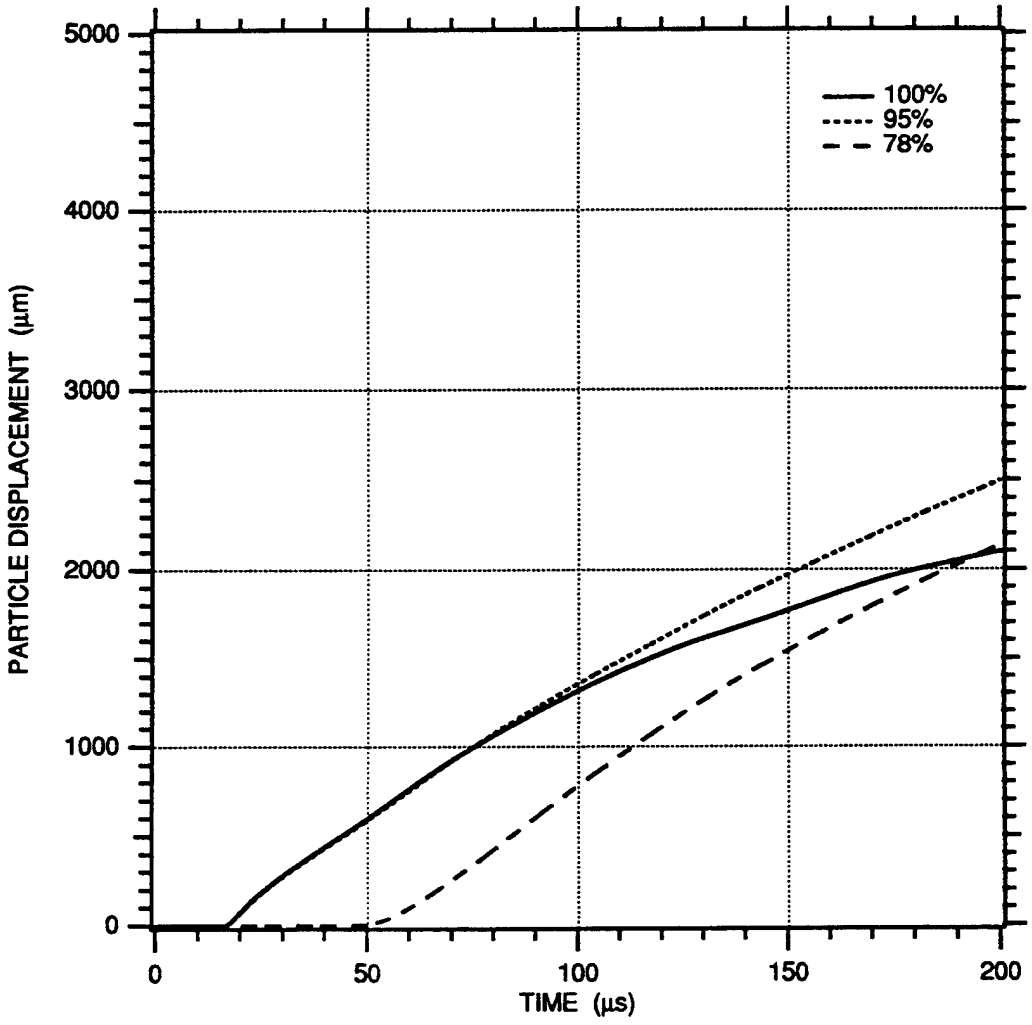

FIGURE 8-16. COMPARISON OF PARTICLE DISPLACEMENT-TIME HISTORIES MEASURED IN 100%, 95%, AND 78% SATURATED EGLIN BEACH SAND FOR A 3/8 g PETN EXPLOSIVE CHARGE AT A RANGE OF 4.05 cm

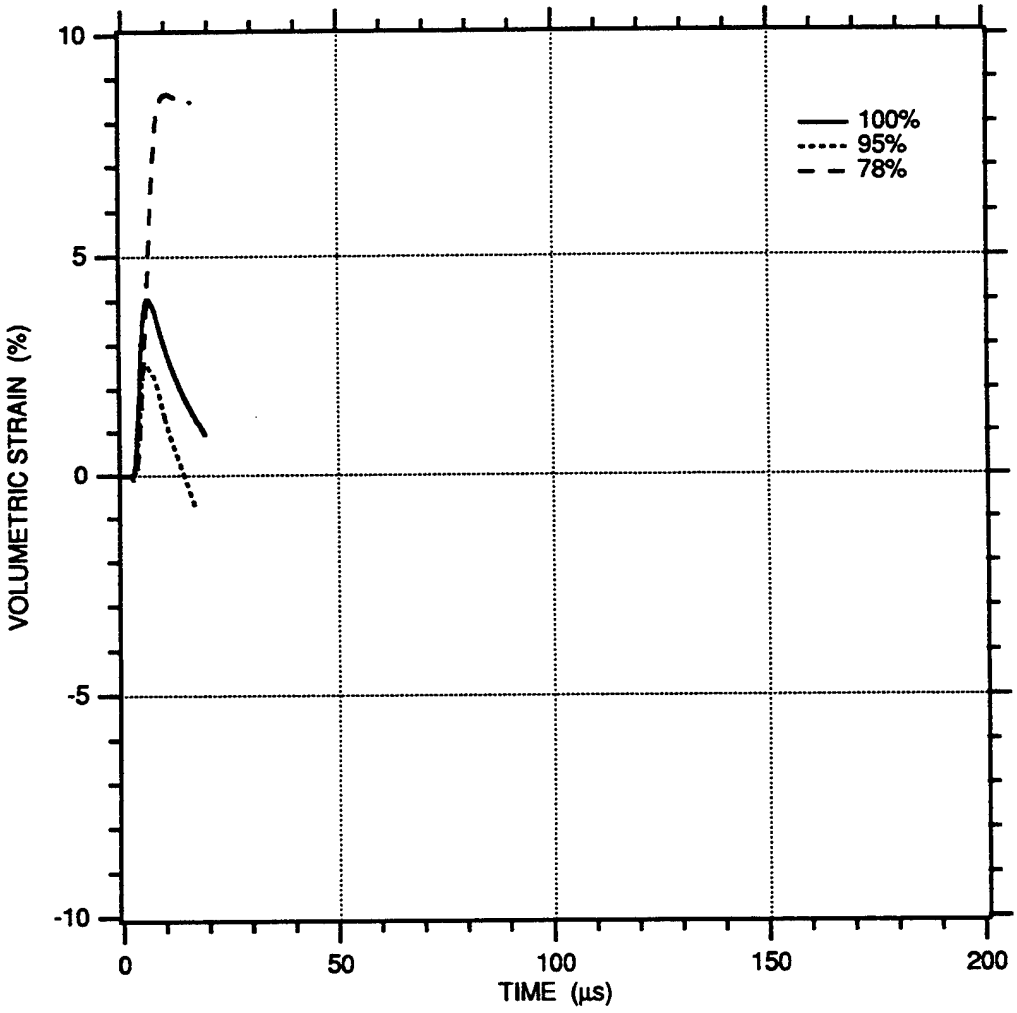

FIGURE 8-17. COMPARISON OF VOLUMETRIC STRAIN-TIME HISTORIES MEASURED IN 100%, 95%, AND 78% SATURATED EGLIN BEACH SAND FOR A 3/8 g PETN EXPLOSIVE CHARGE AT A RANGE BETWEEN 1.01 AND 1.54 cm

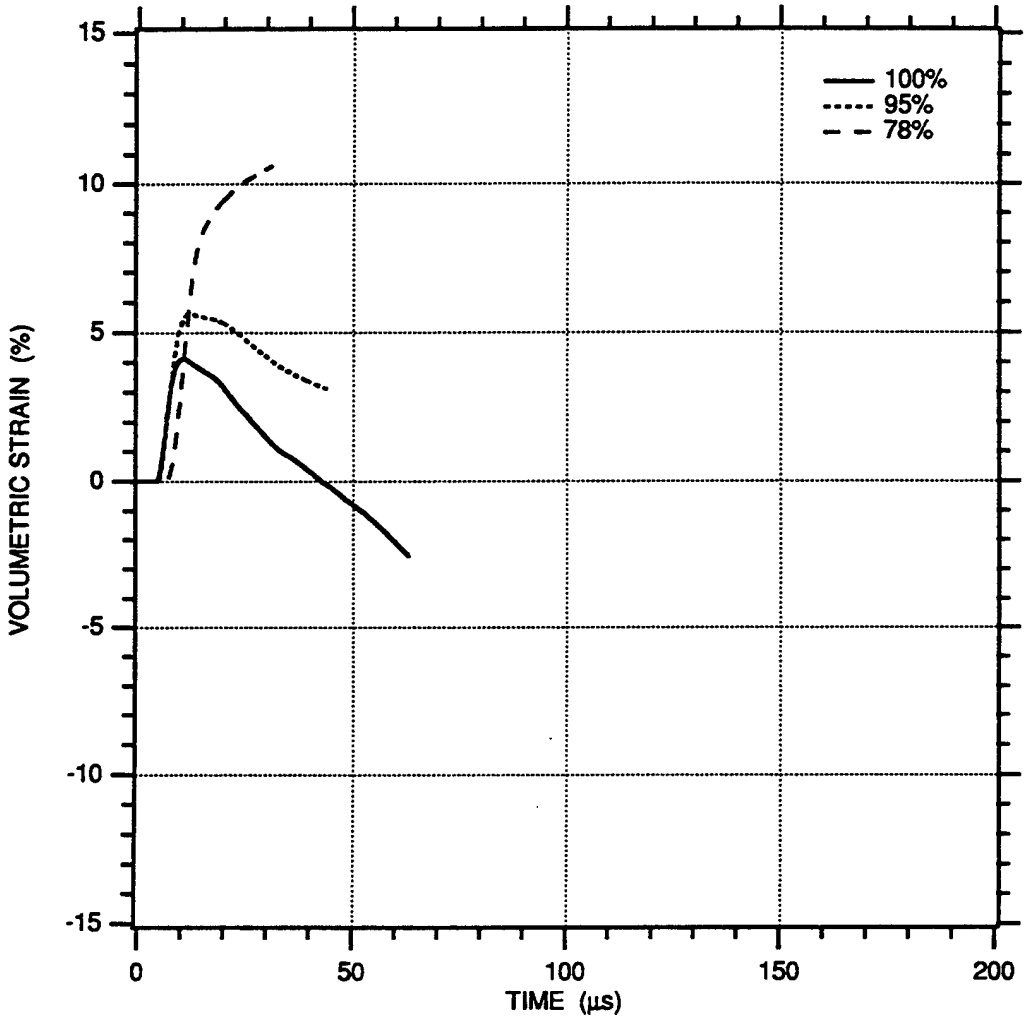

FIGURE 8-18. COMPARISON OF VOLUMETRIC STRAIN-TIME HISTORIES MEASURED IN 100%, 95%, AND 78% SATURATED EGLIN BEACH SAND FOR A 3/8 g PETN EXPLOSIVE CHARGE AT A RANGE BETWEEN 1.54 AND 2.04 cm

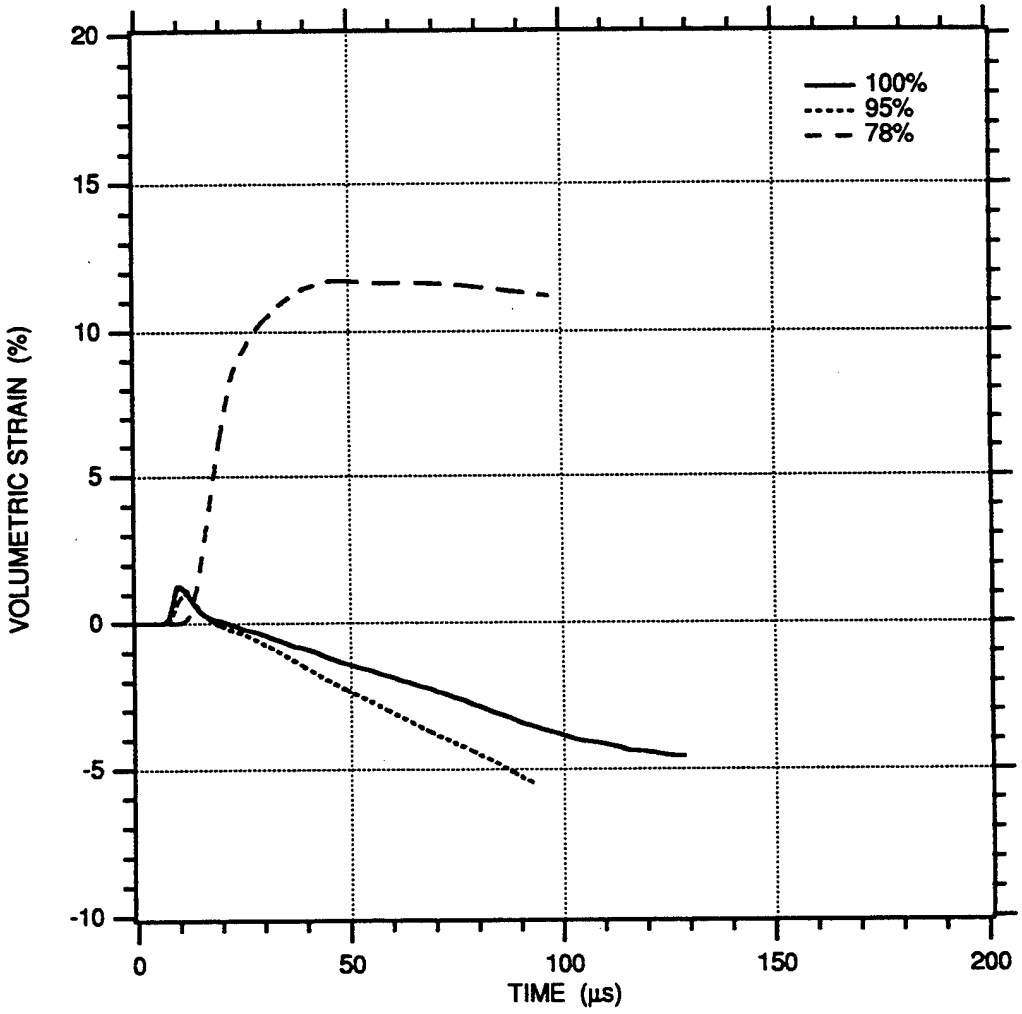

FIGURE 8-19. COMPARISON OF VOLUMETRIC STRAIN-TIME HISTORIES MEASURED IN 100%, 95%, AND 78% SATURATED EGLIN BEACH SAND FOR A 3/8 g PETN EXPLOSIVE CHARGE AT A RANGE BETWEEN 2.04 AND 2.54 cm

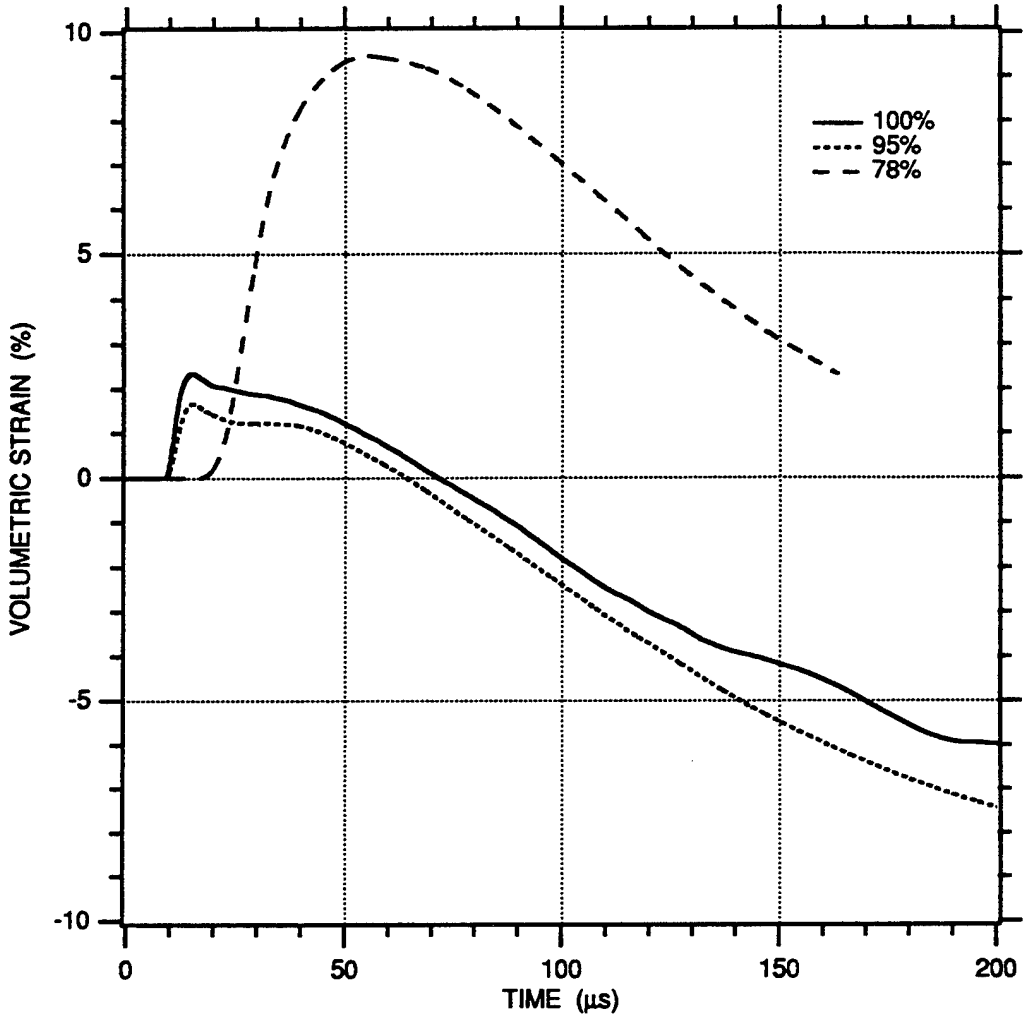

FIGURE 8-20. COMPARISON OF VOLUMETRIC STRAIN-TIME HISTORIES MEASURED IN 100%, 95%, AND 78% SATURATED EGLIN BEACH SAND FOR A 3/8 g PETN EXPLOSIVE CHARGE AT A RANGE BETWEEN 2.54 AND 3.05 cm

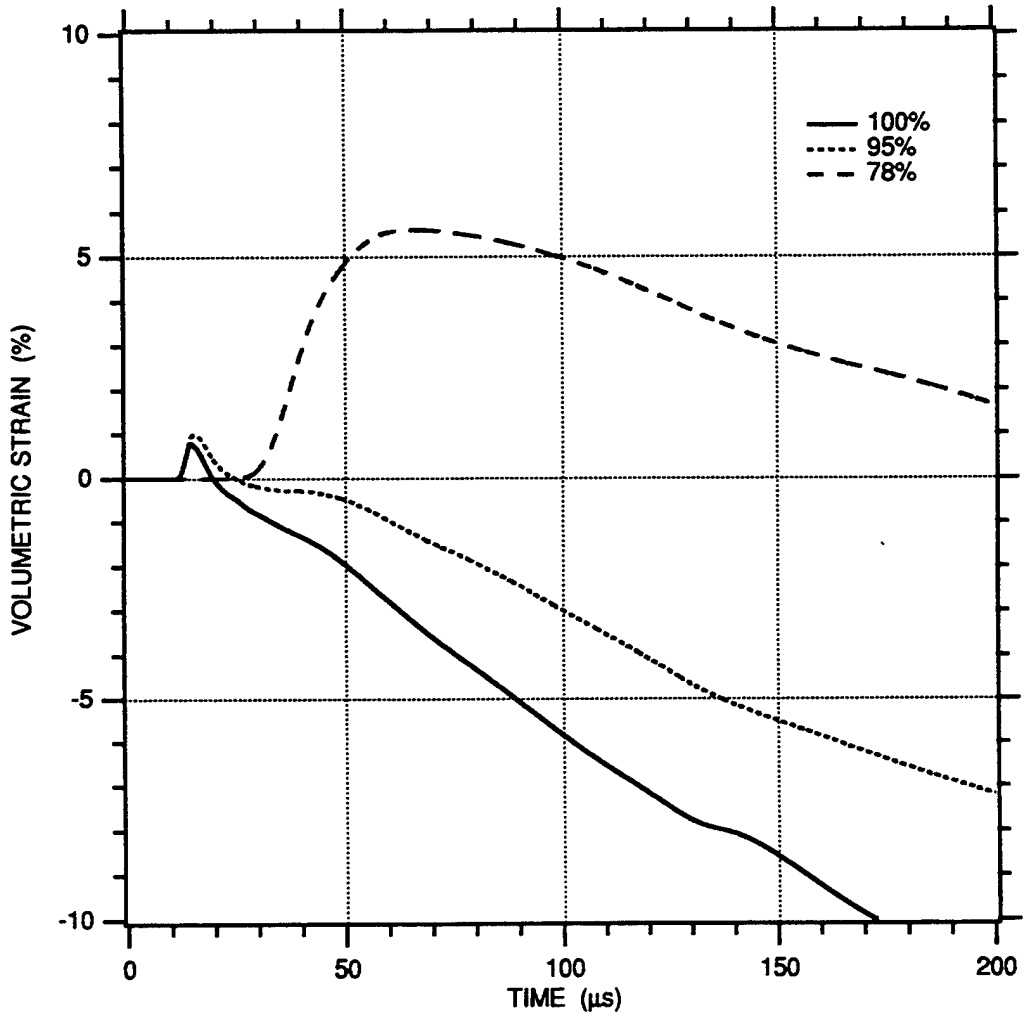

FIGURE 8-21. COMPARISON OF VOLUMETRIC STRAIN-TIME HISTORIES MEASURED IN 100%, 95%, AND 78% SATURATED EGLIN BEACH SAND FOR A 3/8 g PETN EXPLOSIVE CHARGE AT A RANGE BETWEEN 3.05 AND 3.55 cm

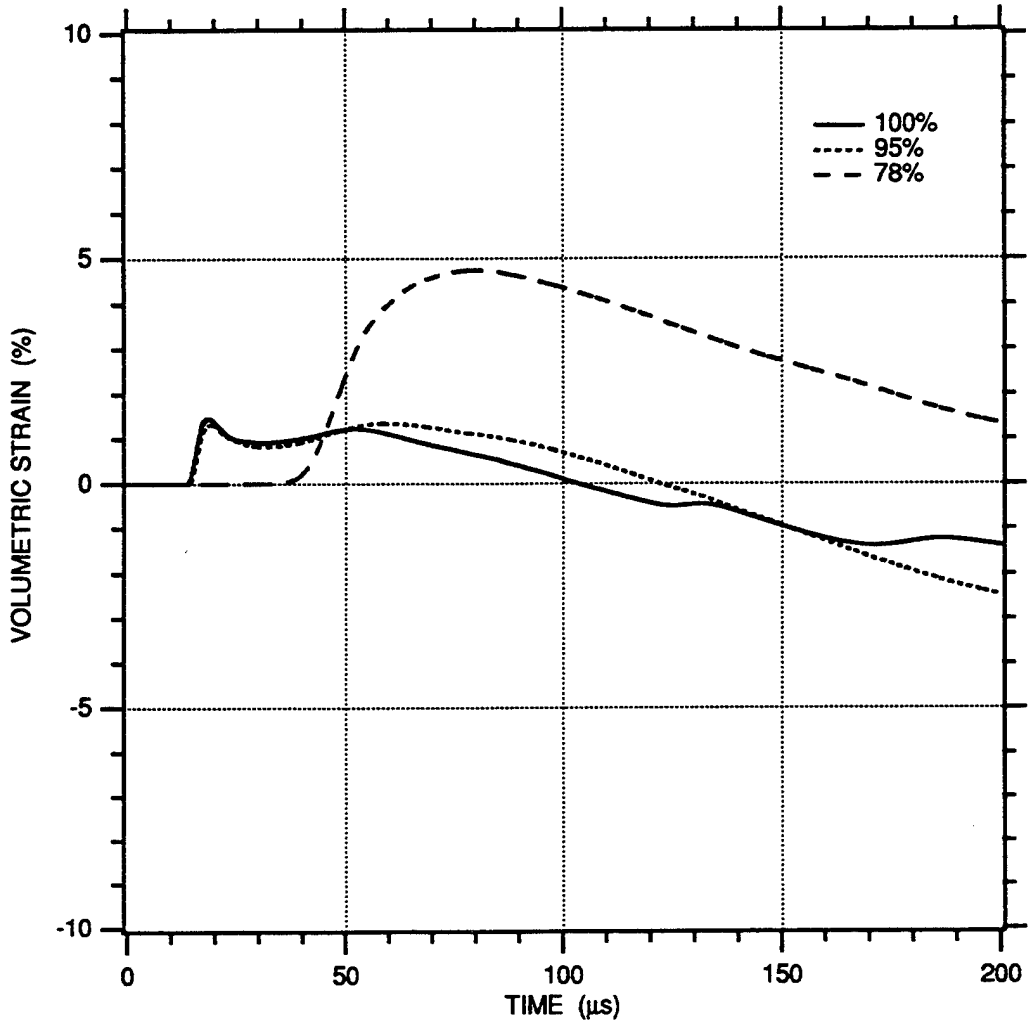

FIGURE 8-22. COMPARISON OF VOLUMETRIC STRAIN-TIME HISTORIES MEASURED IN 100%, 95%, AND 78% SATURATED EGLIN BEACH SAND FOR A 3/8 g PETN EXPLOSIVE CHARGE AT A RANGE BETWEEN 3.55 AND 4.05 cm

SECTION 9

SUMMARY AND RECOMMENDATIONS

SAND MODEL FABRICATION AND SATURATION UNIFORMITY

The sand model fabrication techniques produced the material property conditions summarized in Table 9-1. The estimated error associated with each material parameter for the fabrication techniques used is estimated to be within ±1%. We summarize our error analysis in Appendix C.

TABLE 9-1. SAND MODEL EXPERIMENTAL PROPERTIES

Experiment No.	Dry Density ($g/cm^3 \pm 0.008$)	Porosity (% ± 0.3)	Saturated Density ($g/cm^3 \pm 0.011 g/cm^3$)	Total Saturation (% ± 1%)
1	1.678	36.8	2.051	100
2	1.659	37.5	2.012	95
3	1.465	44.8	1.815	78
4	1.452	45.3	1.802	77

The error associated with making saturation uniformity measurements could be as high as ±7% to ±10%. These possible large errors are the result of having to measure small differences in water amounts compared with relatively large sample sizes. However, the actual saturation uniformity variation was typically much less than the estimated possible maximum error for the 100%, 78%, and 77% saturated models. For the 100% saturated sand model, the average saturation level was 100% and the standard deviation was ±1%. These values are based on ten locations within the sample in which nine locations showed 100% and one location showed 96% saturation. For the 78% and 77% saturated sand models, the standard deviation was ±3% based on approximately 50 locations. Furthermore, the average saturation from 50 locations was within 2% of the average saturation obtained from bulk weight measurements. The largest degree of saturation nonuniformity occurred in the 95% saturated sand model as a result of the fabrication technique used. Here, the saturation level ranged from below 88% near the midplane to near 100% at the bottom.

PARTICLE VELOCITIES AND DISPLACEMENTS

We performed two experiments to illustrate the reproducibility of the particle velocity experimental technique. In one experiment, the saturation level was 78% and in a second experiment the saturation level was 77%. The average difference between peak particle velocities from each experiment was 2.6%. The average difference between wave front TOA between each experiment was 14.2%. In general, the particle velocity waveform shapes compared reasonably well. The largest difference between the two experiments occurred at a range of 4.05 cm. The wave front arrival times differed by 16.7% and the peak particle velocities differed by 6.7%. These differences may be attributed to variation in the saturation uniformity, which is approximately $\pm$4%.

The particle velocity-time histories were very similar between the 100% and 95% saturated sand models. The only noticeable difference was slightly larger postpeak particle velocities in the 95% saturated sand model, which could be attributed to collapse of the 2% of air voids with respect to the total volume in the 95% saturated sand model.

Comparison of the 100% and 78% saturated sand models showed 20% higher peak particle velocities in the 78% saturated sand model at ranges of 1.55 and 2.04 cm, similar peak particle velocities at ranges of 2.54 and 3.05 cm, and 30% lower peak particle velocities in the 78% saturated sand model at ranges of 3.55 and 4.05 cm. The higher peak particle velocity in the 78% saturated sand model near the charge is due to the lower inertial resistance because of less water in the pore space. The lower peak particle velocity in the 78% saturated sand model farther away from the charge is the result of larger attenuation of the particle velocity.

Temporal integration of the particle velocity measurements to obtain particle displacements illustrated a distinct trend among the 100%, 95%, and 78% saturated sand models. The lowest particle displacements occurred in the 100% saturated sand model and the highest particle displacements occurred in the 78% saturated sand model. The particle displacements for the 95% saturated sand model fell between the 100% and 78% saturated sand models.

Typically, the radial (ε_r), circumferential (ε_θ), and volumetric (ε_v) strains followed the same trends as described for the displacements. That is, the lowest strains occurred in the 100% saturated sand model, the highest strains occurred in the 78% saturated sand model, and the strains in the 95% saturated sand model fell between the 100% and 78% saturated sand models. However, at a few gage locations, the 95% saturated model strains were the same as or less than the 100% saturated model strains, particularly with respect to volumetric strain. These deviations from the typical trends are attributed to the fact that the strains are calculated with respect to

differences in displacements between adjacent gage locations. Although the particle displacement magnitudes are higher in the 95% saturated sand model than in the 100% saturated sand model, the particle displacement differences between adjacent gage locations are similar to within the experimental accuracy.

RADIAL STRESS

Typically, the radial stress measurements in each experiment showed reproducible peak stresses, with the peak stresses in good agreement with estimated peak stresses from the particle velocity records. Significant differences were typically observed for the postpeak residual stress levels between gages at the same range. We believe these differences are in part due to the large particle displacements that resulted in different stress flow conditions.

RECOMMENDATIONS FOR FUTURE WORK

Below, we provide a list of possible future research that would complement the research results described in this report.

- Perform a spherical stress bounds analysis using the particle velocity measurements obtained from this project. The results from the analysis could be used to bracket the stress waveform shapes that are consistent with the particle velocity measurements. This would guide us in assessing the validity of the measured stress records. The stress bounds analysis is performed by utilizing the equations of motion and assuming that the circumferential stress is equal to the radical stress (hydrodynamic condition) for one bound and equal to zero for the other bound.

- Perform additional spherical wave experiments with particle velocity gages only and at saturation levels between 95% and 80% using the same initial porosity. Here we would use the sand and water mixing technique to fabricate sand models with possible saturation levels of 85%, 90%, and 95%. The mixing technique would be used, because results from the current research indicate that reasonable saturation uniformity can be obtained with this technique.

- Perform one-dimensional plane wave experiments with particle velocity and stress gage measurements. One-dimensional plane waver experiments would provide data for developing stress-strain relations for different saturation levels. We would expect better success in stress measurements in the planar wave experiment than in the spherical divergent wave. Furthermore, stress-strain relations can be developed using only particle velocity measurements when plan wave Lagrange analysis is used to compute the stress components.[27] The calculated stress would be compared with the measured stress and could, possible, pinpoint the sources of irreproducibility in the spherical wave stress measurements.

SECTION 10

REFERENCES

1. J. C. Cizek and A. L. Florence, "Laboratory Investigation of Containment in Underground Nuclear Tests," SRI International Final Report to Defense Nuclear Agency, DNA 4846F (January 1978).

2. J. C. Cizek and A. L. Florence, "Laboratory Studies of Containment in Underground Nuclear Tests," SRI International Final Report to Defense Nuclear Agency, DNA 4847F (January 1979).

3. J. C. Cizek and A. L. Florence, "Laboratory Studies of Containment in Underground Nuclear Tests," SRI International Final Report to Defense Nuclear Agency, DNA 5601F (January 1980).

4 J. C. Cizek and A. L. Florence, "Laboratory Investigation of Containment in Underground Nuclear Tests," SRI International Final Report to Defense Nuclear Agency, DNA 5731F (February 1981).

5. J. C. Cizek and A. L. Florence, "Laboratory Investigation of Containment in Underground Nuclear Tests," SRI International Final Report to Defense Nuclear Agency, DNA 6121F (February 1982).

6. J. C. Cizek and A. L. Florence, "Laboratory Investigation of Containment of Underground Explosions," SRI International Final Report to Defense Nuclear Agency, DNA-TR-82-83 (December 1982).

7. J. C. Cizek and A. L. Florence, "Laboratory Investigation of Containment of Underground Explosions," SRI International Final Report to Defense Nuclear Agency, DNA-TR-84-11 (December 1983).

8. G. Nagy and A. L. Florence, "Laboratory Investigation of Containment of Underground Nuclear Explosions," SRI International Final Report to Defense Nuclear Agency, DNA-TR-85-137 (March 1985).

9. G. Nagy and A. L. Florence, "Laboratory Investigation of Containment of Underground Nuclear Explosions," SRI International Final Report to Defense Nuclear Agency, DNA-TR-86-271 (July 1986).

10. J. C. Cizek, A. L. Florence, and D. D. Keough, D. D., "Experimental Study of the Effects of Faults on Spherical Wave Propagation," SRI International Final Report to Defense Nuclear Agency, Contract DNA 001-80-C-0287 (January 1981).

11. G. Nagy and A. L. Florence, "Spherical Wave Propagation in Rocks," SRI International Final Report to Defense Nuclear Agency, DNA-TR-85-254 (May1984).

12. G. Nagy and A. L. Florence, "Spherical Wave Propagation in Low Porosity Brittle Rocks," SRI International Technical Report to Defense Nuclear Agency, DNA-TR-86-191 (May 1986).

13. S. A. Miller and A. L. Florence, "Laboratory Investigation of Containment of Underground Explosions," SRI International Technical Report to Defense Nuclear Agency, DNA-TR-89-4-REV (December 1988).

14. S. A. Miller and A. L. Florence, "Laboratory Particle Velocity Experiments on (JVE) Analog Rock," SRI Internaitonal Report CL-TR-90-0279(I) (October 1990).

15. R. W. Klopp, A. L. Florence, J. K. Gran, and J. W. Simons, "Spherical Wave Tunnel (SWAT-1) Test in Large Indiana Limestone Specimen," SRI International Final Report to Defense Nuclear Agency, Contract No. DNA 001-90-C-0032 (August 1992).

16. P. R. Gefken and A. L. Florence, "Spherical Wave Experiments with Frozen Limestone," SRI International Technical Report to U.S. Army Waterways Experiment Station, Contract No. DACA39-92-K-0013 (November 1992).

17. P. R. Gefken and A. L. Florence, "spherical Waves in Jointed Limestone," SRI International Technical Report to Defense Nuclear Agency, DNA-TR-92-122 (February 1993).

18. D. D. Keough et al., "Investigation of the Credibility of *In Situ* Measurements of Radial and Tangential Stress in a Salt Test Bed," SRI International Technical Report to Defense Nuclear Agency, Contract No. DNA 001-82-C-0248 (May 1986).

19. D. D. Keough, S. A. Miller, P. S. DeCarli, D. E. Erlich, and D. F. Walter, "Simulation and Instrumentation Development, Vol. 3: Results and Status of Airblast, Groundshock, and Water Shock Measurements-Validation Experiments," SRI International Technical Report to Defense Nuclear Agency, DNA-TR-99-249-V3 (May 1988).

20. D. D. Keough and J. Drotleff, "Fourier Transforms Used to Compensate for Frequency Response," Paper No. 41, presented at The Fifth State-of-the-Art Blast Instrumentation Meeting, Kirtland Air Force Base, Albuquerque, NM (15-16 November 1988).

21. D. D. Keough, T. Cooper, J. K. Gran, and D. F. Walter, "Validation of the Measurement of Free-Field Stress in Porous Limestone by Flatpack/Limestone-Core Gages," SRI International Final Report to Defense Nuclear Agency, Contract No. DNA 001-89-C-0140.

22. J. K. Gran and B. S. Holmes, "Measurement of Close-In Blast and Shock Loads," SRI International Final Report to U.S.A. Ballistic Research Laboratory, Contract No. DAAA15-89-C-0009 (April 1992).

23. D. D. Keough et al., "DISTANT MOUNTAIN Test Series (Test Bed Designs and Flatpack Stress Gage Measurements)," SRI Technical Report to Defense Nuclear Agency, DNA-TR-93-105 (December 1993).

24. D. D. Keough et al., "Modified Stainless Steel/Ytterbium Small Flatpack (Miniflatpack) Pressure/Stress Gage with Superior Response Characteristics," paper presented at the DNA INWET '93 Conference, November 1993.

25. J. K. Gran and D. D. Keough, "Static Laboratory Experiments for UTP Stress Gage Validation," paper presented at the DNA INWET '93 Conference, November 1993.

26. D.E. Chitty et al., "Mechanical Properties of Sands from Range B-70, Eglin AFB, and Two Natural Beaches to Support Mine Countermeasures Research," Final Report, U.S. Air Force Wright Laboratory, Contract No. F08635-93-C-0020 (March 1994).

27. J.T. Rosenberg and D.D. Keough, "LASS Analysis of CIST23 Data," SRI International Final Report to Defense Nuclear Agency, Contract No. DNA 001-80-C-0178 (October 1983).

APPENDIX A

STRESS MEASUREMENTS

Stress measurements that we have made using the SRI fabricated, miniflatpack, stress gage have focused primarily on measuring the radial stress component from a spherical explosive source in homogeneous materials (such as rock and rock matching grouts). Typically, results in these material types have indicated a precision level within ±20%. Using the miniflatpack stress gage in saturated sand may have a larger level of uncertainty because the saturated sand is lower density and most likely more inhomogeneous. Furthermore, the saturated sand inhomogeneity may be greatest near the miniflatpack stress gage due to the difficulty of placing the granular material around the gage. We expected the fabrication procedure for the 100% saturated sand model to produce a more homogeneous saturated sand material, particularly near the stress gage, than did the fabrication technique for the 95%,78%, and 77% saturated sand models.

The miniflatpack stress gage that we used consisted of a Dynasen, 3.2-mm-square (0.125 in.), ytterbium, sensing element sandwiched between two, 0.15-mm-thick (0.006 in.), stainless steel plates. The ytterbium was electrically isolated from the stainless steel using a 0.025-mm-thick (0.001 in.) layer of Kapton tape. The stainless steel plates were connected to ground for gage shielding. The gage was held in position by a brass tube, which was rigidly fixed into the aluminum container encompassing the saturated sand. However, the end of the stress gage, where the ytterbium sensing element was located, was free to move perpendicular to the gage plane owing to the flexibility of the stainless steel plates. Because of this, the location of the ytterbium sensing element with respect to the charge center may have changed slightly from the nominal placement range locations of 2 cm and 3 cm during the sand model fabrication.

To measure the radial stress component, we oriented the stress gage so that the gage face was perpendicular to the propagating stress wave. To measure the circumferential stress component, we oriented the stress gage so that the gage face was parallel to the propagating stress wave. In Experiments 1 and 2 (100% and 95% saturated sand models), two radial and two circumferential stress gages were each placed at nominal ranges of 2 cm (0.79 in.) and 3 cm (1.18 in.). In Experiments 3 and 4 (78% and 77% saturated sand models) four radial stress gages were each placed at nominal ranges of 2 cm (0.79 in.) and 3 cm (1.18 in.).

Because ytterbium is sensitive to in-plane strain, we made miniflatpack strain gages in the same manner as described above and placed them at the same orientations and ranges as the stress

gages. The strain-time histories from these gages were used in the data reduction for the stress gagse to reduce the ambiguity of the stress measurement due to possible in-plane strain. Typically, the strains measured by these gages were less than 0.5%, which corresponds to a nominal stress correction value of approximately 0.25 kbar.

The stress records from each experiment are listed below:

Figures A-1 through A-4: Radial stress in 100% saturated sand
Figures A-5 through A-8: Circumferential stress in 100% saturated sand
Figures A-9 through A-12: Radial stress in 95% saturated sand
Figures A-13 through A-14: Circumferential stress in 95% saturated sand
Figures A-15 through A-19: Radial stress in 78% saturated sand
Figures A-20 through A-21: Radial stress in 77% saturated sand.

The range locations given in each figure were obtained by adjusting the range so that range versus time of arrival (TOA) profile was the same as determined from the particle velocity records. Here, we have assumed that the stress gages moved from their initial placement position during model fabrication. However, the TOA of the stress measurement would also be different from the TOA of the particle velocity measurements due to different localized material conditions around the stress gage.

Typically, the radial stress measurements in each experiment showed reproducible peak stresses, with the peak stresses in good agreement with estimated peak stresses from the particle velocity records, as shown in Figures A-22 through A-25. Significant differences were typically observed for the postpeak residual stress levels between gages at the same range. Postpeak residual stress levels differed by as much as 90% for gages located approximately at the same range.These differences may be attributable to the large particle displacements that produce different stress flow conditions around the gage or different in-plane strain conditions within each gage. Furthermore, the Dynasen ytterbium sensing elements used are characterized for only uniaxial loading. Thus, there is inherently greater uncertainly in the unloading portion of the stress measurements due to the lack of Dynasen ytterbium behavior data. In our data reduction of the stress measurements, we estimate a Dynasen ytterbium unloading curve by assuming mechanical ytterbium properties obtained from experiments performed at SRI on other ytterbium element types.

Circumferential stress measurements made in Experiments 1 and 2 for 100% and 95% saturated sand models, respectively, showed as much as 30% variation in peak stress and post peak residual stress for gages at the same range. Furthermore, the trends in the circumferential stress waveforms were not qualitatively consistent with radial stress waveforms at some range

locations. For example, some circumferential peak stress measurements exceeded the peak radial stress measurements.

Because of the ambiguities described above in the majority of the stress measurements, we suggest that only the peak radial stress information from the stress measurements be quantitatively used. The postpeak, residual, radial stress and the complet,e circumferential, stress waveforms should not be used due to the lack of reproducibility.

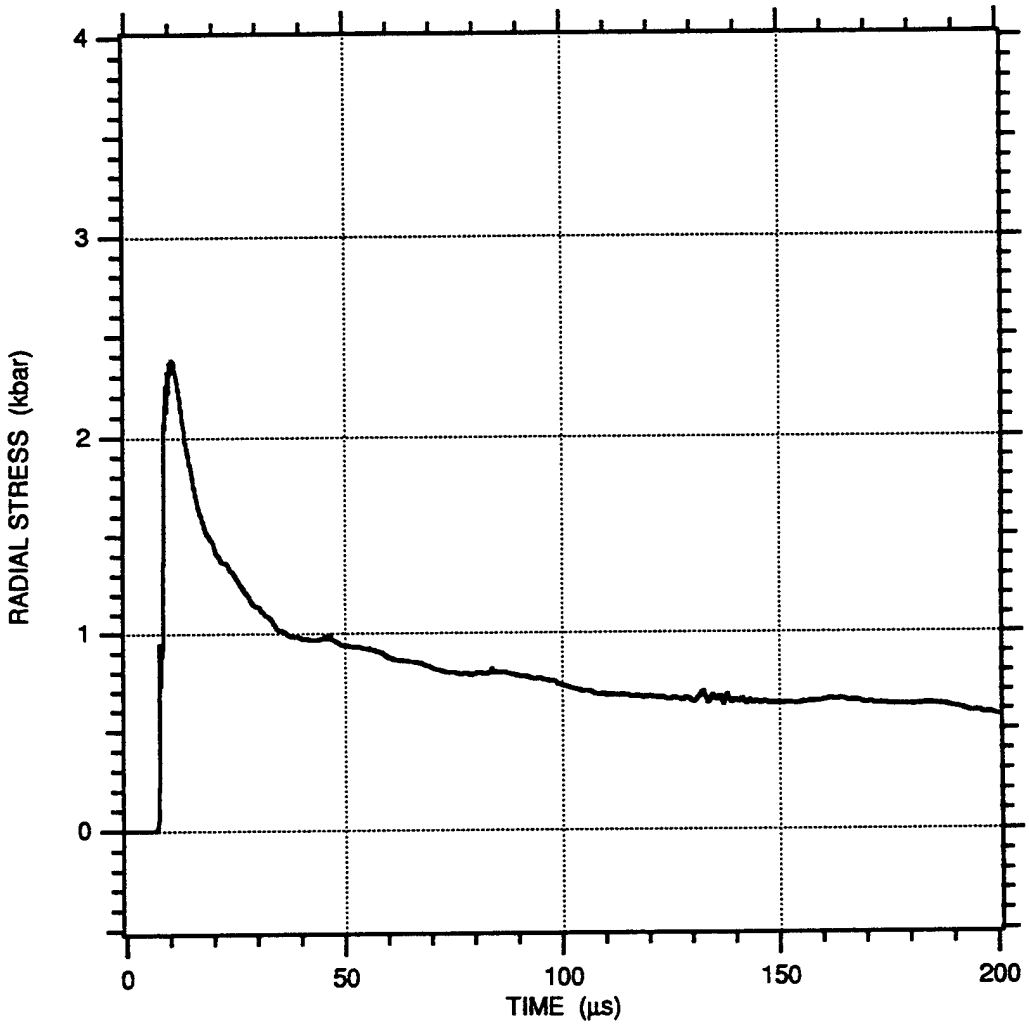

FIGURE A-1. RADIAL STRESS-TIME HISTORY MEASURED IN 100% SATURATED EGLIN BEACH SAND FOR A 3/8 g PETN EXPLOSIVE CHARGE AT A RANGE OF 2.34 cm (Gage 1)

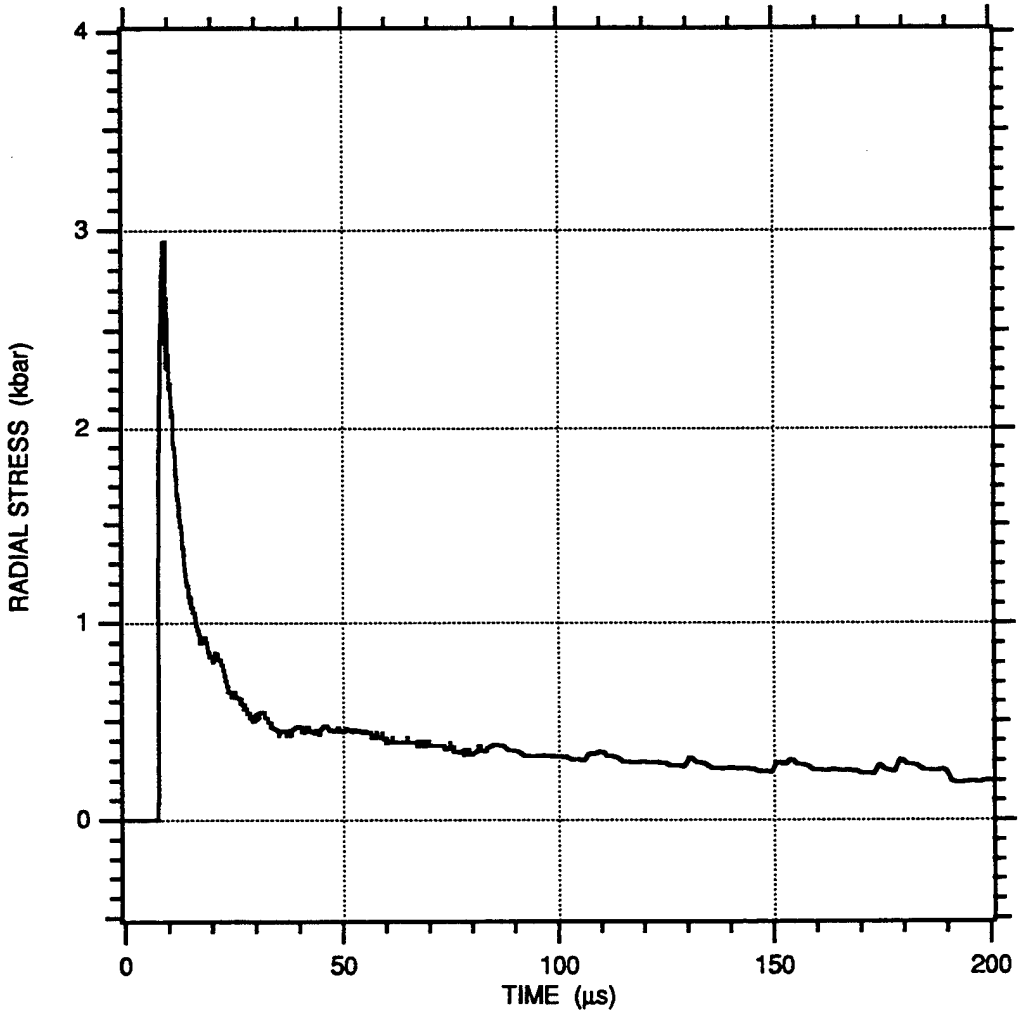

FIGURE A-2. RADIAL STRESS-TIME HISTORY MEASURED IN 100% SATURATED EGLIN BEACH SAND FOR A 3/8 g PETN EXPLOSIVE CHARGE AT A RANGE OF 2.34 cm (Gage 2)

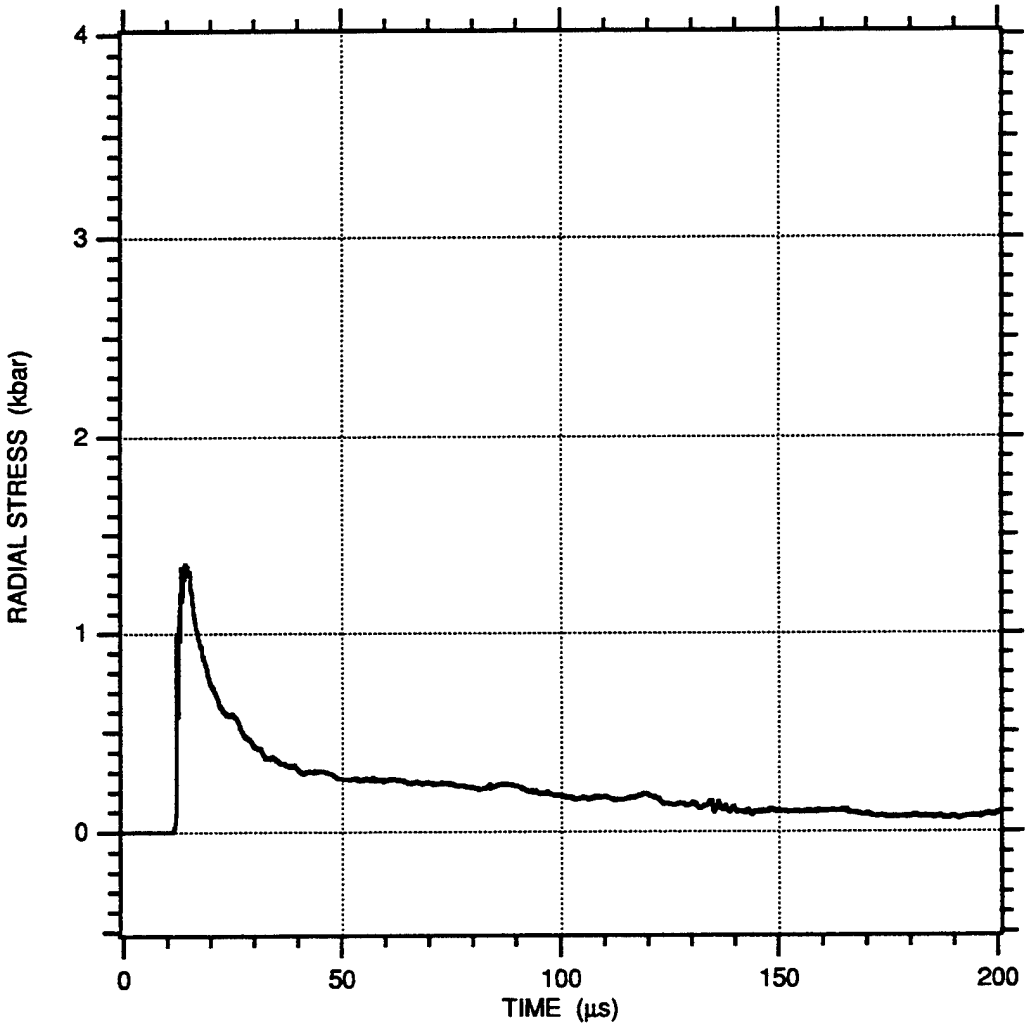

FIGURE A-3. RADIAL STRESS-TIME HISTORY MEASURED IN 100% SATURATED EGLIN BEACH SAND FOR A 3/8 g PETN EXPLOSIVE CHARGE AT A RANGE OF 3.25 cm

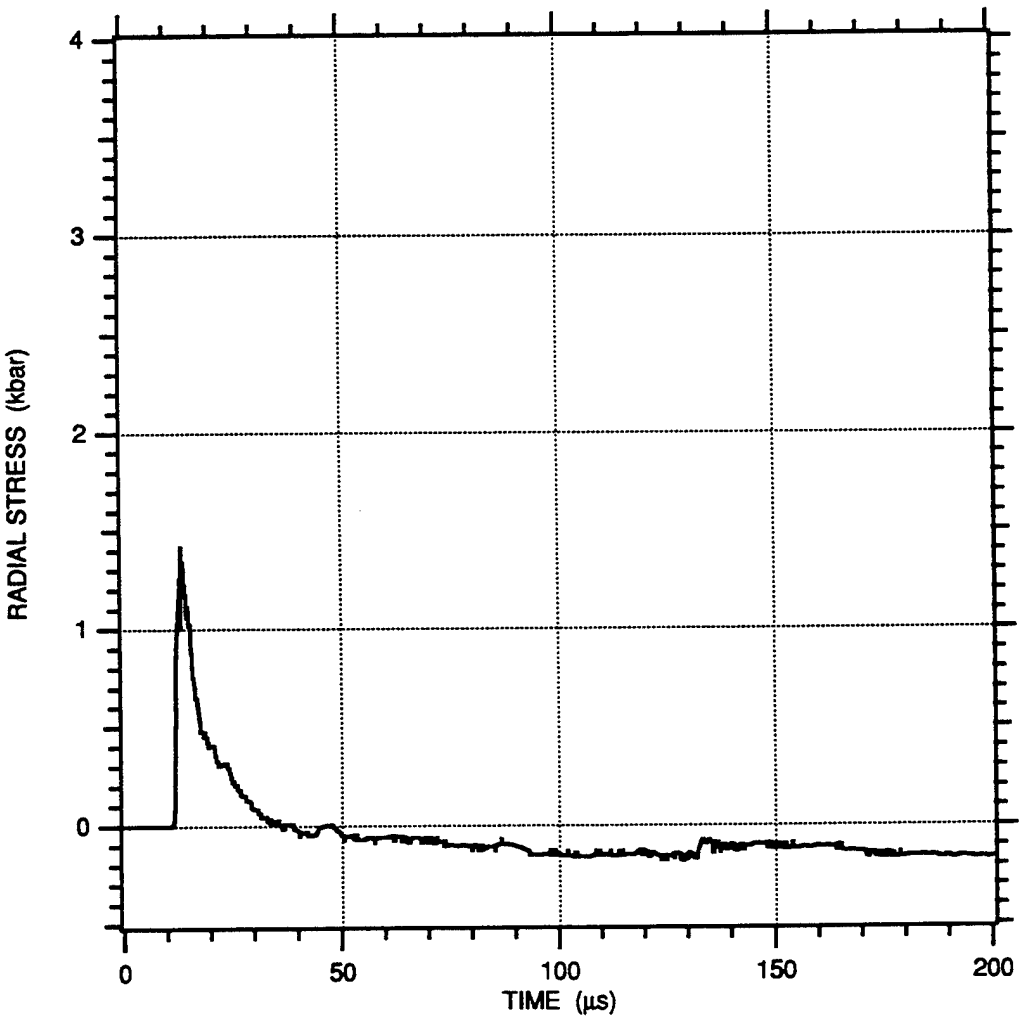

FIGURE A-4. RADIAL STRESS-TIME HISTORY MEASURED IN 100% SATURATED EGLIN BEACH SAND FOR A 3/8 g PETN EXPLOSIVE CHARGE AT A RANGE OF 3.26 cm

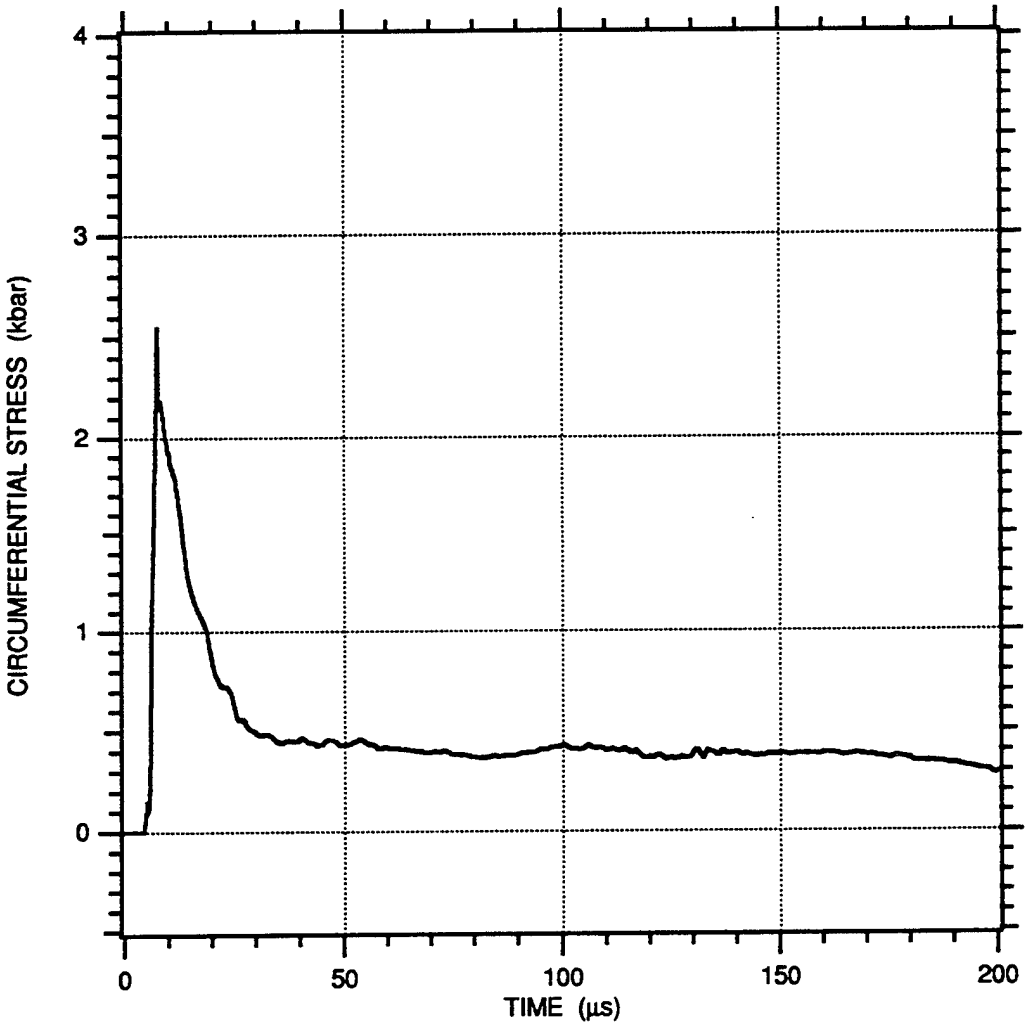

FIGURE A-5. CIRCUMFERENTIAL STRESS-TIME HISTORY MEASURED IN 100% SATURATED EGLIN BEACH SAND FOR A 3/8 g PETN EXPLOSIVE CHARGE AT A RANGE OF 1.97 cm

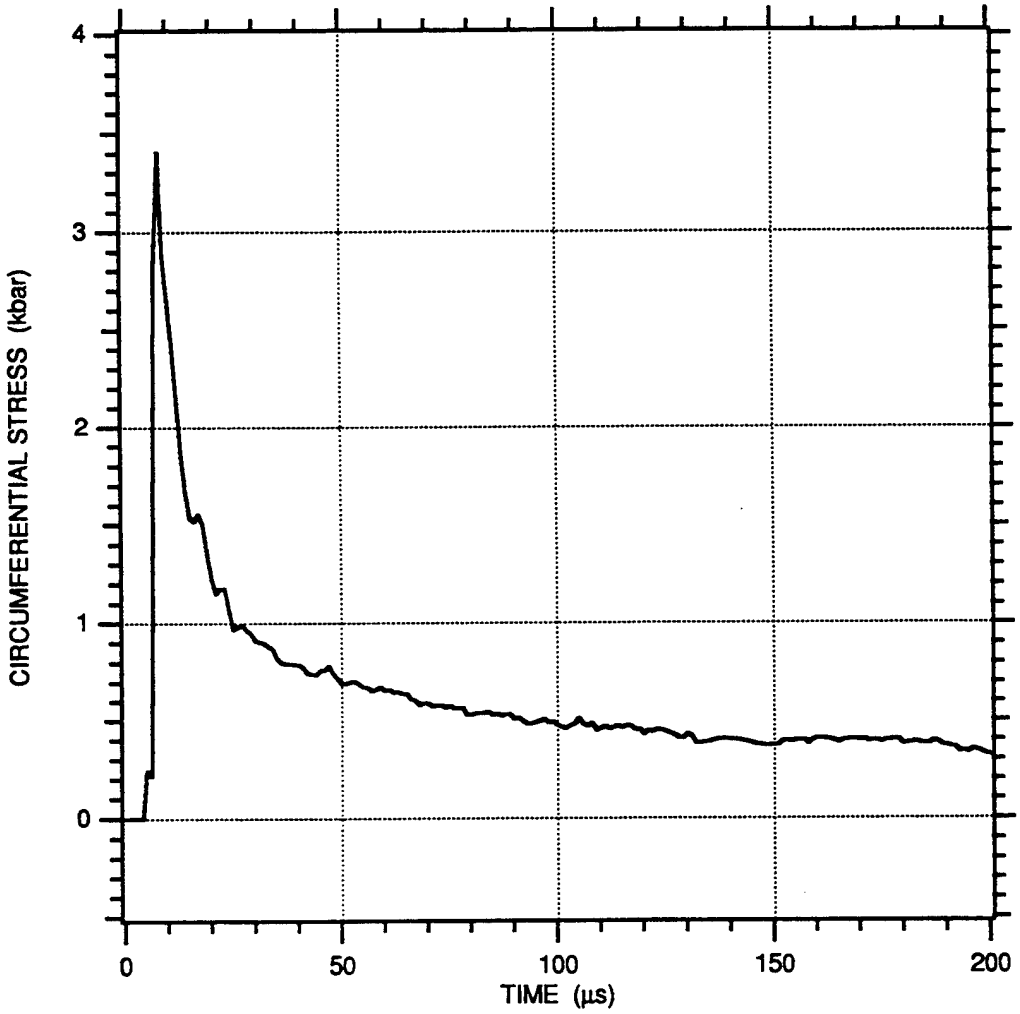

FIGURE A-6. CIRCUMFERENTIAL STRESS-TIME HISTORY MEASURED IN 100% SATURATED EGLIN BEACH SAND FOR A 3/8 g PETN EXPLOSIVE CHARGE AT A RANGE OF 2.53 cm

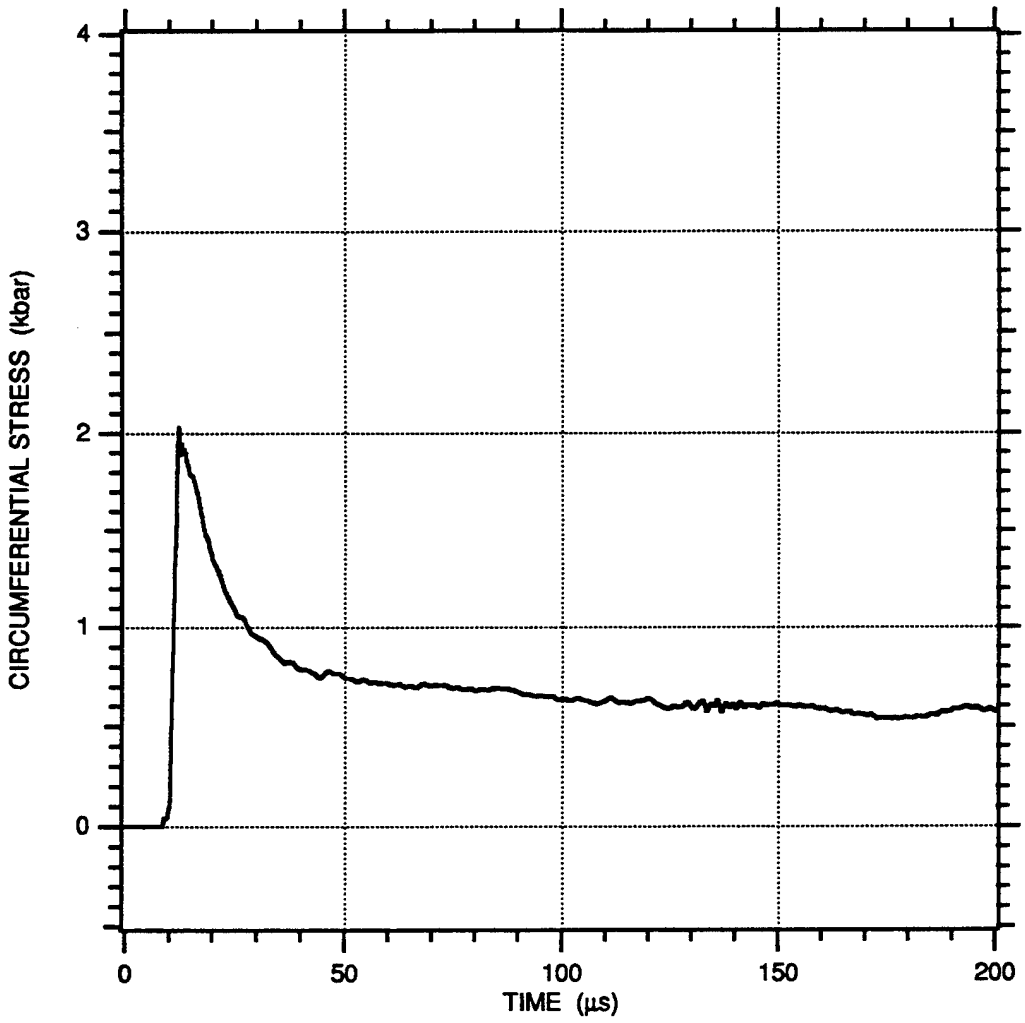

FIGURE A-7. CIRCUMFERENTIAL STRESS-TIME HISTORY MEASURED IN 100% SATURATED EGLIN BEACH SAND FOR A 3/8 g PETN EXPLOSIVE CHARGE AT A RANGE OF 3.00 cm

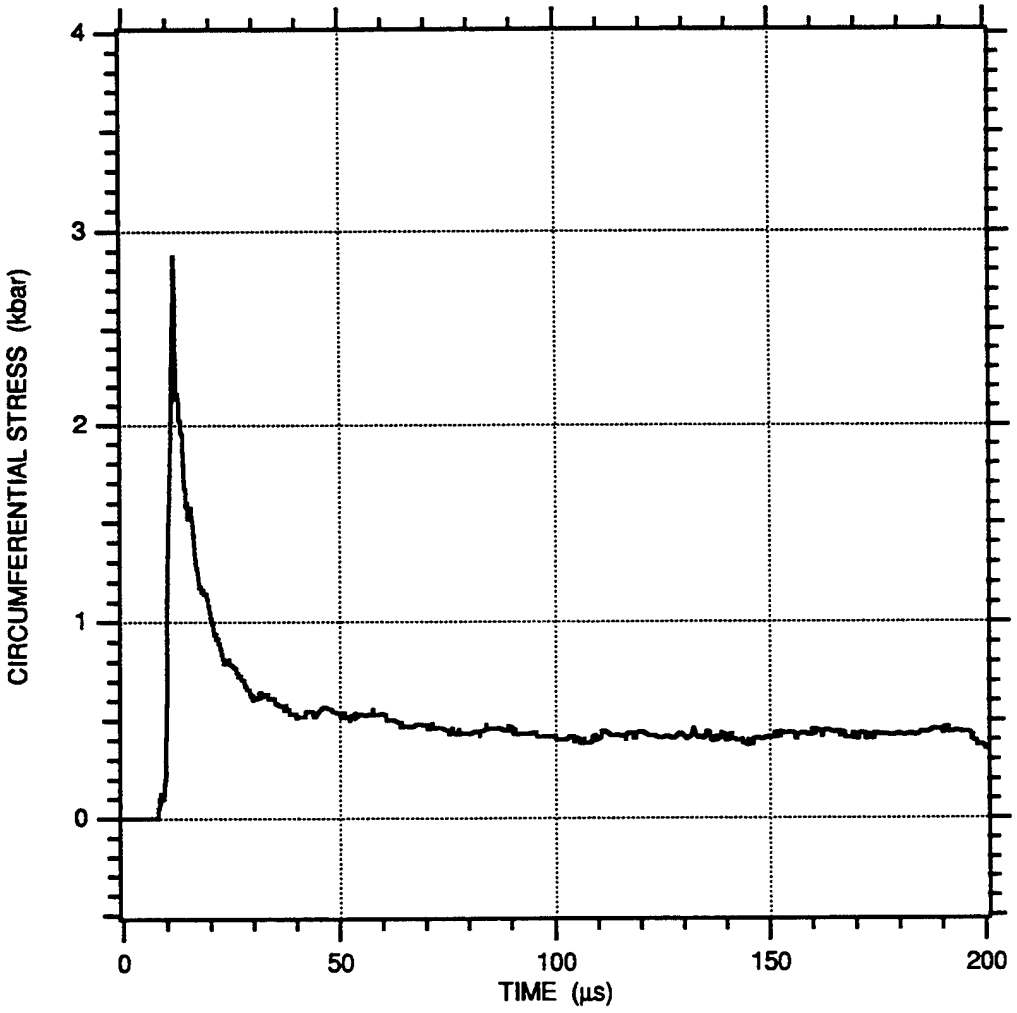

FIGURE A-8. CIRCUMFERENTIAL STRESS-TIME HISTORY MEASURED IN 100% SATURATED EGLIN BEACH SAND FOR A 3/8 g PETN EXPLOSIVE CHARGE AT A RANGE OF 2.978 cm

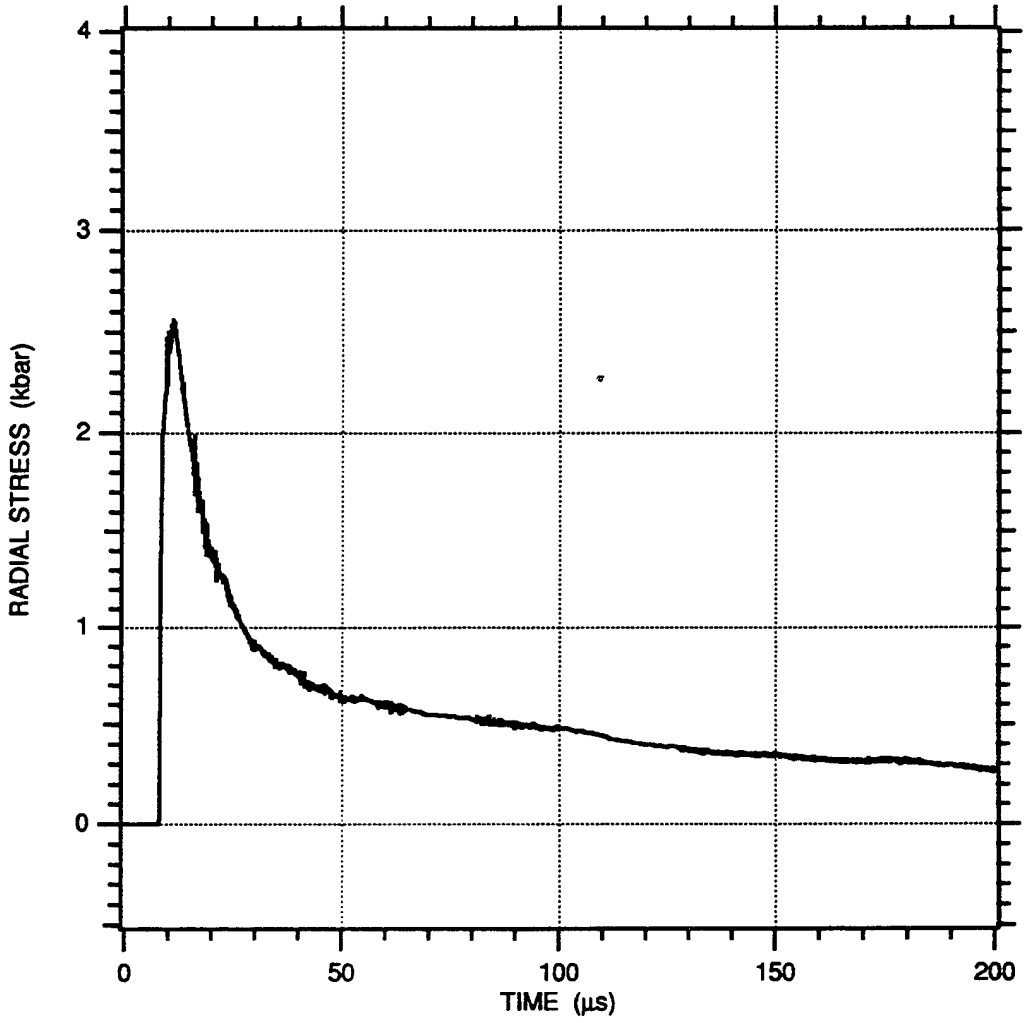

FIGURE A-9. RADIAL STRESS-TIME HISTORY MEASURED IN 95% SATURATED EGLIN BEACH SAND FOR A 3/8 g PETN EXPLOSIVE CHARGE AT A RANGE OF 2.308 cm

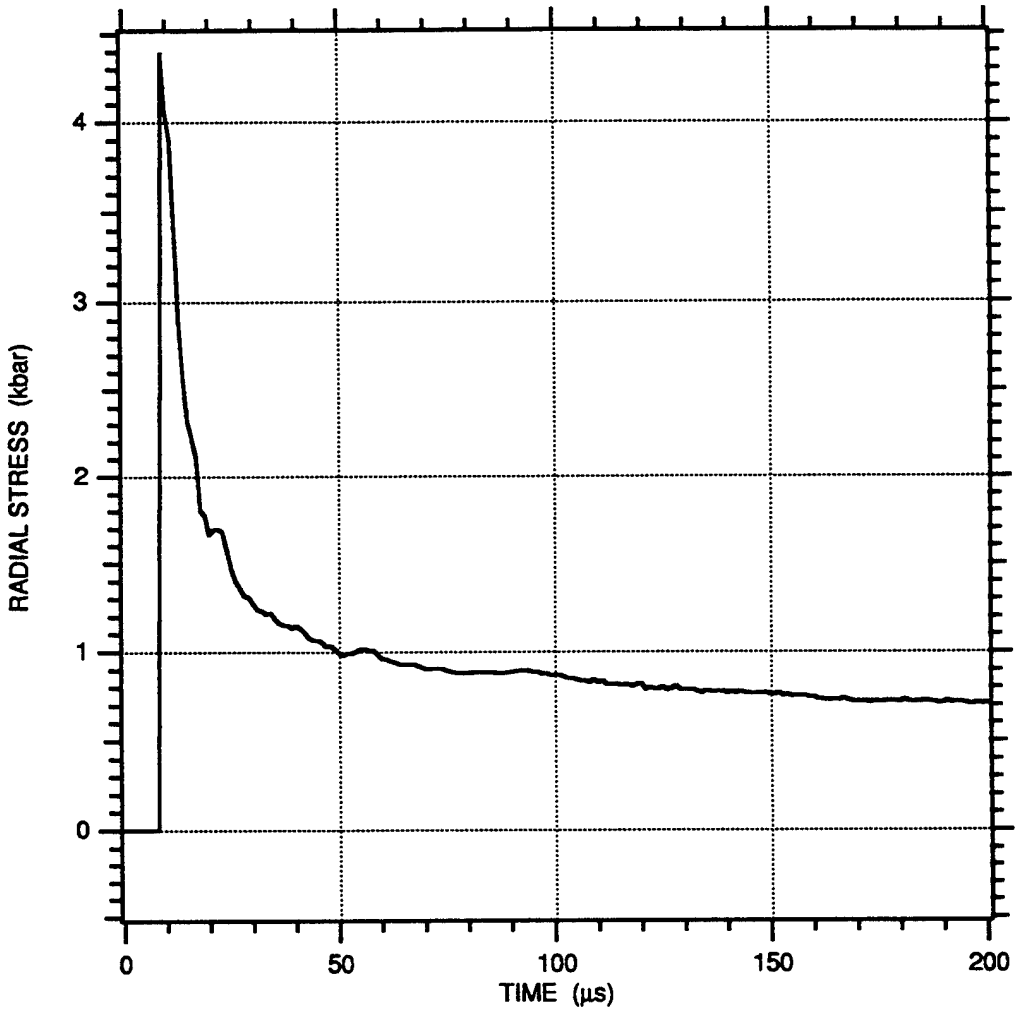

FIGURE A-10. RADIAL STRESS-TIME HISTORY MEASURED IN 95% SATURATED EGLIN BEACH SAND FOR A 3/8 g PETN EXPLOSIVE CHARGE AT A RANGE OF 2.35 cm

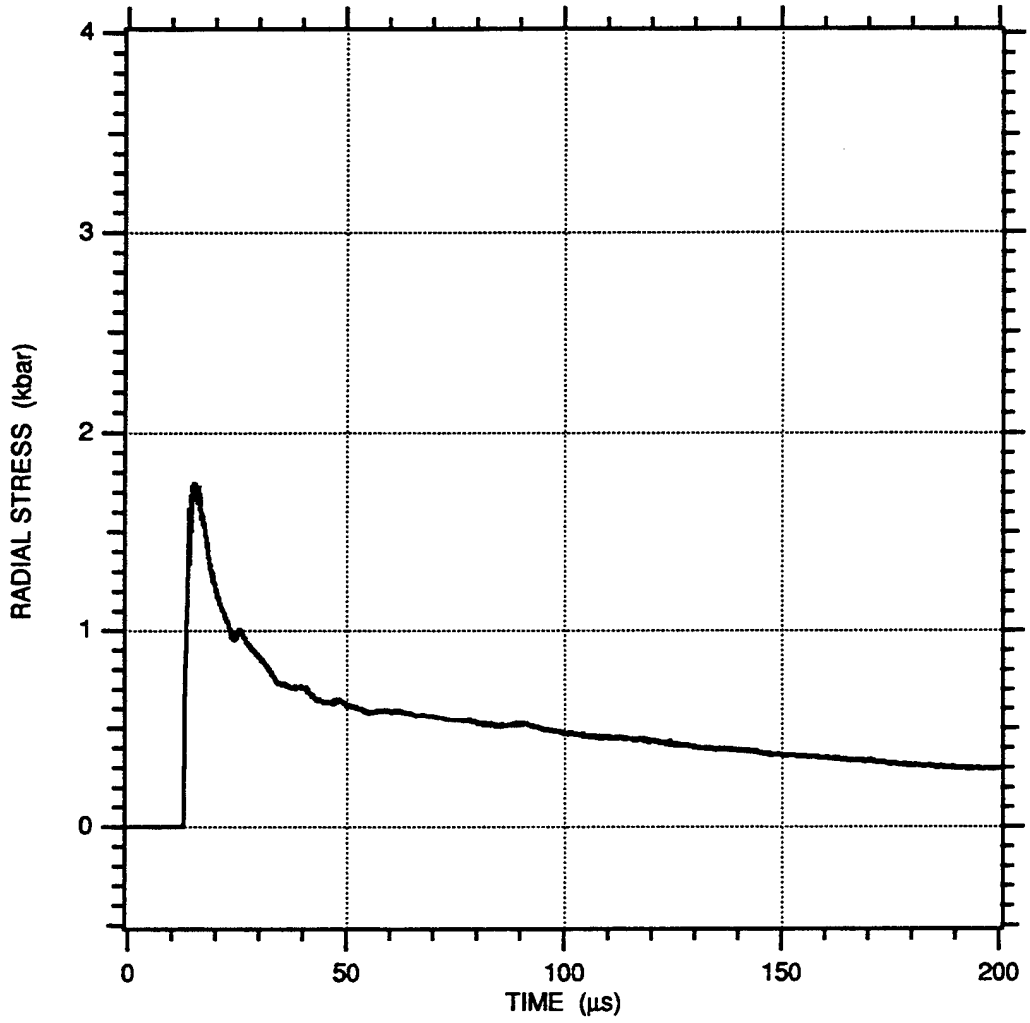

FIGURE A-11. RADIAL STRESS-TIME HISTORY MEASURED IN 95% SATURATED EGLIN BEACH SAND FOR A 3/8 g PETN EXPLOSIVE CHARGE AT A RANGE OF 3.308 cm

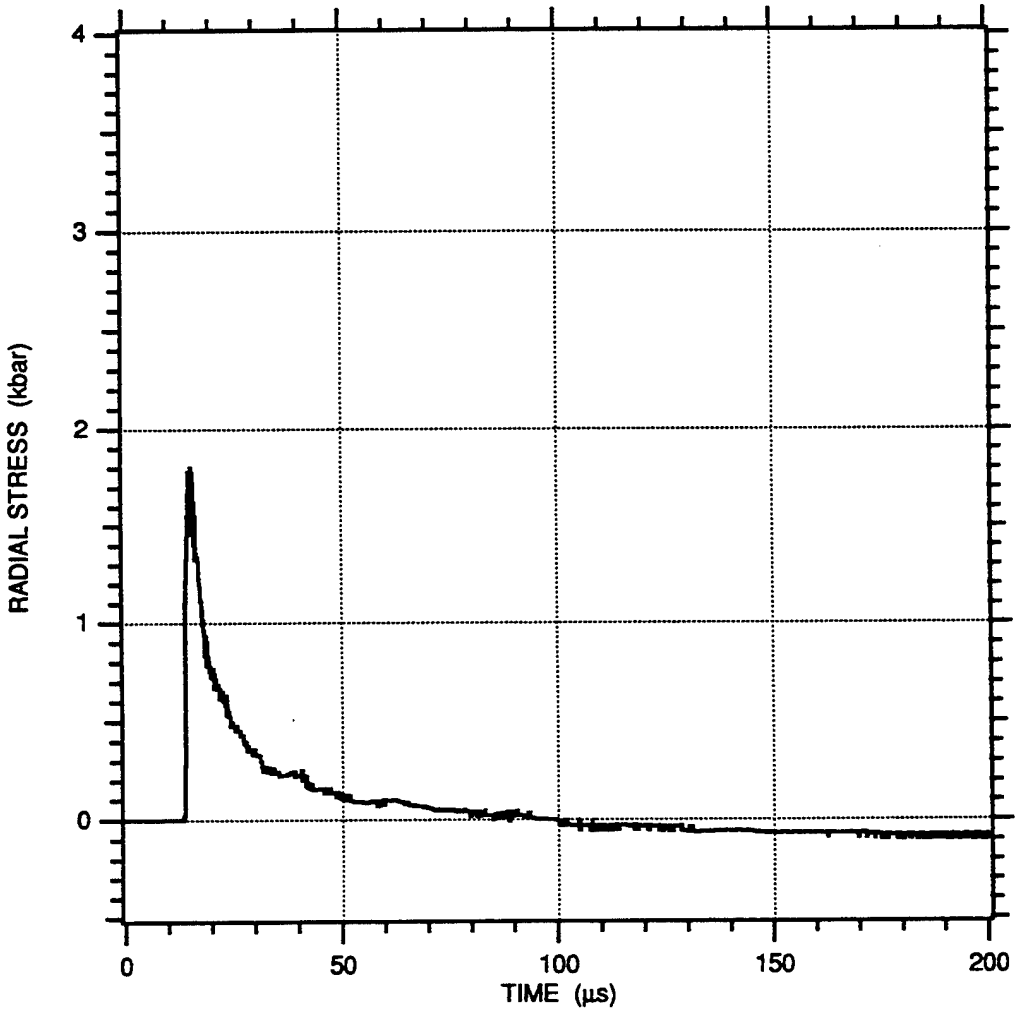

FIGURE A-12. RADIAL STRESS-TIME HISTORY MEASURED IN 95% SATURATED EGLIN BEACH SAND FOR A 3/8 g PETN EXPLOSIVE CHARGE AT A RANGE OF 3.45 cm

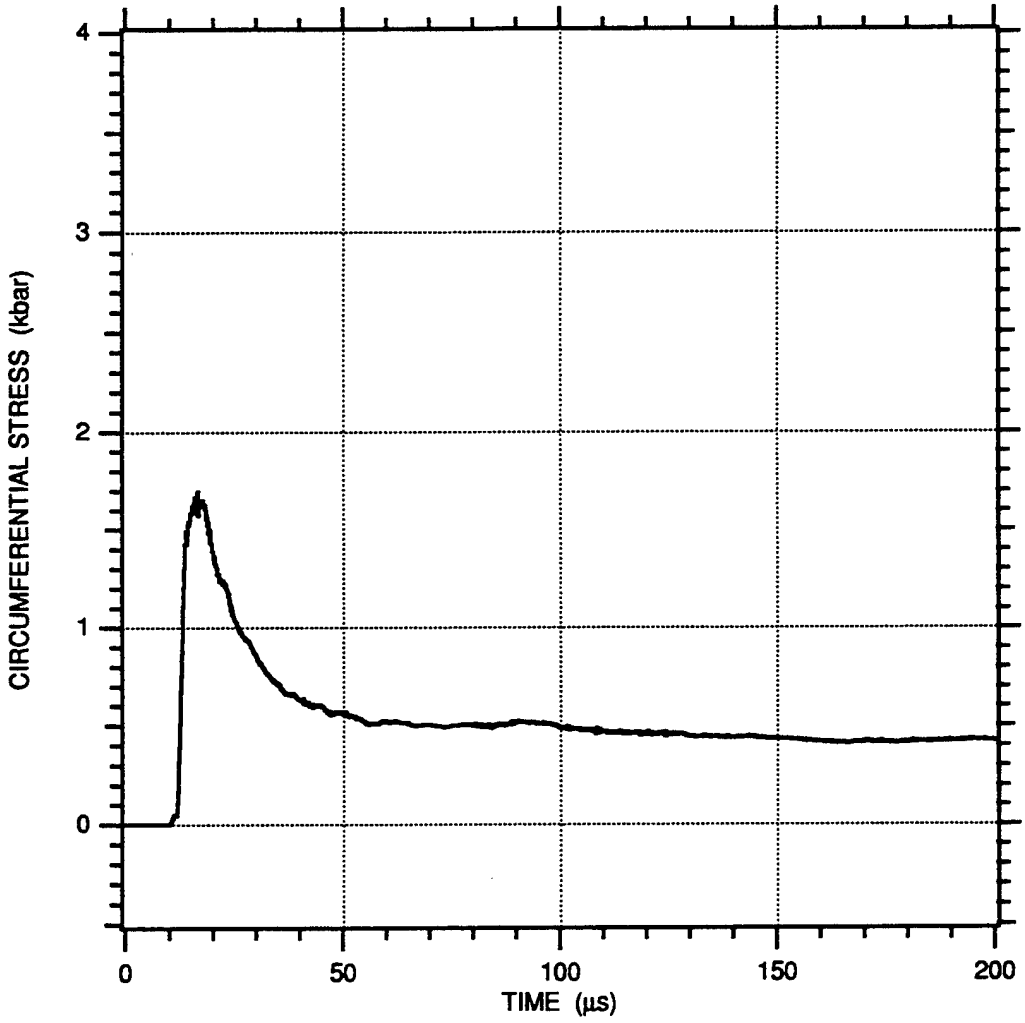

FIGURE A-13. CIRCUMFERENTIAL STRESS-TIME HISTORY MEASURED IN 95% SATURATED EGLIN BEACH SAND FOR A 3/8 g PETN EXPLOSIVE CHARGE AT A RANGE OF 3.224 cm

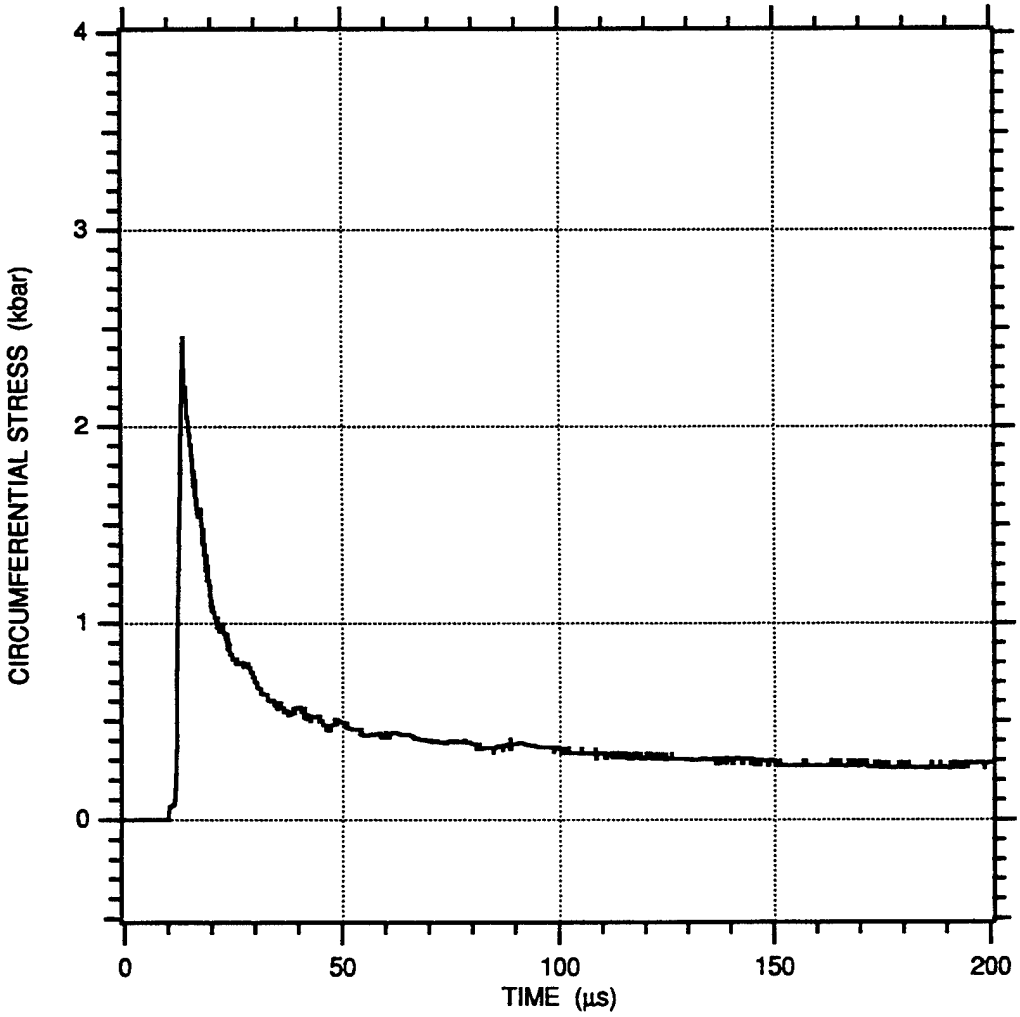

FIGURE A-14. CIRCUMFERENTIAL STRESS-TIME HISTORY MEASURED IN 95% SATURATED EGLIN BEACH SAND FOR A 3/8 g PETN EXPLOSIVE CHARGE AT A RANGE OF 3.212 cm

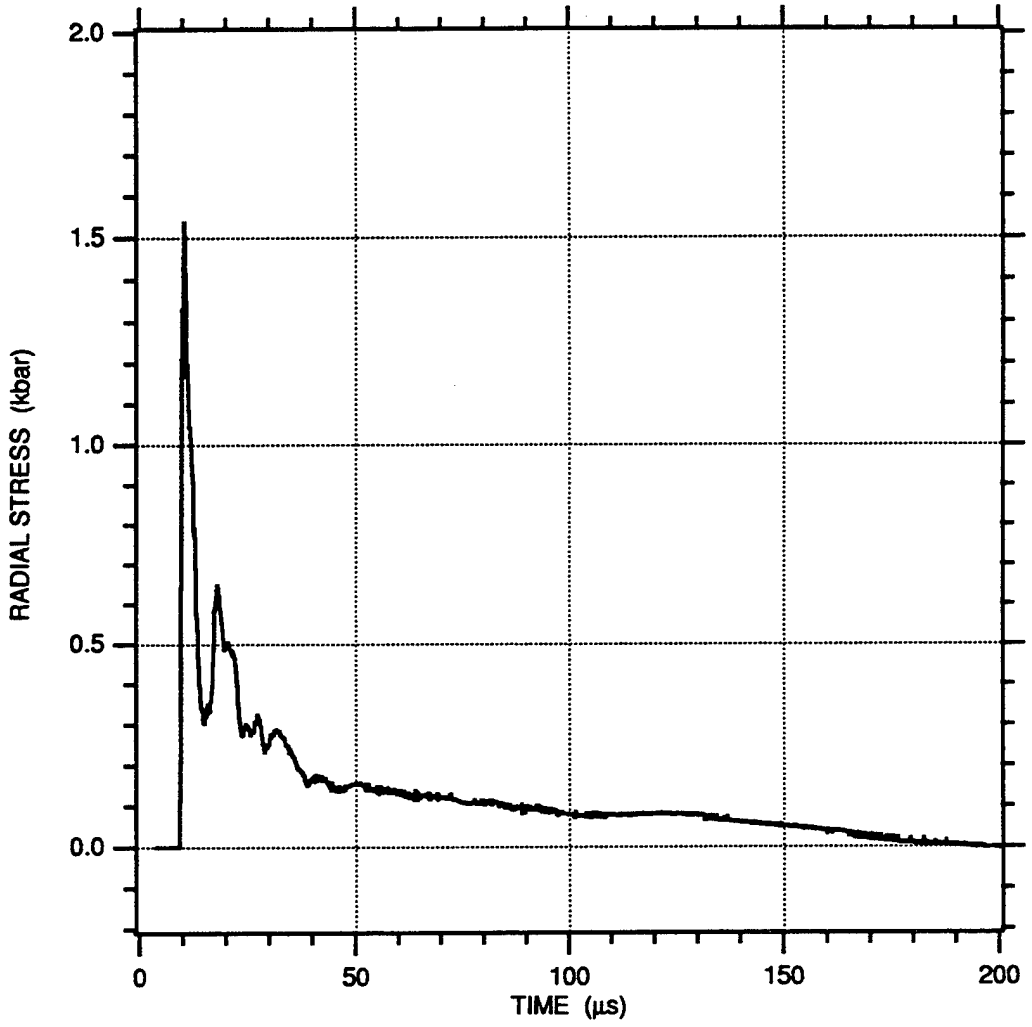

FIGURE A-15. RADIAL STRESS-TIME HISTORY MEASURED IN 78% SATURATED EGLIN BEACH SAND FOR A 3/8 g PETN EXPLOSIVE CHARGE AT A RANGE OF 1.87 cm

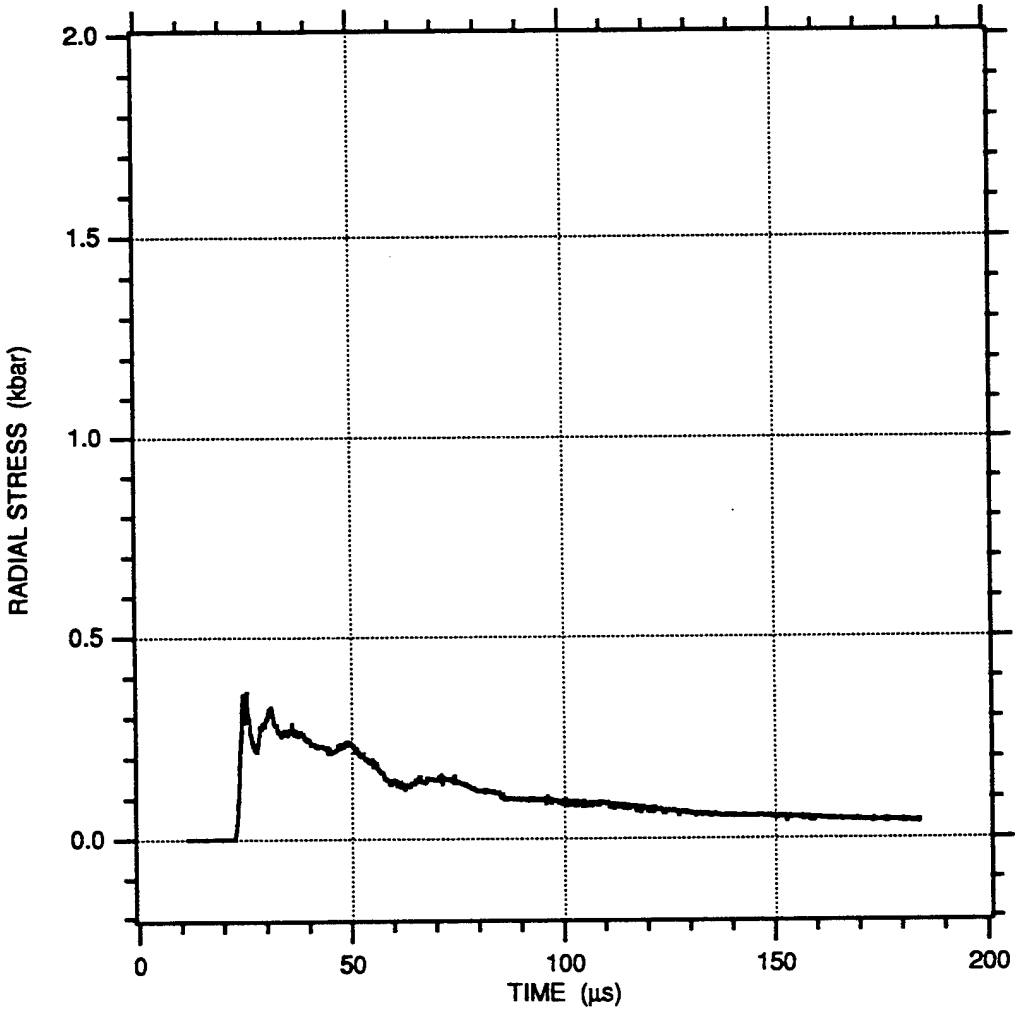

FIGURE A-16. RADIAL STRESS-TIME HISTORY MEASURED IN 78% SATURATED EGLIN BEACH SAND FOR A 3/8 g PETN EXPLOSIVE CHARGE AT A RANGE OF 3.05 cm

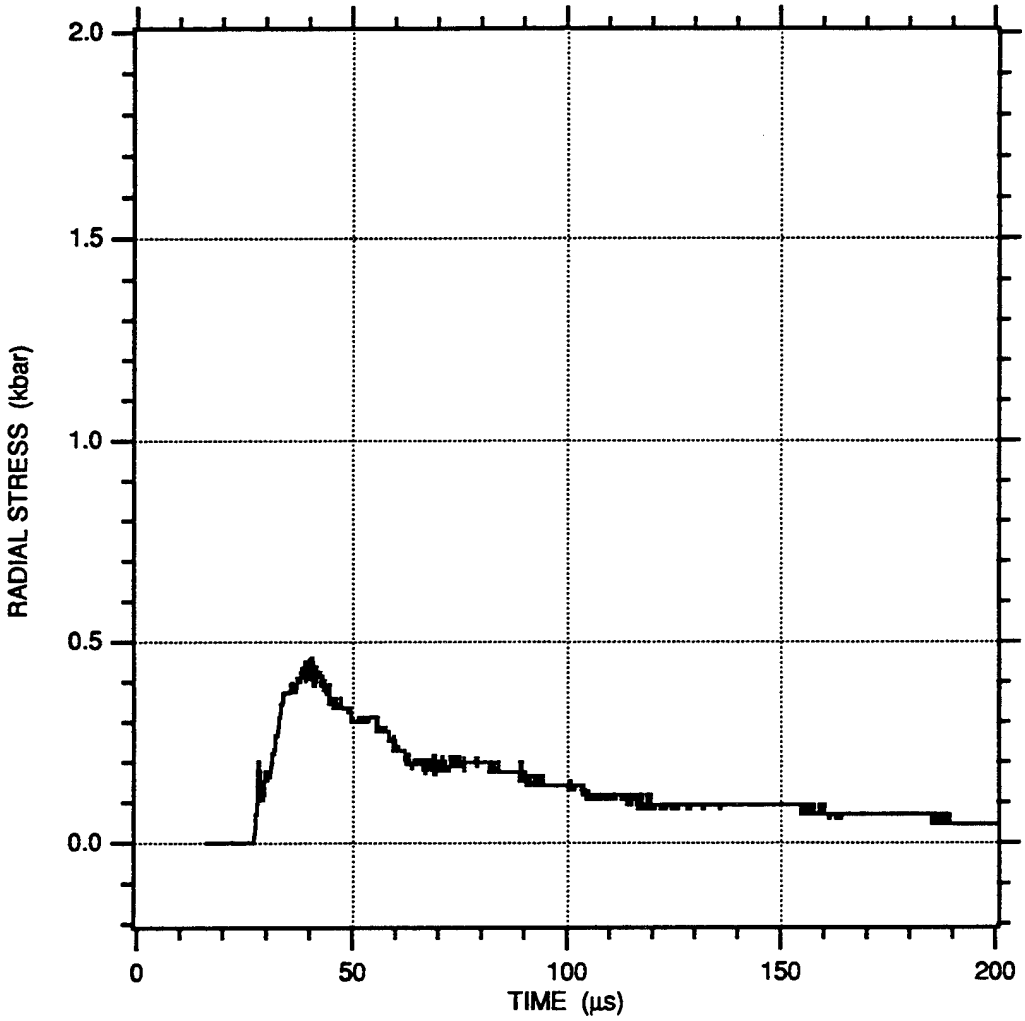

FIGURE A-17. RADIAL STRESS-TIME HISTORY MEASURED IN 78% SATURATED EGLIN BEACH SAND FOR A 3/8 g PETN EXPLOSIVE CHARGE AT A RANGE OF 3.29 cm

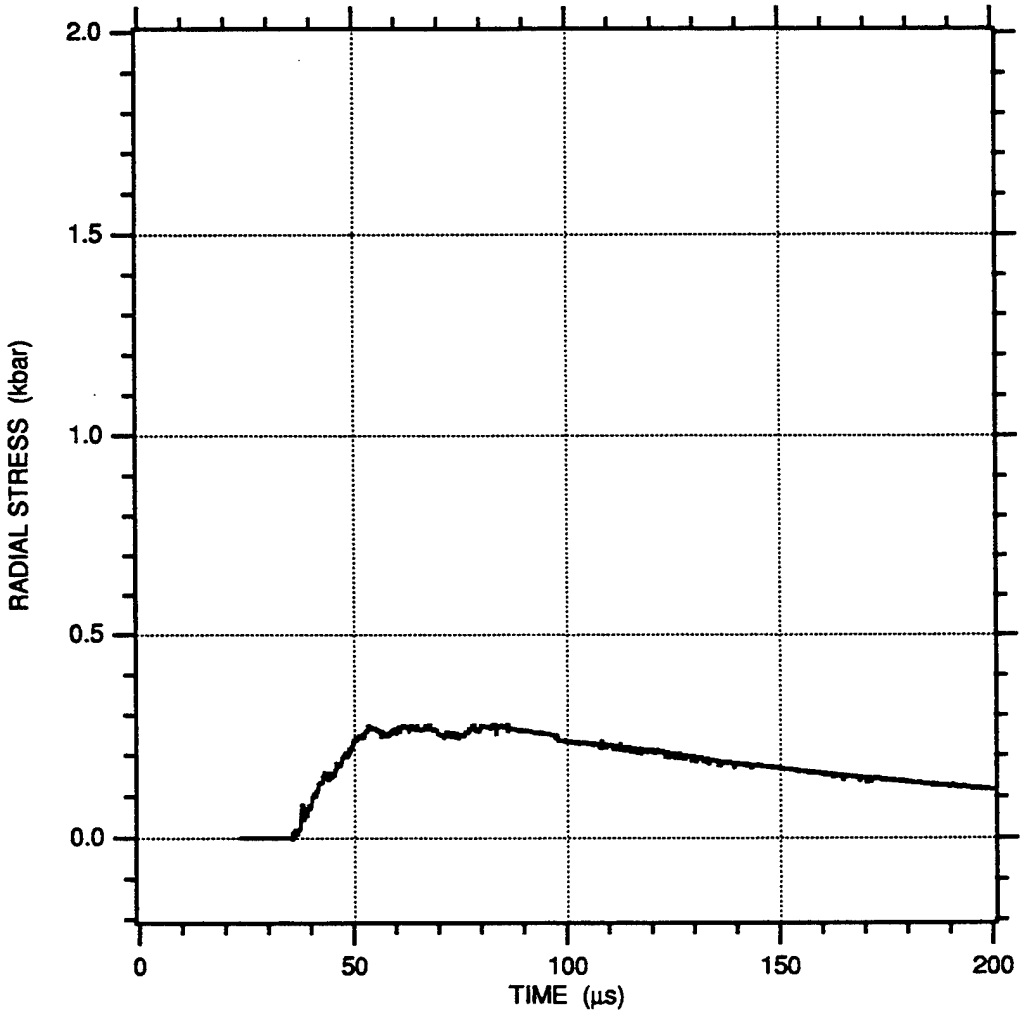

FIGURE A-18. RADIAL STRESS-TIME HISTORY MEASURED IN 78% SATURATED EGLIN BEACH SAND FOR A 3/8 g PETN EXPLOSIVE CHARGE AT A RANGE OF 3.59 cm

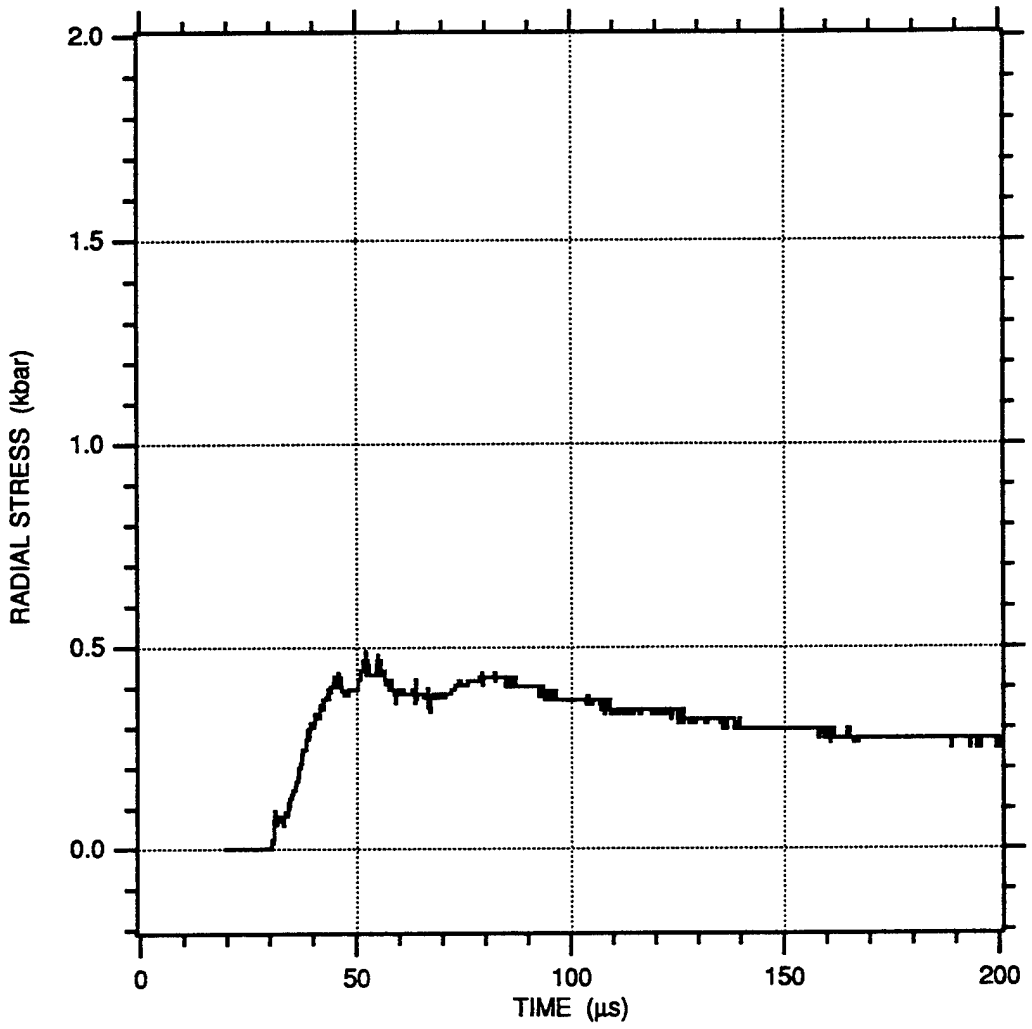

FIGURE A-19. RADIAL STRESS-TIME HISTORY MEASURED IN 78% SATURATED EGLIN BEACH SAND FOR A 3/8 g PETN EXPLOSIVE CHARGE AT A RANGE OF 3.44 cm

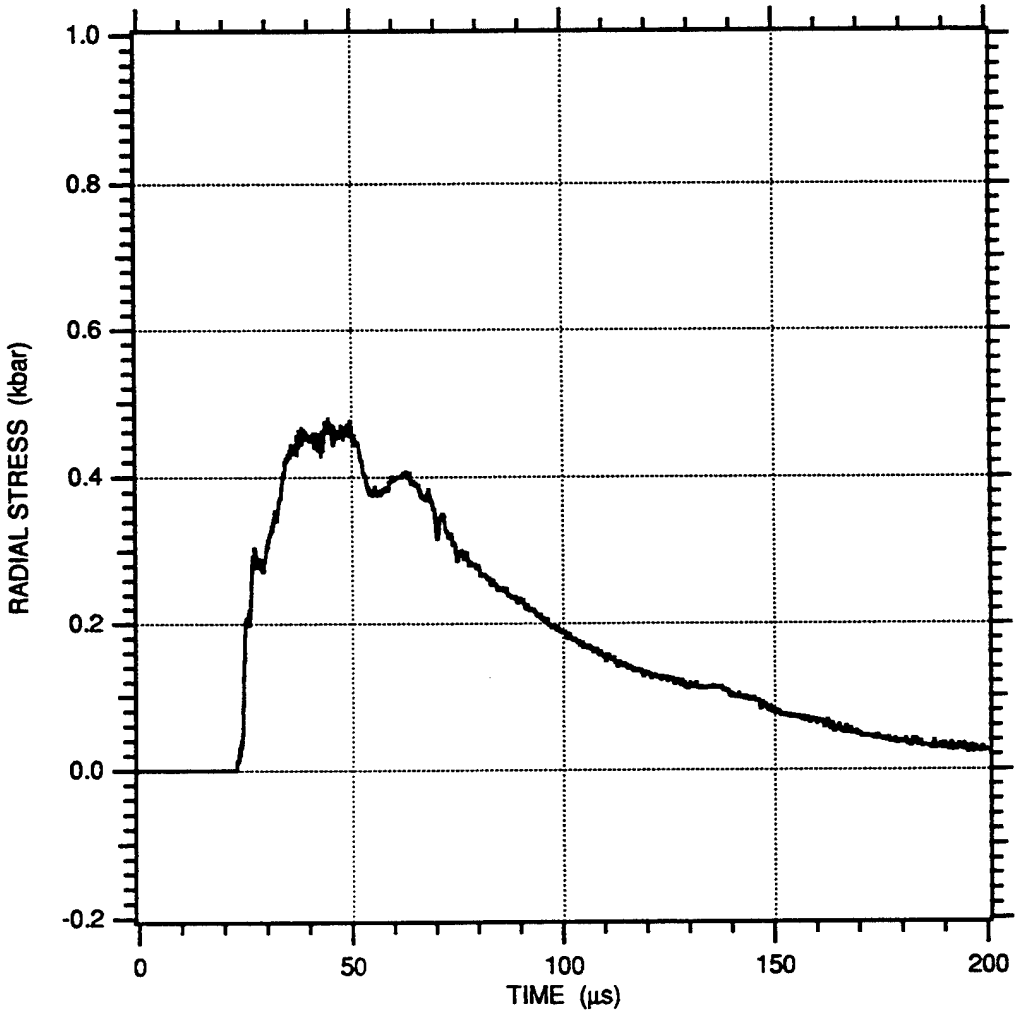

FIGURE A-20. RADIAL STRESS-TIME HISTORY MEASURED IN 77% SATURATED EGLIN BEACH SAND FOR A 3/8 g PETN EXPLOSIVE CHARGE AT A RANGE OF 3.376 cm

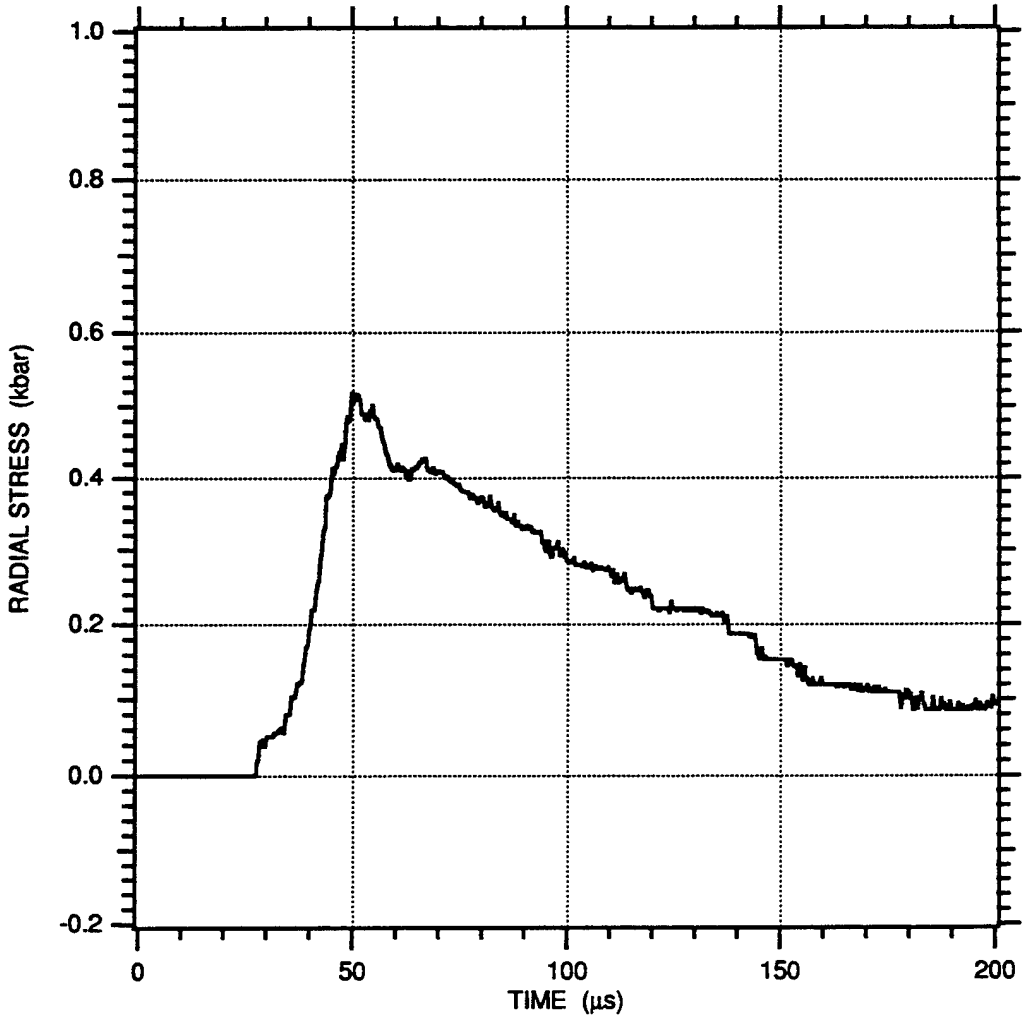

FIGURE A-21. RADIAL STRESS-TIME HISTORY MEASURED IN 77% SATURATED EGLIN BEACH SAND FOR A 3/8 g PETN EXPLOSIVE CHARGE AT A RANGE OF 3.638 cm

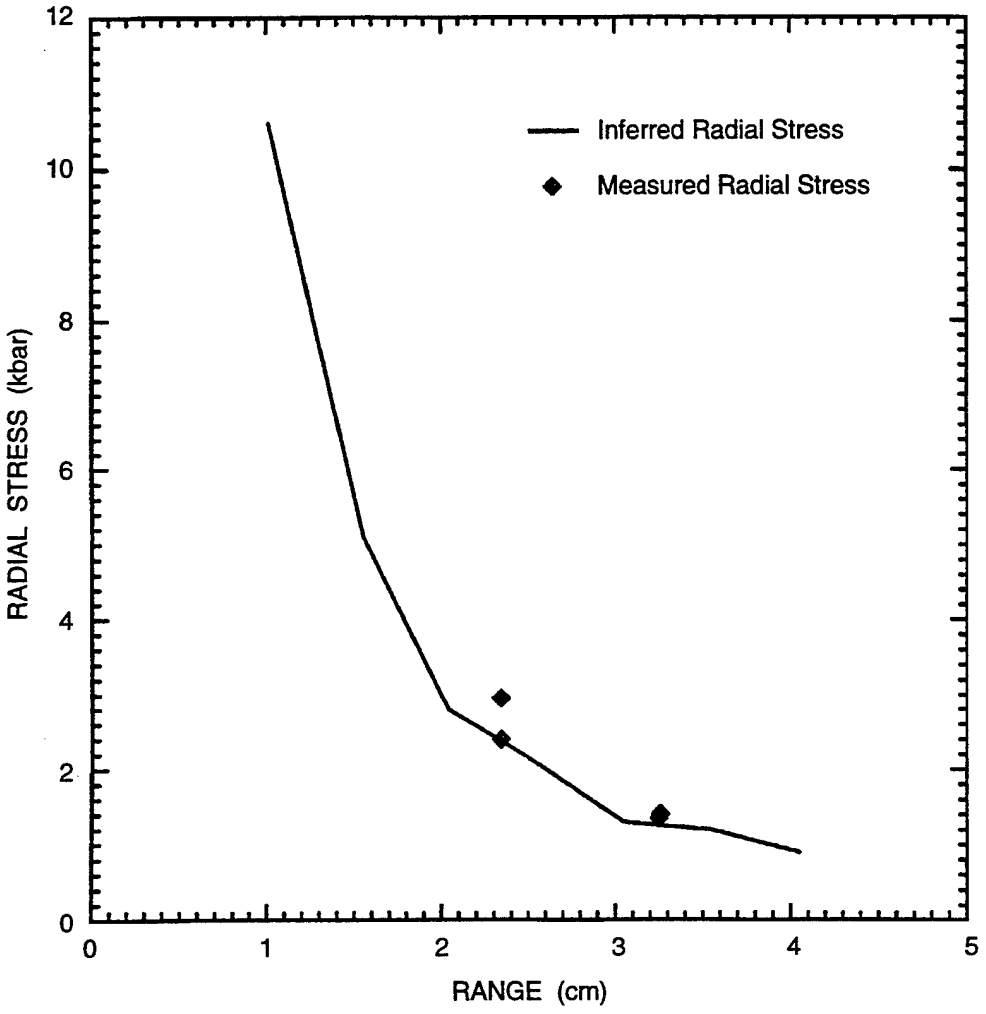

FIGURE A-22. COMPARISON BETWEEN INFERRED RADIAL STRESS FROM PEAK PARTICLE VELOCITY AND MEASURED RADIAL STRESS IN 100% SATURATED EGLIN BEACH SAND.

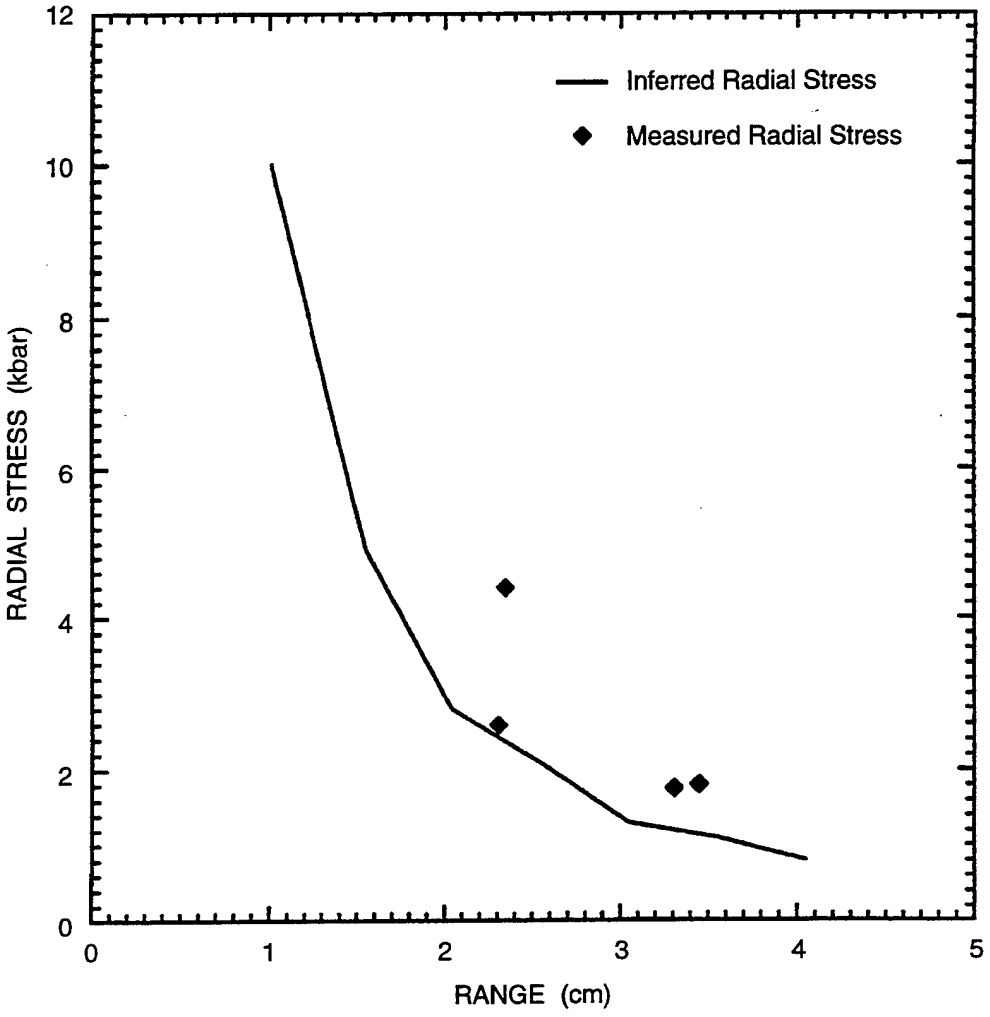

FIGURE A-23. COMPARISON BETWEEN INFERRED RADIAL STRESS FROM PEAK PARTICLE VELOCITY AND MEASURED RADIAL STRESS IN 95% SATURATED EGLIN BEACH SAND.

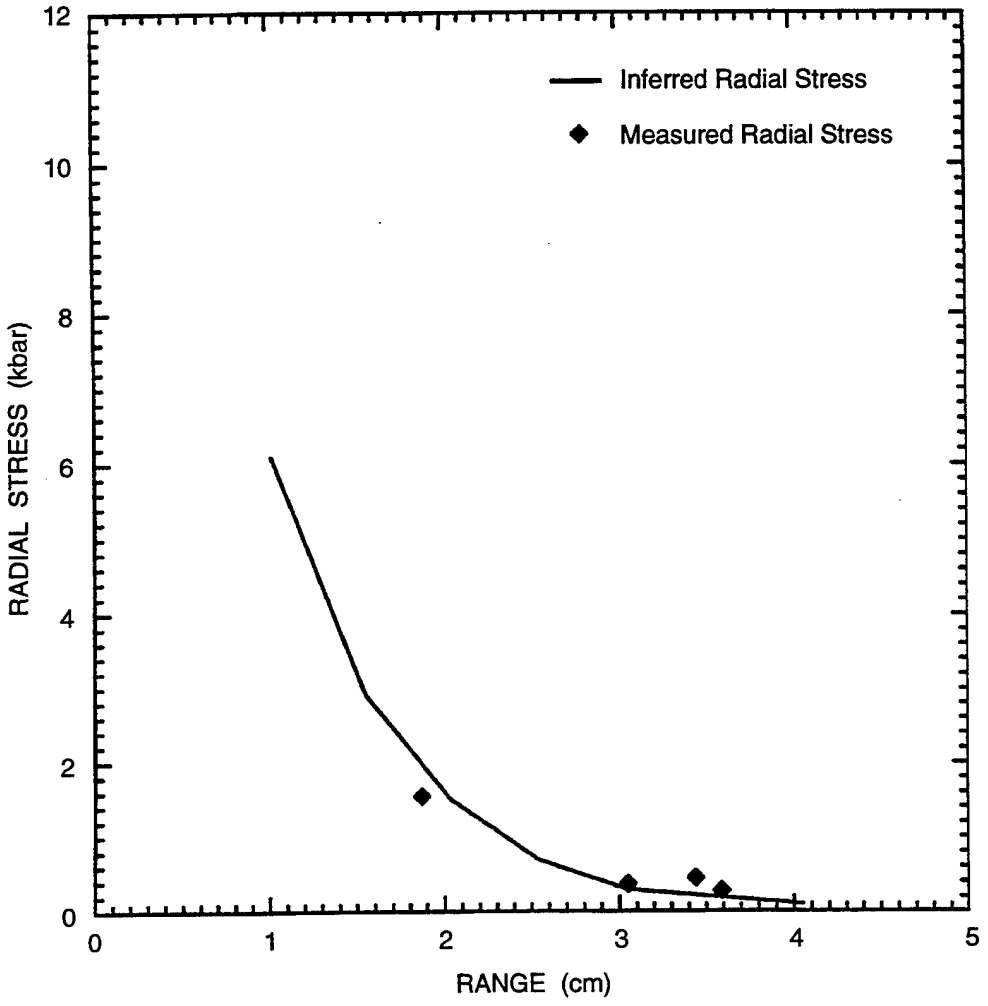

FIGURE A-24. COMPARISON BETWEEN INFERRED RADIAL STRESS FROM PEAK PARTICLE VELOCITY AND MEASURED RADIAL STRESS IN 78% SATURATED EGLIN BEACH SAND.

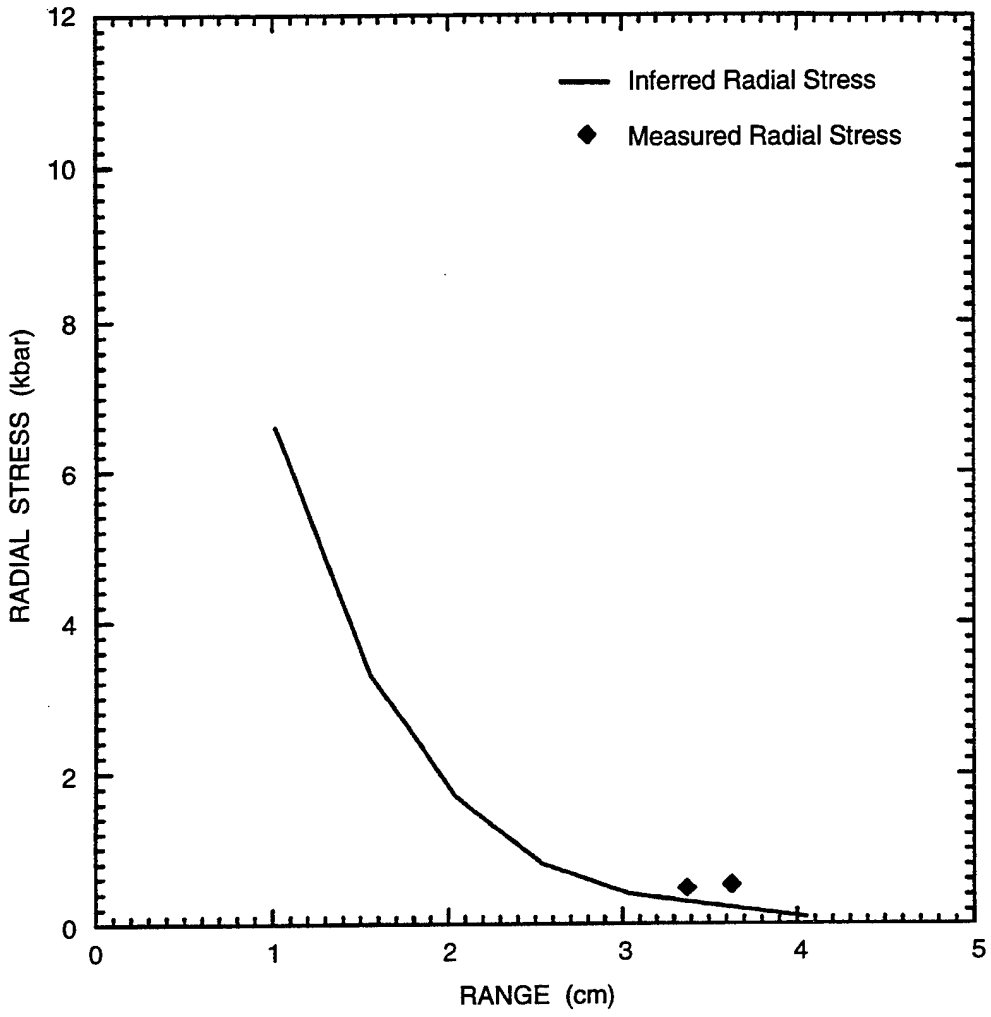

FIGURE A-25. COMPARISON BETWEEN INFERRED RADIAL STRESS FROM PEAK PARTICLE VELOCITY AND MEASURED RADIAL STRESS IN 77% SATURATED EGLIN BEACH SAND.

APPENDIX B

SPHERICAL WAVE EQUATIONS

An outline of the treatment of spherical waves is provided here to show how the experimental data are processed and interpreted. The data consist of radial particle velocities at several ranges. Radial displacements are obtained by temporal integration of the particle velocity-time histories. Below we show how we obtain the radial, circumferential, and volumetric engineering strains.

The radial strain is calculated using

$$\varepsilon_r = \{d_i - d_{i+1}\} / (a_i - a_{i+1}) \times 100$$

The circumferential strain is calculated using

$$\varepsilon_\theta = -0.5\{d_i / a_i + d_{i+1} / a_{i+1}\} \times 100$$

The volumetric strain is calculated using

$$\varepsilon_v = \left\{\left[(a_{i+1} + d_{i+1})^3 - (a_i + d_i)^3\right] - \left(a_{i+1}^3 - a_i^3\right)\right\} / \left(a_{i+1}^3 - a_i^3\right) \times 100$$

In these equations, d_i is the displacement obtained through temporal integration of the particle velocity records, a_i is the range, and i is the gage number.

APPENDIX C

ERROR ANALYSIS FOR EXPERIMENTAL MEASUREMENTS

An outline of the error analysis performed on the experimental measurements is provided here. The final error associated with a particular measurement may be a direct error or an indirect error. Direct errors are strictly associated with the measurement type. For example, for weight measurements a direct error is associated with the manufacturer's specified scale accuracy. Indirect errors are the accumulation of other direct or indirect errors. For example, the error associated with density is an indirect error when it is obtained through determining the direct errors associated with the mass and volume used to determine the density. Below, we give our error analysis for the experimental measurements associated with sand model fabrication and particle velocity measurements.

SAND MODEL PREPARATION AND CHARACTERIZATION

Table C-1 summarizes the direct errors associated with sand model preparation and characterization.

Table C-1. DIRECT ERROR VALUES FOR SAND MODEL PREPARATION AND CHARACTERIZATION MEASUREMENT TYPE

Measurement Type	Error
Sand Model Container Volume	$\pm 30.198\ cm^3$
Sample Cup Container Volume	$\pm 0.025\ cm^3$
Core Container Volume	$\pm 0.248\ cm^3$
NCI 3825 70 kg Scale (for bulk measurements)	± 23 g
Mettler PC 6000 Scale (for sample cup measurements)	± 0.1 g
Mettler PC 2000 Scale (for core measurements)	± 0.01 g

Bulk Measurements

To estimate the bulk, dry density, indirect error we used the direct error values for sand volume and mass measurements associated with the dry density. The dry sand volume error is the sum of the container volume error and the actual sand volume error. The container volume error

was estimated from the design fabrication tolerances and is ± 30.198 cm^3. The actual sand volume error is the difference between the actual sand volume and the container volume. This error is primarily associated with the difference between the height of the free sand surface and the top edge of the container. This difference could be equivalent to the average grain size diameter of 0.040 cm. Multiplying the average grain size diameter by the container volume surface area gives an error of ± 20.782 cm^3. Thus, the dry sand volume error is ± 50.980 cm^3. The sand mass error is associated with having to make two measurements with the NCI 3825 scale, which gives a direct error of ± 46 g. Considering that the maximum error is for the case where there are opposite trends between sand volume error and sand mass error, the indirect error equation for the sand dry density becomes

$$(26209 \text{ g} \pm 46 \text{ g})/(15836.096 \text{ cm}^3 \mp 50.980 \text{ cm}^3) - 1.655 \text{ g/cm}^3 = \pm 0.008 \text{ g/cm}^3 \quad \text{(C.1)}$$

where 26209 g is the measured bulk sand mass and 15836.096 cm^3 is the bulk sand volume. The sand saturated density indirect error is obtained by adding to the numerator of Equation (C.1) the bulk water mass (5957 g) and associated direct error (± 23 g) and substituting the saturated density of 2.031 g/cm^3 for the dry density of 1.655 g/cm^3, which gives an error of ± 0.011 g/cm^3.

To estimate the bulk saturation indirect error, we first estimate the porosity indirect error by dividing the dry density sand error by the grain density (because the standard deviation from 20 grain density measurements was 0.0004 g/cm^3, we have neglected the grain density direct error), which gives ± 0.302 %. The porosity error is multiplied by the sand volume (15836.096 + 50.302 = 15886.398 cm^3) to obtain the possible water volume error of ± 47.977 cm^3 for 100% saturated sand. Assuming a water density of 1.000 g/cm^3, the water mass error is ± 47.977 g. The measured error is the scale accuracy of ± 23 g. For a nominal, 100% saturated, bulk water mass of 5957 g, the maximum error occurs for opposite trends between measured and calculated water masses and is represented by the equation

$$(5957 \text{ g} \pm 23 \text{ g})/(5957 \text{ g} \mp 47.977 \text{ g}) - 1 = \pm 1\% \quad \text{(C.2)}$$

Sample Cup and Core Measurements

The error bars for the sample cup and core measurements are determined in the same manner as for the bulk measurements described above. For the sample cup (2.540 ± 0.002 cm diameter by $2.540 + 0.001$ cm long), the container volume direct error is ± 0.025 cm^3 and the actual sand volume direct error is ± 0.203 cm^3, giving a dry sand volume direct error of ± 0.228 cm^3. The Mettler PC 6000 scale was used to measure the dry sand mass. Because two measurements are required to determine the dry sand mass, the direct error is ± 0.2 g. Combining

these values with the nominal sand volume and mass values, and considering that the maximum error occurs for opposite trends between the sand volume error and the sand mass error, the indirect error equation for the dry density is

$$(21.40\ g \pm 0.2\ g)/(12.870\ cm^3 \mp 0.228\ cm^3) - 1.663 = \pm 0.045\ g/cm^3 \qquad (C.3)$$

where 21.40 g is the sample cup sand mass and 12.870 cm^3 is the sample cup sand volume. The sand saturated density indirect error is obtained by adding to the numerator of Equation (C.3) the water mass (4.9 g) and associated direct error ($\pm$0.1 g) and substituting the saturated density of 2.044 g/cm^3 for the dry density of 1.663 g/cm^3, which gives an error of $\pm$0.059 g/cm^3.

To estimate the bulk saturation indirect error, we first estimate the porosity indirect error by dividing the dry density sand error by the grain density, which gives $\pm$1.70 %. The porosity error is multiplied by the sand volume (12.870 + 0.223 = 13.093 cm^3) to obtain the possible water volume error of $\pm$0.223 cm^3 for 100% saturated sand. Assuming a water density of 1.000 g/cm^3, the water mass error is $\pm$0.223 g. The measured error is the scale accuracy of $\pm$0.1 g. For a nominal, 100% saturated, sand water mass of 4.9 g, the maximum error occurs for opposite trends between measured and calculated water masses and is represented by the equation

$$(4.9\ g \pm 0.1\ g)/(4.9\ g \mp 0.223\ g) - 1.0 = \pm 7\ \% \qquad (C.4)$$

Determination of the core (2.230 $\pm$ 0.025 cm diameter by 2.540 $\pm$ 0.006 cm long) measurement errors is similar to the determination of sample cup errors, except that the container volume direct error is 0.248 cm^3 (this is larger than for the sample cup, because the diameter tolerance for the manufactured tubing used is larger than for the machined diameter of the sample cup), the dry sand volume direct error is 0.312 cm^3 (this is larger than the diameter tolerance for the sample cup, because there are two free surfaces), and the mass direct error is 0. 01 g for each measurement (this is less than the sample cup, because the Mettler PC 2000 scale was used). Given these differences and the slight differences in nominal sand volume, sand mass, and water mass the indirect dry sand error is $\pm$0.091 g/cm^3, the saturated sand indirect error is $\pm$0.11 g/cm^3, the porosity indirect error is $\pm$3.43%, and the saturation indirect error is $\pm$10%.

INSTRUMENTATION

Particle Velocity Measurements

The particle velocity (u) indirect error is the product of direct errors associated with the gage length (l), magnetic field strength (B), and measured electromagnetic force (ε). The estimated

error associated with the gage radial location is estimated to be $\pm$ 0.05 cm. The magnetic field strength and measured electromagnetic force direct errors are both estimated to be negligible due to the sophistication of the instrumentation used to measure these quantities. Using the following governing equation for the particle velocity indirect error

$$\frac{(\varepsilon)/\{[B] \times [1 \pm 0.05(2\pi)]\}}{\varepsilon / B\ell} = \pm \text{Error}$$

the indirect error ranges from $\pm$5% at the 1.01 cm range to $\pm$1% at the 4.05 cm range. At the average range of 2.54 cm, the particle velocity indirect error is approximately $\pm$2%.

The particle velocity time-of-arrival (TOA) direct error is related to the sampling rate of 0.1 μs. Because the TOA is determined from two recorded points (i.e., the explosive detonation time and the particle velocity TOA), the total direct error is $\pm$0.2 μs.

The wave speed indirect error is determined by considering the error between two adjacent particle velocity gages. The maximum distance error between two gages is $\pm$0.1 cm and the maximum time error is $\pm$0.2 μs. Given that the maximum error is for opposite trends between the distance and time measurements, the wave velocity error equation is governed by

$$\frac{(D \pm 0.1 \text{ cm}) / (T \mp 0.2 \ \mu\text{s}) - D/T}{D/T} = \pm \text{Error} \qquad \text{(C.5)}$$

where D and T are the differential distances and times between adjacent particle velocity gages. Equation (C.5) gives, on average, a wave speed indirect error of $\pm$10%.

DISTRIBUTION

ADMINISTRATOR
DEFENSE TECH INFO CTR
ATTN DTIC-OCP
8725 JOHN J KINGMAN RD STE 0944
FT BELVOIR VA 22060-6218 1

JHU/CPIA
ATTN SECURITY OFFICER
10630 LITTLE PATUXENT PKWY STE 202
COLUMBIA MD 21044-3200 1

CENTER FOR NAVAL ANALYSES
4401 FORD AVENUE
ALEXANDRIA VA 22302-0268 1

OFFICE OF NAVAL RESEARCH
ATTN 311 (R MALEK-MADANI)
BALLSTON TOWER 1
800 NORTH QUINCY STREET
ARLINGTON VA 22217-5660 1

OFFICE OF NAVAL RESEARCH
ATTN 33 (S LEKOUDIS)
BALLSTON TOWER 1
800 NORTH QUINCY STREET
ARLINGTON VA 22217-5660 1

OFFICE OF NAVAL RESEARCH
ATTN 333 (J FEIN)
BALLSTON TOWER 1
800 NORTH QUINCY STREET
ARLINGTON VA 22217-5660 1

OFFICE OF NAVAL RESEARCH
ATTN 333 (J GOLDWASSER)
BALLSTON TOWER 1
800 NORTH QUINCY STREET
ARLINGTON VA 22217-5660 1

OFFICE OF NAVAL RESEARCH
ATTN 4524 (J GAGORIK)
BALLSTON TOWER 1
800 NORTH QUINCY STREET
ARLINGTON VA 22217-5660 1

OFFICE OF NAVAL RESEARCH
ATTN 321 (W CHING)
BALLSTON TOWER 1
800 NORTH QUINCY STREET
ARLINGTON VA 22217-5660 1

OFFICE OF NAVAL RESEARCH
ATTN 321 (T SWEAN)
BALLSTON TOWER 1
800 NORTH QUINCY STREET
ARLINGTON VA 22217-5660 1

OFFICE OF NAVAL RESEARCH
ATTN 32CM (B. ALMQUIST)
BALLSTON TOWER 1
800 NORTH QUINCY STREET
ARLINGTON VA 22217-5660 1

NAVAL RESEARCH LABORATORY
ATTN 6386 (L D FLIPPEN)
4555 OVERLOOK DR SW
WASHINGTON DC 20375-5320 1

NAVAL RESEARCH LABORATORY
TECHNICAL LIBRARY
4555 OVERLOOK DR SW
WASHINGTON DC 20375-5320 1

NAVAL RESEARCH LABORATORY
ATTN 6440 (M EMERY)
4555 OVERLOOK DR SW
WASHINGTON DC 20375-5320 1

COMMANDER
DAHLGREN DIVISION
NAVAL SURFACE WARFARE CENTER
ATTN B44 (A. WARDLAW)
DAHLGREN VA 22448-5000 1

SUPERINTENDENT
NAVAL POST GRADUATE SCHOOL
ATTN TECHNICAL LIBRARY
MONTEREY CA 93940 1

SUPERINTENDENT
NAVAL POST GRADUATE SCHOOL
ATTN 69SG (Y SHIN)
MONTEREY CA 93940 1

DIRECTOR
DEFENSE SPECIAL WEAPONS AGENCY
ATTN TECHNICAL LIBRARY
6801 TELEGRAPH RD
ALEXANDRIA VA 22310-3398 1

DIRECTOR
DEFENSE SPECIAL WEAPONS AGENCY
ATTN SPSD (K GOERING)
6801 TELEGRAPH RD
ALEXANDRIA VA 22310-3398 1

DIRECTOR
DEFENSE SPECIAL WEAPONS AGENCY
ATTN SPSD (D BRUDER)
6801 TELEGRAPH RD
ALEXANDRIA VA 22310-3398 1

DIRECTOR
DEFENSE SPECIAL WEAPONS AGENCY
ATTN SPSD (M GILTRUD)
6801 TELEGRAPH RD
ALEXANDRIA VA 22310-3398 1

DIRECTOR
DEFENSE SPECIAL WEAPONS AGENCY
ATTN SPWE (E TREMBA)
6801 TELEGRAPH RD
ALEXANDRIA VA 22310-3398 1

LIBRARY OF CONGRESS
ATTN GIFT AND EXCHANGE
WASHINGTON DC 20540 1

LOS ALAMOS NATIONAL LABORATORY
ATTN TECHNICAL LIBRARY
PO BOX 1663
LOS ALAMOS NM 87545 1

LOS ALAMOS NATIONAL LABORATORY
ATTN B216 (B A KASHIWA)
PO BOX 1663
LOS ALAMOS NM 87545 1

LOS ALAMOS NATIONAL LABORATORY
ATTN F668 (J REPA)
PO BOX 1663
LOS ALAMOS NM 87545 1

LOS ALAMOS NATIONAL LABORATORY
ATTN EES5 (T DEY)
PO BOX 1663
LOS ALAMOS NM 87545 1

LOS ALAMOS NATIONAL LABORATORY
ATTN EES5 (R P SWIFT)
PO BOX 1663
LOS ALAMOS NM 87545 1

MECHANICAL ENGINEERING
JOHNS HOPKINS UNIVERSITY
ATTN A PROSPERETTI
BALTIMORE MD 21218 1

DYNAFLOW INC
ATTN G L CHAHINE
7210 PINDELL SCHOOL RD
FULTON MD 20759 1

DYNAFLOW INC
ATTN R DURAISWAMI
7210 PINDELL SCHOOL RD
FULTON MD 20759 1

SRI INTERNATIONAL
ATTN P GEFKEN
333 RAVENSWOOD AV
MENLO PARK CA 94025-3434 1

SRI INTERNATIONAL
ATTN M SANAI
333 RAVENSWOOD AV
MENLO PARK CA 94025-3434 1

ATR
ATTN J C S YANG
15210 DINO DRIVE
BURTONSVILLE MD 20866 1

ATR
ATTN C SMITH
15210 DINO DRIVE
BURTONSVILLE MD 20866 1

ATR
ATTN J GOELLER
15210 DINO DRIVE
BURTONSVILLE MD 20866 1

WEIDLINGER ASSOCIATES
ATTN I SANDLER
333 SEVENTH AV
NEW YORK NY 10001 1

SAIC
ATTN R BRITT
PO BOX 469
ST JOSEPH LA 71366-0469 1

SAIC
ATTN MS C2 (R ALLEN)
10260 CAMPUS POINT DR
SAN DIEGO CA 92121-1570 1

ROYAL SYSTEMS
ATTN O DENGEL
6294 BROWNTOWN RD
FRONT ROYAL VA 22630 1

D E PHILLIPS ASSOCIATES
ATTN D PHILLIPS
PO BOX 671
MIDDLETOWN MD 21769-0671 1

APPLIED RESEARCH ASSOCIATES
ATTN S BLOUIN
SOUTH ROYALTON VT 05068 1

APPLIED RESEARCH ASSOCIATES
ATTN D CHITTY
SOUTH ROYALTON VT 05068 1

APPLIED RESEARCH ASSOCIATES
ATTN W BROWN
2750 EISENHOWER AVE SUITE 104
ALEXANDRIA VA 22314 1

APPLIED RESEARCH ASSOCIATES
ATTN P DZWILESKI
2750 EISENHOWER AVE SUITE 104
ALEXANDRIA VA 22314 1

Internal:

PM3 (R. KAVETSKY)	1
40 (W. HINCKLEY)	1
40E (E. JOHNSON)	1
40P4 (L. TAYLOR)	1
410 (R. PLENGE)	1
4130 (P. ONG)	1
4140 (R. GARRETT)	1
420 (R. MCKEOWN)	1
4210 (D. TAM)	1
4210 (A. DARE)	1
4210 (T. YOUNG)	8
4220 (J. BURNS)	1
4220 (H. CHEN)	3
4220 (J. MCKIRGAN)	1
4220 (D. NELL)	1
4610 (H. MAIR)	1
4620 (W. MCDONALD)	1
4630 (J. GASPIN)	1
4630 (G. HARRIS)	1
9210 (R. GUIRGUIS)	1
9220 (D. TASKER)	1
9220 (W. WILSON)	1
8510	1
8530	3